NASA/TM-2006-214305

Shuttle Return To Flight Experimental Results: Cavity Effects on Boundary Layer Transition

Derek S. Liechty, Thomas J. Horvath, and Scott A. Berrry
Langley Research Center, Hampton, Virginia

June 2006

The NASA STI Program Office . . . in Profile

Since its founding, NASA has been dedicated to the advancement of aeronautics and space science. The NASA Scientific and Technical Information (STI) Program Office plays a key part in helping NASA maintain this important role.

The NASA STI Program Office is operated by Langley Research Center, the lead center for NASA's scientific and technical information. The NASA STI Program Office provides access to the NASA STI Database, the largest collection of aeronautical and space science STI in the world. The Program Office is also NASA's institutional mechanism for disseminating the results of its research and development activities. These results are published by NASA in the NASA STI Report Series, which includes the following report types:

- TECHNICAL PUBLICATION. Reports of completed research or a major significant phase of research that present the results of NASA programs and include extensive data or theoretical analysis. Includes compilations of significant scientific and technical data and information deemed to be of continuing reference value. NASA counterpart of peer-reviewed formal professional papers, but having less stringent limitations on manuscript length and extent of graphic presentations.

- TECHNICAL MEMORANDUM. Scientific and technical findings that are preliminary or of specialized interest, e.g., quick release reports, working papers, and bibliographies that contain minimal annotation. Does not contain extensive analysis.

- CONTRACTOR REPORT. Scientific and technical findings by NASA-sponsored contractors and grantees.

- CONFERENCE PUBLICATION. Collected papers from scientific and technical conferences, symposia, seminars, or other meetings sponsored or co-sponsored by NASA.

- SPECIAL PUBLICATION. Scientific, technical, or historical information from NASA programs, projects, and missions, often concerned with subjects having substantial public interest.

- TECHNICAL TRANSLATION. English-language translations of foreign scientific and technical material pertinent to NASA's mission.

Specialized services that complement the STI Program Office's diverse offerings include creating custom thesauri, building customized databases, organizing and publishing research results ... even providing videos.

For more information about the NASA STI Program Office, see the following:

- Access the NASA STI Program Home Page at ***http://www.sti.nasa.gov***

- E-mail your question via the Internet to help@sti.nasa.gov

- Fax your question to the NASA STI Help Desk at (301) 621-0134

- Phone the NASA STI Help Desk at (301) 621-0390

- Write to:
  NASA STI Help Desk
  NASA Center for AeroSpace Information
  7121 Standard Drive
  Hanover, MD 21076-1320

NASA/TM-2006-214305

Shuttle Return To Flight Experimental Results: Cavity Effects on Boundary Layer Transition

Derek S. Liechty, Thomas J. Horvath, and Scott A. Berrry
Langley Research Center, Hampton, Virginia

National Aeronautics and
Space Administration

Langley Research Center
Hampton, Virginia 23681-2199

June 2006

Available from:

NASA Center for AeroSpace Information (CASI)
7121 Standard Drive
Hanover, MD 21076-1320
(301) 621-0390

National Technical Information Service (NTIS)
5285 Port Royal Road
Springfield, VA 22161-2171
(703) 605-6000

Table of Contents

List of Figures

List of Tables

Abstract

The effect of an isolated rectangular cavity on hypersonic boundary layer transition of the windward surface of the Shuttle Orbiter has been experimentally examined in the Langley Aerothermodynamics Laboratory in support of an agency-wide effort to prepare the Shuttle Orbiter for return to flight. This experimental study was initiated to provide a cavity effects database for developing hypersonic transition criteria to support on-orbit decisions to repair a damaged thermal protection system. Boundary layer transition results were obtained using 0.0075-scale Orbiter models with simulated tile damage (rectangular cavities) of varying length, width, and depth. The cavities were positioned at a fixed location (x/L = 0.3) along the model centerline in a region of constant pressure gradient. Cavity length-to-depth ratio was systematically varied from 2.5 to 17.7 and length-to-width ratio of 1 to 8.5. Global heat transfer images using phosphor thermography of the Orbiter windward surface and the corresponding centerline heating distributions were used to infer the state of the boundary layer (laminar, transitional, or turbulent). Test parametrics include angles-of-attack of 30˚ and 40˚, sideslip angle of 0˚, free stream Reynolds numbers from 0.02×10^6 *to* 7.3×10^6 *per foot, edge-to-wall temperature ratio from 0.4 to 0.8, and normal shock density ratios of approximately 5 (Mach 6 and Mach 10 Air) and 12 (Mach 6* CF_4*). The database contained within this report will be used to formulate cavity-induced transition correlations using predicted boundary layer edge parameters.*

Introduction

In August of 2003, the Columbia Accident Investigation Board (CAIB) released the final report[1] of the investigation into the February 1, 2003 loss of the Space Shuttle *Columbia* and its seven-member crew. The report concluded that:

> *"The physical cause of the loss of Columbia and its crew was a breach in the Thermal Protection System on the leading edge of the left wing, caused by a piece of insulating foam which separated from the left bipod ramp section of the External Tank at 81.7 seconds after launch, and struck the wing in the vicinity of the lower half of Reinforced Carbon-Carbon panel number 8. During reentry this breach in the Thermal Protection System allowed superheated air to penetrate through the leading edge insulation and progressively melt the aluminum structure of the left wing, resulting in a weakening of the structure until increasing aerodynamic forces caused loss of control, failure of the wing, and breakup of the Orbiter."*

From the report came many recommendations, some specifically identified and prefaced as "before return to flight." These return-to-flight (RTF) recommendations were largely related to the physical cause of the accident, such as preventing the loss of foam, and on-orbit inspection and repair of the Thermal Protection System (TPS). For instance, recommendation R6.4-1 was listed for the TPS:

> *"For missions to the International Space Station, develop a practicable capability to inspect and effect emergency repairs to the widest possible range of damage to the Thermal Protection System, including both tile and Reinforced Carbon-Carbon, taking advantage of the additional capabilities available when near to or docked at the International Space Station.*
>
> *For non-Station missions, develop a comprehensive autonomous (independent of Station) inspection and repair capability to cover the widest possible range of damage scenarios.*
>
> *Accomplish an on-orbit Thermal Protection System inspection, using appropriate*

assets and capabilities, early in all missions.

The ultimate objective should be a fully autonomous capability for all missions to address the possibility that an International Space Station mission fails to achieve the correct orbit, fails to dock successfully, or is damaged during or after undocking."

Resolving and implementing these recommendations in a timely manner has facilitated return to flight.

In response to recommendation R6.4-1, strategies for a TPS repair capability have been developed. Figure 1 illustrates the potential steps associated with TPS damage disposition and repair at the time of this publication. For the first reflight missions, an on-orbit inspection, using a newly developed Orbiter Boom Sensor System (OBSS), will be used to characterize any impact damage to the Orbiter TPS prior to entry. Damage to the Reinforced Carbon-Carbon (RCC) will be assessed and repaired if possible. For the Orbiter wing leading edge, the RCC repair project team has selected a plug concept (shown conceptually in Fig. 1). Damage to the ceramic tiles that cover a majority of the windward surface is typically in the form of cavities resulting from debris impacts (from either foam or ice shed from the External Tank). Depending on the size and location of the resulting cavity, the disposition of the damage site will be either "use-as-is" or "repair" (as shown in Fig. 1) using a cure in place ablator (CIPA) using silicone. Of particular concern with ablative materials is the fact that under entry aeroheating environments, the repair material will not be shape stable and the local repair will likely swell and outgas into (and perhaps destabilize) the boundary layer. All three of these scenarios, use-as-is (cavity), repair with an ablator (protuberance and/or ablation products), or repair with the plug concept (protuberance), represent significant perturbations to the existing Shuttle outer mold lines (OML).

The present cavity boundary layer transition tests are part of a series of wind tunnel tests were performed[2,3] to characterize the effect of these localized OML changes on the Shuttle windward surface boundary layer. Hypersonic facilities at the NASA Langley Research Center (LaRC) that had a profound impact on the direction and utilization of agency resources[4] in the Columbia Accident Investigation (CAI) were subsequently requested to support RTF based upon prior experience with developing an Orbiter roughness-dominated boundary layer transition database[5,6]. The intent of experimental wind tunnel cavity, protuberance, and ablation investigations are to develop a technical basis to assess tile damage and to determine thresholds for deciding when to repair Shuttle TPS damage, whether a candidate repair material is feasible from a boundary layer transition perspective, and finally how large can a repair site be without adversely affecting the aerothermodynamic performance of the TPS. This report documents three wind tunnel tests conducted in the NASA Langley Aerothermodynamics Laboratory (LAL) to assess the effect of simulated impact damage (cavities) on the windward surface boundary layer of a 0.0075-scale Shuttle Orbiter. The corresponding analysis and development of the boundary layer transition correlation can be found in Ref. 7. A literature review was performed on the effects of cavities on boundary layer transition and additional reports not referenced are included at the end of this document.

Nomenclature

d	cavity depth (in.)
h	heat transfer coefficient, $h=q/(H_{aw}-H_w)$, (lbm/ft^2/s)
H	enthalpy (btu/lbm)
l	cavity length (in.)
L	model reference length (in)
p	pressure (psi)
q	surface heat transfer rate (btu/ft^2/s)
R_n	model reference nose radius (in)
Re	unit Reynolds number (1/ft)
T	temperature (˚R)
U	velocity magnitude (ft/s)
w	cavity width (in.)
x	axial distance from nose of model (in)

y	spanwise distance from centerline of model (in.)
α	angle-of-attack (deg)
ρ	density (slugs/ft^3)

Subscripts

∞	freestream static conditions
aw	adiabatic wall conditions
FR	conditions from Fay-Riddell calculation for a hemisphere
$t1$	reservoir conditions
$t2$	stagnation conditions behind a normal shock
w	wall conditions

Experimental Methods

Test Facilities

20-Inch Mach 6 Air Tunnel

The 20-Inch Mach 6 Air Tunnel (Fig. 2) is a blow-down facility in which heated, dried and filtered air is used as the test gas. The tunnel has a two-dimensional, contoured nozzle which opens into a 20.5-in. by 20-in. test section. The tunnel is equipped with a bottom-mounted injection system that can transfer a model from the sheltered model box to the tunnel center-line in less than 0.5 seconds. Run times of up to 15 minutes are possible in this facility, although for the current aeroheating study run times of only a few seconds were required. The nominal reservoir conditions of this facility are stagnation pressures of 30 psi to 500 psi with stagnation temperatures of 760 ˚R to 1000 ˚R, which very nearly produce perfect gas (γ = 1.4) free stream flows with Mach numbers between 5.8 and 6.1 and Reynolds numbers of 0.5x10^6/ft to 7.3x10^6/ft. The nominal flow conditions for this facility are listed in Table 1. A more detailed description of this facility is presented in Ref. 8.

Recent studies[9] have measured quantitative RMS free stream noise levels in the LaRC 20-Inch Mach 6 Air Tunnel obtained with a constant voltage anemometer (CVA) and a hybrid constant current anemometer (CCA). At reservoir conditions of p_{t1} = 130 psi and T_{t1} = 350° F, the CCA measurements yielded mass flux and total temperature fluctuations of 0.83% and 0.17%, respectively. The corresponding fluctuations from the CVA measurements were determined to be somewhat lower at 0.74% and 0.12%. In addition, the relative disturbance environment of the 20-Inch Mach 6 Air Tunnel has been deduced[10] via differences in smooth wall transition onset locations measured on a conical model previously tested in the LaRC Mach 6 Nozzle Test Chamber (NTC) Quiet Tunnel.

31-Inch Mach 10 Air Tunnel

The 31-Inch Mach 10 Air Tunnel (Fig. 2) is a blow-down facility in which heated, filtered air is used as the test gas. The tunnel has a square, contoured nozzle which opens into a 31 in. square test section. Models are supported on a hydraulically-operated, sidewall-mounted injection system that can transfer a model from the pneumatically sealed model box to the tunnel centerline in less than 0.6 seconds. Run times of approximately 60 seconds can be achieved, but the current study requires only a few seconds. The nominal reservoir conditions of this facility are stagnation pressures of 350 psi to 1450 psi with stagnation temperatures of 1740 ˚R to 1810 ˚R, which very nearly produce perfect gas (γ= 1.4) free stream flows with a Mach number of approximately 10 and Reynolds numbers of 0.2x10^6/ft to 2.2x10^6/ft. The nominal flow conditions for this facility are listed in Table 2. A more detailed description of this test facility is presented in Ref. 8. No free stream disturbance data is currently available for this facility.

20-Inch CF_4 Tunnel

The 20-Inch CF_4 Tunnel (Fig. 2) is a blow-down facility in which heated, filtered CF_4 is used as the test gas. The flow is expanded through a contoured, axisymmetric nozzle having a throat diameter of 0.446 in. and an exit diameter of 20 in., providing Mach 6 flow at the open-jet nozzle exit, which, due to the use of a heavy gas, more appropriately simulates (based upon normal shock density ratio) the Orbiter windward flow field at a Mach 18 flight condition. Models are supported at the nozzle exit by a hydraulically-driven injection/ support mechanism that can transfer the model to the tunnel center-line in about 0.5 seconds. Nominal run times are on the order of 10 seconds, but run times for the current study were only a few seconds. The low enthalpy (as opposed to impulse-type) CF_4 tunnel avoids complex chemistry typically associated with high enthalpy facilities by the use of a heavier than air test gas with a low ratio of specific heats and a correspondingly high normal shock density ratio characteristic of hypervelocity flight. In conjunction with the Mach 6 Air Tunnel, this tunnel provides the capability to test at the same free-stream Mach and Reynolds numbers, but at two values of density ratio (approximately 5 in air and 12 in CF_4). This density ratio of 12 for CF_4 is relatively close to the values of 15-18 encountered near peak heating during entry of the Orbiter. The nominal reservoir conditions of this facility are stagnation pressures of 100 psi to 2000 psi with stagnation temperatures of 1100 ˚R to 1480 ˚R, which produce Reynolds numbers of $0.05x10^6$/ft to $0.75x10^6$/ft, a free stream gamma of 1.21 and a post normal shock gamma of 1.1, and a normal shock density ratio of 11.7. The nominal flow conditions for this facility are listed in Table 3. A more detailed description of this facility is presented in Ref. 8. No free stream disturbance data is currently available for this facility.

Phosphor Thermography Technique

Global surface heating distributions were calculated using the digital optical measurement method of two-color, relative-intensity, phosphor thermography[11-14]. Ceramic wind tunnel models are coated with a phosphor compound that fluoresces in two separate regions (green and red) of the visible light spectrum. During a wind tunnel run, the phosphor-coated model is illuminated by ultraviolet (UV) light sources, and the resulting fluorescent intensity of the model is recorded and digitized through a color CCD (charge coupled device) camera (Fig. 3). The fluorescent intensity is dependent on both the intensity of the incident UV light and the local model surface temperature. The UV intensity dependence is removed by taking the ratio of the green to red intensity images, from which surface temperature distributions can be determined through prior calibrations. Images are acquired before the wind tunnel run and after injection of the model to the tunnel centerline during a run. Global heat transfer distributions are then computed from these temperature data using one-dimensional heat conduction theory assuming a constant step increase in heat transfer coefficient[14].

The global phosphor thermography technique is now the standard method for aeroheating studies in the LAL. The global data obtained using this method can be used to identify the surface heating effects of complex three-dimensional flow phenomena such as transition fronts, vortex structures, and shock interactions which are difficult to examine using conventional discrete-sensor methods such as thin-film resistance gages or coaxial surface thermocouples.

Test Model Description

To support the cavity boundary layer transition testing, cast ceramic models (9.6-inch long from nose to body-flap hinge) were manufactured, all of which share a common construction technique. To accomplish this quickly, a pre-existing epoxy based mold constructed from the 0.0075-scale metallic force and moment model used during aerodynamic testing[15] in support of the CAI was used to fabricate models. Specifically, wax patterns created from this mold were used to cast each individual Orbiter model using a patented[16] silica ceramic slip casting technique. The cast silica shells were then back-filled with a hydraulically setting magnesia ceramic for strength and support of the base mounted cylindrical sting. Finally, the models were coated with a mixture of phosphors suspended in a silica-based colloidal binder. The phosphor coatings typically do not require refurbishment between runs in the wind tunnel and have been measured to be approximately 0.001-in. thick. Global surface roughness measurements associated with a phosphor coated model were obtained with a non-intrusive laser-based system. Nominal surface roughness was determined to be approximately 400 micro-inches. For a detailed description of the fabrication process and surface integrity measurements used for this test, see Ref. 17. The set of models constructed for both the present cavity testing as well as the protuberance testing is shown in Fig. 4.

As shown in Fig. 5, small, ink-based identification marks were transferred to the model windward surface to assist in the model alignment process when installed in the test section and to aid in geometric scaling used during the data reduction process. These marks, referred to as fiducial marks, do not influence the flow over the model surface. The fiducial marks can be seen in processed run images as small discolorations and in the heating distributions as “noise” in the immediate vicinity of the identification marker. The locations of these marks, shown in Fig. 6, were used primarily in support of the protuberance testing and are listed in Table 4. A laser alignment system (Fig. 7) is then used in the tunnel to align the model with the flow by lining the centerline fiducial marks to the laser reference line that is projected onto the Orbiter model.

Each ceramic model possessed a single rectangular cavity located along the windward centerline with the entrance to the cavity at x/L = 0.3. The cavities that simulated TPS damage were added to the ceramic models by a CO_2 based laser ablation system (Fig. 8, Ref. 17). The laser system uses galvanometrically driven beam scanners to remove silica material to form a single cavity in each of the fused silica ceramic test models. The system was originally configured and used to remove or ablate material from flat surfaces or films and modified, as shown in Fig. 8, to accommodate the ceramic models. To form a cavity on the model surface, the orbiter model is first clamped by the sting to the precision V-block just off the X-Y stage of the positioning system. A Starrett precision level is placed on the lower surface tail section to vertically align the model. Using the video camera alignment system, the model is aligned in the x-y lane using fiducial marks on the model. The camera cross-hairs are used to locate the fiducial mark a the desired cavity site.

Cavity dimensions are controlled by programming the laser for the desired cavity length, width, and depth. Typical CO_2 laser parameter settings are 15 percent power, 4 KHz frequency, and 100 μs pulse width. The scanning density is 1429 passes per inch (0.0007-in. step) with a 0.002-in. diameter spot size and a scanning speed of 10 in./sec. The cavity depth is controlled by the number of passes made by the laser. A typical pass removes approximately 0.003 to 0.004-in. of surface material. As the cavity depth increases, the focal point of the laser must be adjusted to keep the laser spot size consistent. The depth of the cavity is measured with the laser system’s vertical height sensor and verified with a depth micrometer. The x-y dimensions of each cavity are verified using the video camera alignment system. Table 5 summarizes the cavity dimensions on each Orbiter model. Close-up images and the relations between cavity designations are presented in Fig. 9. The nominal cavities are shown in the center of the figure as length parametrics. Variations of the nominal cavities are then show at the top of the figure as depth parametrics and at the bottom of the figure as width parametrics.

Data Reduction

One-dimensional, semi-infinite solid heat conduction theory[14] was used to compute surface heating distributions from the global surface temperature data acquired through the technique of two-color, relative-intensity, phosphor thermography. A constant heat-transfer coefficient is assumed in this theory, and empirical corrections[14] are made to account for changes in model substrate thermal properties with temperature. Phosphor images were acquired shortly after injection of the model to the tunnel centerline, which requires less than one second.

Data were extracted in the IHEAT[14] software package axially along the centerline. Results are presented herein in terms of a non-dimensional heat transfer coefficient ratio, h/h_{FR}, where h_{FR} is the theoretical stagnation point heating coefficient to a 0.09-in. radius sphere (the nose radius of a scaled Orbiter model) computed using the method of Fay-Riddell[18] for a wall temperature of 540 ˚R.

Error Analysis

Absolute heating measurements are not required for determining the location of transition onset as this location on the model surface is determined by the departure of the measured non-laminar heating level from a baseline undisturbed laminar value. Discussion of measurement uncertainty is included for the sake of completeness. The estimated experimental uncertainty of the heating results as obtained by the thermographic phosphor system is a function of fluorescent intensity, which is dependent on model surface temperature. For higher surface temperatures (greater than 720˚R), such as those on most of the windward surface, the uncertainty[14] is approximately ±8% to ±10%, while for lower temperatures (less than 585 ˚R), the uncertainty is approximately ±15% to ±20%. Additional measurement uncertainty can be introduced due to internal three-dimensional heat conduction in high-gradient regions such as the leading edge of the Shuttle Orbiter. This uncertainty is estimated to vary from less than ±5% at the lowest test Reynolds number to greater than ±10% at the highest Reynolds numbers.

Uncertainties can be introduced when extracting line cut data from an image due to perspective distortion of the image, lack of pixel resolution in high-gradient regions, and lack of precision in locating fiducial marks. These errors are estimated to be less than ±5% on relatively flat surfaces and up to ±10% on highly curved surfaces.

A square root of the sum-of-the-squares estimate for the total uncertainty based on the above factors gives a worst-case experimental uncertainty range of ±13% on flat areas of the windward surface to ±25% on areas such as the leeward surface (not shown in this study) at high Reynolds numbers. In addition to the sources of experimental uncertainty discussed above, additional uncertainty in transition onset may also be influenced by inherent differences in model surface roughness between models or coating degradation which occurs over the length of a test due to handling of the model and pitting of the surface from particle impacts. Because this uncertainty increases over time and varies from model to model, no fixed value for the uncertainty is assigned.

Test Matrix and Tunnel Conditions

The data were obtained on the Space Shuttle Orbiter models at angles-of-attack of 30-deg and 40-deg and free stream Reynolds numbers between 0.02×10^6 and 7.38×10^6 per foot. The run matrices for the cavity boundary layer transition test series is listed in chronological order in Tables 6-8. For each run, test section flow conditions were computed using the GASPROPS[19] code with the measured reservoir stagnation pressures and temperatures and pitot pressure calibrations of the facility as inputs.

Experimental Results

Preface

Heating images and distributions are presented in normalized form. For the global images, a constant color bar maximum value was selected for data presentation to maintain consistency when viewing or comparing the images. On the contour scale, the colors tending towards red indicate areas of higher heating (temperatures) while the colors towards blue represent areas of lower heating. In areas where the local heating exceeded the selected maximum color bar value, such as the nose region or wing leading edges, a purple "over-scale" will be evident.

In the global images, transition to turbulence is readily identified downstream of the cavity by the wedge-shaped "footprint" of increased temperature (heating). Centerline heating distributions are used to more quantitatively determine transition onset and the spatial location is interpreted herein as the departure of the measured non-laminar heating level from a baseline undisturbed laminar value.

Global surface heating data in this report are organized by wind tunnel and presented in three appendices. Within each appendix, sequential run images (Reynolds number) and corresponding centerline heating distributions are organized by cavity dimension and angle-of-attack. Each global phosphor thermography image is appended by the averaged Reynolds number as computed with all runs targeting the same free stream conditions. The Reynolds numbers listed in the corresponding centerline heating plot are the Reynolds numbers based on the actual reservoir pressure and temperature. As such, the two Reynolds numbers may not be identical (see Tables 1-3 for average tunnel conditions and associated uncertainties). A discussion of model surface roughness and run to run variability can be viewed in Ref. 2.

Cavity-Induced Transition Trends from Surface Heating Data

Isolated cavity hypersonic boundary layer transition effects were obtained in all three LAL facilities based upon the existing Reynolds number capability of the wind tunnel (cavity depth-to local boundary layer thickness range of 0.5 to 4.8). General trends observed from the images and centerline heating distributions are summarized:

1) Longer cavities were more likely to force transition. Systematic variation of cavity length-to-depth ratio from 2.5 to 17.7 was found to promote hypersonic boundary layer transition earlier.

2) Wider cavities were more likely to force transition. For a fixed unit Reynolds number, increasing cavity width-to-depth ratio from 0.1 to 0.4 was found to move the transition onset location forward, closer to the cavity site.

3) Deeper cavities were more likely to force transition. For a fixed unit Reynolds number, increasing cavity depth-to-length ratio from 0.05 to 0.2 was found to move the transition onset location aft, away from the cavity site.

4) For a fixed cavity geometry, decreasing the angle-of-attack from 40˚ to 30˚ was found to move transition onset location aft, away from the cavity site.

5) Increasing Mach number appeared to change the character of the transition movement and spreading on the windward surface. At Mach 6, transition onset generally followed a systematic movement from the aft forward to the cavity site. In contrast, at Mach 10 the movement of transition onset was observed to move forward, to the cavity site in a rather abrupt fashion. As expected, for comparable Reynolds numbers, increasing Mach number appeared to delay transition onset and decrease the spreading angle associated with the turbulent footprint.

Summary

The effect of an isolated rectangular cavity on hypersonic boundary layer transition of the windward surface of the Shuttle Orbiter has been experimentally examined in the Langley Aerothermodynamics Laboratory. The tests were in support of an agency-wide effort to prepare the Shuttle Orbiter for return to flight. This experimental study was initiated to provide a cavity effects database for developing hypersonic transition prediction methodologies and to provide a technical basis to support on-orbit decisions to repair a damaged thermal protection system. Boundary layer transition data were obtained using 0.0075-scale Orbiter models with simulated tile damage (rectangular cavities) of varying length, width, and depth.

Acknowledgements

The authors would like to acknowledge the contributions of the following individuals to this research: Harry Stotler, Grace Gleason, Roland Hatten, and Teck-Seng Kwa for operation of the 20-Inch Mach 6 Air Tunnel and data acquisition support; Melanie Lawhorne, Christal Kellam, and Glenn Bittner for operation of the 20-Inch CF_4 Tunnel and data acquisition support; Johnny Ellis Rhonda Mills, Henry Fitzgerald, and Kevin Hollingsworth for operation of the 31-Inch Mach 10 Air Tunnel and data acquisition support; Mike Powers and Mark Griffith for fabrication of the ceramic test models; and Ed Covington and Pete Veneris for model fidelity measurements and fiducial mark placement.

References

1. http://www.caib.us/news/report/default.html

2. Liechty, D. S., Berry, S. A., and Horvath, T. J., “Shuttle Return To Flight Experimental Results: Protuberance Effects on Boundary Layer Transition,” NASA TM 2006-214306, 2006.

3. Merski, N. R., “A Preliminary Investigation of the Effect of Mass Addition on Boundary Layer Transi-

tion for Shuttle Return To Flight," OEAN-0305-010, 2005.

4. Horvath, T. J., "Experimental Aerothermodynamics In Support of the Columbia Accident Investigation," AIAA Paper 2004-1387, January 2004.

5. Berry, S. A. and Hamilton, H. H. II, "Discrete Roughness Effects on Shuttle Orbiter at Mach 6," AIAA Paper 2002-2744, June 2002.

6. Berry, S. A., Bouslog, S. A., Brauckmann, G. J. and Caram, J. M., "Shuttle Orbiter Experimental Boundary-Layer Transition Results with isolated Roughness," *Journal of Spacecraft and Rockets*, Vol. 35, No. 3, pp. 241-248, May-June 1998.

7. Horvath, T. J., "Orbiter Cavity Boundary Layer Transition: Experimental Observations, Analysis, and Correlations," OEAN-0305-009, 2005.

8. Micol, J.R., "Hypersonic Aerodynamic/Aerothermodynamic Testing Capabilities at Langley Research Center: Aerothermodynamic Facilities Complex," AIAA Paper 95-2107, June 1995.

9. Chokani, N., Shipluk, A. N., Sidorenko, A. A., and McGinley, C. B., "Comparison Between a Hybrid Constant-Current Anemometer and Constant-Voltage Anemometer in Hypersonic Flow," AIAA Paper 2004-2248, June 2004.

10. Horvath, T. J., Berry, S. A., Hollis, B. R., Chang, C. and Singer, B. A., "Boundary Layer Transition On Slender Cones in Conventional and Low Disturbance Mach 6 Wind Tunnels," AIAA Paper 2002-2743, June 2002.

11. Buck, G.M., "Automated Thermal Mapping Techniques Using Chromatic Image Analysis," NASA TM 101554, April 1989.

12. Buck, G.M., "Surface Temperature/Heat Transfer Measurement Using a Quantitative Phosphor Thermography System," AIAA Paper 91-0064, January 1991.

13. Merski, N.R., "A Relative-Intensity, Two-Color Phosphor Thermography System," NASA TM 104123, September 1991.

14. Merski, N.R., "An Improved Two-Color Relative-Intensity Phosphor Thermography Method For Hypersonic Wind Tunnel Aeroheating Measurements," NASA CDTP-1017, February 2001.

15. Brauckmann, G. J., and Scallion, W. I., "Experimental Hypersonic Aerodynamic Characteristics of the Shuttle Orbiter for a Range of Damage Scenarios," 27th Airbreathing Propulsion Subcommittee, JANNAF, 2003.

16. Buck, G.M., and Vasques, P., "An Investment Ceramic Slip-Casting Technique for Net-Form, Precision, Detailed Casting of Ceramic Models," U.S. Patent 5,266,252, November 1993.

17. Buck, G. M., "Fabrication of 0.0075-Scale Orbiter Phosphor Thermography Test Models for Shuttle RTF Aeroheating Studies," NASA TM 2006-214303, 2006.

18. Fay, J.A., and Riddell, F.R., "Theory of Stagnation Point Heat Transfer in Dissociated Air," *Journal of Aeronautical Sciences*, Vol. 25, No. 2, 1958, pp. 73-85.

19. Hollis, B.R., "Real-Gas Flow Properties for NASA Langley Research Center Aerothermodynamic Facilities Complex Wind Tunnels," NASA CR 4755, September 1996.

Literature Search

Adams, J. C., Jr., "Numerical Calculation of Hypersonic Laminar Cavity Flows," AIAA 74-707, July 1974.

Ahuja, K. K. and Mendoza, J., "Effects of Cavity Dimensions, Boundary Layer, and Temperature on Cavity Noise with emphasis on Benchmark Data to Validate Computational Aeroacoustics codes," NASA CR-4653, 1995.

Avery, D. E., "Aerodynamic Heating in Gaps of Thermal Protection System Tile Arrays in Laminar and Turbulent Boundary Layers," NASA TP-1187, July 1978.

Avery, D. E., "Experimental Aerodynamic Heating to Simulated Space Shuttle Tiles in Laminar and Turbulent Boundary Layers with Variable Flow Angles at a Nominal Mach Number of 7," NASA TP-2307, August 1985.

Babinsky, H. and Edwards, J. A., "The Influence of Large Scale Roughness on a Turbulent Hypersonic Boundary Layer Approaching a Compression Corner," AIAA 1995-0334, January 1995.

Bertin, J. J. and Goodrich, W. D., "Aerodynamic Heating for Gaps in Laminar and Transitional Boundary Layers," AIAA 1980-0287, January 1980.

Bertin, J. J., Tedeschi, W. J., Kelly, D. P., Bustamante, A. C. and Reece, E. W., "Analysis of Shear-Layer

Probe Data for Holes in Hypersonic Configurations," AIAA 1988-0373, January 1988.

Blair, A. B., Jr. and Stallings, R. L., Jr., "Supersonic Axial-Force Characteristics of a Rectangular-Box Cavity with Varis Length-to-Depth Ratios in a Flat Plate," NASA TM-87659, 1986.

Bouslog, S. A., An, M. T. and Derry, S. M., "Orbiter Windward-Surface Boundary-Layer Transition Flight Data," *NASA Langley Research Center, Orbiter Experiments (OEX) Aerothermodynamics Symposium*, Part 2, pp 703-739, April 1995.

Brandon, H. J., Masek, R. V. and Dunavant, J. C., "Aerodynamic Heating to Corrugation Stiffened Structures in Thick Turbulent Boundary Layers," *AIAA Journal*, Vol. 13, No. 11, pp 1460-1466, November 1975.

Brew, R. A., Saydah, A. R., Nestler, D. E. and Florence, D. E., "Thermal Performance Evaluation of RSI Panel Gaps for Space Shuttle Orbiter," *Journal of Spacecraft and Rockets*, Vol. 10, No. 1, pp 23-28, January 1973.

Burggraf, O. R., "A Model of Steady Separated Flow in Rectangular Cavities at High Reynolds Number," Proceedings of the 1965 Heat Transfer and Fluid Mechanics Conference, Stanford University Press, pp 190-229, 1965.

Chang, P. K., "The Reattachment of Laminar Cavity Flow with Heat Transfer at Hypersonic Speed," AFOSR TR-66-0135, April 1966.

Charbonnier, J. M. and Boerrigter, H. L., "Contribution to the Study of Gap Induced Boundary Layer Transition in Hypervelocity Flow," AIAA 1993-5111, November 1993.

Charwat, A. F., Roos, J. N., Dewey, C. F., Jr. and Hitz, J. A., "An Investigation of Separated Flow Regions - Part I: The Pressure Field," *Journal of Aerospace Sciences*, Vol. 28, No. 6, pp 457-470, June 1961.

Charwat, A. F., Dewey, C. F., Jr., Roos, J. N. and Hitz, J. A., "An Investigation of Separated Flow Regions - Part II: Flow in the Cavity and Heat Transfer," *Journal of Aerospace Sciences*, Vol. 28, No. 7, pp 513-527, July 1961.

Cheatwood, F. M., Merski Jr., N. R., Riley, C. J. and Mitcheltree, R. A., "Aerothermodynamic Definition for the Genesis Sample Return Capsule," AIAA 2001- 2889, June 2001.

Chin, E., Rafiinejad, and Seban, R. A., "Prediction of the Flow and Heat Transfer in a Rectangular Wall Cavity with Turbulent Flow," *Transactions of the ASME, Journal of Applied Mechanics*, Vol. 39, Series E, No. 2, pp 351-358, June 1972.

Coats, J. D., Rhudy, R. W. and Edmunds, E. W., "Effects of Surface Gaps and Steps on Laminar Heat-Transfer Rates at Local Mach Numbers From 3 to 10," AEDC TR-70-17, February 1970.

Driftmyer, R. T., "A Forward Facing Step Study: The Step Height Less than the Boundary Layer Thickness," NOLTR 73-98, May 1973.

Dunavant, J. C. and Throckmorton, D. A., "Aerodynamic Heat Transfer to RSI Tile Surfaces and Gap Intersections," *Journal of Spacecraft and Rockets*, Vol. 11, No. 6, pp 373-440, June 1974.

Emery, A. F., Loll, M. and Sadunas, A. A., "Heat Transfer and Pressure Distribution in Open-Cavity Flow," ASME 65-WA/HT-37.

Emery, A. F., "Recompression Step Heat Transfer Coefficients for Supersonic Open Cavity Flow," *Journal of Heat Transfer*, pp 168-170, 1969.

Fletcher, L. S., Brigss, D. G. and Page, R. H., "A Review of Heat Transfer in Separated and Reattached Flows," AIAA 1970-767.

Foster, T. F. and Dye, W. H., "Convective Heat-Transfer Test Results for a Gap, Cylindrical-Protuberance, and Shock-Impingement Flap-Plate Model (15-0 insert VIII) in the NASA Ames 3.5-foot Hypersonic Wind Tunnel (IH27)," NASA CR-151372, April 1979.

Galenter, S. A., "An Experimental Summary of Plasma Arc Exposures of Space Shuttle High-Temperature Reusable Surface Insulation Tile Array with a Single Missing Tile (Conducted at Ames Research Center)," NASA SP-379, Paper 18, 1975.

Gineaux, J. J., "The Existence of Three-Dimensional Perturbations in the Reattachment of a Two-Dimensional Supersonic Boundary Layer After Separation," AGARD 272, April 1960.

Hahn, M., "Experimental Investigation of Separated Flow over a Cavity at Hypersonic Speed," *AIAA Journal*, Vol. 7, No. 6, pp. 1092-1098, June 1969.

Haugen, R. L. and Dhanak, A. M., "Heat Transfer in Turbulent Boundary Layer Separation over a Surface Cavity," *Journal of Heat Transfer*, Vol. 89, pp 335-340, 1967.

Heller, H. H. and Bliss, D. B., "The Physical Mechanism of Flow-Induced Pressure Fluctuations in Cavities and the Concepts for their Suppression," AIAA 1975-491, March 1975.

Hodgson, J. W., "Heat Transfer in Separated Laminar Hypersonic Flow," *AIAA Journal*, Vol. 8, No. 12, pp. 2291-2293, December 1970.

Hollis, B. R. and Liechty, D. S., "Boundary Layer Transition Correlations and Aeroheating Predictions for Mars Smart Lander," AIAA 2002-2745, June 2002.

Holloway, P. F., Sterrett, J. R. and Creekmore, H. S., "An Investigation of Heat Transfer within Regions of Separated Flow at a Mach Number of 6.0," NASA TN D-3074, November 1965.

Hunt, L. R., "Aerodynamic Heating and Loading within Large Open Cavities in Cone and Cone-Cylinder-Flare Models at Mach 6.7," NASA TN D-7403, March 1974.

Hunt, L. R., "Aerodynamic Heating in Large Cavities in an Array of RSI Tiles," NASA TN D-8400, 1977.

Jackson, A., Soltani, S. and Hillier, R., "Two-Dimensional and Three-Dimensional Cavity Flows at Hypersonic Speeds," *Proceedings of the Third European Symposium on Aerothermodynamics for Space Vehicles*, November 1998.

Johnson, C. B., "Heat Transfer Data to Cavities Between Simulated RSI Tiles at Mach 8," NASA CR-128770, June 1973.

King, R. A., Creel Jr., T. R. and Bushnell, D. M., "Experimental Transition Investigation of a Free-Shear Layer Above a Cavity at Mach 3.5," *Journal of Propulsion*, Vol. 7, No. 4, July-August 1991.

Lamb, J. P., "Analysis and Correlation of Convective Heat Transfer Measurements for Open Cavities in Supersonic Flow," AIAA 1980-1526, July 1980.

Larson, H. K., "Heat Transfer in Separated Flows," *Journal of the Aero/Space Sciences*, Vol. 26, No. 11, November 1959.

Larson, H. K. and Keating, Jr., S. L., "Transition Reynolds Numbers of Separated Flows at Supersonic Speeds," NASA TN D-349, December 1960.

Liechty, D. S., Berry, S. A., Hollis, B. R. and Horvath, T. J., "Comparison of Methods for Determining Boundary Layer Edge Conditions for Transition Correlations," AIAA 2003-3590, June 2003.

Martindale, W. R., "Pressure and Heat-Transfer Tests of the ABRV at Mach Numbers 6 and 10," AEDC TSR-78-V50, November 1978.

Morgenstern, A. and Chokani, N., "Hypersonic Flow Past Open Cavities," *AIAA Journal*, Vol. 32, pp 2387-2393, 1994.

Nestler, D. E. and Saydah, A. R., "Heat Transfer to Steps and Cavities in Hypersonic Turbulent Flow," AIAA 1968-673.

Nestler, D. E., Saydah, A. R. and Auxer, W. L., "Heat Transfer to Steps and Cavities in Hypersonic Turbulent Flow," *AIAA Journal*, Vol. 7, No. 7, pp. 1368-1370, July 1969.

Nestler, D. E., "Hypersonic Laminar Cavity Heat Transfer," Presented at 4th International Heat Transfer Conference, August 31-September 5 1970, Versailles, France.

Nestler, D. E., "An Experimental and Analytical Study of Antenna Window Effects on Aerothermodynamics," BMO TR-80-54, December 1979.

Nestler, D. E., "An Experimental Study of Cavity Flow on Sharp and Blunt Cones at Mach 8," AIAA 1981-0335, January 1981.

Nestler, D. E., "The Effects of Surface Discontinuities on Convective Heat Transfer in Hypersonic Flow," AIAA 1985-0971, June 1985.

Netterfield, M. P. and Hilier, R., "Experiment and Computation in Hypersonic Cavity Flows," AIAA 1989-1842, June 1989.

Nicoll, K. M., "An Experimental Investigation of Laminar Hypersonic Cavity Flows Part II: Heat Transfer and Recovery Factors Measurements," ARL 63-73.

Nicoll, K. M., "A Study of Laminar Hypersonic Cavity Flows," *AIAA Journal*, Vol. 2, No. 9, September 1964.

Noble, J. A., "Wind Tunnel Tests of the Performance Technology Program, Phase II, GE Vehicle at Mach 8 (Phase 3, Heat Transfer Tests)", AEDC-TSR-79-V57, October 1979.

Plentovich, E. B., Stallings, Jr., R. L. and Tracy, M. B., "Experimental Cavity Pressure Measurements at Subsonic and Transonic Speeds - Static-Pressure Results," NASA TP-3358, 1993.

Rhudy, R. P. and Magnan, Jr., J. D., "Investigations of Heat-Transfer Distribution in Several Cavity and Step Configurations at Mach 10," AEDC TDR-64-220, October 1964.

Rhudy, J. P. and Magnan, Jr., J. D., "Turbulent Cavity Flow Investigation at Mach Numbers 4 and 8," AEDC TD-66-73, June 1966.

Shchukin, V. K., Gortyshov, Y. F., Varfolomeev, I. M. and Nadyrov, N. A., "Influence of Relative Depth and Reynolds Number on Heat Transfer in Cavities in Compressible Gas Flow," *Soviet Aeronautics*, Vol. 23, No. 3, pp 83-86, 1980.

Stallings, R. L., Jr. and Wilcox, F. J., Jr., "Experimental Cavity Pressure Distributions at Supersonic Speeds," NASA TP-2683, June 1987.

Stallings, R. L., Jr., Wilcox, F. J., Jr. and Forrest, D. K., "Measurements of Forces, Moments, and Pressures on a Generic Store Separating From a Box Cavity at Supersonic Speeds," NASA TP-3110, September 1991.

Throckmorton, D. A., "Heat Transfer to Surface and Gaps of RSI Tile Arrays in Turbulent Flow at Mach 10.3," NASA TM-X-71945, April 1974.

Tracy, M. B., Plentovich, E. B. and Chu, J., "Measurements of Fluctuating Pressure in a Rectangular Cavity in Transonic Flow at High Reynolds Numbers," NASA TM-4363, 1992.

Tracy, M. B. and Plentovich, E. B., "Characterization of Cavity Flow Fields Using Pressure Data Obtained in the Langley 0.3-Meter Transonic Cryogenic Tunnel," NASA TM-4436, March 1993.

Tracy, M. B. and Plentovich, E. B., "Cavity Unsteady-Pressure Measurements at Subsonic and Transonic Speeds," NASA TP-3669, December 1997.

Unalmis, O. H., Clemens, N. T. and Dolling, D. S., "Experimental Study of Shear-Layer/Acoustics Coupling in Mach 5 Cavity Flow," *AIAA Journal*, Vol. 39, No. 2, pp. 242-252, February 2001.

Weinstein, I., Avery, D. E. and Chapman, A. J., "Aerodynamic Heating to the Gaps and Surfaces of Simulated Reusable-Surface-Insulation Tile Arrays in Turbulent Flow at Mach 6.6," NASA TM-X-3225, November 1975.

Wieting, A. R., "Experimental Investigation of Heat Transfer Distributions in Deep Cavities in Hypersonic Separated Flow," NASA TN-D-5908, 1970.

Wyborny, W., Kabelitz, H. P. and Schepers, H. J., "Hypersonic Investigation on the Local and Average Heat Transfer in Cavities and After Steps of Bodies of Revolution," AGARD Conference Proceedings No. 19, Fluid Physics of Hypersonic Wakes.

Zhang, J., Morishita, E., Okunuki, T. and Itoh, H., "Experimental and Computational Investigation of Supersonic Cavity Flows," AIAA 2001-1755,

Tables

Table 1: 20-Inch Mach 6 Air Tunnel Average Flow Conditions.

Re_∞ (1/ft)	M_∞	p_{t1} (psi)	T_{t1} (˚R)
0.56×10^6	5.93	30.63	856.33
0.84×10^6	5.91	46.20	863.70
1.07×10^6	5.93	61.02	875.05
1.39×10^6	5.95	81.19	887.51
1.71×10^6	5.96	101.52	896.23
2.08×10^6	5.97	126.25	904.11
2.48×10^6	5.98	151.16	905.37
2.97×10^6	5.99	181.86	905.38
3.46×10^6	6.00	212.52	906.28
4.12×10^6	6.00	252.54	906.36
4.65×10^6	6.01	292.75	920.01
5.41×10^6	6.02	343.57	924.47
6.13×10^6	6.02	393.28	929.03
6.98×10^6	6.03	450.89	933.62
7.38×10^6	6.03	476.62	933.80

Table 2: 31-Inch Mach 10 Air Tunnel Average Flow Conditions.

Re_∞ (1/ft)	M_∞	p_{t1} (psi)	T_{t1} (˚R)
0.57×10^6	9.33	351.86	1792.29
0.83×10^6	9.52	539.82	1804.22
1.08×10^6	9.63	722.73	1803.13
1.16×10^6	9.66	783.66	1800.33
1.26×10^6	9.69	855.92	1797.45
1.31×10^6	9.70	894.09	1801.57
1.45×10^6	9.74	1004.46	1808.34
1.55×10^6	9.76	1076.36	1803.24
1.62×10^6	9.78	1125.83	1799.00
1.81×10^6	9.81	1253.88	1792.10
2.07×10^6	9.86	1453.24	1792.49

Table 3: 20-Inch CF_4 Tunnel Average Flow Conditions.

Re_∞ (1/ft)	M_∞	p_{t1} (psi)	T_{t1} (˚R)
0.02×10^6	5.86	63.02	1254.10
0.05×10^6	5.82	165.81	1256.95
0.09×10^6	5.89	255.12	1181.28
0.17×10^6	5.85	507.55	1225.04
0.25×10^6	5.85	766.93	1237.49
0.32×10^6	5.93	863.55	1180.20
0.35×10^6	5.86	1050.07	1230.49
0.46×10^6	5.92	1270.56	1191.76
0.50×10^6	5.87	1510.81	1236.31
0.60×10^6	5.82	2066.55	1293.28

Table 4: Shuttle Orbiter Fiducial Mark Locations.

x/L	y/L 30-deg. INV	y/L 40-deg. INV	y/L 40-deg. VIS
0.10	0.2020	0.0134	0.0017
0.20	0.0370	0.0269	0.0084
0.30	0.0571	0.0454	0.0236
0.40	0.0824	0.0706	0.0504
0.50	0.1092	0.1008	0.0874
0.60	0.1462	0.1429	0.1311
0.62		0.1590	0.1489
0.64		0.1754	0.1701
0.66		0.1937	0.1908
0.68		0.2130	0.2111
0.70		0.2320	0.2298
0.80		0.3070	0.2937
1.00			

Table 5: Cavity Dimensions.

Model	*l* (in)	*w* (in)	*d* (in)	*l/d*	*w/d*
RTF-BLT-C1	0.074	0.071	0.0300	2.47	2.37
RTF-BLT-C2	0.157	0.078	0.0300	5.23	2.60
RTF-BLT-C3	0.217	0.071	0.0297	7.31	2.39
RTF-BLT-C4	0.299	0.072	0.0300	9.97	2.40
RTF-BLT-C5	0.445	0.072	0.0350	12.71	2.06
RTF-BLT-C6	0.602	0.072	0.0340	17.71	2.12
RTF-BLT-C7	0.218	0.072	0.0423	5.15	1.70
RTF-BLT-C8	0.218	0.072	0.0210	10.38	3.43
RTF-BLT-C9	0.453	0.073	0.0460	9.85	1.59
RTF-BLT-C10	0.451	0.071	0.0220	20.50	3.23
RTF-BLT-C11	0.220	0.047	0.0300	7.33	1.57
RTF-BLT-C12	0.218	0.096	0.0330	6.61	2.91
RTF-BLT-C13	0.448	0.046	0.0290	15.45	1.59
RTF-BLT-C14	0.449	0.096	0.0310	14.48	3.10

Table 6: Chronological Text Matrix for Test 6887 in the 20-Inch Mach 6 Air Tunnel.

Model ID	Run	α	Mach No.	Re_∞/ft x 10^6	p_{t1} psi	T_{t1} ˚R	Trip Setup *x/L*	Trip Setup k_{CL}
RTF-BLT-C1	1	30	6.02	4.12	253.5	904.2		
RTF-BLT-C1	2	30	5.99	2.04	124.4	903.9		
RTF-BLT-C1	3	40	6.01	2.96	181.7	903.4		
RTF-BLT-C1	7	40	6.00	3.52	214.6	903.0		
RTF-BLT-C1	9	40	6.01	4.10	252.0	904.8		
RTF-BLT-C1	10	40	5.97	2.10	126.5	899.6		
RTF-BLT-C1	11	40	6.02	4.53	292.9	932.0		
RTF-BLT-C1	12	40	6.02	5.28	343.7	937.4		
RTF-BLT-C1	13	30	6.02	4.53	291.8	931.1		

Table 6: (Continued)Chronological Text Matrix for Test 6887 in the 20-Inch Mach 6 Air Tunnel.

Model ID	Run	α	Mach No.	Re_∞/ft x 10^6	p_{t1} psi	T_{t1} ˚R	Trip Setup *x/L*	Trip Setup k_{CL}
RTF-BLT-C1	14	30	6.02	5.26	343.7	938.4		
RTF-BLT-C1	15	30	6.03	5.95	392.9	944.9		
RTF-BLT-C1	17	30	6.03	6.95	447.4	931.1		
RTF-BLT-C2	19	30	5.96	2.13	127.9	900.5		
RTF-BLT-C2	22	30	6.00	4.09	250.8	906.7		
RTF-BLT-C2	23	30	5.99	3.43	210.3	907.2		
RTF-BLT-C2	24	30	5.99	2.99	182.4	904.6		
RTF-BLT-C2	25	40	6.00	4.13	253.0	906.2		
RTF-BLT-C2	26	40	5.99	3.00	182.2	902.9		
RTF-BLT-C2	29	30	6.00	4.66	291.6	918.2		
RTF-BLT-C2	30	30	6.01	5.42	342.2	922.0		
RTF-BLT-C2	31	30	6.01	6.08	392.6	935.4		
RTF-BLT-C2	32	30	6.03	6.91	445.4	932.2		
RTF-BLT-C3	33	30	6.01	4.13	253.1	904.4		
RTF-BLT-C3	34	30	5.97	2.07	125.3	903.6		
RTF-BLT-C3	35	40	5.94	1.39	80.7	884.1		
RTF-BLT-C3	36	40	5.98	2.07	125.8	904.4		
RTF-BLT-C3	37	40	6.00	2.95	181.1	905.9		
RTF-BLT-C3	38	40	6.01	4.09	252.0	907.6		
RTF-BLT-C3	39	30	6.01	4.80	294.5	904.7		
RTF-BLT-C3	40	30	6.02	5.51	346.0	916.3		
RTF-BLT-C3	41	30	6.02	6.11	392.2	929.2		
RTF-BLT-C3	42	30	6.03	6.95	450.0	933.7		
RTF-BLT-C3	43	30	6.03	7.31	476.3	938.6		
RTF-BLT-C4	45	30	6.02	4.07	251.9	905.4		
RTF-BLT-C4	46	30	6.02	3.43	211.9	905.5		
RTF-BLT-C4	47	30	6.01	2.96	182.1	904.7		
RTF-BLT-C4	48	30	5.99	2.06	125.9	904.2		
RTF-BLT-C4	49	40	5.96	1.72	100.8	887.3		
RTF-BLT-C4	51	40	5.98	2.09	126.9	900.3		
RTF-BLT-C4	52	40	5.99	2.51	152.4	902.1		
RTF-BLT-C4	53	40	6.00	2.99	181.9	901.3		
RTF-BLT-C4	54	40	6.01	4.11	252.0	904.4		
RTF-BLT-C4	55	30	6.01	4.70	292.4	911.9		
RTF-BLT-C4	56	30	6.02	5.37	342.4	924.4		
RTF-BLT-C4	57	30	6.03	6.15	393.4	927.2		
RTF-BLT-C4	58	30	6.03	7.03	453.2	931.1		
RTF-BLT-C6	62	40	6.00	4.15	253.4	904.3		
RTF-BLT-C6	63	40	5.99	2.99	181.7	901.0		
RTF-BLT-C6	64	40	5.98	2.09	126.2	900.1		
RTF-BLT-C6	65	40	5.93	1.07	60.6	873.1		
RTF-BLT-C6	66	40	5.92	1.09	61.4	870.5		
RTF-BLT-C6	67	40	5.90	0.84	45.7	860.8		
RTF-BLT-C6	68	40	5.95	1.41	82.0	885.5		
RTF-BLT-C6	69	40	5.97	2.09	126.2	902.3		

Table 6: (Continued)Chronological Text Matrix for Test 6887 in the 20-Inch Mach 6 Air Tunnel.

Model ID	Run	α	Mach No.	Re_∞/ft x 10^6	p_{t1} psi	T_{t1} ˚R	Trip Setup x/L	Trip Setup k_{CL}
RTF-BLT-C6	70	40	5.98	3.02	183.2	902.4		
RTF-BLT-C6	71	40	5.99	4.08	252.4	912.9		
RTF-BLT-C6	72	30	6.01	4.67	292.0	916.2		
RTF-BLT-C6	73	30	6.02	5.46	343.1	917.9		
RTF-BLT-C6	74	30	6.02	6.14	393.7	929.7		
RTF-BLT-C6	75	30	6.03	6.95	450.7	935.6		
RTF-BLT-C5	77	30	6.00	4.12	253.4	907.1		
RTF-BLT-C5	78	30	5.98	2.98	182.3	908.1		
RTF-BLT-C5	79	30	5.96	2.09	125.9	903.4		
RTF-BLT-C5	80	30	5.95	1.71	100.6	891.9		
RTF-BLT-C5	81	40	5.91	1.08	60.7	873.3		
RTF-BLT-C5	82	40	5.89	0.84	46.1	866.2		
RTF-BLT-C5	83	40	5.93	1.42	82.6	890.8		
RTF-BLT-C5	84	40	5.96	2.12	127.3	903.4		
RTF-BLT-C5	85	40	6.00	2.97	181.4	902.9		
RTF-BLT-C5	87	30	6.01	4.68	292.9	916.8		
RTF-BLT-C5	88	30	6.02	5.25	336.9	929.6		
RTF-BLT-C5	89	30	6.02	6.15	393.7	927.9		
RTF-BLT-C5	90	30	6.03	6.89	450.0	938.3		
RTF-BLT-C7	91	30	5.99	4.13	254.1	909.9		
RTF-BLT-C7	92	30	5.97	2.99	182.2	906.7		
RTF-BLT-C7	93	30	5.99	3.46	210.9	904.1		
RTF-BLT-C7	94	40	5.96	2.11	126.7	902.3		
RTF-BLT-C7	95	40	5.93	1.40	81.4	887.2		
RTF-BLT-C7	96	40	5.94	1.72	101.2	893.3		
RTF-BLT-C7	97	40	5.97	3.01	182.3	904.9		
RTF-BLT-C7	98	40	5.99	4.10	250.8	907.5		
RTF-BLT-C7	99	40	6.01	5.34	340.8	929.1		
RTF-BLT-C7	100	30	5.99	4.68	293.2	920.4		
RTF-BLT-C7	101	30	6.00	5.41	343.4	927.0		
RTF-BLT-C7	102	30	6.01	6.17	393.5	928.0		
RTF-BLT-C7	103	30	6.02	6.99	450.7	933.5		
RTF-BLT-C8	104	30	5.99	4.20	254.1	900.4		
RTF-BLT-C8	105	30	5.99	3.46	211.8	905.8		
RTF-BLT-C8	106	30	5.96	2.10	126.1	901.7		
RTF-BLT-C8	107	40	5.97	2.10	126.5	902.1		
RTF-BLT-C8	108	40	5.94	1.74	102.3	894.1		
RTF-BLT-C8	109	40	5.93	1.41	81.5	886.4		
RTF-BLT-C8	110	40	5.96	2.52	151.5	901.5		
RTF-BLT-C8	111	40	5.99	4.09	251.3	909.2		
RTF-BLT-C8	112	40	6.00	4.67	291.4	917.0		
RTF-BLT-C8	113	40	6.01	5.46	345.0	922.7		
RTF-BLT-C8	114	30	6.00	4.65	291.7	920.5		
RTF-BLT-C8	115	30	6.02	6.92	449.9	939.3		
RTF-BLT-C8	116	30	6.02	7.38	475.0	933.7		

Table 6: (Continued)Chronological Text Matrix for Test 6887 in the 20-Inch Mach 6 Air Tunnel.

Model ID	Run	α	Mach No.	Re_∞/ft x 10^6	p_{t1} psi	T_{t1} ˚R	Trip Setup x/L	Trip Setup k_{CL}
RTF-BLT-C8	117	40	6.01	3.00	181.6	902.8		
RTF-BLT-C8	118	30	6.04	5.42	344.7	919.6		
RTF-BLT-C8	119	30	6.04	6.12	393.3	925.3		
RTF-BLT-C3	120	30	6.01	3.44	213.1	906.3		
RTF-BLT-C3	121	40	6.03	4.66	294.0	916.4		
RTF-BLT-C6	122	40	6.02	4.66	293.5	916.6		
RTF-BLT-C6	123	30	5.95	1.39	81.1	887.0		
RTF-BLT-C6	124	30	5.97	1.71	101.4	890.8		
RTF-BLT-C4	125	40	6.02	4.65	293.1	918.6		
RTF-BLT-C4	126	40	5.96	1.43	83.8	887.2		
RTF-BLT-C4	127	40	6.01	4.66	292.4	917.4		
RTF-BLT-C1	128	30	6.04	7.40	477.5	931.2		
RTF-BLT-C9	129	30	6.01	4.05	248.9	906.0		
RTF-BLT-C9	130	30	5.98	2.08	126.1	902.4		
RTF-BLT-C9	131	30	5.96	1.74	103.0	890.8		
RTF-BLT-C9	132	30	5.99	2.97	181.5	905.7		
RTF-BLT-C9	133	40	5.97	2.08	126.1	904.1		
RTF-BLT-C9	134	40	5.99	2.97	181.0	903.1		
RTF-BLT-C9	135	40	5.92	1.07	60.1	874.3		
RTF-BLT-C9	136	40	5.92	0.83	46.1	862.5		
RTF-BLT-C9	137	40	5.95	1.39	80.9	884.6		
RTF-BLT-C9	138	40	6.01	4.12	256.7	904.6		
RTF-BLT-C9	139	30	6.01	4.70	294.0	915.4		
RTF-BLT-C9	140	30	6.01	5.38	342.4	925.8		
RTF-BLT-C9	141	30	6.03	7.05	453.3	929.7		
RTF-BLT-C10	142	30	6.00	4.10	252.0	906.9		
RTF-BLT-C10	143	30	5.97	2.06	124.7	903.7		
RTF-BLT-C10	144	30	5.99	3.00	183.3	905.9		
RTF-BLT-C10	145	30	5.98	2.50	152.2	903.6		
RTF-BLT-C10	146	40	6.00	4.09	251.6	908.0		
RTF-BLT-C10	147	40	5.99	2.97	181.6	906.2		
RTF-BLT-C10	148	40	5.98	2.08	125.8	902.5		
RTF-BLT-C10	149	40	5.93	1.08	61.2	873.8		
RTF-BLT-C10	150	40	5.95	1.38	80.6	885.9		
RTF-BLT-C10	151	30	6.01	4.64	292.2	919.7		
RTF-BLT-C10	152	30	6.01	5.49	345.4	919.4		
RTF-BLT-C10	153	30	6.03	7.00	453.6	934.8		
RTF-BLT-C10	154	40	6.00	5.47	344.1	921.7		
RTF-BLT-C10	155	40	6.03	6.17	395.3	927.5		
RTF-BLT-C9	156	40	6.02	5.45	345.9	922.3		
RTF-BLT-C9	157	40	6.02	6.17	393.1	925.2		
RTF-BLT-C5	158	40	6.00	4.11	252.6	907.6		
RTF-BLT-C5	159	40	6.01	5.45	343.8	922.0		
RTF-BLT-C5	160	40	6.02	6.19	393.8	925.7		
RTF-BLT-C11	161	30	5.99	4.12	251.6	905.6		

Table 6: (Continued)Chronological Text Matrix for Test 6887 in the 20-Inch Mach 6 Air Tunnel.

Model ID	Run	α	Mach No.	Re_∞/ft x 10^6	p_{t1} psi	T_{t1} °R	Trip Setup x/L	k_{CL}
RTF-BLT-C11	162	30	5.98	2.07	125.5	903.0		
RTF-BLT-C11	163	40	5.99	4.09	250.9	908.7		
RTF-BLT-C11	164	40	5.98	2.98	181.5	904.8		
RTF-BLT-C11	165	40	5.97	2.08	125.8	902.4		
RTF-BLT-C11	166	40	5.98	2.48	151.0	903.7		
RTF-BLT-C11	167	40	6.01	5.44	343.1	922.5		
RTF-BLT-C11	168	40	6.02	6.19	393.8	925.7		
RTF-BLT-C11	169	30	6.00	4.67	290.6	915.9		
RTF-BLT-C11	170	30	6.01	6.15	392.3	928.1		
RTF-BLT-C11	171	30	6.02	7.03	451.2	931.9		
RTF-BLT-C11	172	30	6.02	7.43	476.7	930.9		
RTF-BLT-C12	173	30	6.00	4.12	252.1	905.4		
RTF-BLT-C12	174	30	5.98	2.08	126.3	902.8		
RTF-BLT-C12	175	30	5.99	2.99	182.7	905.0		
RTF-BLT-C12	176	30	5.99	2.48	151.3	903.2		
RTF-BLT-C12	177	40	6.00	4.11	251.8	906.5		
RTF-BLT-C12	178	40	5.98	3.01	182.3	901.7		
RTF-BLT-C12	179	40	5.98	2.10	127.2	902.4		
RTF-BLT-C12	180	40	5.94	1.07	60.8	875.8		
RTF-BLT-C12	181	40	5.96	1.35	79.7	891.1		
RTF-BLT-C12	182	40	6.01	5.46	343.4	920.6		
RTF-BLT-C12	183	40	6.01	6.09	391.9	933.9		
RTF-BLT-C12	184	30	6.01	5.43	343.4	923.4		
RTF-BLT-C12	185	30	6.02	7.07	453.5	930.8		
RTF-BLT-C13	186	30	5.99	4.20	254.5	901.4		
RTF-BLT-C13	187	30	5.98	2.97	181.1	905.4		
RTF-BLT-C13	188	30	5.98	3.51	213.8	906.4		
RTF-BLT-C13	189	40	5.99	4.12	250.8	903.7		
RTF-BLT-C13	190	40	5.98	2.09	126.5	901.6		
RTF-BLT-C13	191	40	5.96	1.70	101.0	983.8		
RTF-BLT-C13	192	40	5.99	2.96	180.9	904.9		
RTF-BLT-C13	193	40	6.01	5.47	344.4	919.6		
RTF-BLT-C13	194	40	6.02	6.17	394.0	927.9		
RTF-BLT-C13	195	30	6.01	5.42	343.5	923.1		
RTF-BLT-C13	196	30	6.02	7.01	453.5	935.1		
RTF-BLT-C13	197	30	6.03	7.38	477.6	934.6		
RTF-BLT-C14	198	30	6.00	4.11	251.2	905.7		
RTF-BLT-C14	199	30	5.99	2.97	181.0	903.9		
RTF-BLT-C14	200	30	5.98	2.09	126.7	903.3		
RTF-BLT-C14	201	30	6.04	5.42	346.0	922.3		
RTF-BLT-C14	202	30	6.00	1.69	101.4	892.8		
RTF-BLT-C14	203	30	5.95	1.05	60.5	875.6		
RTF-BLT-C14	204	40	6.02	4.06	252.7	909.3		
RTF-BLT-C14	205	40	6.01	2.95	182.1	905.6		
RTF-BLT-C14	206	40	6.00	2.07	125.7	899.5		

Table 6: (Continued)Chronological Text Matrix for Test 6887 in the 20-Inch Mach 6 Air Tunnel.

Model ID	Run	α	Mach No.	Re_∞/ft x 10^6	p_{t1} psi	T_{t1} ˚R	Trip Setup	
							x/L	k_{CL}
RTF-BLT-C14	207	40	5.95	1.06	60.7	875.7		
RTF-BLT-C14	208	40	5.93	0.83	46.0	863.9		
RTF-BLT-C14	209	40	5.96	1.37	80.0	883.3		
RTF-BLT-C14	210	40	6.03	5.46	347.2	921.9		
RTF-BLT-C14	211	40	6.03	6.14	393.6	926.9		
RTF-BLT-C14	214	30	6.04	6.93	450.0	933.6		
RTF-BLT-C14	215	30	6.04	6.10	392.2	926.4		
RTF-BLT-C3	216	40	6.00	2.98	181.7	902.5		
RTF-BLT-C3	217	40	5.99	2.51	152.3	900.8		
RTF-BLT-C3	218	40	6.00	3.50	213.3	901.1		
RTF-BLT-C3	219	40	6.03	5.26	341.6	935.3		
RTF-BLT-C2	220	40	5.99	2.47	150.4	904.1		
RTF-BLT-C2	221	40	6.00	3.49	213.5	904.4		
RTF-BLT-C2	222	40	5.98	2.07	126.0	903.5		
RTF-BLT-C2	223	40	6.02	5.38	343.5	926.8		
RTF-BLT-C2	224	40	5.97	1.69	100.5	891.7		
RTF-BLT-C4	225	40	6.02	5.42	343.7	921.7		
RTF-BLT-C4	226	40	5.97	1.72	101.9	890.3		
RTF-BLT-C5	227	40	5.97	1.71	101.4	892.0		
RTF-BLT-C5	228	40	6.00	2.47	151.0	902.8		
RTF-BLT-C1	230	40	6.03	6.14	393.8	927.7		
RTF-BLT-C7	231	40	5.99	2.48	151.2	903.8		
RTF-BLT-C11	232	40	6.00	3.52	213.9	900.8		
RTF-BLT-C12	233	40	5.96	1.72	101.5	891.6		

Table 7: Chronological Test Matrix for Test 392 in the 31-Inch Mach 10 Air Tunnel.

Model ID	Run	α	Mach No.	Re_∞/ft x 10^6	p_{t1} psi	T_{t1} ˚R	Trip Setup	
							x/L	k_{CL}
RTF-BLT-C6	6	40	9.74	1.43	1002.8	1818.0		
RTF-BLT-C6	7	40	9.81	1.78	1252.7	1805.8		
RTF-BLT-C6	8	40	9.86	2.02	1450.7	1814.8		
RTF-BLT-C6	9	40	9.78	1.62	1125.6	1799.7		
RTF-BLT-C6	10	40	9.76	1.55	1074.9	1803.7		
RTF-BLT-C6	11	40	9.69	1.26	883.0	1831.5		
RTF-BLT-C6	12	40	9.66	1.16	783.9	1800.2		
RTF-BLT-C6	13	40	9.63	1.07	720.9	1811.2		
RTF-BLT-C6	14	40	9.53	0.84	550.9	1808.9		
RTF-BLT-C6	15	40	9.33	0.58	351.3	1789.9		
RTF-BLT-C5	16	40	9.85	2.00	1452.1	1828.3		
RTF-BLT-C5	17	40	9.81	1.79	1257.6	1805.0		
RTF-BLT-C5	19	40	9.78	1.61	1125.9	1809.8		
RTF-BLT-C5	20	40	9.76	1.55	1077.8	1803.8		
RTF-BLT-C5	21	40	9.70	1.31	901.1	1812.0		
RTF-BLT-C5	22	40	9.66	1.16	783.7	1799.7		
RTF-BLT-C5	24	40	9.63	1.07	721.4	1810.3		

Table 7: (Continued)Chronological Test Matrix for Test 392 in the 31-Inch Mach 10 Air Tunnel.

Model ID	Run	α	Mach No.	Re_∞/ft x 10^6	p_{t1} psi	T_{t1} ˚R	Trip Setup	
							x/L	k_{CL}
RTF-BLT-C5	25	40	9.53	0.84	551.3	1803.3		
RTF-BLT-C5	26	40	9.33	0.57	352.0	1802.6		
RTF-BLT-C4	28	40	9.82	1.84	1255.8	1772.2		
RTF-BLT-C4	29	40	9.87	2.09	1451.7	1779.5		
RTF-BLT-C4	30	40	9.78	1.65	1126.6	1783.7		
RTF-BLT-C4	31	40	9.76	1.55	1077.1	1803.7		
RTF-BLT-C4	32	40	9.70	1.31	905.0	1814.1		
RTF-BLT-C4	33	40	9.66	1.15	783.9	1809.8		
RTF-BLT-C3	34	40	9.87	2.08	1453.7	1785.3		
RTF-BLT-C3	35	40	9.81	1.81	1258.1	1793.2		
RTF-BLT-C2	37	40	9.87	2.09	1453.7	1779.6		
RTF-BLT-C2	38	40	9.81	1.82	1255.1	1787.4		
RTF-BLT-C1	39	40	9.87	2.09	1452.3	1783.1		
RTF-BLT-C1	40	40	9.82	1.82	1253.1	1784.5		
RTF-BLT-C9	42	40	9.82	1.82	1256.3	1784.4		
RTF-BLT-C9	43	40	9.87	2.10	1451.6	1774.3		
RTF-BLT-C9	44	40	9.78	1.63	1125.7	1796.5		
RTF-BLT-C9	45	40	9.76	1.55	1076.2	1804.3		
RTF-BLT-C9	48	40	9.70	1.30	902.1	1816.3		
RTF-BLT-C9	49	40	9.66	1.16	783.9	1807.4		
RTF-BLT-C9	51	40	9.63	1.06	721.7	1818.1		
RTF-BLT-C9	52	40	9.53	0.85	551.2	1797.8		
RTF-BLT-C10	53	40	9.87	2.09	1452.8	1779.2		
RTF-BLT-C10	54	40	9.82	1.83	1254.4	1777.3		
RTF-BLT-C10	55	40	9.78	1.63	1126.0	1793.7		
RTF-BLT-C10	56	40	9.76	1.56	1076.4	1798.5		
RTF-BLT-C10	57	40	9.70	1.31	900.9	1805.5		
RTF-BLT-C10	58	40	9.66	1.16	783.0	1806.1		
RTF-BLT-C10	59	40	9.63	1.07	721.4	1812.1		
RTF-BLT-C10	60	40	9.53	0.84	548.9	1802.2		
RTF-BLT-C14	61	40	9.87	2.01	1455.4	1779.0		
RTF-BLT-C14	62	40	9.82	1.82	1256.1	1784.6		
RTF-BLT-C14	63	40	9.78	1.63	1126.4	1797.7		
RTF-BLT-C14	64	40	9.76	1.55	1076.5	1802.6		
RTF-BLT-C14	65	40	9.70	1.31	901.8	1806.5		
RTF-BLT-C14	66	40	9.66	1.16	783.1	1802.9		
RTF-BLT-C14	67	40	9.63	1.06	720.1	1815.3		
RTF-BLT-C14	68	40	9.53	0.84	549.7	1805.1		
RTF-BLT-C13	69	40	9.87	2.07	1452.1	1789.4		
RTF-BLT-C13	70	40	9.82	1.82	1256.5	1784.5		
RTF-BLT-C13	71	40	9.78	1.62	1125.5	1800.5		
RTF-BLT-C13	72	40	9.76	1.55	1075.6	1806.1		

Table 8: Chronological Test Matrix for Test 159 in the 20-Inch CF_4 Tunnel.

Model ID	Run	α	Mach No.	Re_∞/ft x 10^6	p_{t1} psi	T_{t1} ˚R	Trip Setup x/L	Trip Setup k_{CL}
RTF-BLT-C6	6	40	5.80	0.15	496.7	1272.0		
RTF-BLT-C6	7	40	5.80	0.22	715.1	1266.9		
RTF-BLT-C6	8	40	5.82	0.61	2052.1	1284.2		
RTF-BLT-C6	9	40	5.82	0.07	216.0	1254.2		
RTF-BLT-C6	11	40	5.83	0.32	1003.6	1249.9		
RTF-BLT-C6	12	40	5.86	0.02	63.0	1254.1		
RTF-BLT-C6	13	40	5.82	0.03	115.6	1259.7		
RTF-BLT-C6	14	40	5.81	0.44	1488.1	1281.4		
RTF-BLT-C1	15	40	5.86	0.48	1514.3	1245.9		
RTF-BLT-C1	16	40	5.82	0.61	2069.9	1289.1		
RTF-BLT-C5	17	40	5.83	0.61	2061.2	1282.5		
RTF-BLT-C5	18	40	5.81	0.15	482.5	1254.0		
RTF-BLT-C5	19	40	5.83	0.23	740.8	1255.3		
RTF-BLT-C5	20	40	5.83	0.32	1016.8	1254.5		
RTF-BLT-C5	21	40	5.83	0.46	1485.9	1260.6		
RTF-BLT-C4	22	40	5.83	0.45	1483.1	1266.8		
RTF-BLT-C4	23	40	5.82	0.61	2077.6	1286.7		
RTF-BLT-C4	24	40	5.82	0.31	1020.7	1267.4		
RTF-BLT-C3	25	40	5.85	0.47	1510.7	1253.8		
RTF-BLT-C3	26	40	5.84	0.63	2061.7	1270.8		
RTF-BLT-C2	27	40	5.83	0.61	2067.9	1283.7		
RTF-BLT-C2	28	40	5.81	0.22	734.9	1267.4		
RTF-BLT-C2	29	40	5.51	0.30	1000.8	1268.6		
RTF-BLT-C2	30	40	5.83	0.45	1495.3	1268.4		
RTF-BLT-C9	31	40	5.82	0.61	2064.7	1285.7		
RTF-BLT-C9	32	40	5.81	0.15	498.0	1260.6		
RTF-BLT-C9	33	40	5.81	0.22	733.7	1266.4		
RTF-BLT-C9	34	40	5.81	0.30	997.3	1272.2		
RTF-BLT-C9	35	40	5.82	0.44	1481.8	1277.6		
RTF-BLT-C10	36	40	5.83	0.61	2065.3	1280.3		
RTF-BLT-C10	37	40	5.80	0.15	485.6	1268.4		
RTF-BLT-C10	38	40	5.81	0.23	760.9	1263.6		
RTF-BLT-C10	39	40	5.82	0.31	1016.1	1263.0		
RTF-BLT-C10	40	40	5.82	0.45	1488.0	1271.9		
RTF-BLT-C14	41	40	5.78	0.14	481.4	1283.2		
RTF-BLT-C14	43	40	5.83	0.62	2054.9	1278.2		
RTF-BLT-C14	44	40	5.81	0.23	763.9	1262.6		
RTF-BLT-C14	45	40	5.82	0.32	1037.7	1263.4		
RTF-BLT-C14	46	40	5.82	0.45	1503.0	1273.2		
RTF-BLT-C13	47	40	5.78	0.15	497.8	1284.6		
RTF-BLT-C13	48	40	5.79	0.22	755.0	1284.5		
RTF-BLT-C13	49	40	5.80	0.31	1042.8	1284.6		
RTF-BLT-C13	50	40	5.80	0.44	1503.9	1290.4		
RTF-BLT-C13	51	40	5.84	0.62	2065.4	1275.0		
RTF-BLT-P9	57	40	5.83	0.46	1502.8	1264.1		

Table 8: (Continued)Chronological Test Matrix for Test 159 in the 20-Inch CF_4 Tunnel.

Model ID	Run	α	Mach No.	Re_∞/ft x 10^6	p_{t1} psi	T_{t1} ˚R	Trip Setup x/L	Trip Setup k_{CL}
RTF-BLT-P9	58	40	5.85	0.63	2059.1	1265.2		
RTF-BLT-P9	59	40	5.79	0.15	512.8	1276.7		
RTF-BLT-P9	60	40	5.80	0.23	775.9	1278.0		
RTF-BLT-P9	61	40	5.80	0.31	1041.0	1280.0		
RTF-BLT-C6	67	40	5.73	0.39	1532.7	1364.4	0.10	0.0115
RTF-BLT-C6	68	40	5.73	0.52	2076.7	1377.5	0.10	0.0115
RTF-BLT-C6	69	40	5.71	0.13	515.7	1363.9	0.10	0.0115
RTF-BLT-C6	70	40	5.73	0.20	777.5	1346.6	0.10	0.0115
RTF-BLT-C6	71	40	5.72	0.27	1078.5	1364.7	0.10	0.0115
RTF-BLT-P9	72	30	5.73	0.38	1501.7	1358.4		
RTF-BLT-P9	73	30	5.75	0.39	1494.7	1342.3		
RTF-BLT-P9	74	30	5.75	0.54	2088.7	1353.7		
RTF-BLT-P9	75	30	5.80	0.15	505.0	1270.6		
RTF-BLT-P9	76	30	5.72	0.20	788.5	1350.6		
RTF-BLT-P9	77	30	5.72	0.27	1068.3	1364.3		

Figures

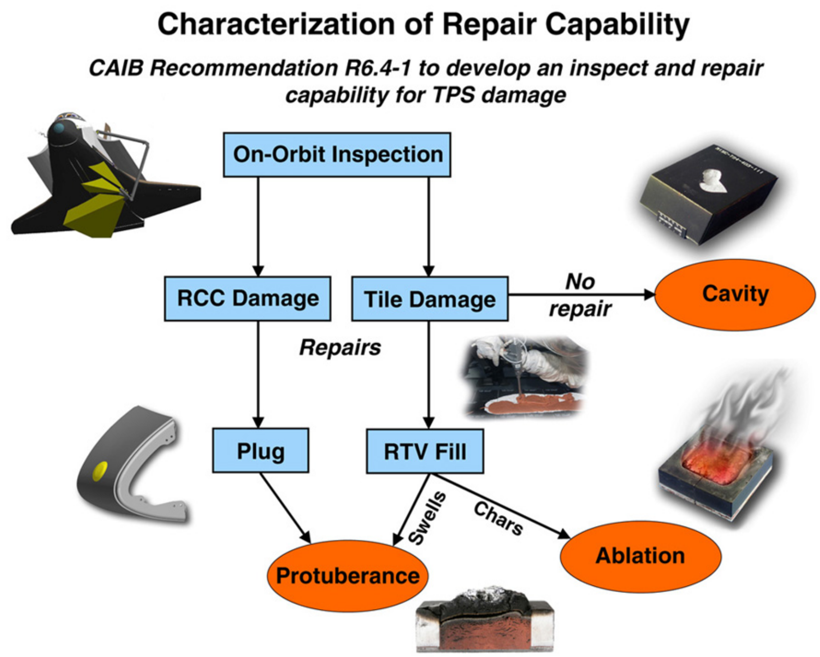

Figure 1: Development of a repair capability for Shuttle return to flight.

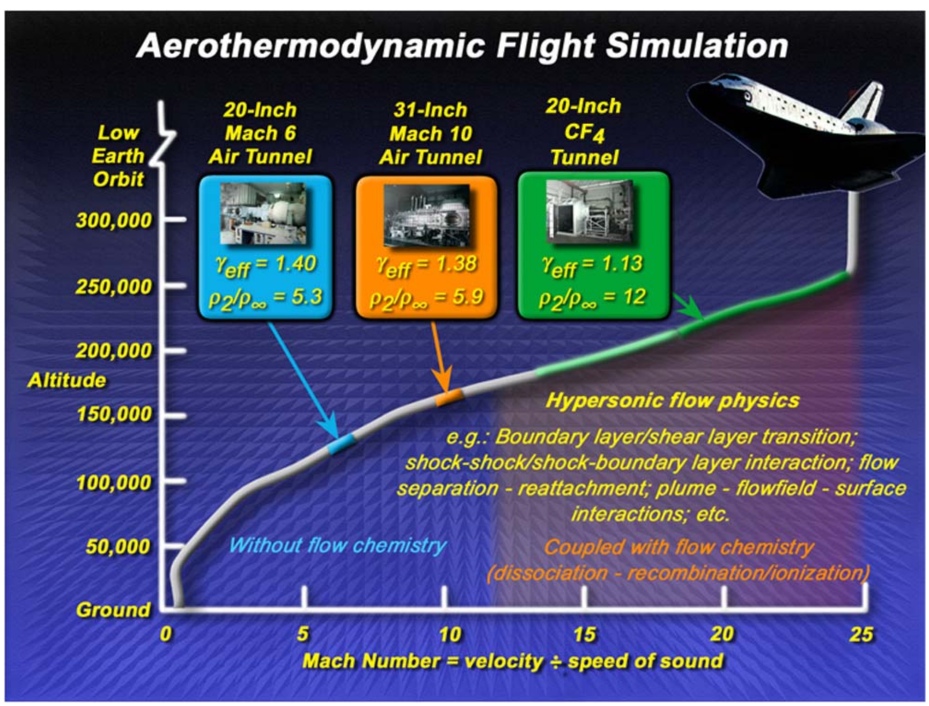

Figure 2: Test facilities utilized in the current study.

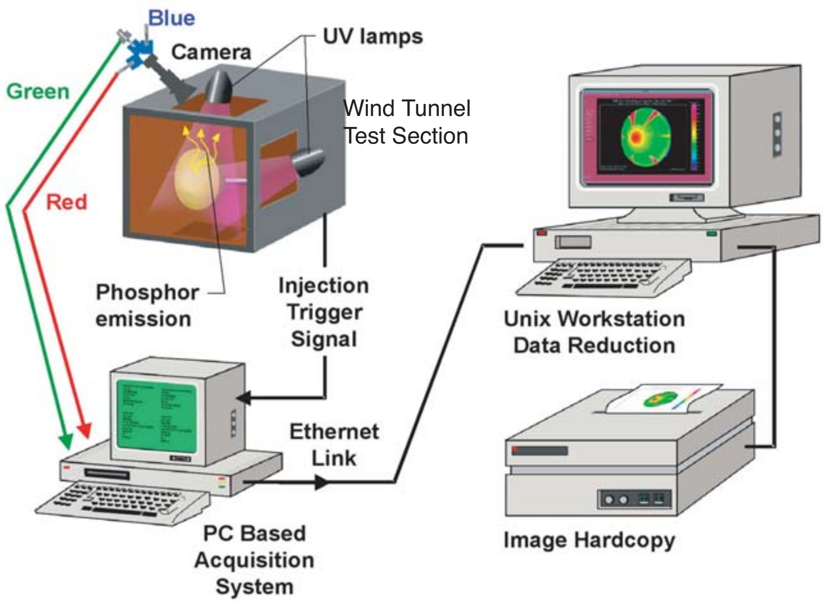

Figure 3: Schematic of thermographic phosphor system.

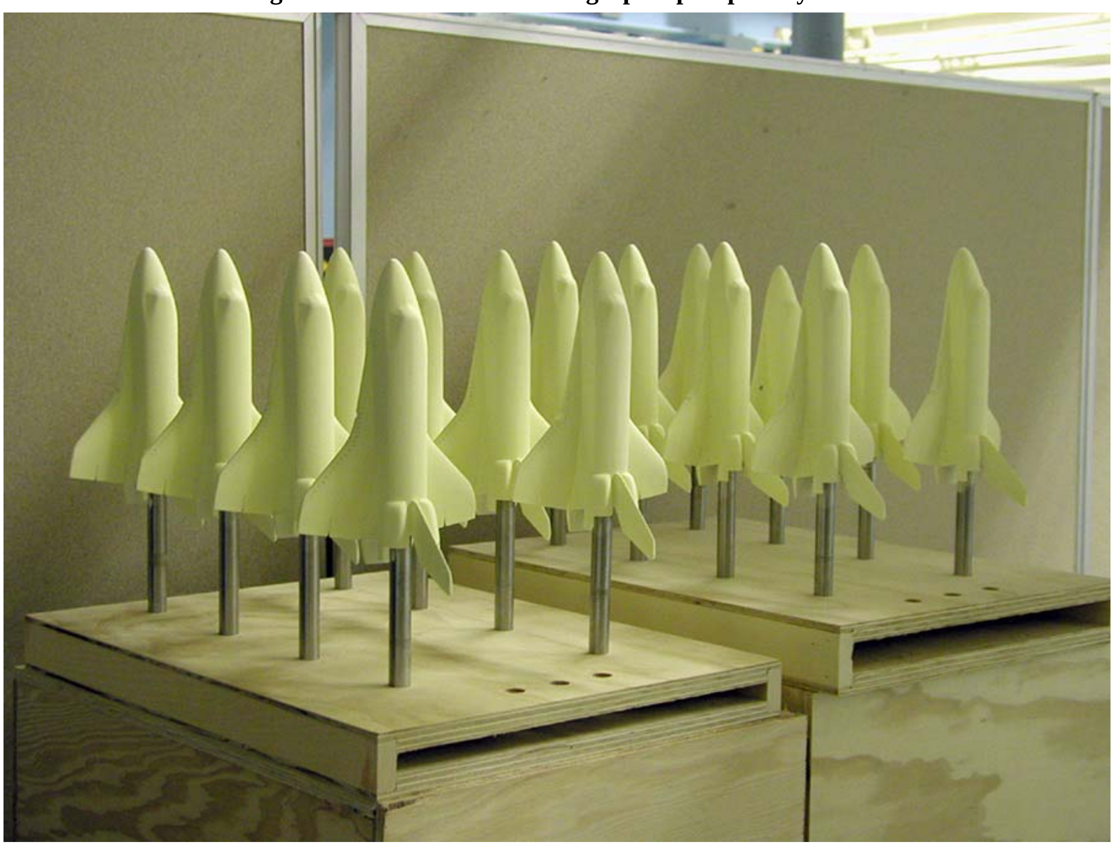

Figure 4: Ceramic Shuttle Orbiter models.

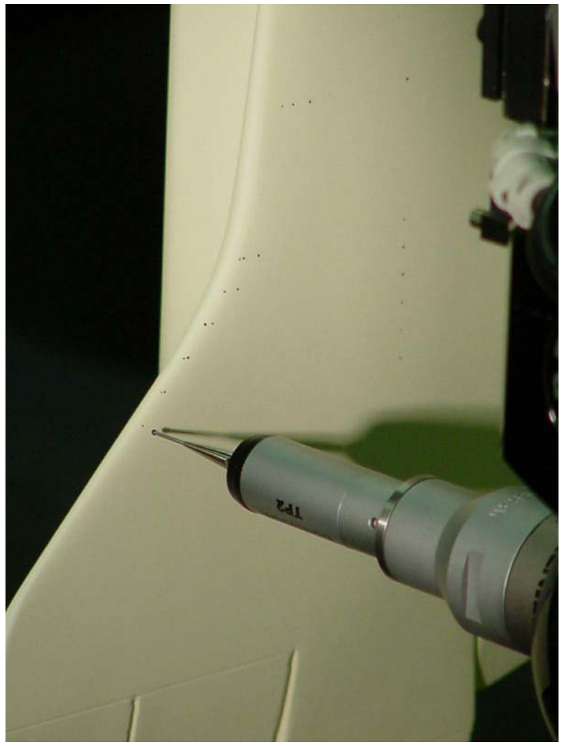

Figure 5: Placement of fiducial marks.

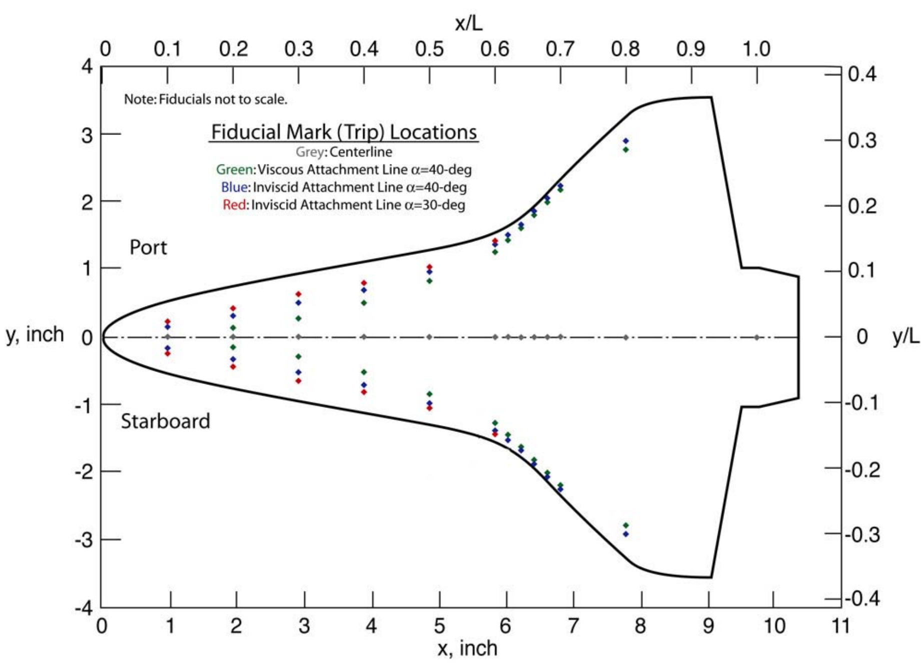

Figure 6: Fiducial mark locations.

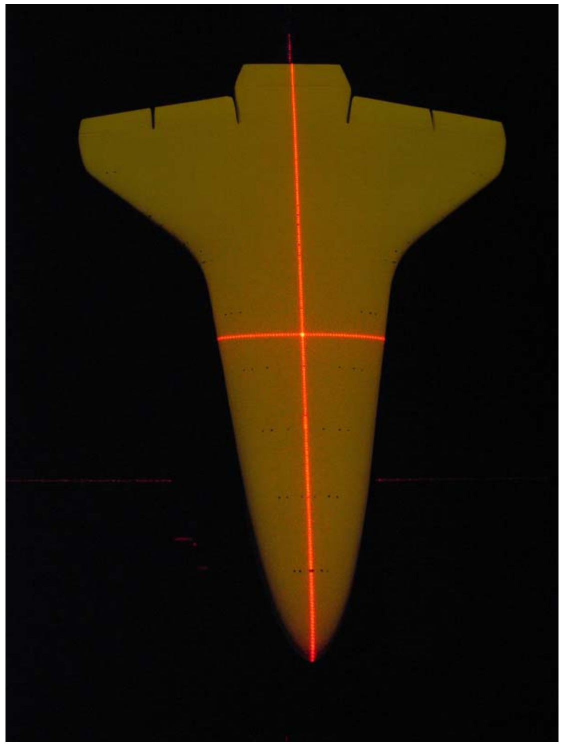

Figure 7: Model setup using laser alignment system.

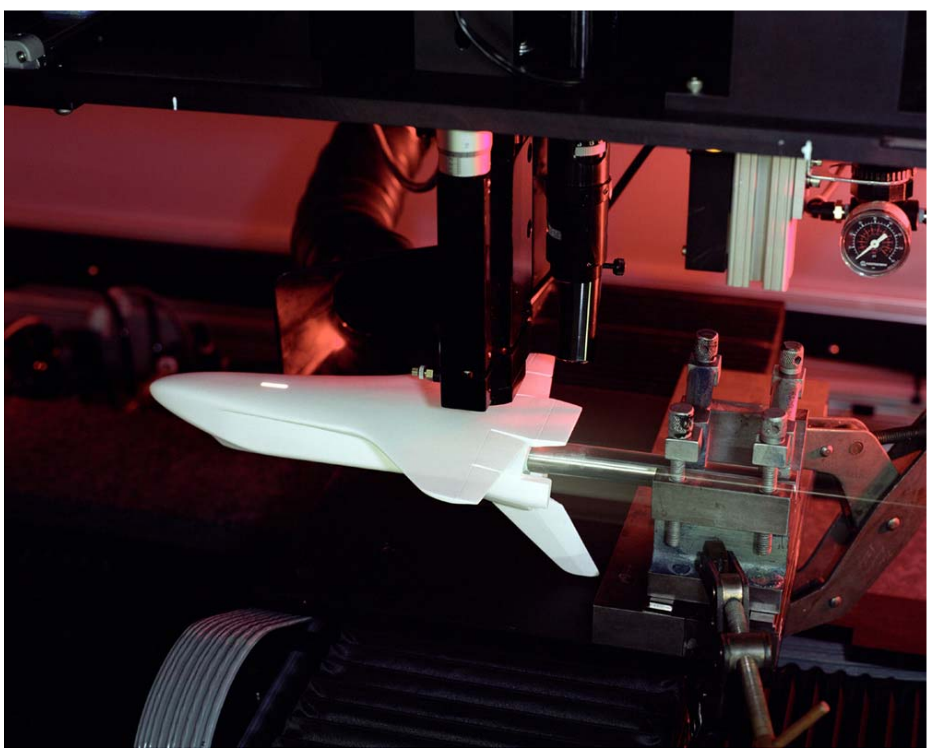

Figure 8: Cavity being added to ceramic Shuttle model.

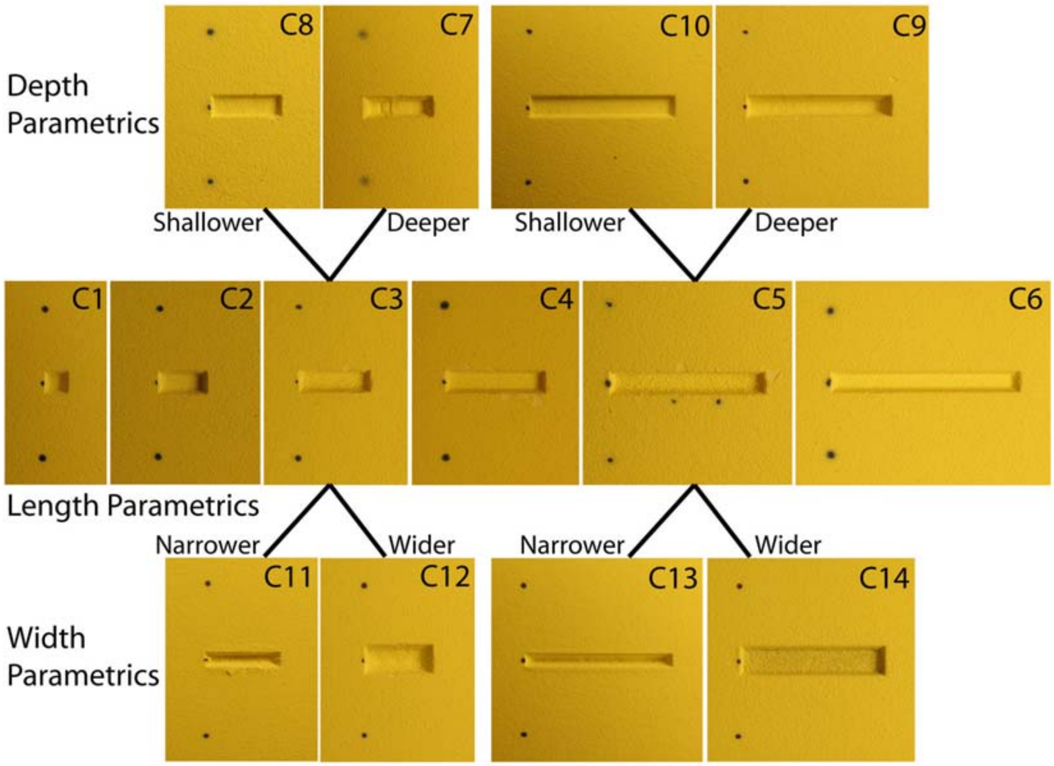

Figure 9: Close up of cavities and relations between cavity designations.

Appendix A: 20-Inch Mach 6 Air Tunnel Aeroheating

Table A.1: Cross Reference of Figure Numbers Versus Parametrics for Phosphor Images from the 20-Inch Mach 6 Air Tunnel.

α (deg.)	Model	$(x/L)_{CL}$ (in.)	k_{CL} (in.)	Figure
30	RTF-BLT-C1	-	-	A.1
40	RTF-BLT-C1	-	-	A.4
30	RTF-BLT-C2	-	-	A.7
40	RTF-BLT-C2	-	-	A.10
30	RTF-BLT-C3	-	-	A.13
40	RTF-BLT-C3	-	-	A.16
30	RTF-BLT-C4	-	-	A.19
40	RTF-BLT-C4	-	-	A.22
30	RTF-BLT-C5	-	-	A.25
40	RTF-BLT-C5	-	-	A.28
30	RTF-BLT-C6	-	-	A.31
40	RTF-BLT-C6	-	-	A.34
30	RTF-BLT-C7	-	-	A.37
40	RTF-BLT-C7	-	-	A.40
30	RTF-BLT-C8	-	-	A.43
40	RTF-BLT-C8	-	-	A.46
30	RTF-BLT-C9	-	-	A.49
40	RTF-BLT-C9	-	-	A.52
30	RTF-BLT-C10	-	-	A.55
40	RTF-BLT-C10	-	-	A.58
30	RTF-BLT-C11	-	-	A.61
40	RTF-BLT-C11	-	-	A.64
30	RTF-BLT-C12	-	-	A.67
40	RTF-BLT-C12	-	-	A.70
30	RTF-BLT-C13	-	-	A.73
40	RTF-BLT-C13	-	-	A.76
30	RTF-BLT-C14	-	-	A.79
40	RTF-BLT-C14	-	-	A.82

Note: Corresponding data cuts are located immediately after figures.

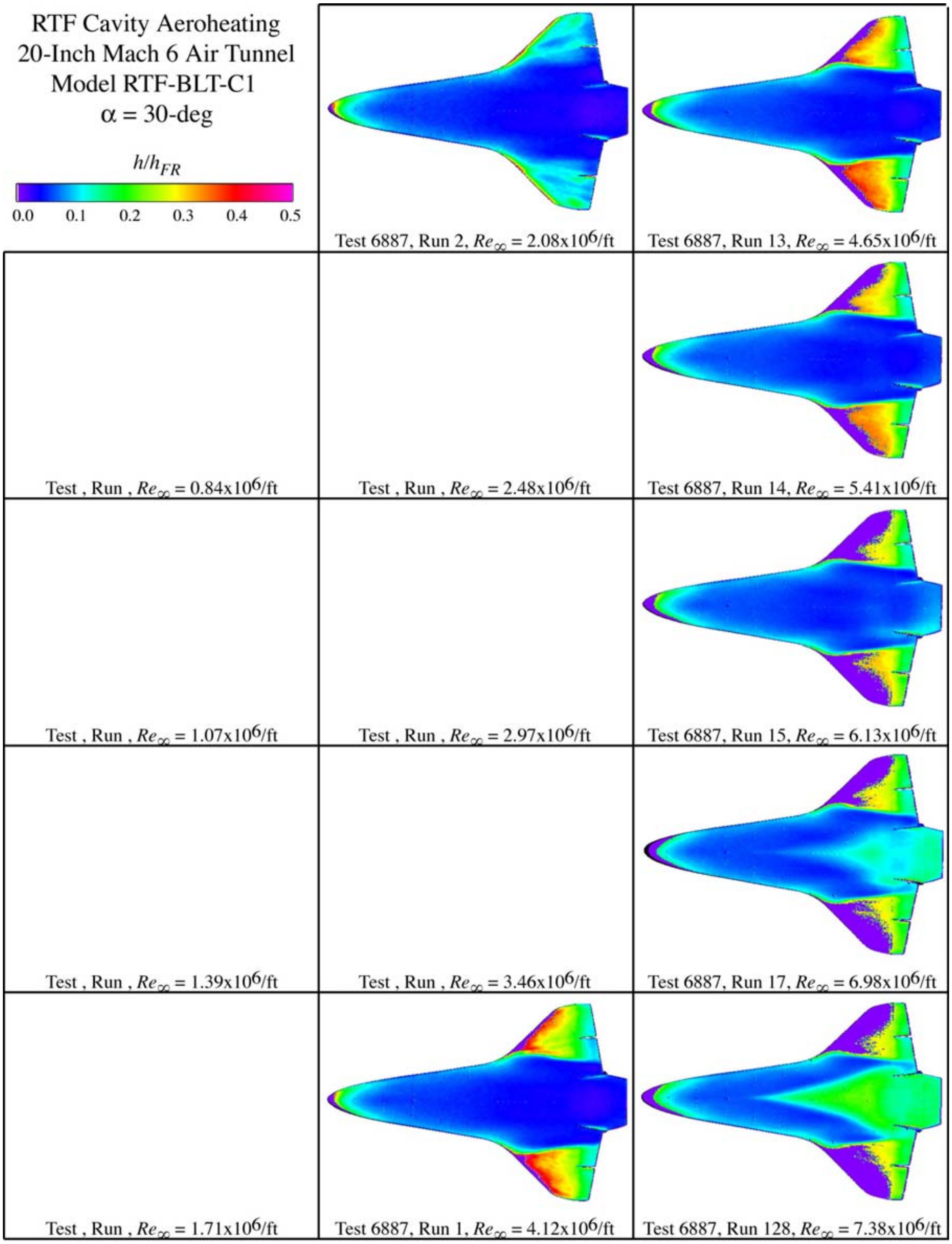

Figure A.1: RTF-BLT-C1 global aeroheating in the 20-Inch Mach 6 Air Tunnel at α = 30-deg.

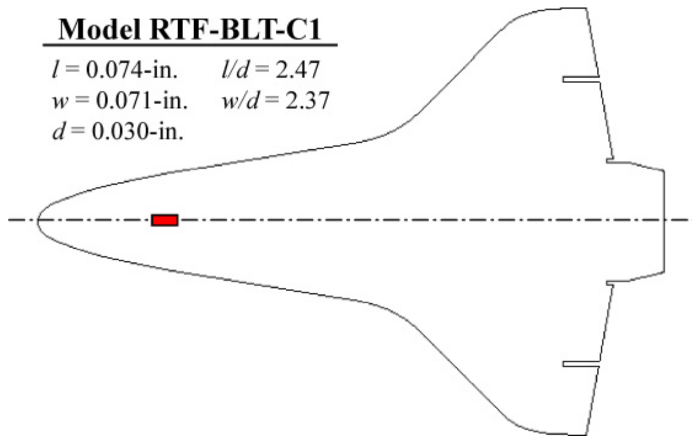

Figure A.2: RTF-BLT-C1 Cavity Information.

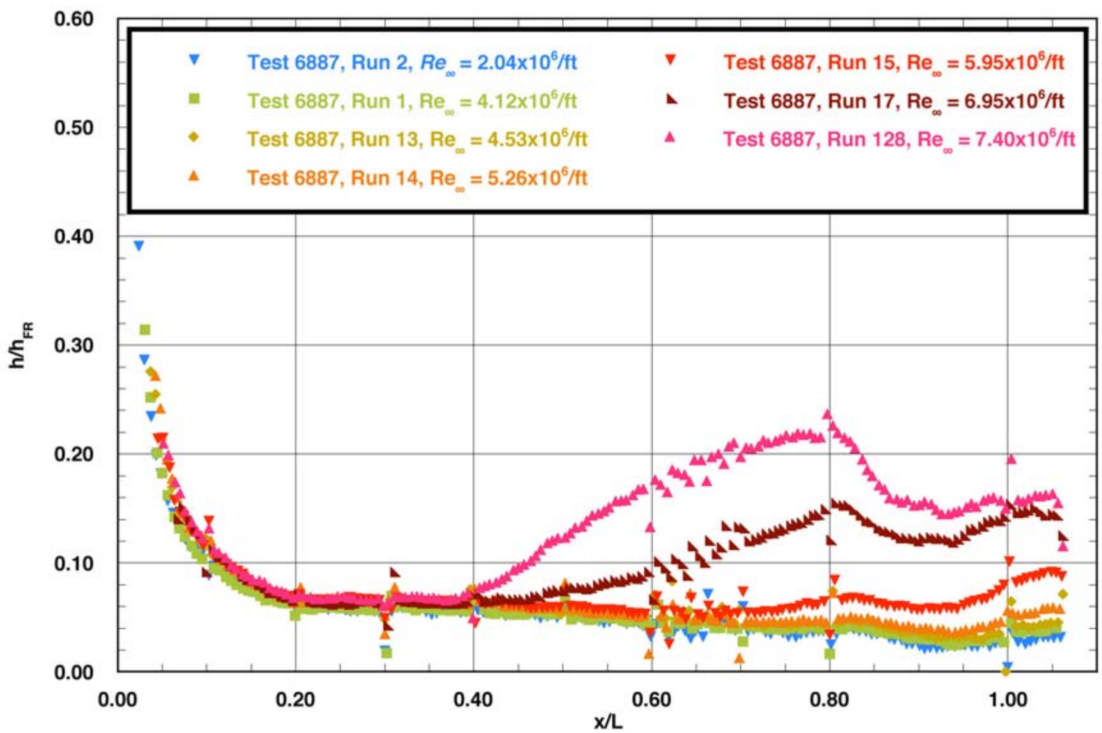

Figure A.3: RTF-BLT-C1 centerline data in the 20-Inch Mach 6 Air Tunnel at α = 30-deg.

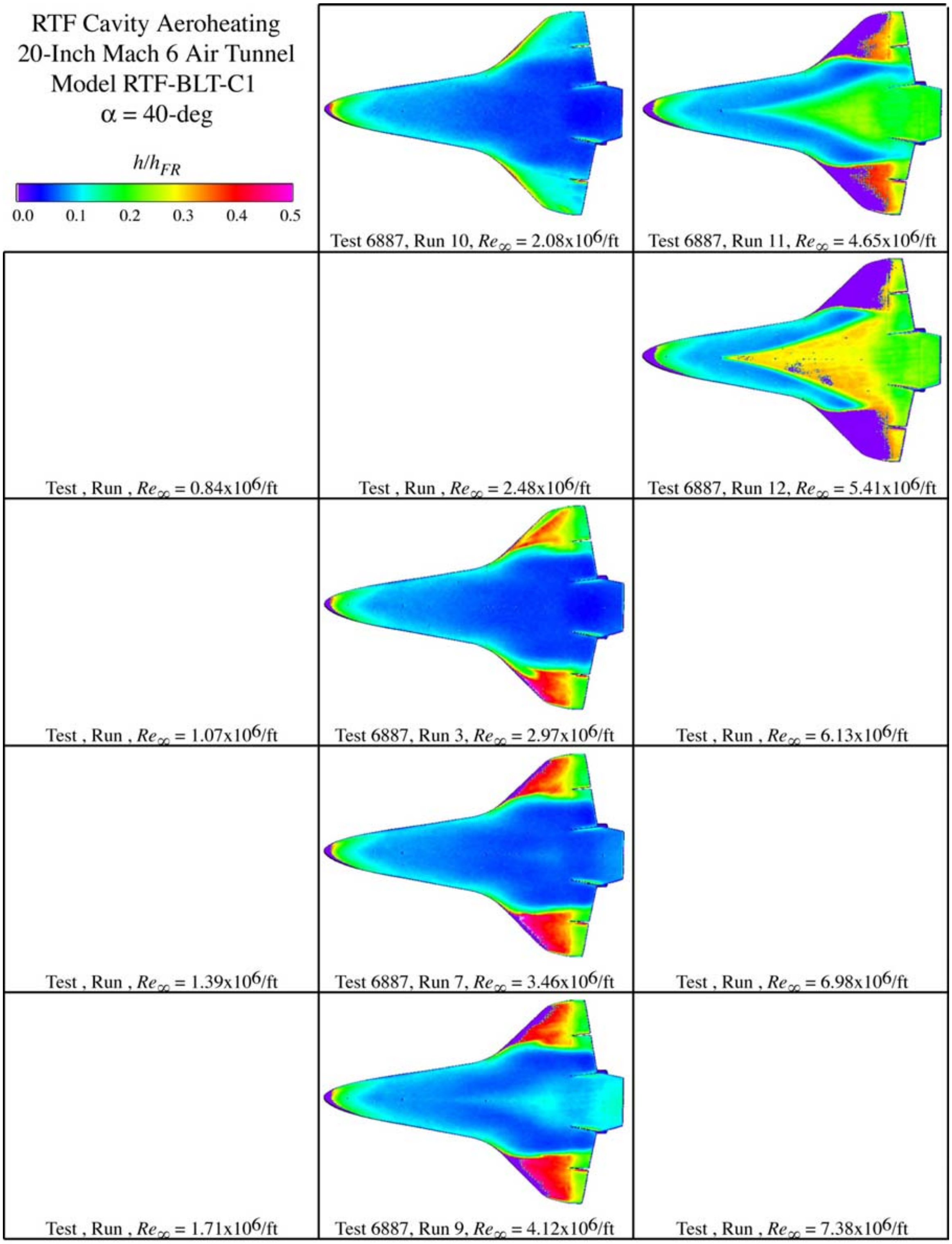

Figure A.4: RTF-BLT-C1 global aeroheating in the 20-Inch Mach 6 Air Tunnel at α = 40-deg.

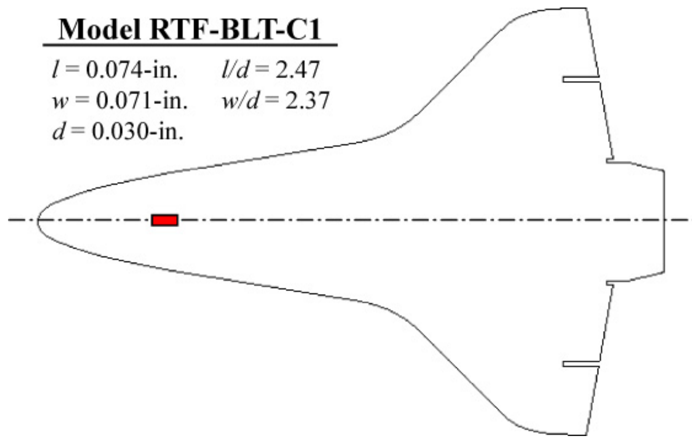

Figure A.5: RTF-BLT-C1 cavity information.

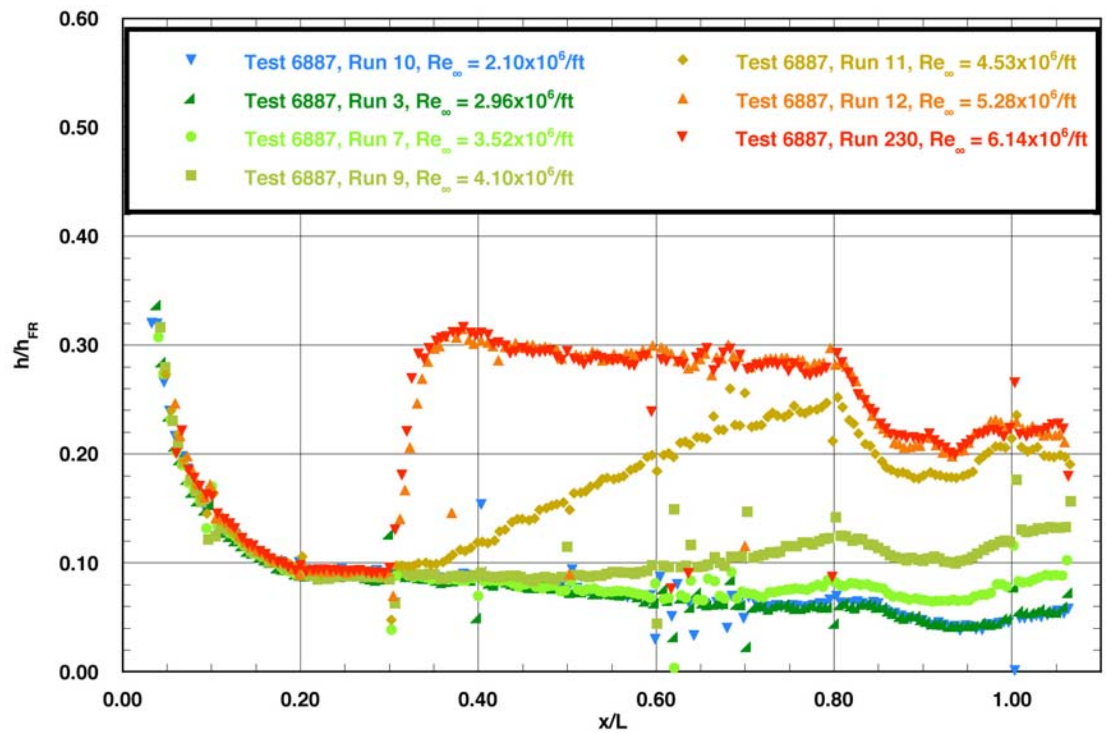

Figure A.6: RTF-BLT-C1 centerline data in the 20-Inch Mach 6 Air Tunnel at α = 40-deg.

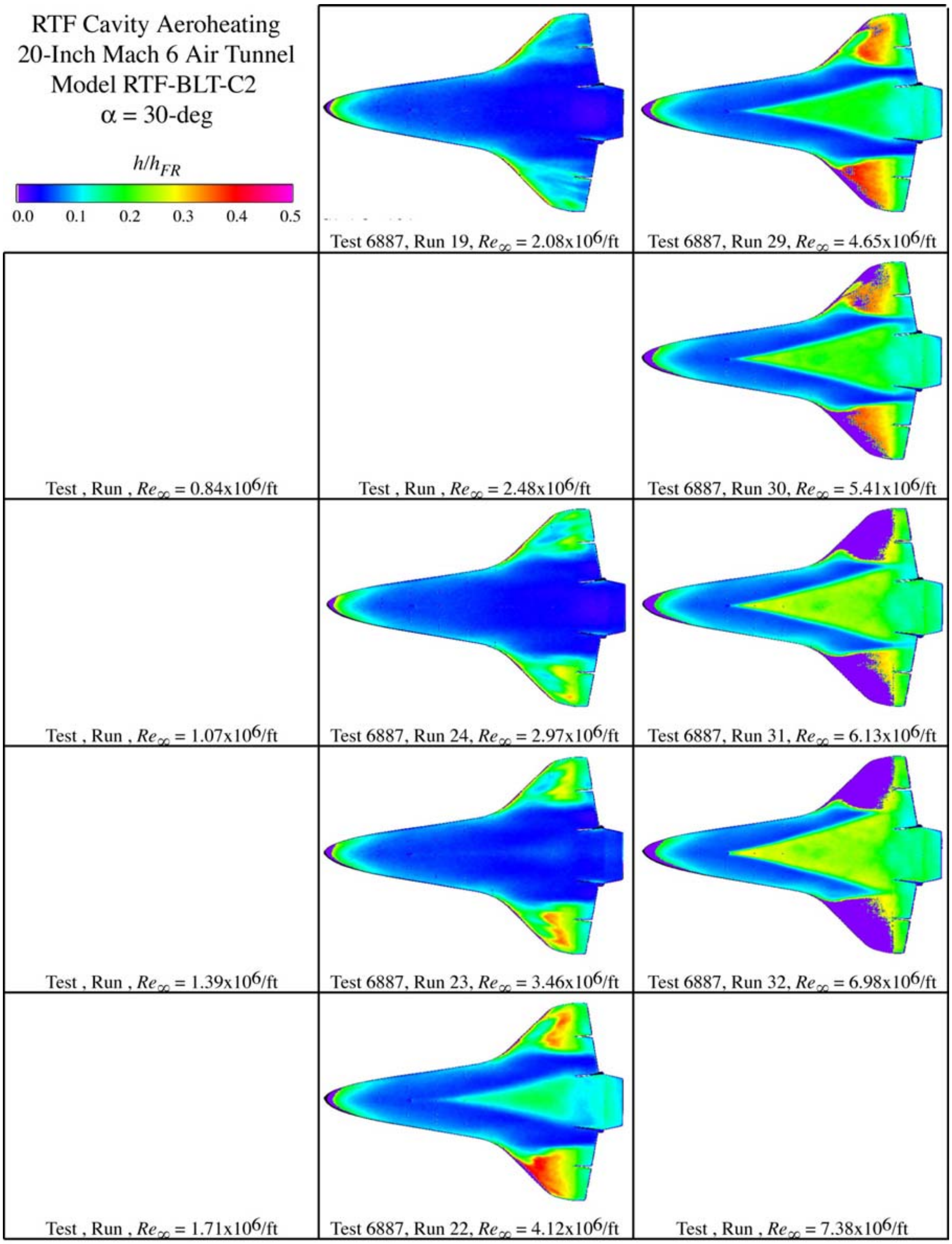

Figure A.7: RTF-BLT-C2 global aeroheating in the 20-Inch Mach 6 Air Tunnel at α = 30-deg.

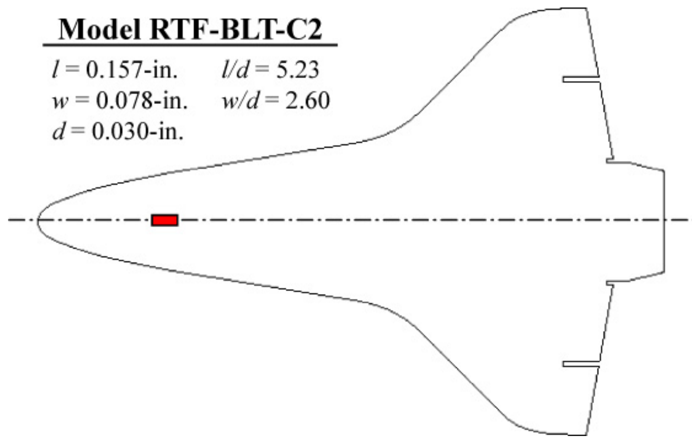

Figure A.8: RTF-BLT-C2 cavity information.

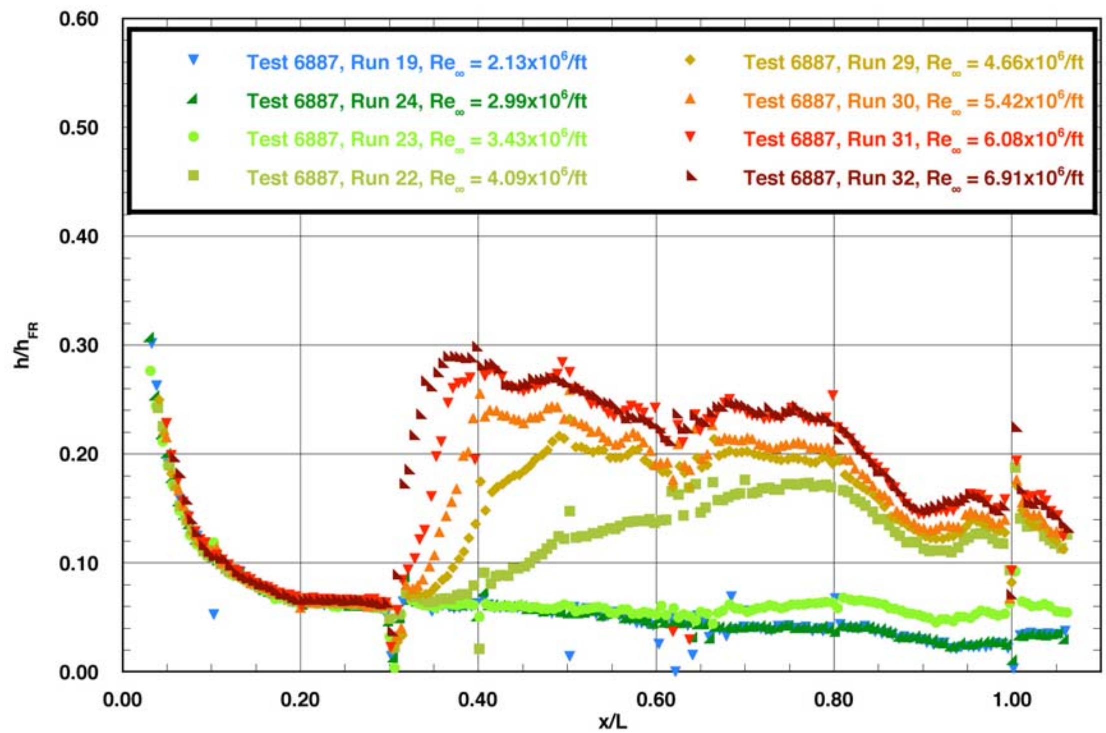

Figure A.9: RTF-BLT-C2 centerline data in the 20-Inch Mach 6 Air Tunnel at α = 30-deg.

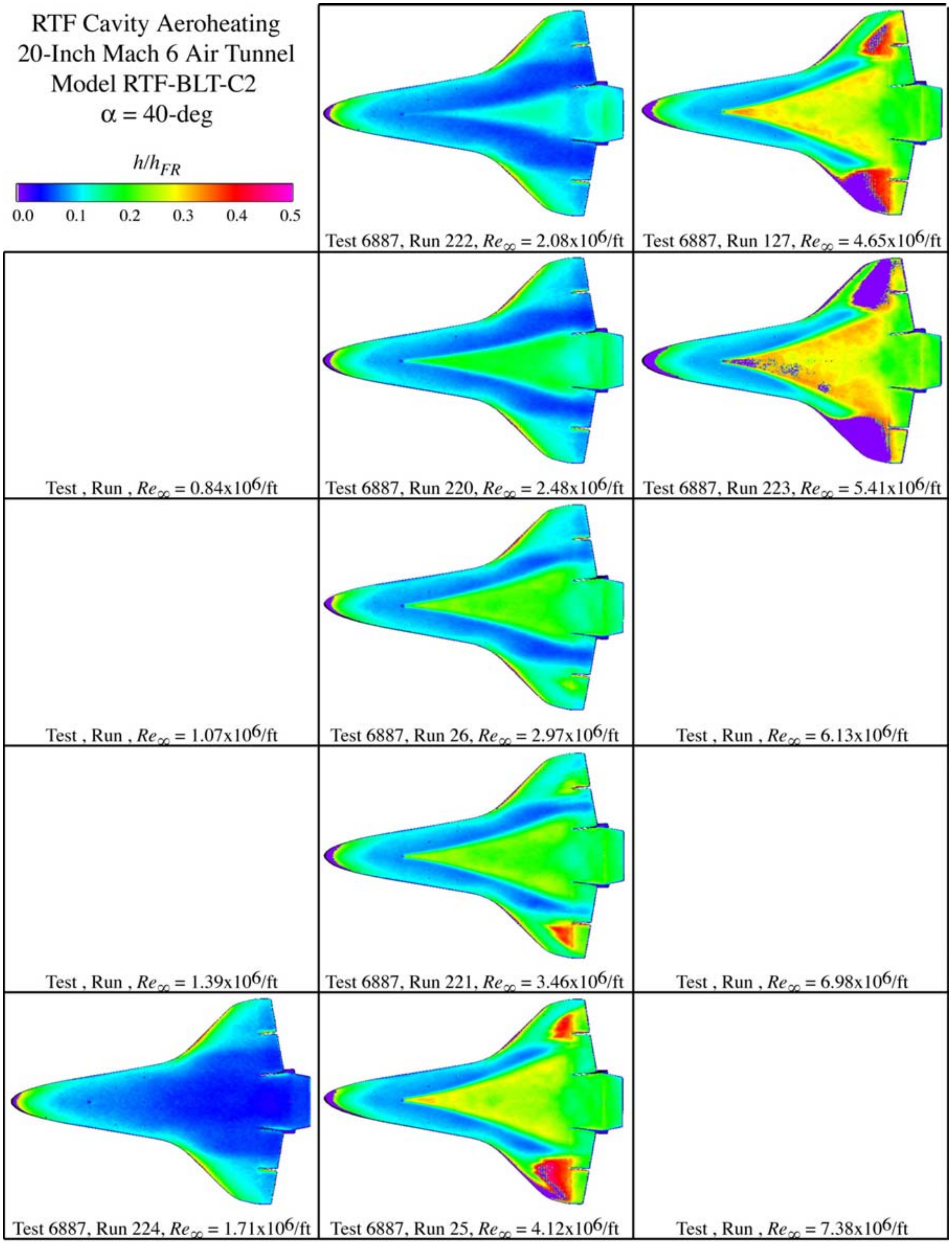

Figure A.10: RTF-BLT-C2 global aeroheating in the 20-Inch Mach 6 Air Tunnel at α = 40-deg.

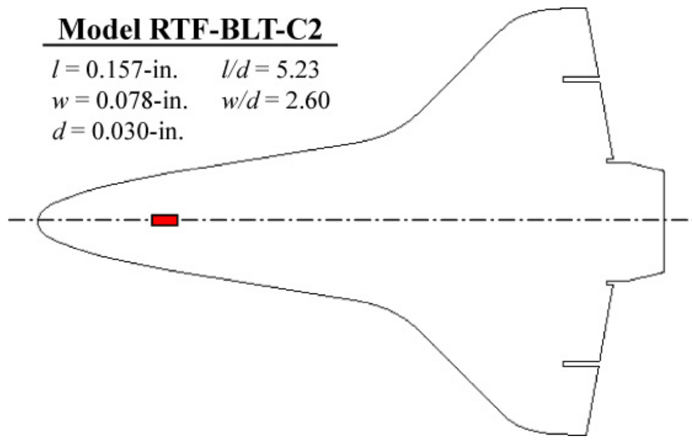

Figure A.11: RTF-BLT-C2 cavity information.

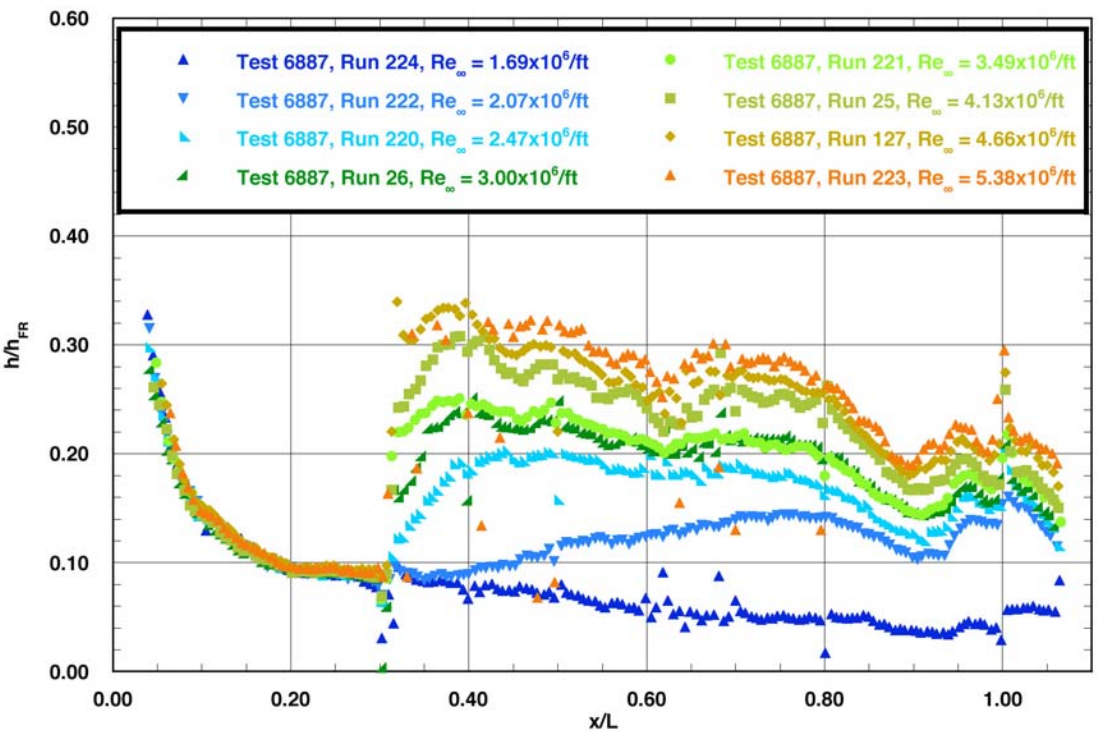

Figure A.12: RTF-BLT-C2 centerline data in the 20-Inch Mach 6 Air Tunnel at α = 40-deg.

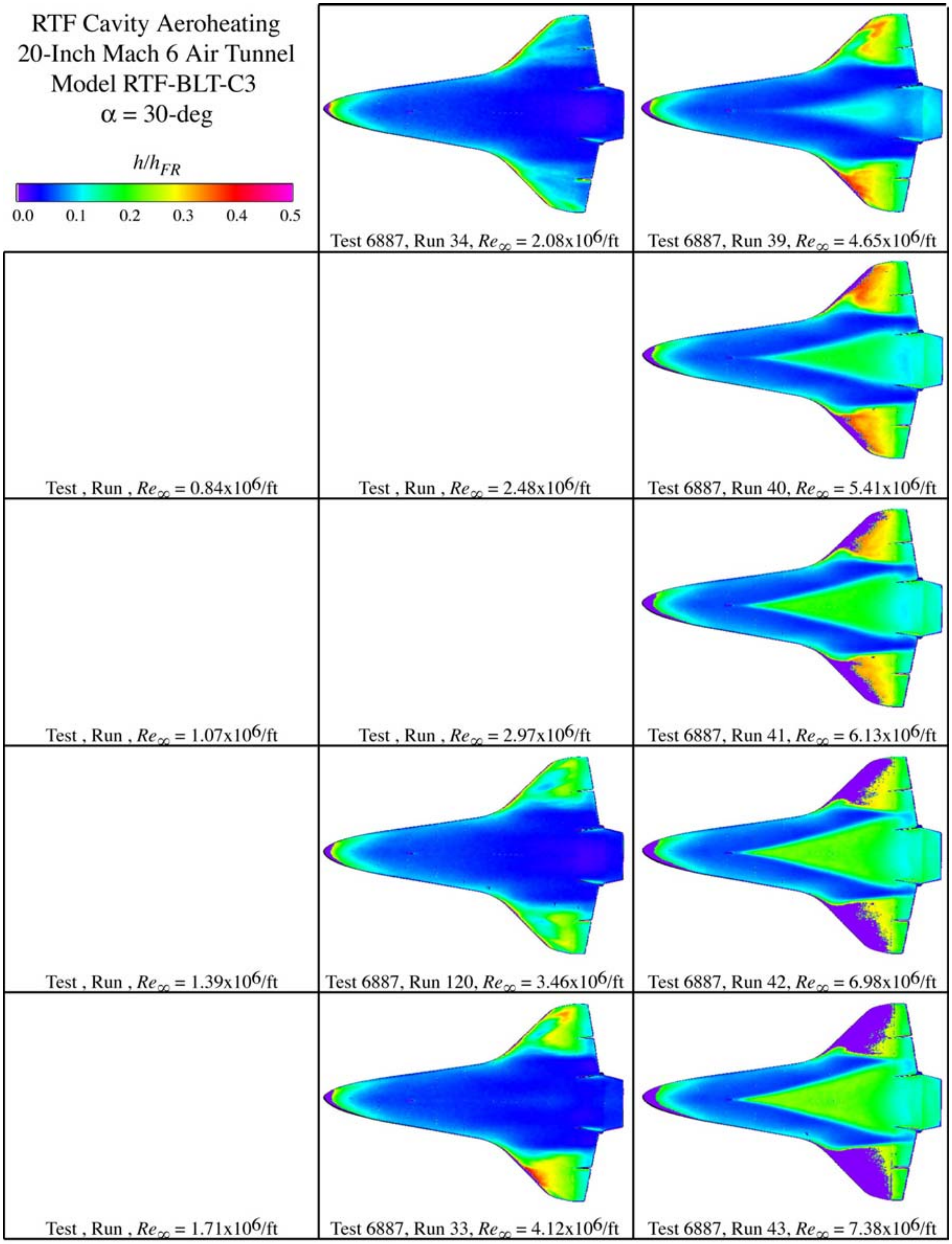

Figure A.13: RTF-BLT-C3 global aeroheating in the 20-Inch Mach 6 Air Tunnel at α = 30-deg.

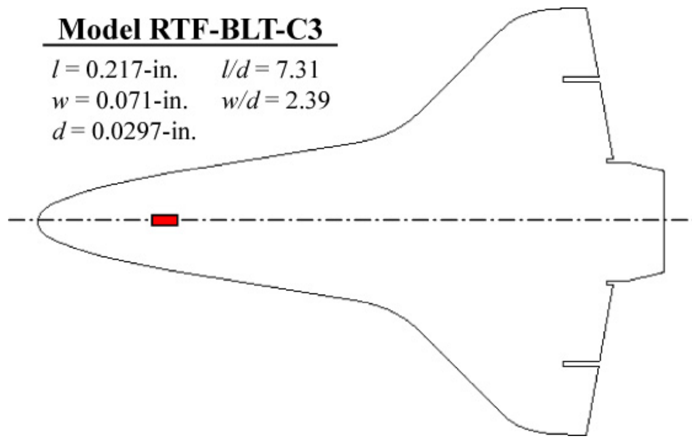

Figure A.14: RTF-BLT-C3 cavity information.

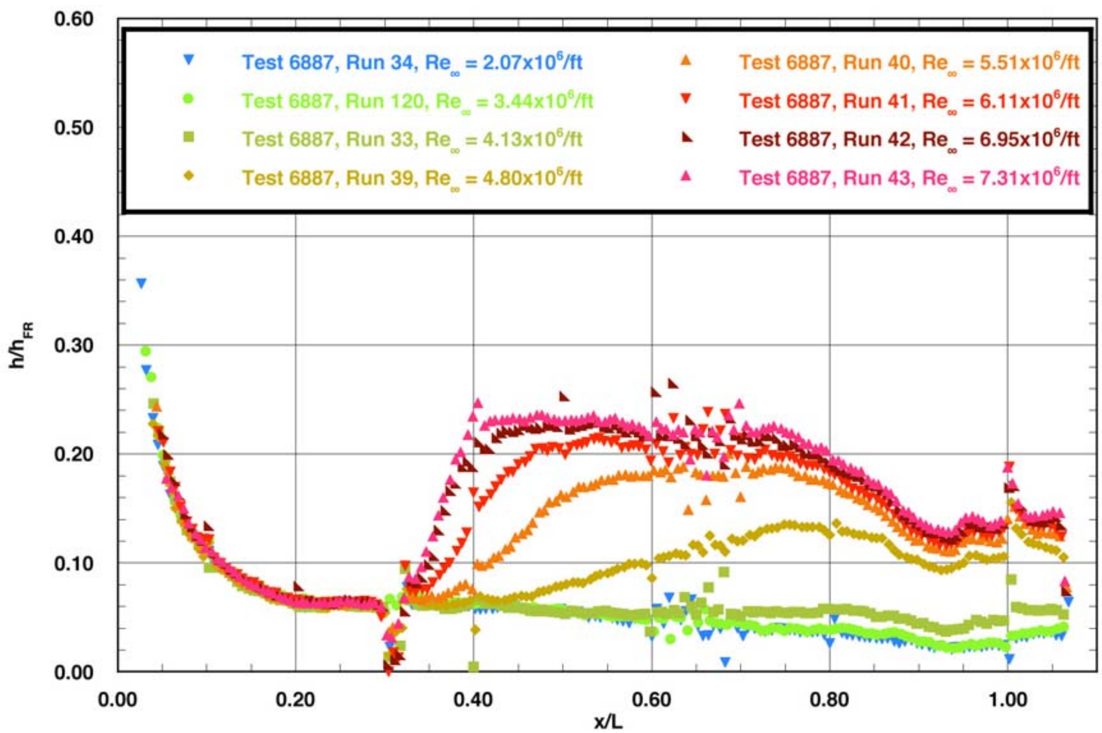

Figure A.15: RTF-BLT-C3 centerline data in the 20-Inch Mach 6 Air Tunnel at α = 30-deg.

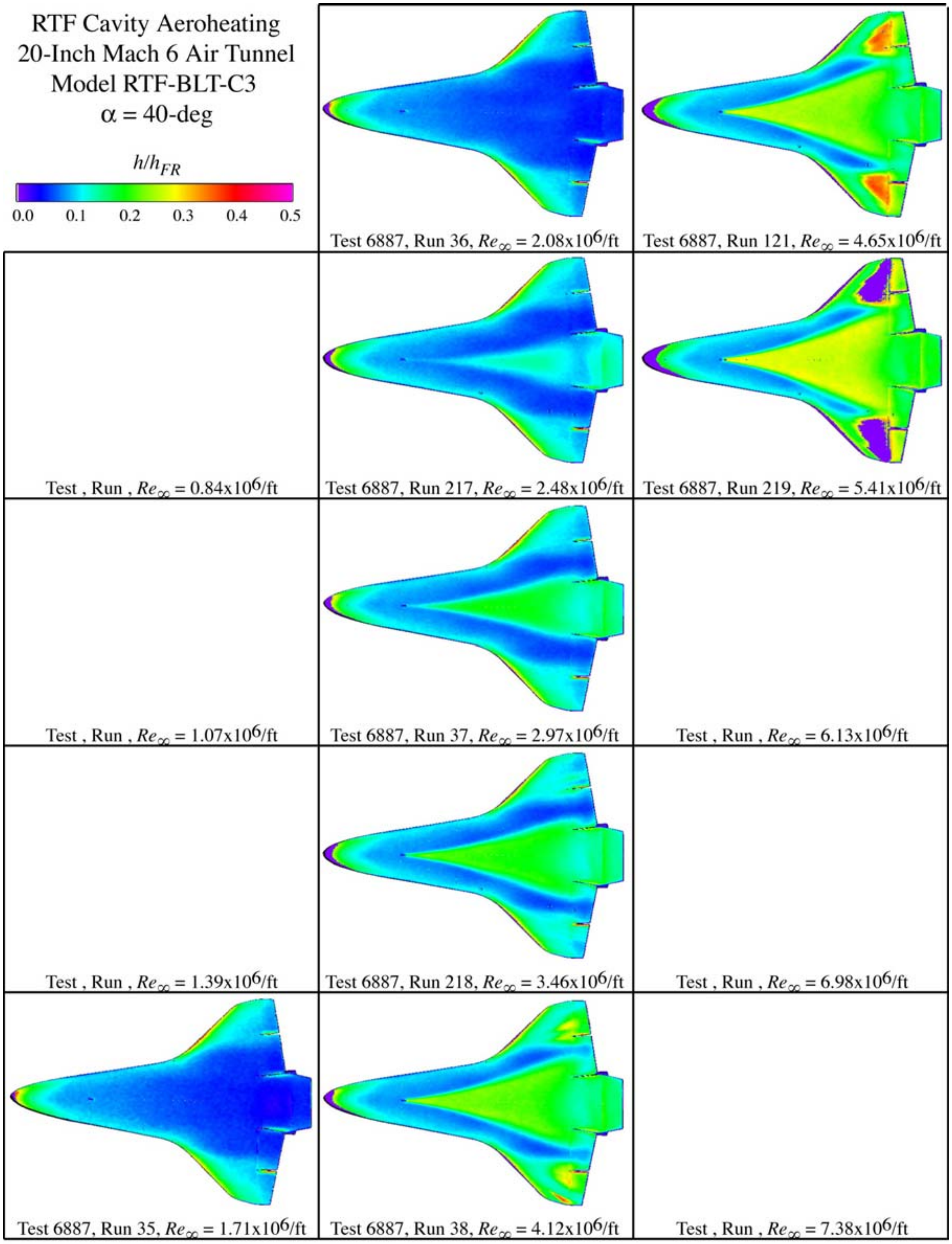

Figure A.16: RTF-BLT-C3 global aeroheating in the 20-Inch Mach 6 Air Tunnel at α = 40-deg.

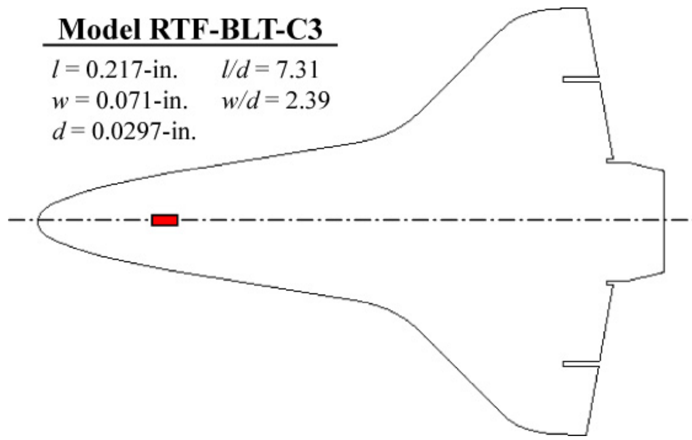

Figure A.17: RTF-BLT-C3 cavity information.

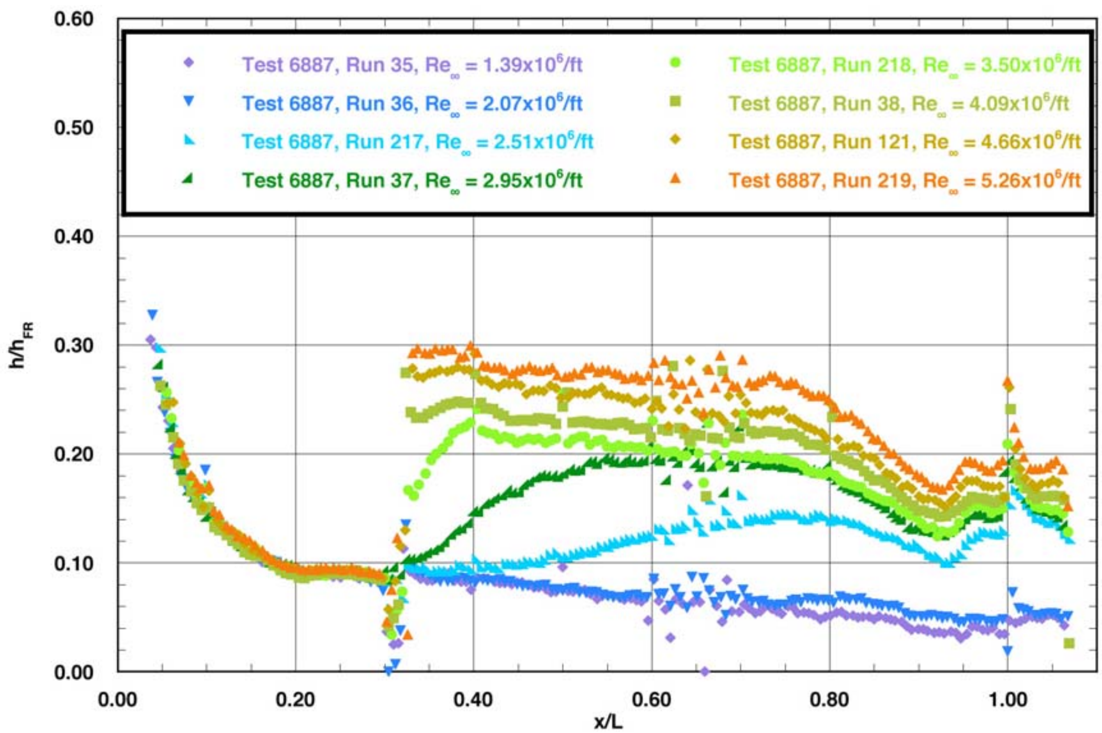

Figure A.18: RTF-BLT-C3 centerline data in the 20-Inch Mach 6 Air Tunnel at α = 40-deg.

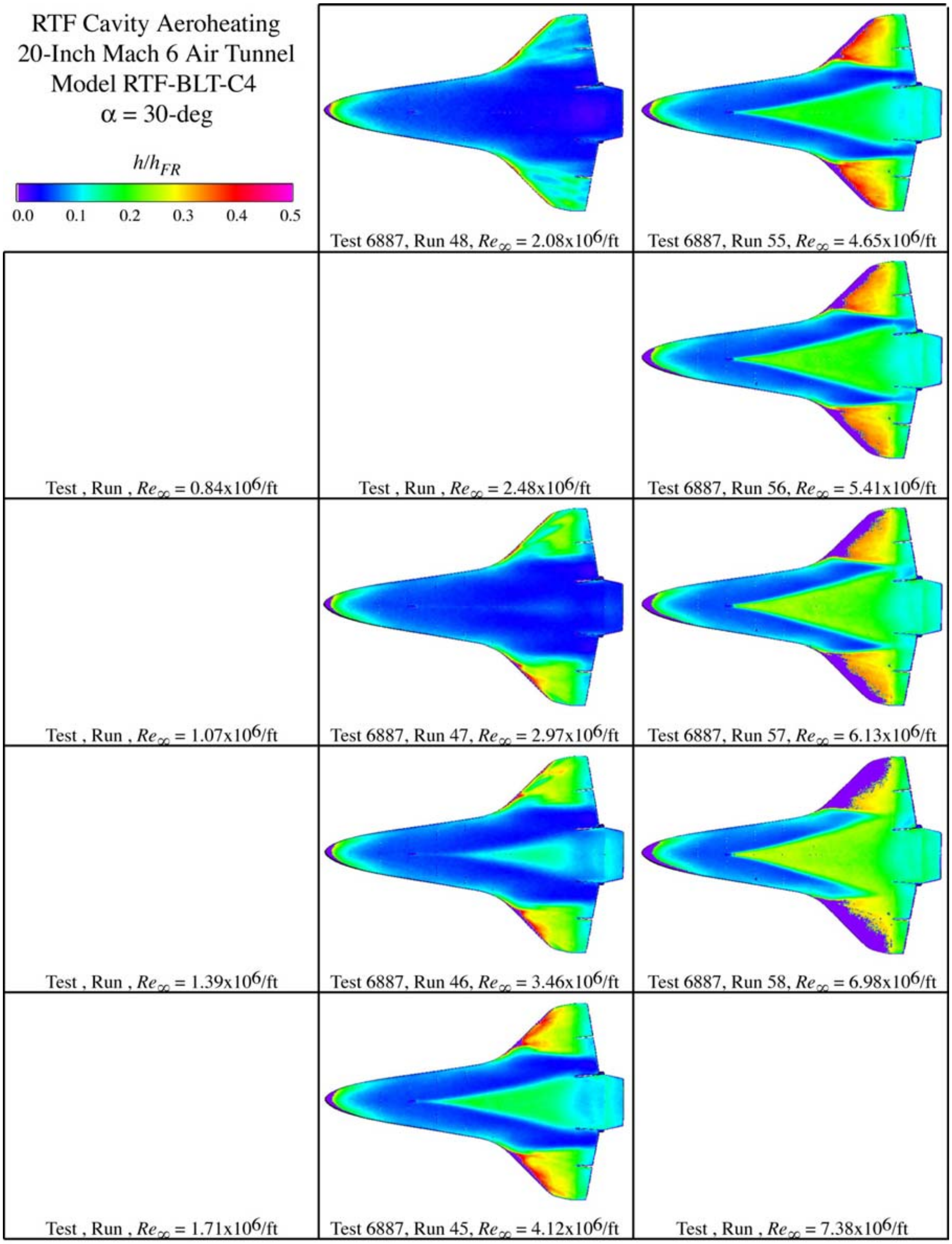

Figure A.19: RTF-BLT-C4 global aeroheating in the 20-Inch Mach 6 Air Tunnel at α = 30-deg.

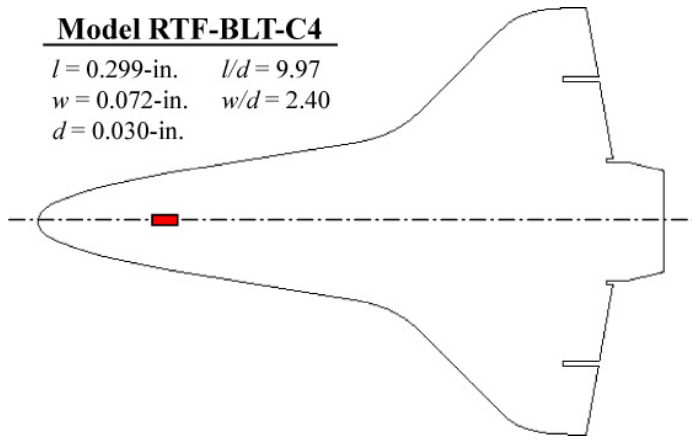

Figure A.20: RTF-BLT-C4 cavity information.

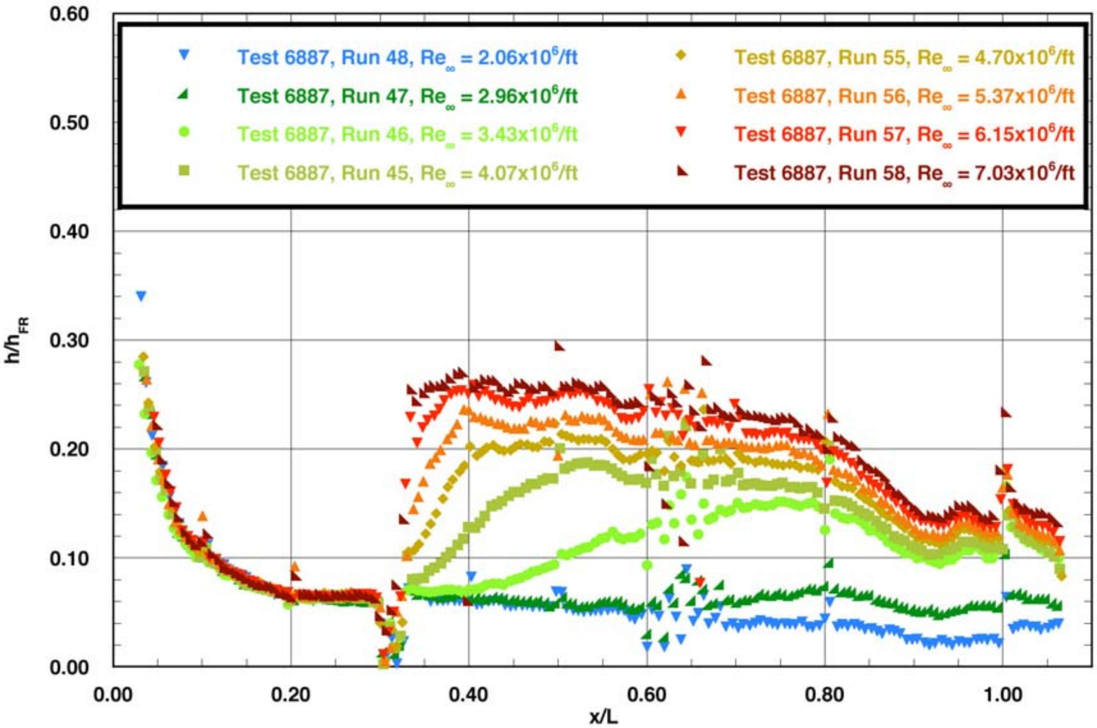

Figure A.21: RTF-BLT-C4 centerline data in the 20-Inch Mach 6 Air Tunnel at α = 30-deg.

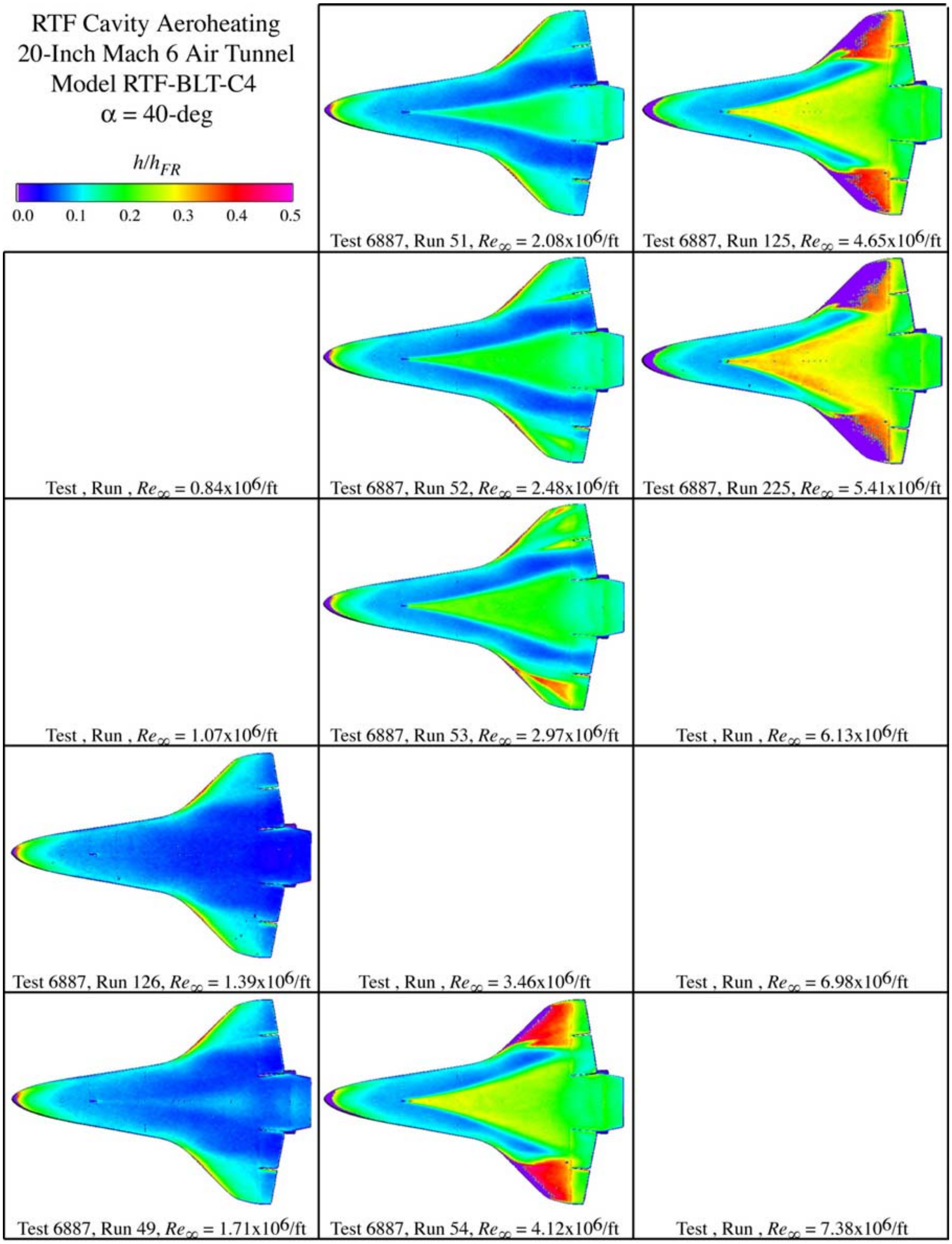

Figure A.22: RTF-BLT-C4 global aeroheating in the 20-Inch Mach 6 Air Tunnel at α = 40-deg.

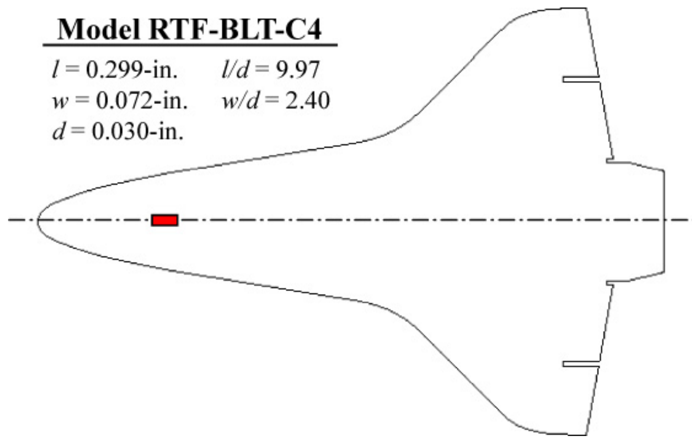

Figure A.23: RTF-BLT-C4 cavity information.

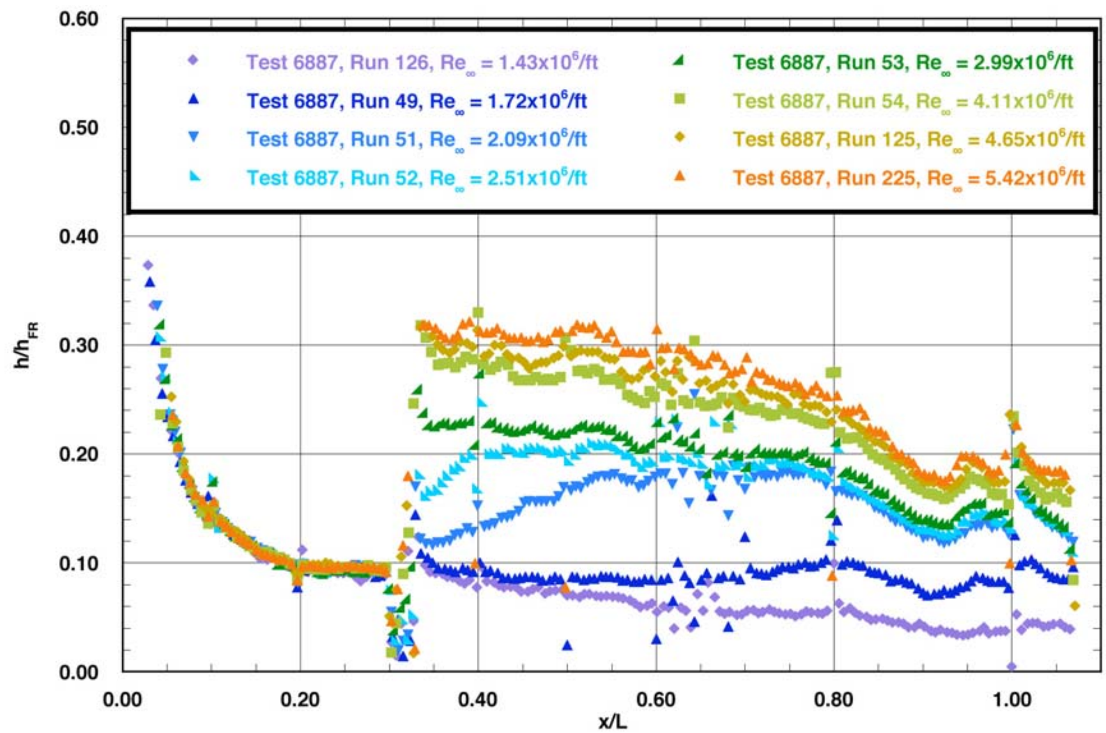

Figure A.24: RTF-BLT-C4 centerline data in the 20-Inch Mach 6 Air Tunnel at α = 40-deg.

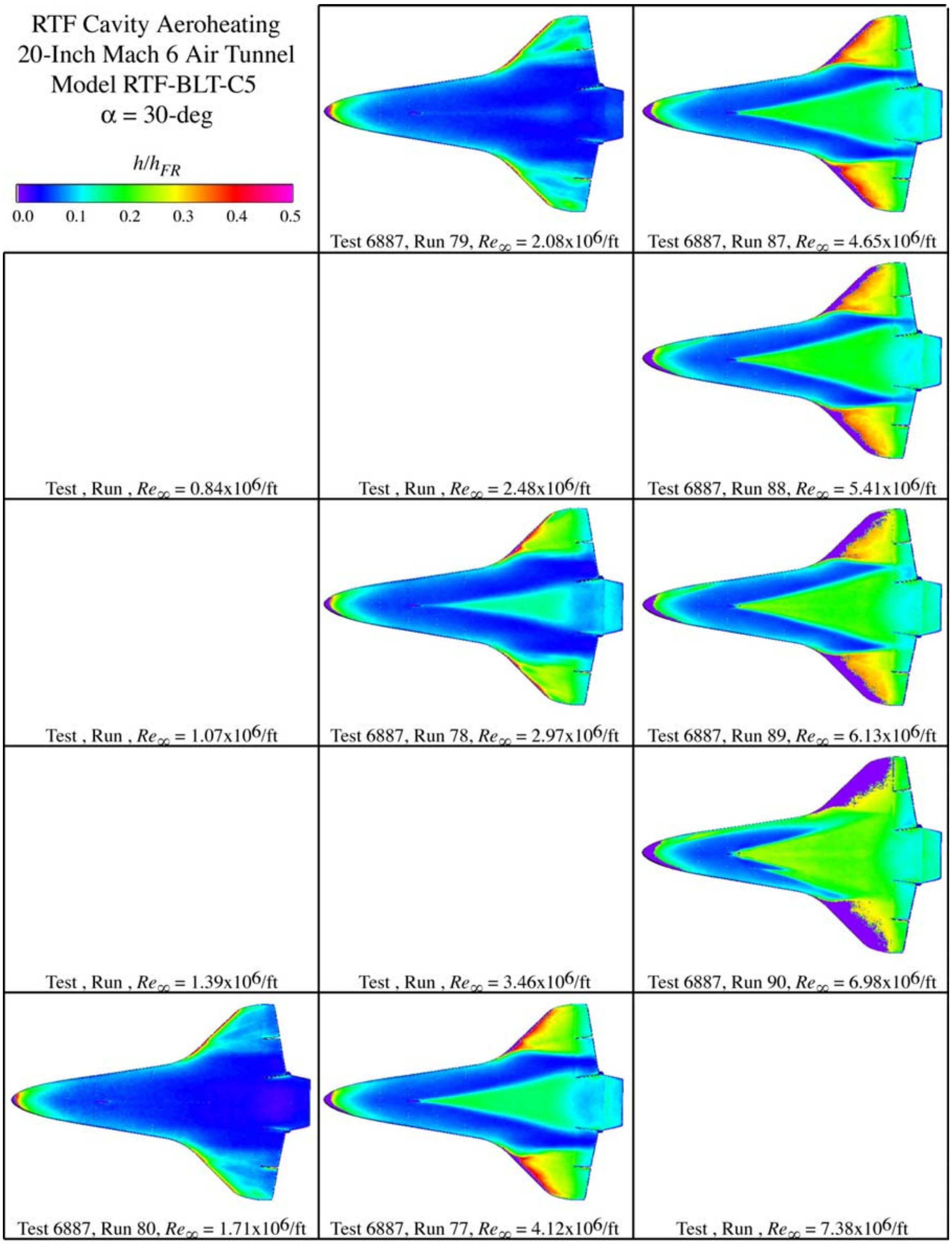

Figure A.25: RTF-BLT-C5 global aeroheating in the 20-Inch Mach 6 Air Tunnel at α = 30-deg.

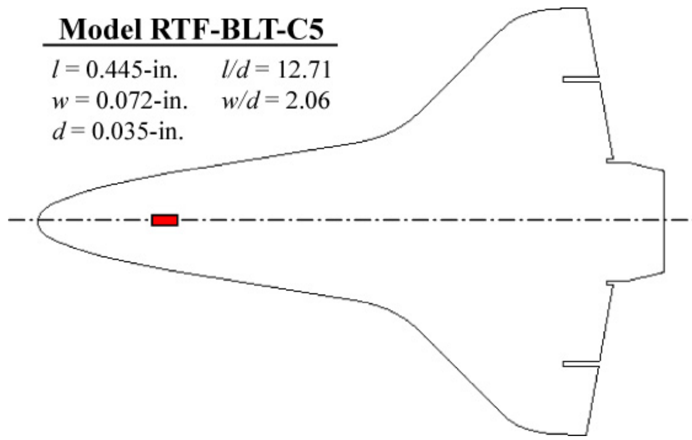

Figure A.26: RTF-BLT-C5 cavity information.

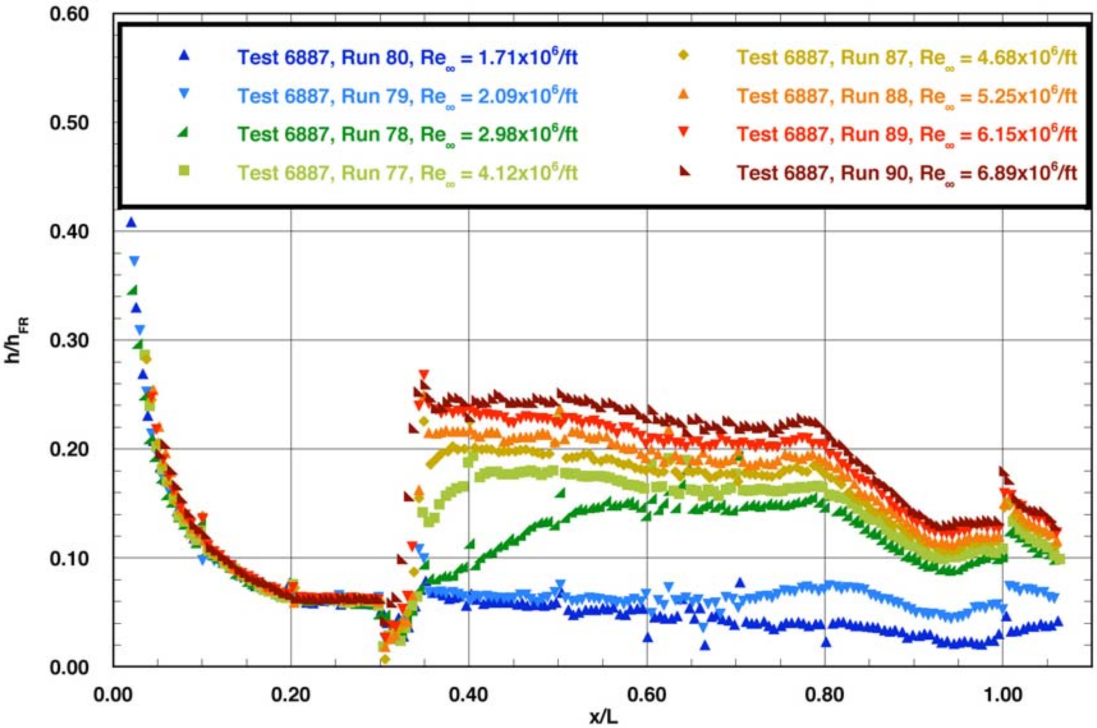

Figure A.27: RTF-BLT-C5 centerline data in the 20-Inch Mach 6 Air Tunnel at α = 30-deg.

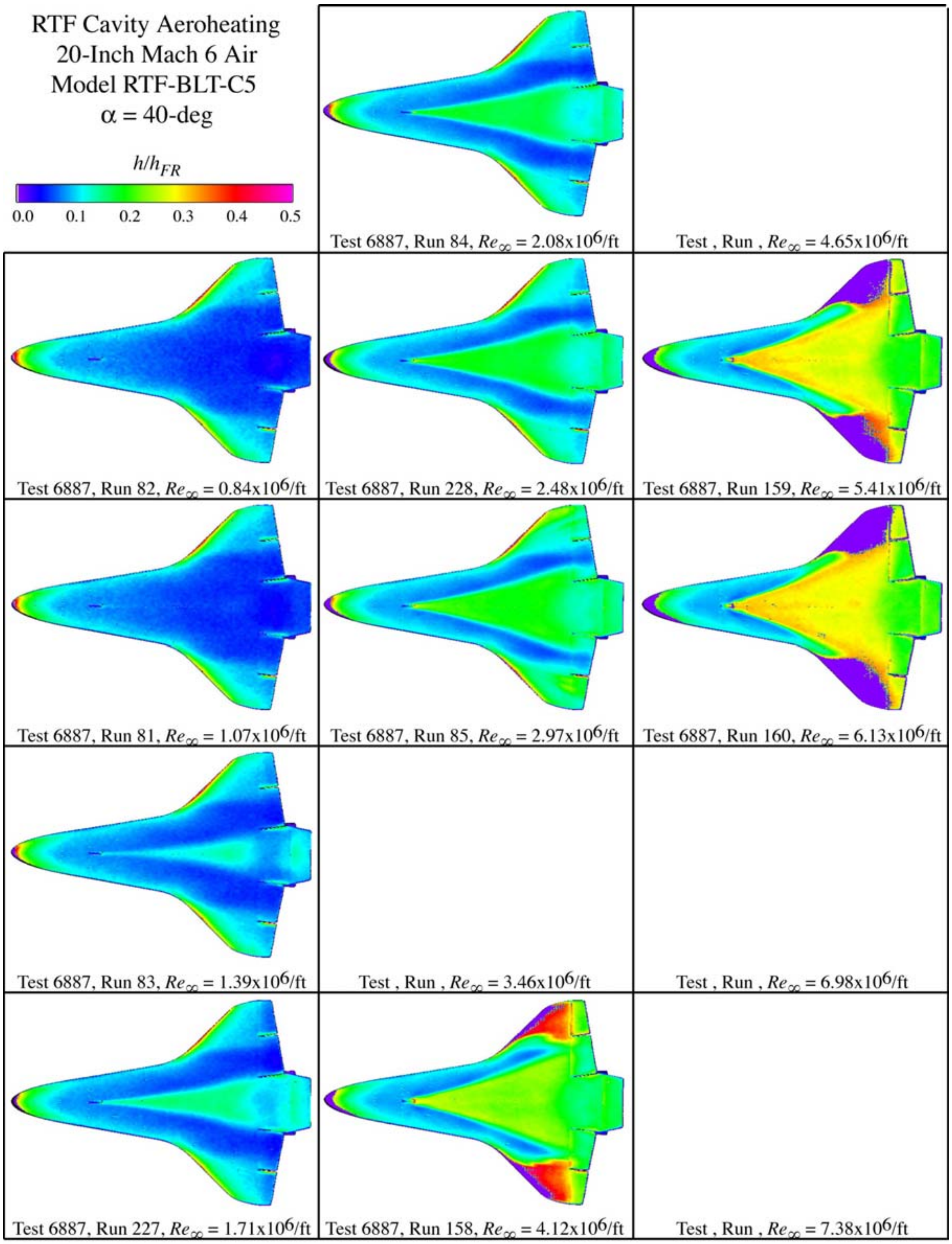

Figure A.28: RTF-BLT-C5 global aeroheating in the 20-Inch Mach 6 Air Tunnel at $\alpha = 40$-deg.

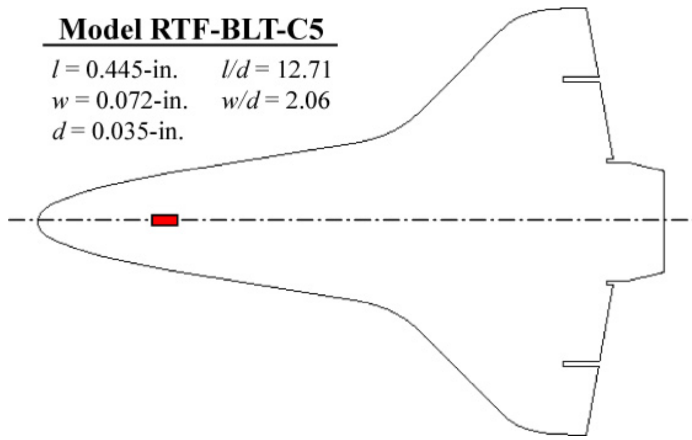

Figure A.29: RTF-BLT-C5 cavity information.

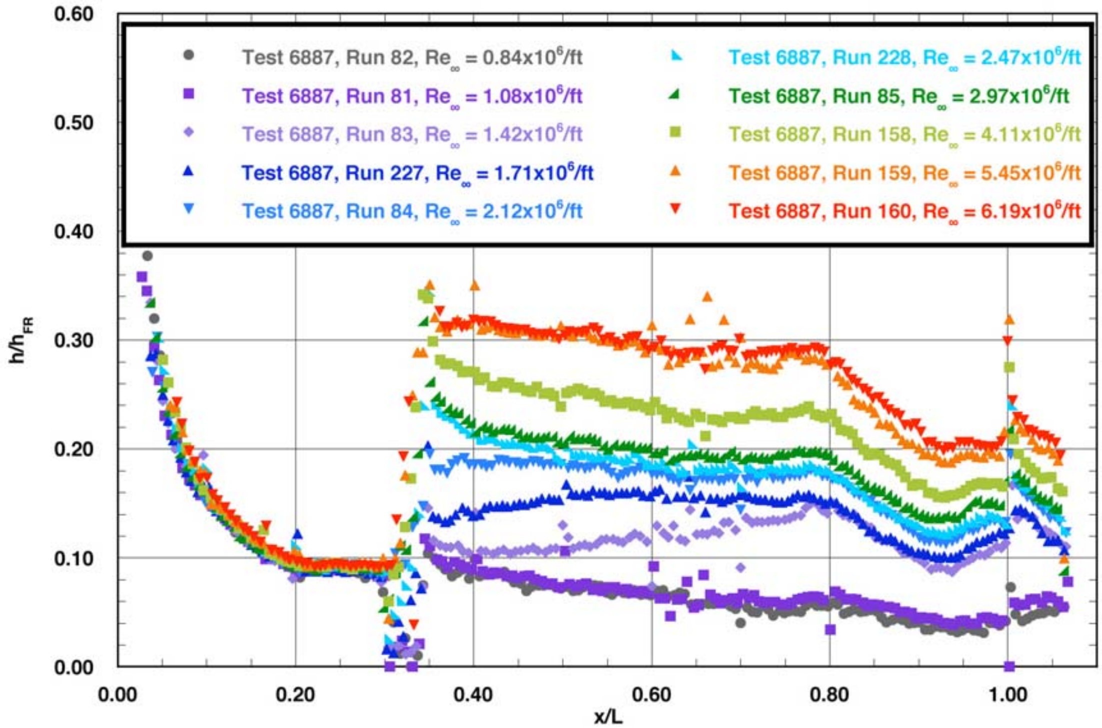

Figure A.30: RTF-BLT-C5 centerline data in the 20-Inch Mach 6 Air Tunnel at α = 40-deg.

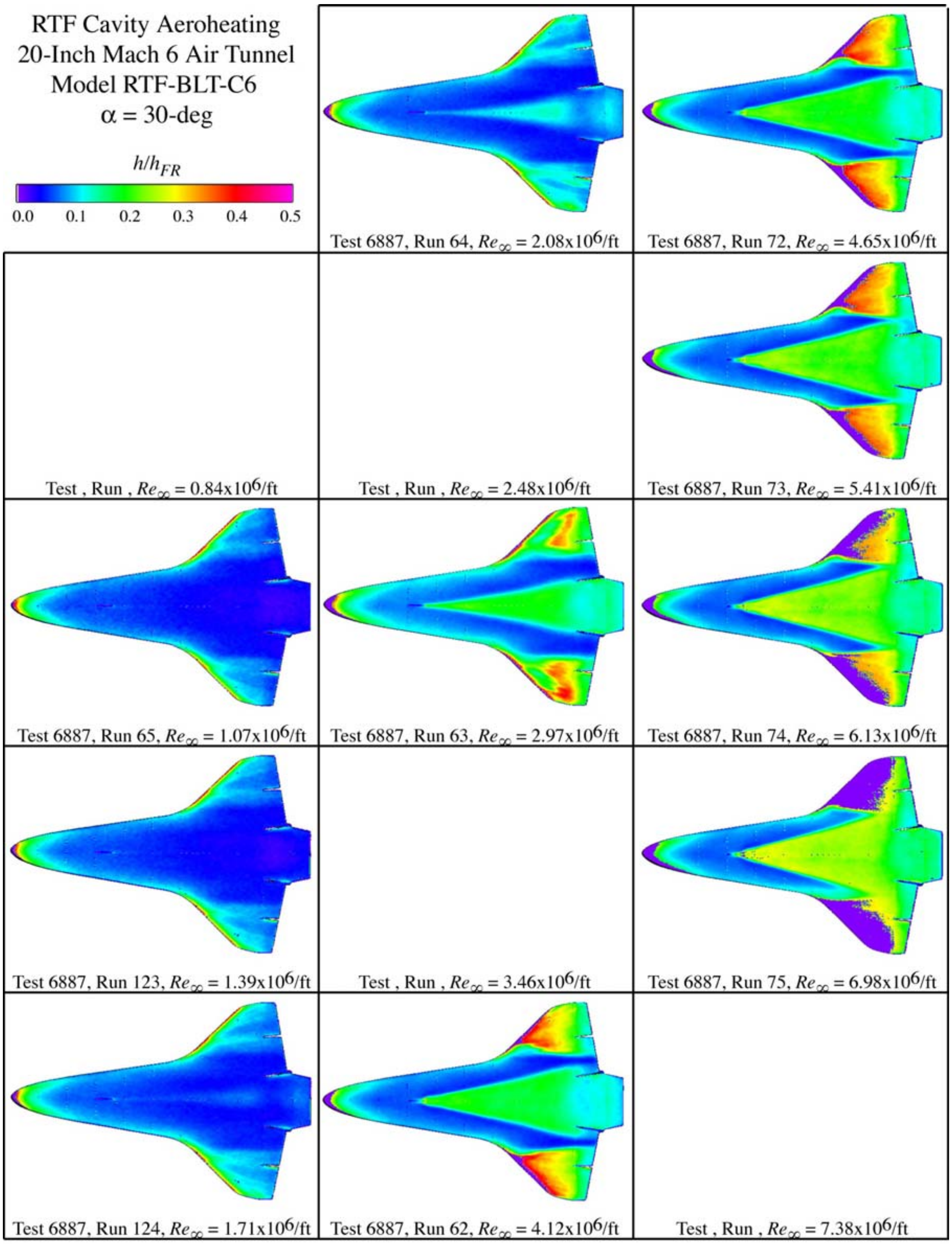

Figure A.31: RTF-BLT-C6 global aeroheating in the 20-Inch Mach 6 Air Tunnel at α = 30-deg.

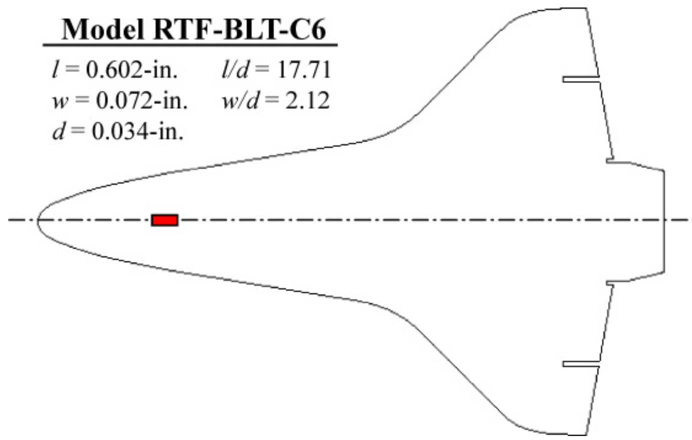

Figure A.32: RTF-BLT-C6 cavity information.

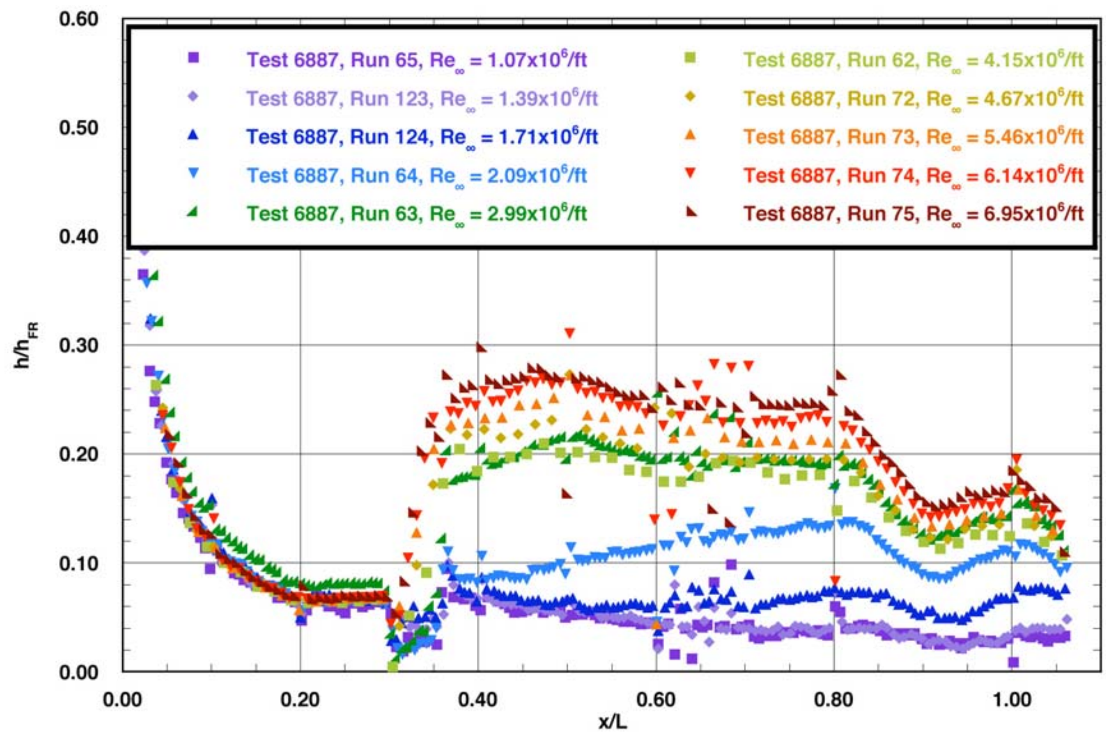

Figure A.33: RTF-BLT-C6 centerline data in the 20-Inch Mach 6 Air Tunnel at α = 30-deg.

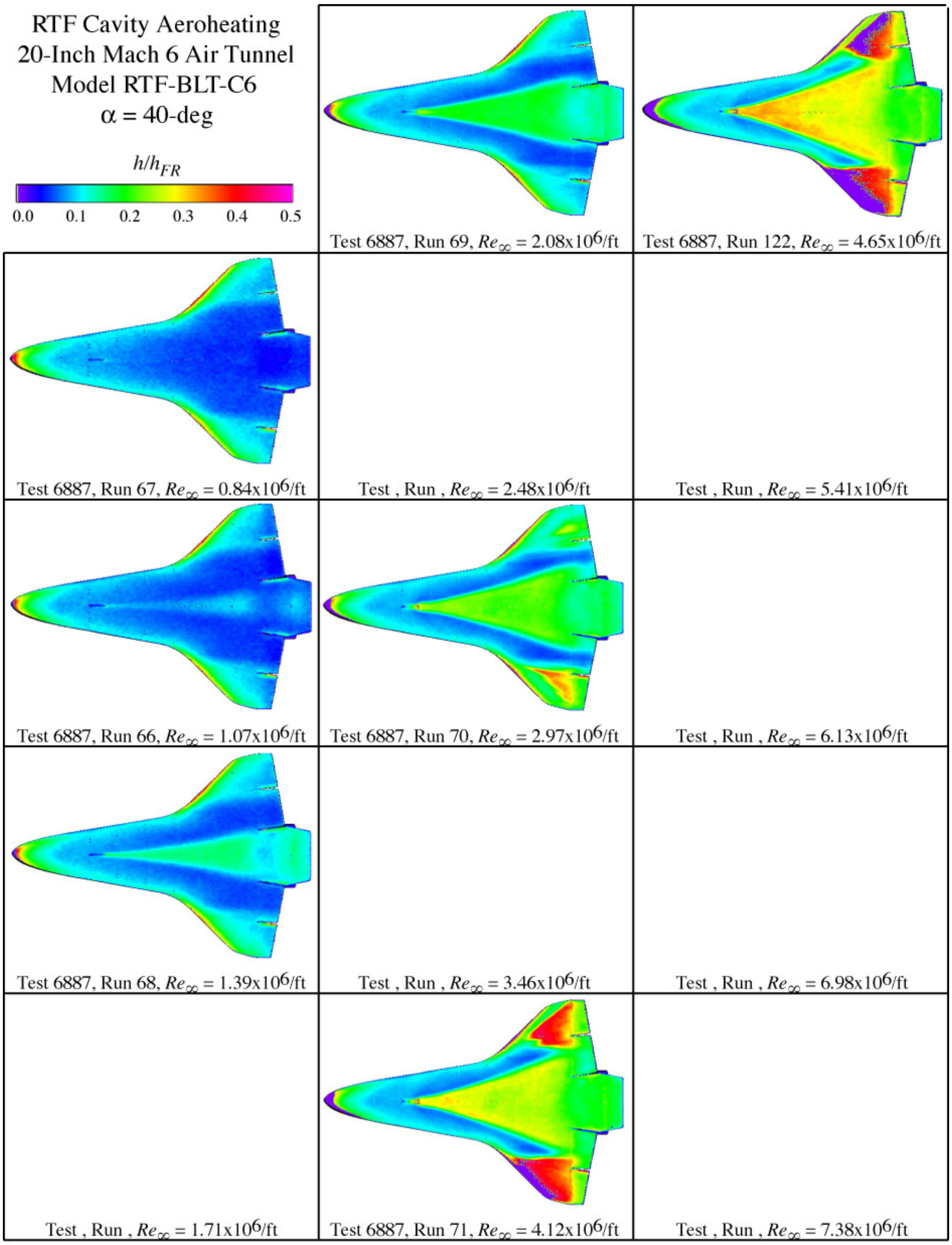

Figure A.34: RTF-BLT-C6 global aeroheating in the 20-Inch Mach 6 Air Tunnel at α = 40-deg.

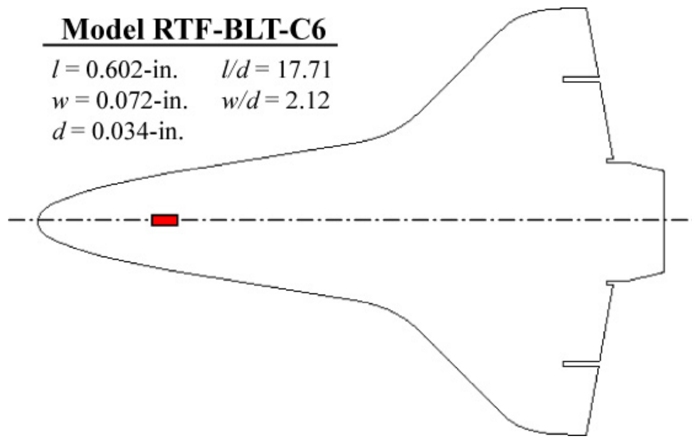

Figure A.35: RTF-BLT-C6 cavity information.

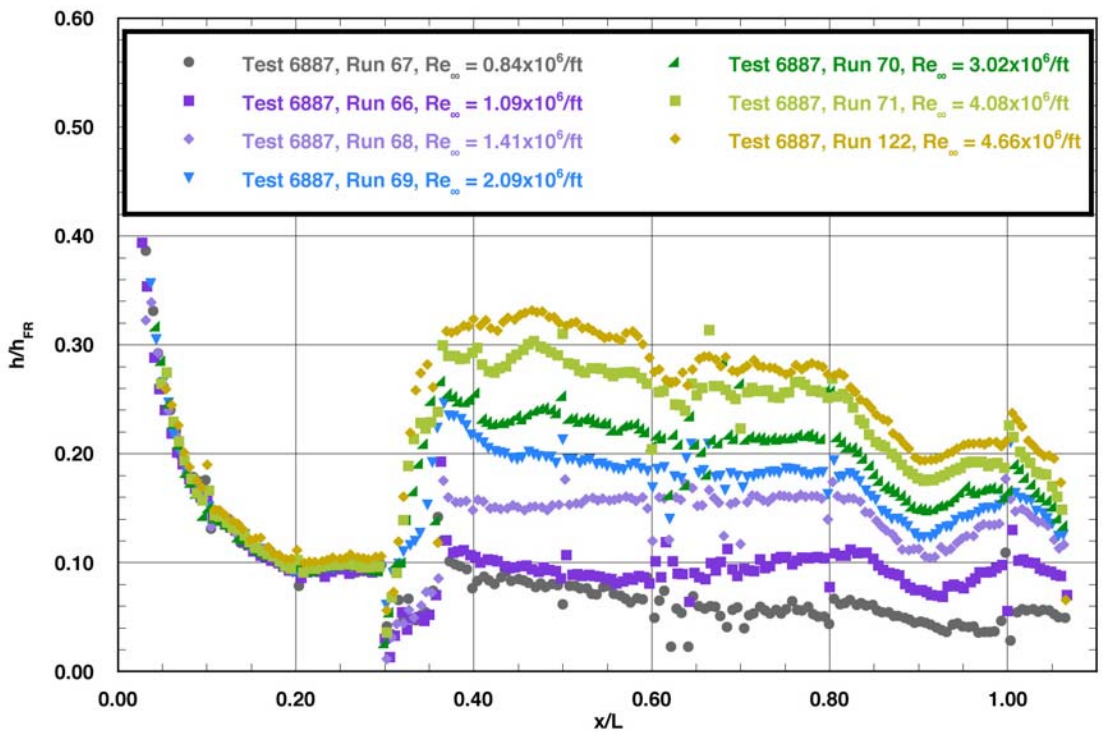

Figure A.36: RTF-BLT-C6 centerline data in the 20-Inch Mach 6 Air Tunnel at α = 40-deg.

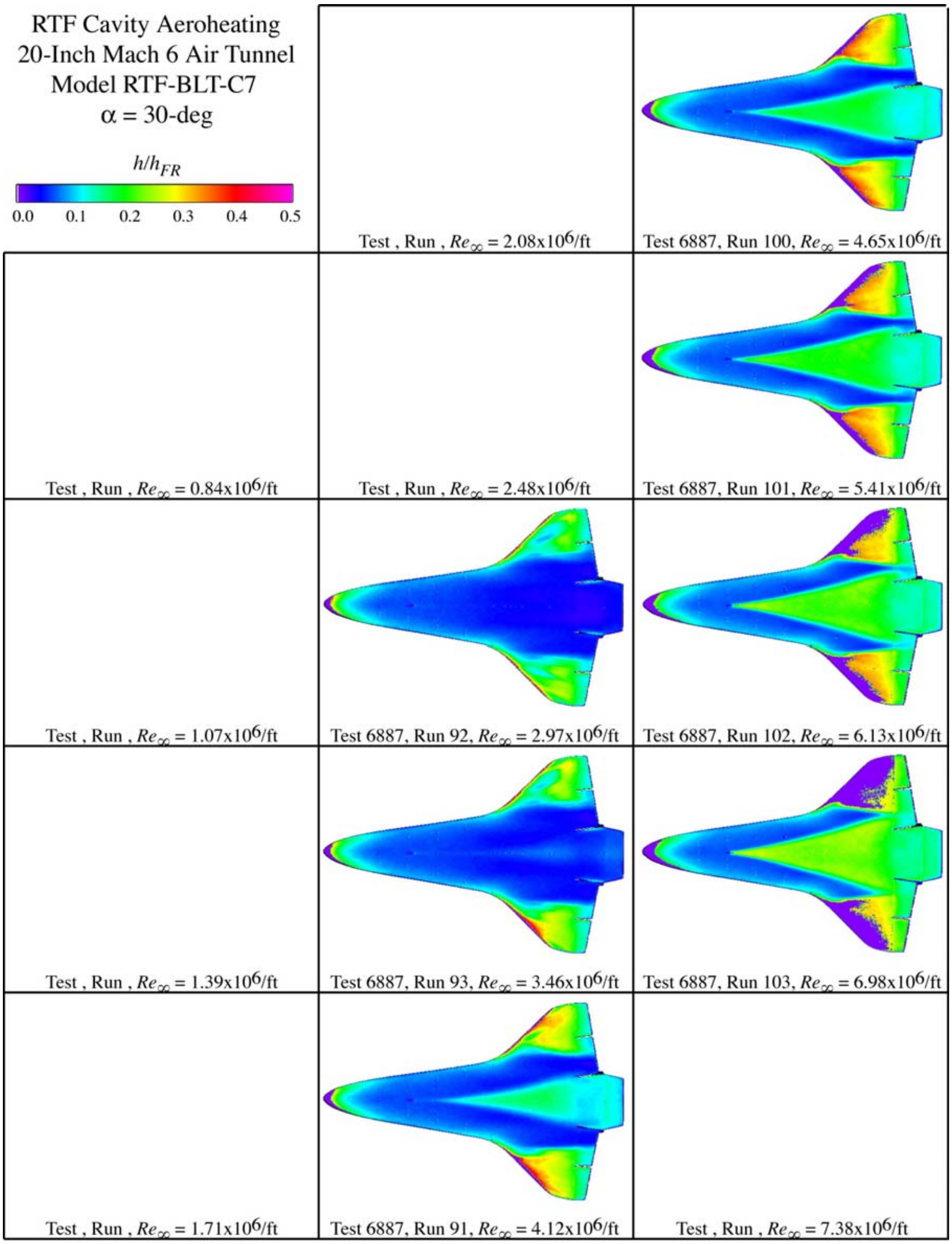

Figure A.37: RTF-BLT-C7 global aeroheating in the 20-Inch Mach 6 Air Tunnel at α = 30-deg.

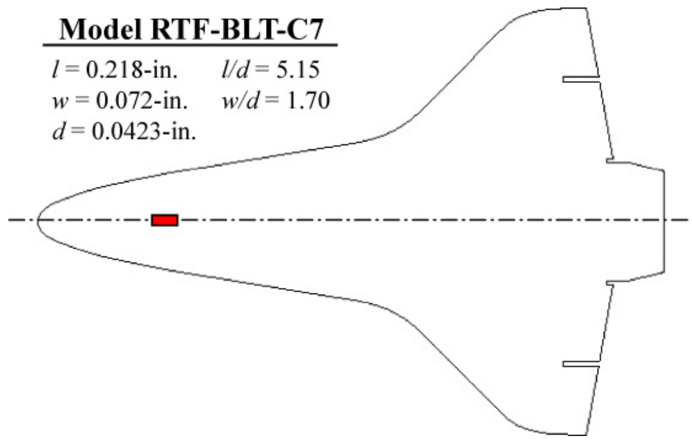

Figure A.38: RTF-BLT-C7 cavity information.

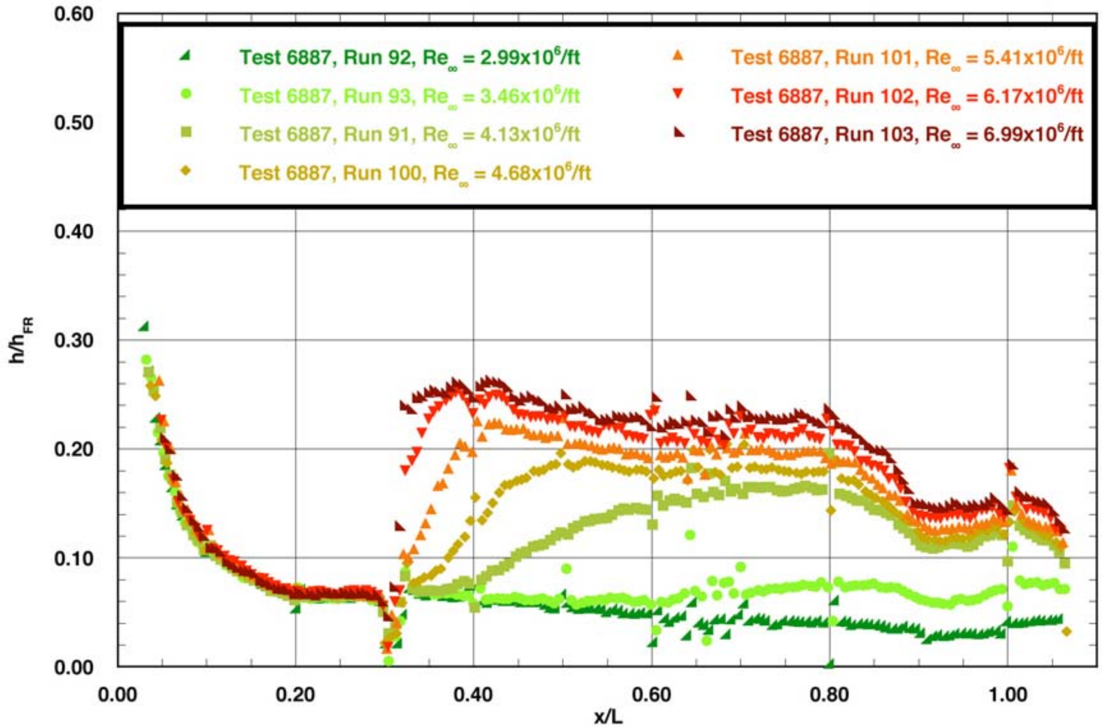

Figure A.39: RTF-BLT-C7 centerline data in the 20-Inch Mach 6 Air Tunnel at α = 30-deg.

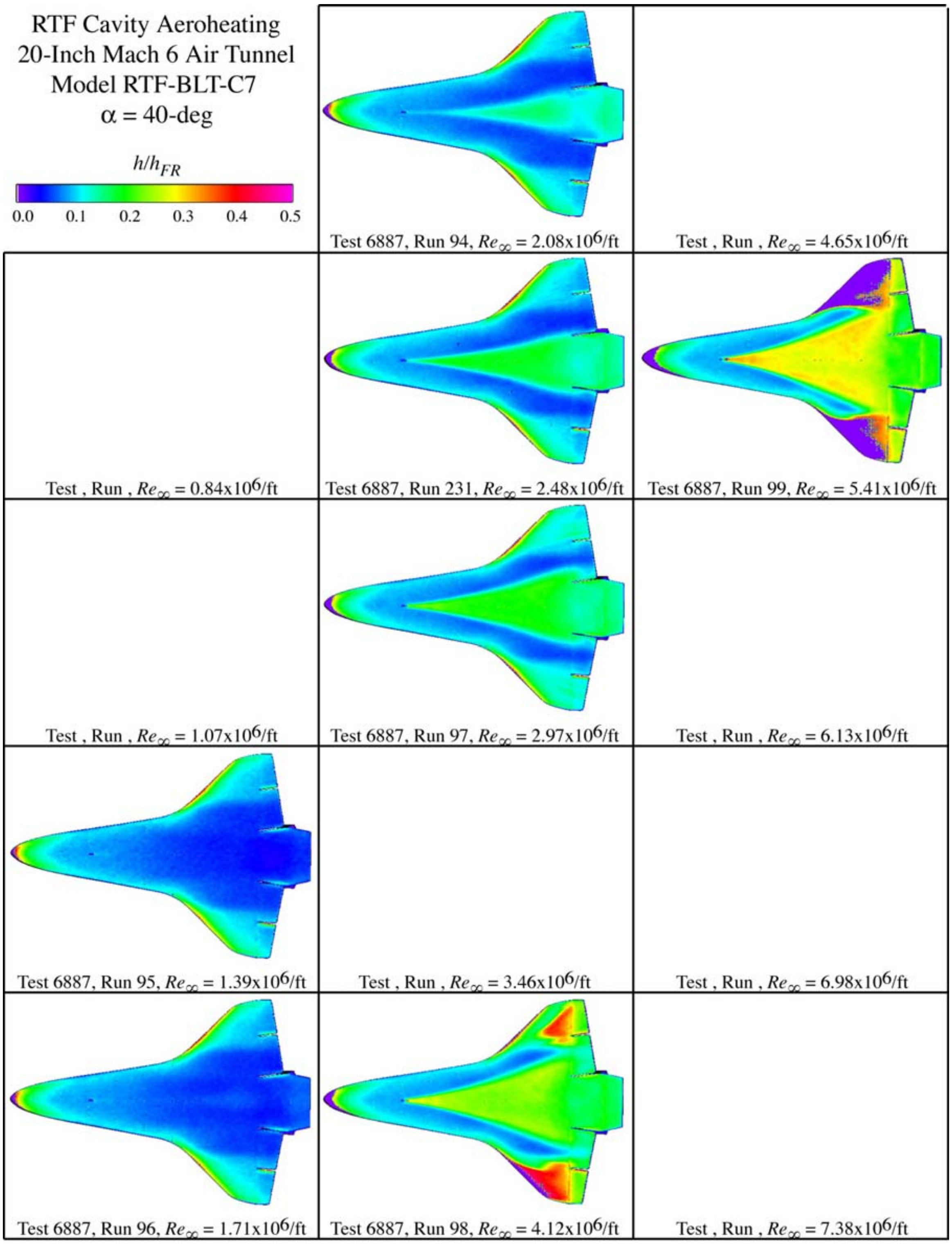

Figure A.40: RTF-BLT-C7 global aeroheating in the 20-Inch Mach 6 Air Tunnel at α = 40-deg.

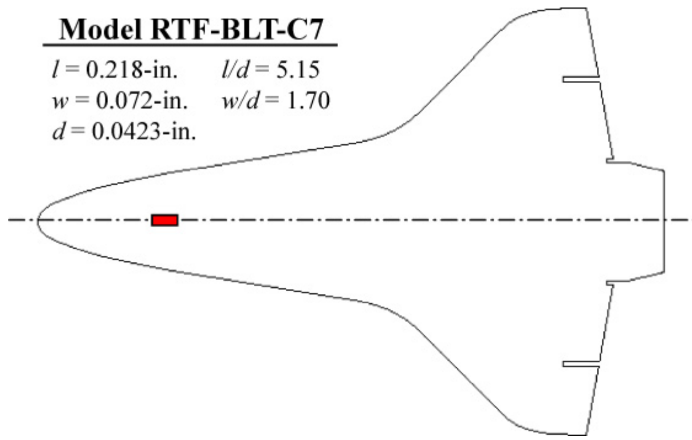

Figure A.41: RTF-BLT-C7 cavity information.

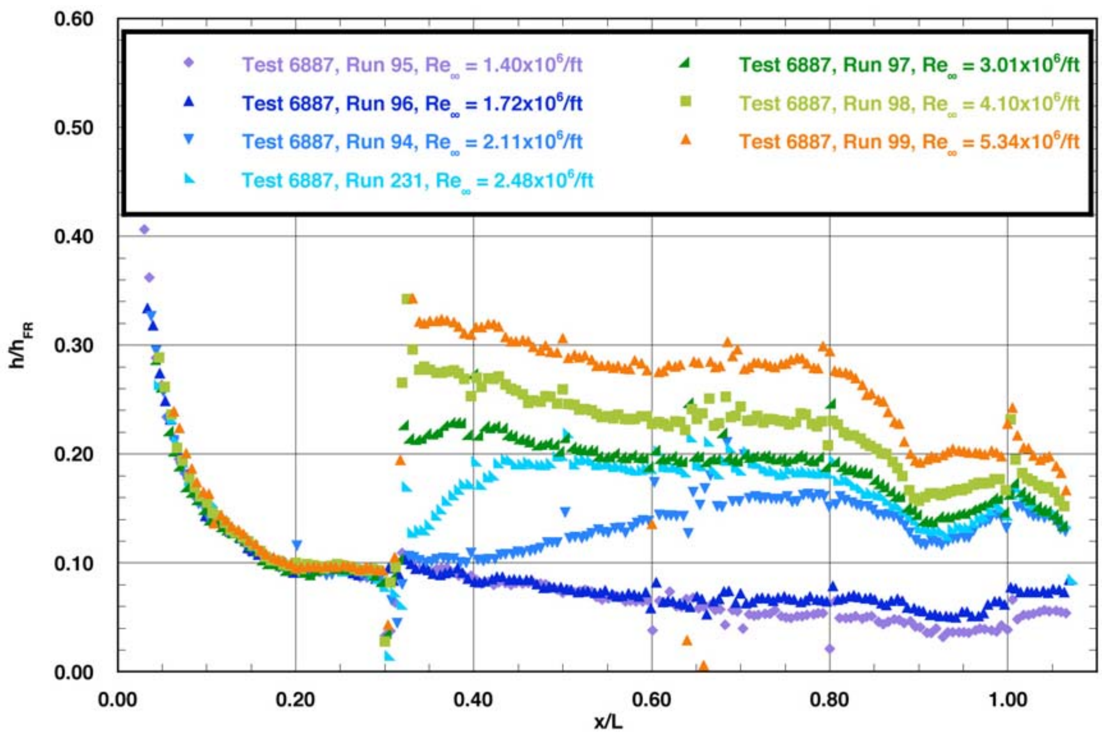

Figure A.42: RTF-BLT-C7 centerline data in the 20-Inch Mach 6 Air Tunnel at α = 40-deg.

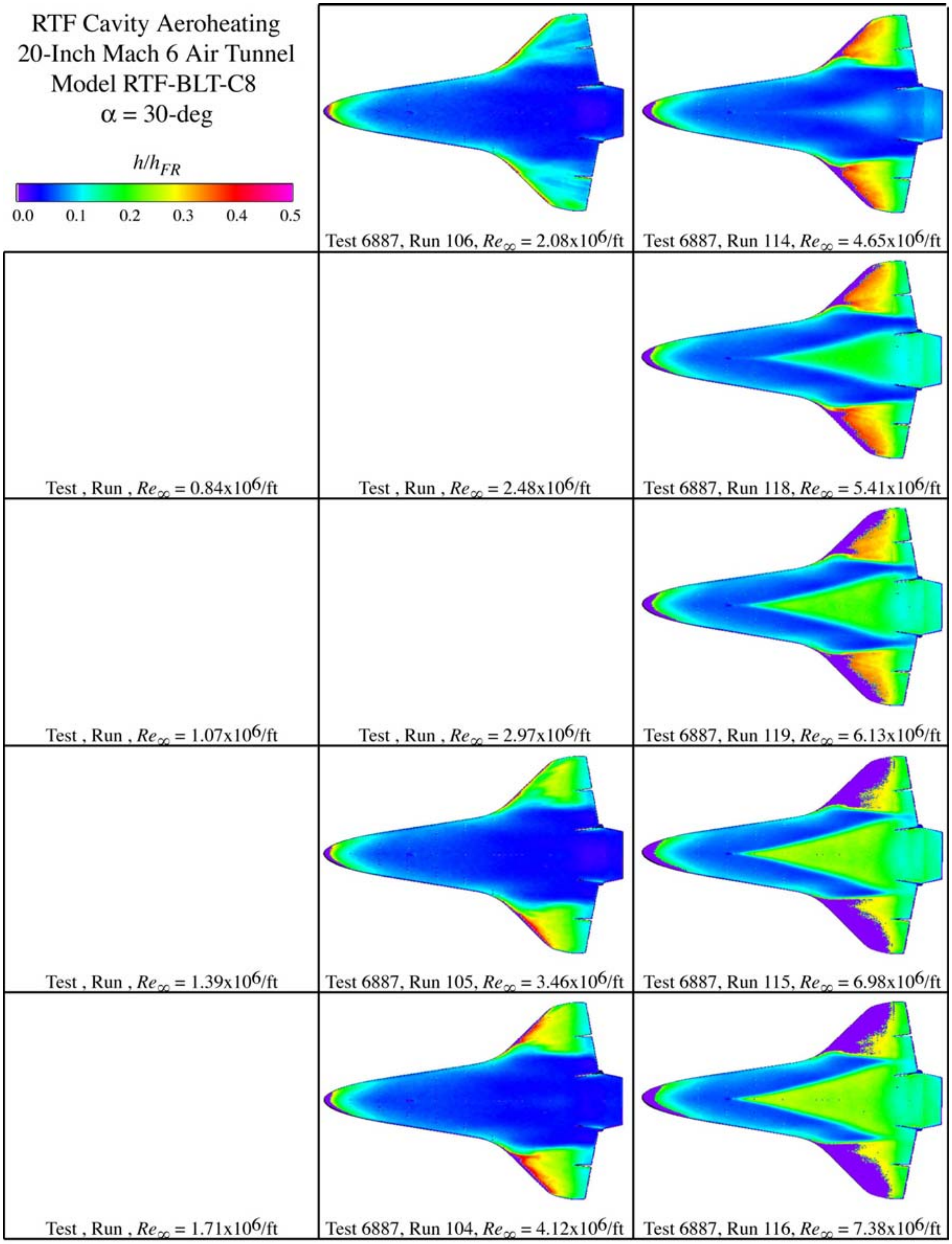

Figure A.43: RTF-BLT-C8 global aeroheating in the 20-Inch Mach 6 Air Tunnel at α = 30-deg.

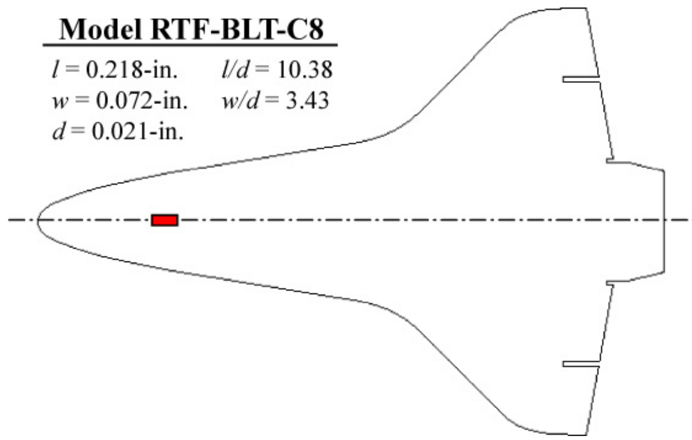

Figure A.44: RTF-BLT-C8 cavity information.

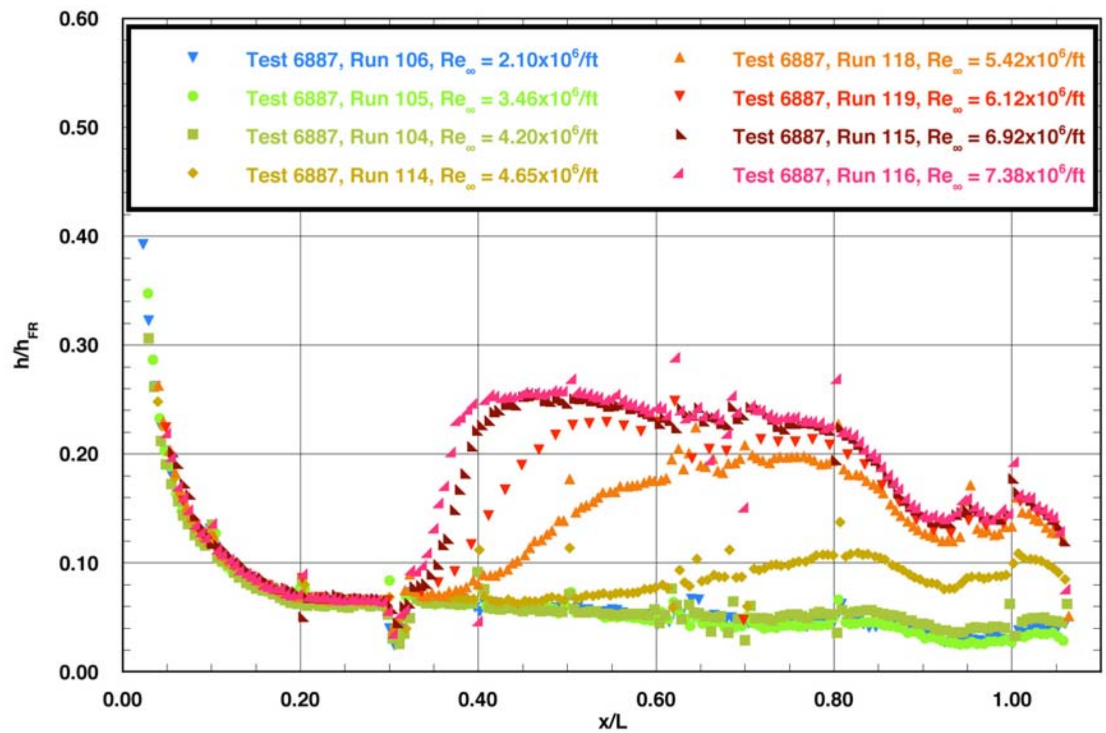

Figure A.45: RTF-BLT-C8 centerline data in the 20-Inch Mach 6 Air Tunnel at α = 30-deg.

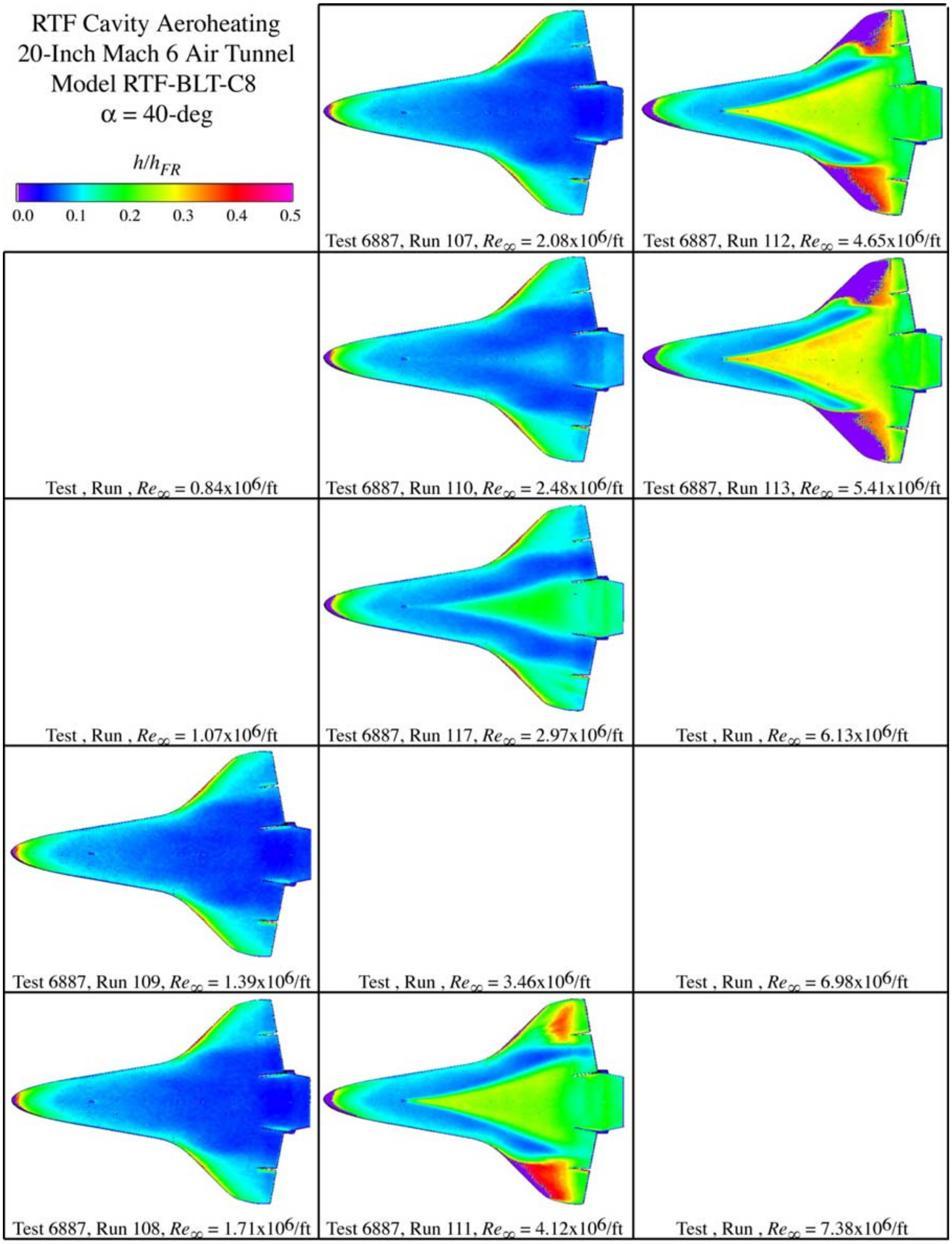

Figure A.46: RTF-BLT-C8 global aeroheating in the 20-Inch Mach 6 Air Tunnel at α = 40-deg.

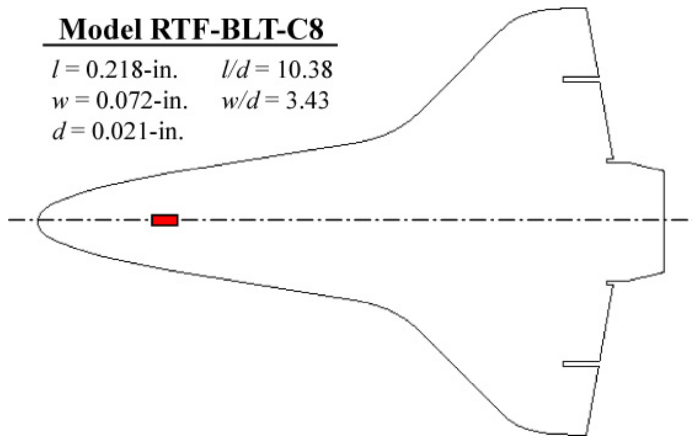

Figure A.47: RTF-BLT-C8 cavity information.

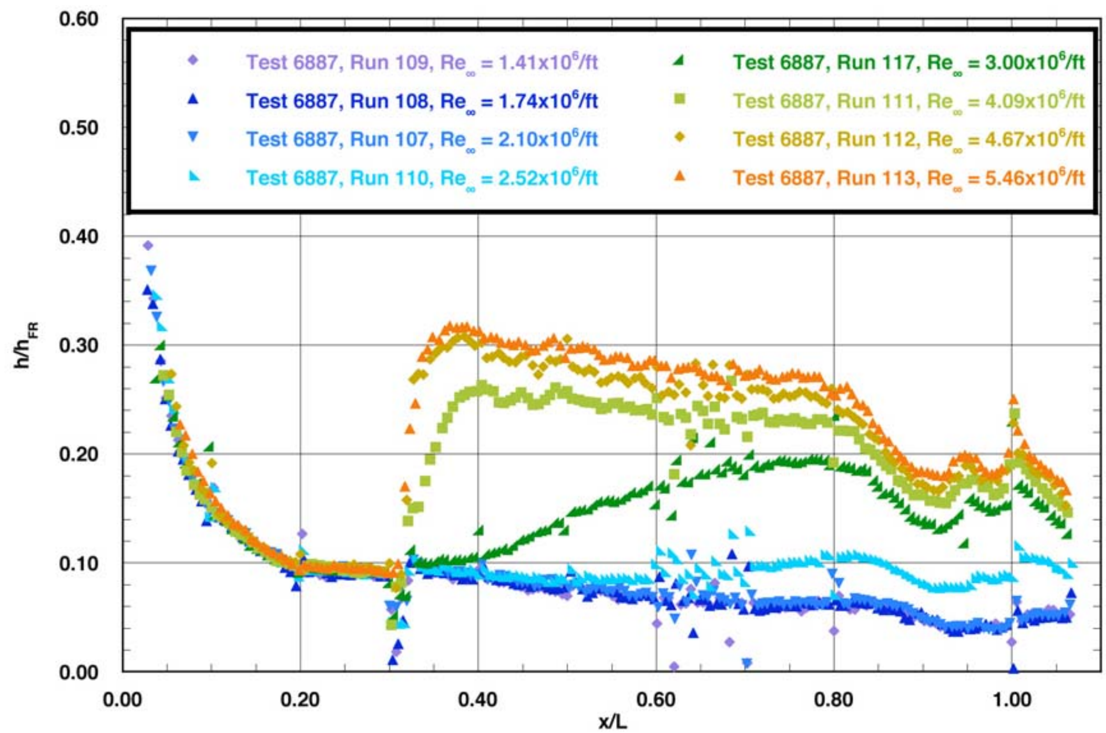

Figure A.48: RTF-BLT-C8 centerline data in the 20-Inch Mach 6 Air Tunnel at α = 40-deg.

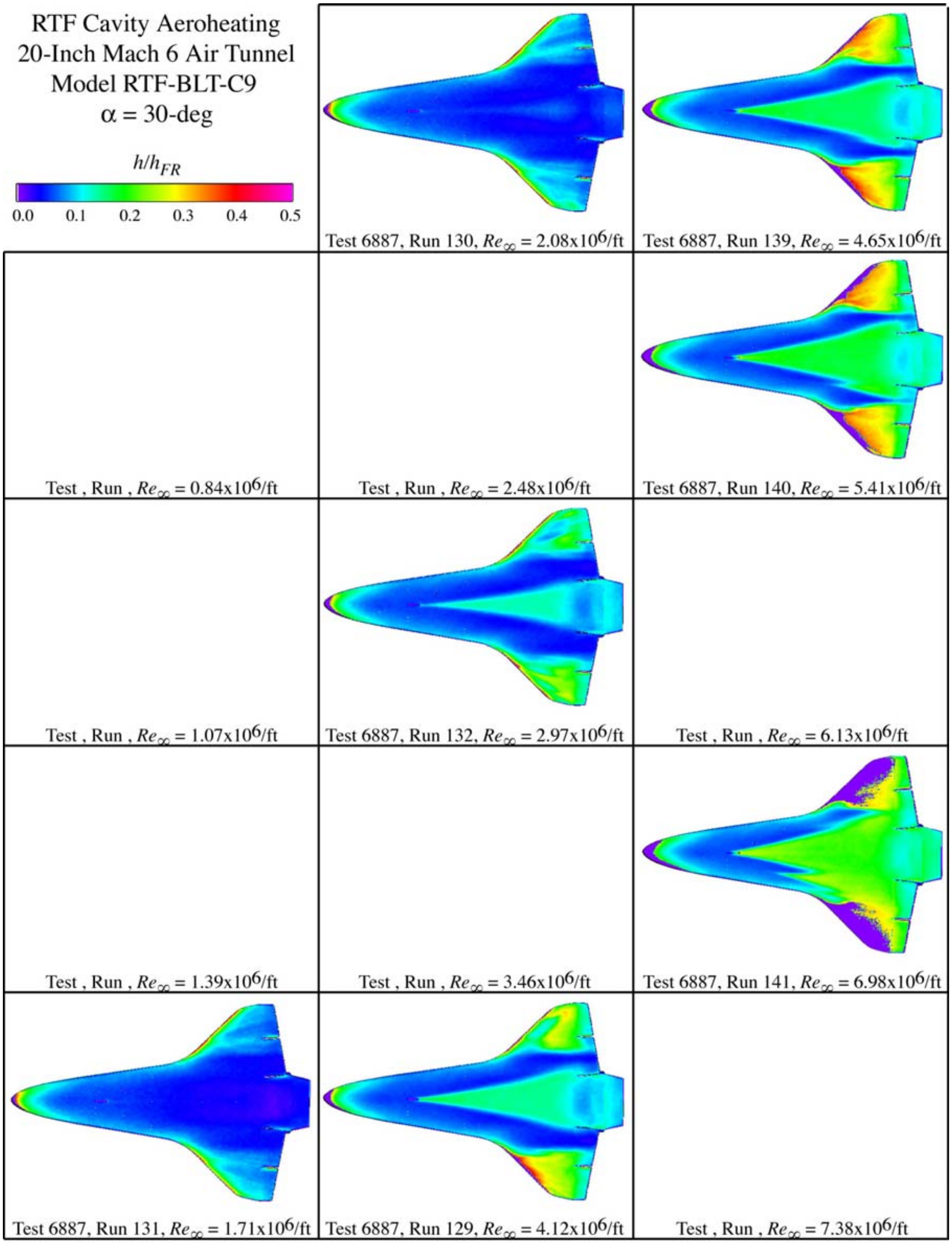

Figure A.49: RTF-BLT-C9 global aeroheating in the 20-Inch Mach 6 Air Tunnel at α = 30-deg.

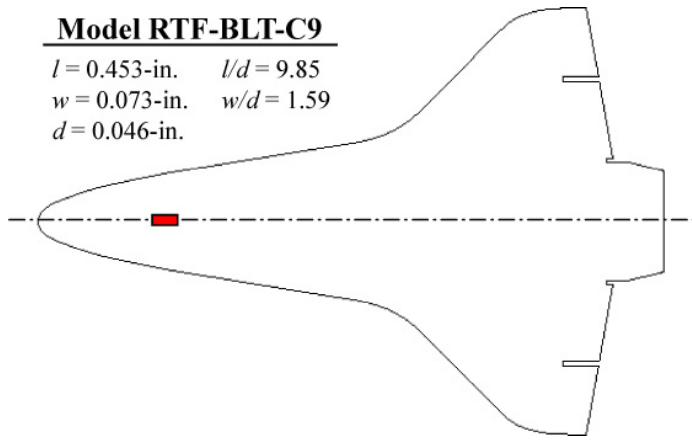

Figure A.50: RTF-BLT-C9 cavity information.

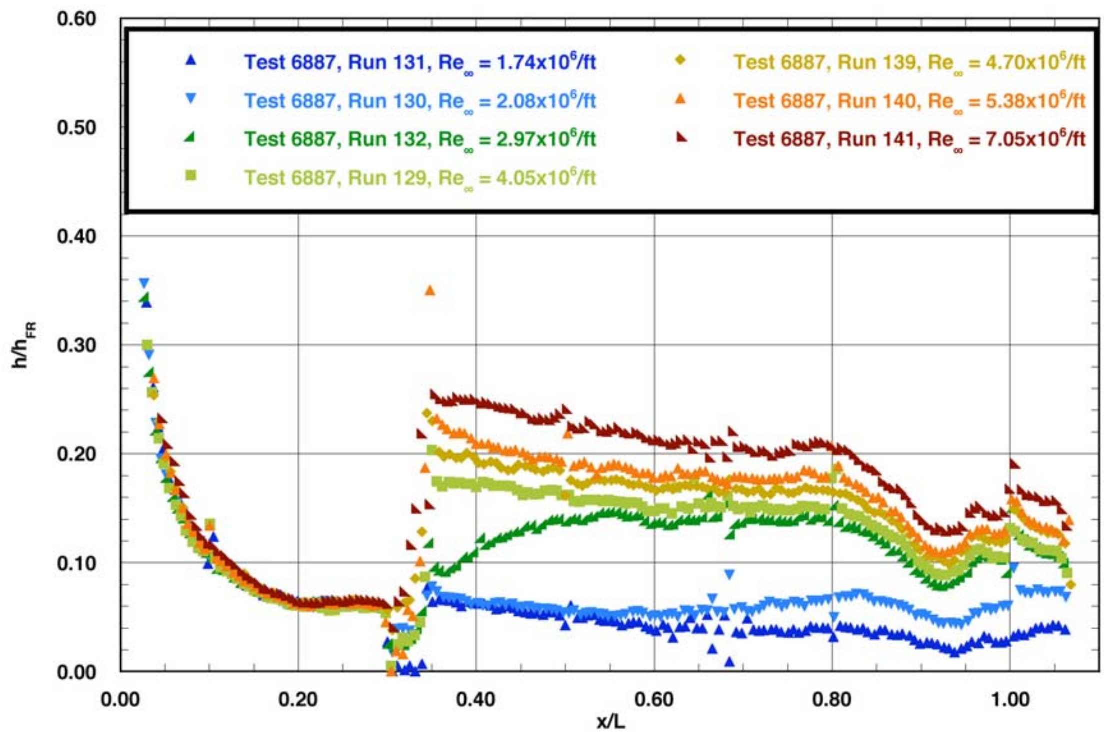

Figure A.51: RTF-BLT-C9 centerline data in the 20-Inch Mach 6 Air Tunnel at α = 30-deg.

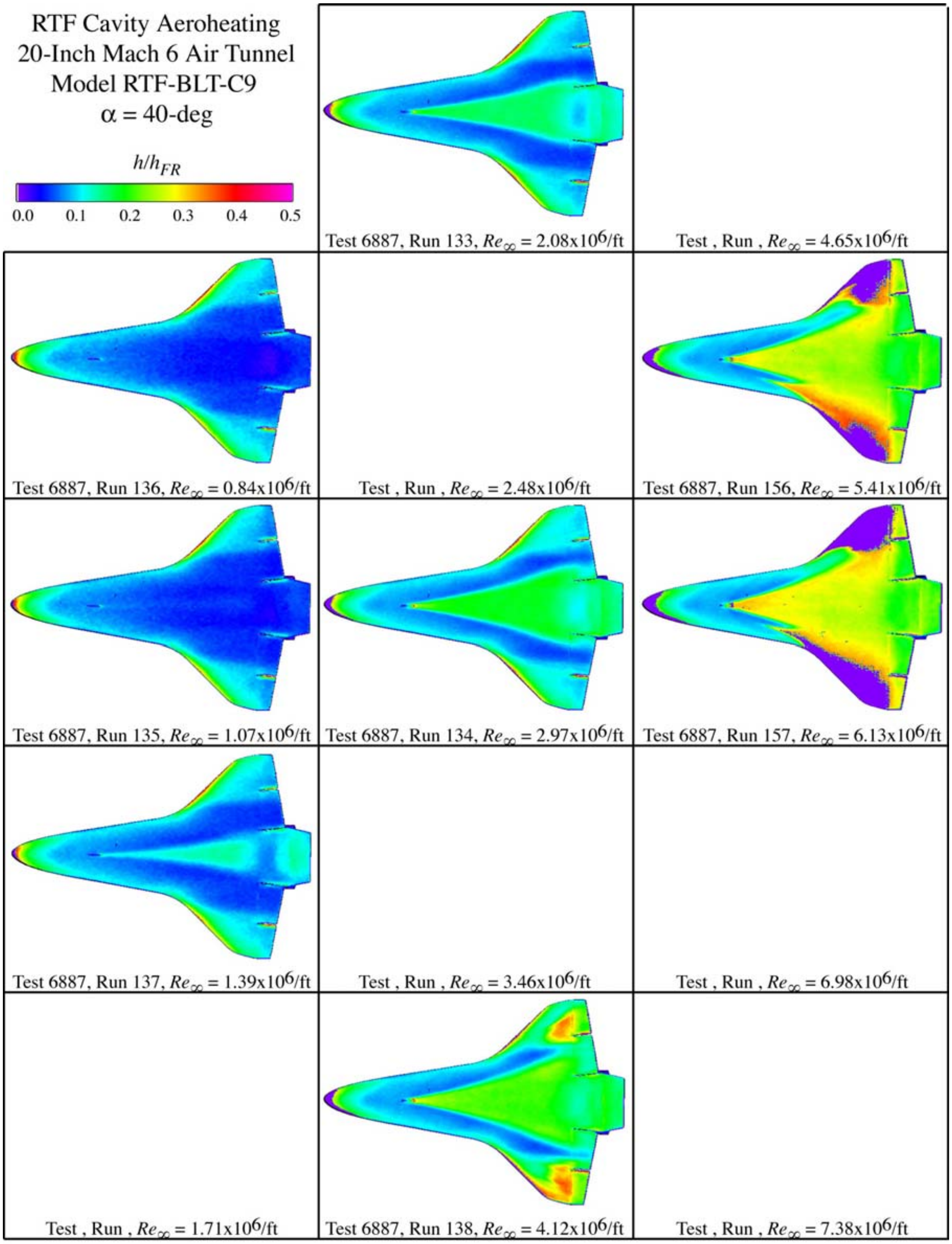

Figure A.52: RTF-BLT-C9 global aeroheating in the 20-Inch Mach 6 Air Tunnel at α = 40-deg.

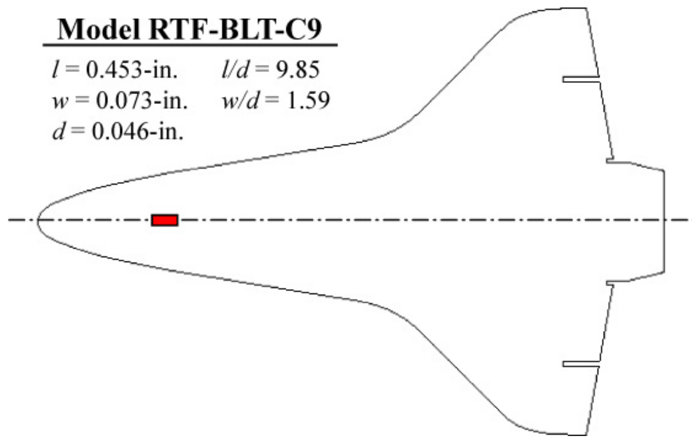

Figure A.53: RTF-BLT-C9 cavity information.

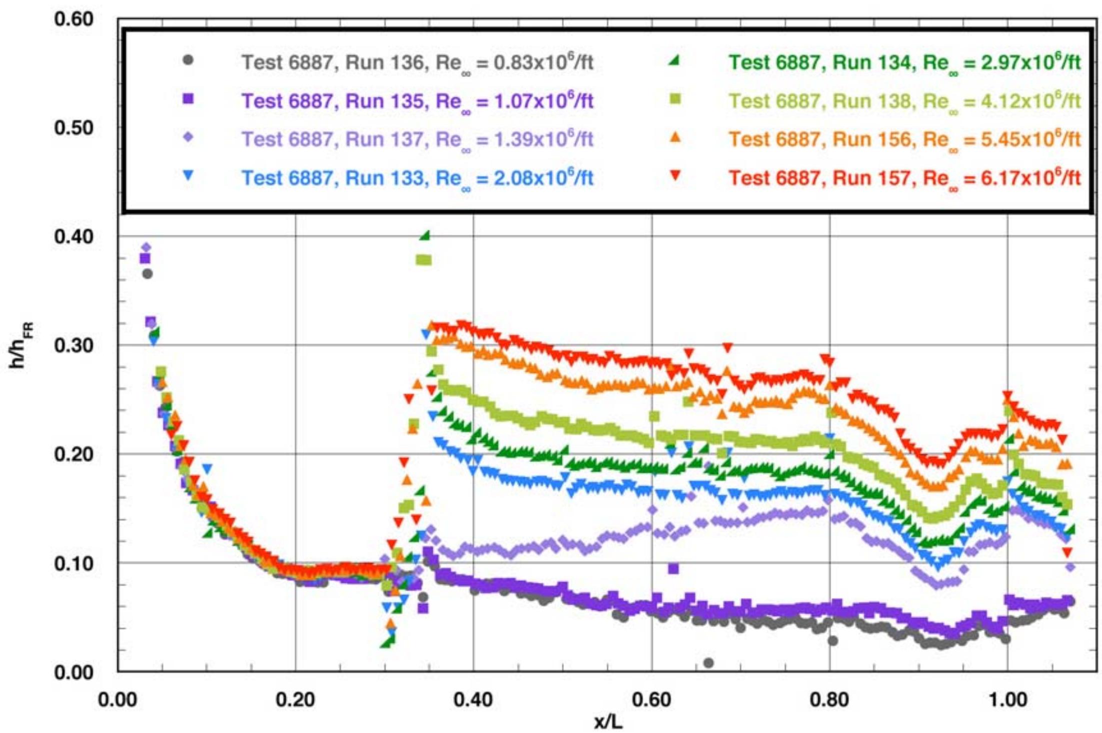

Figure A.54: RTF-BLT-C9 centerline data in the 20-Inch Mach 6 Air Tunnel at α = 40-deg.

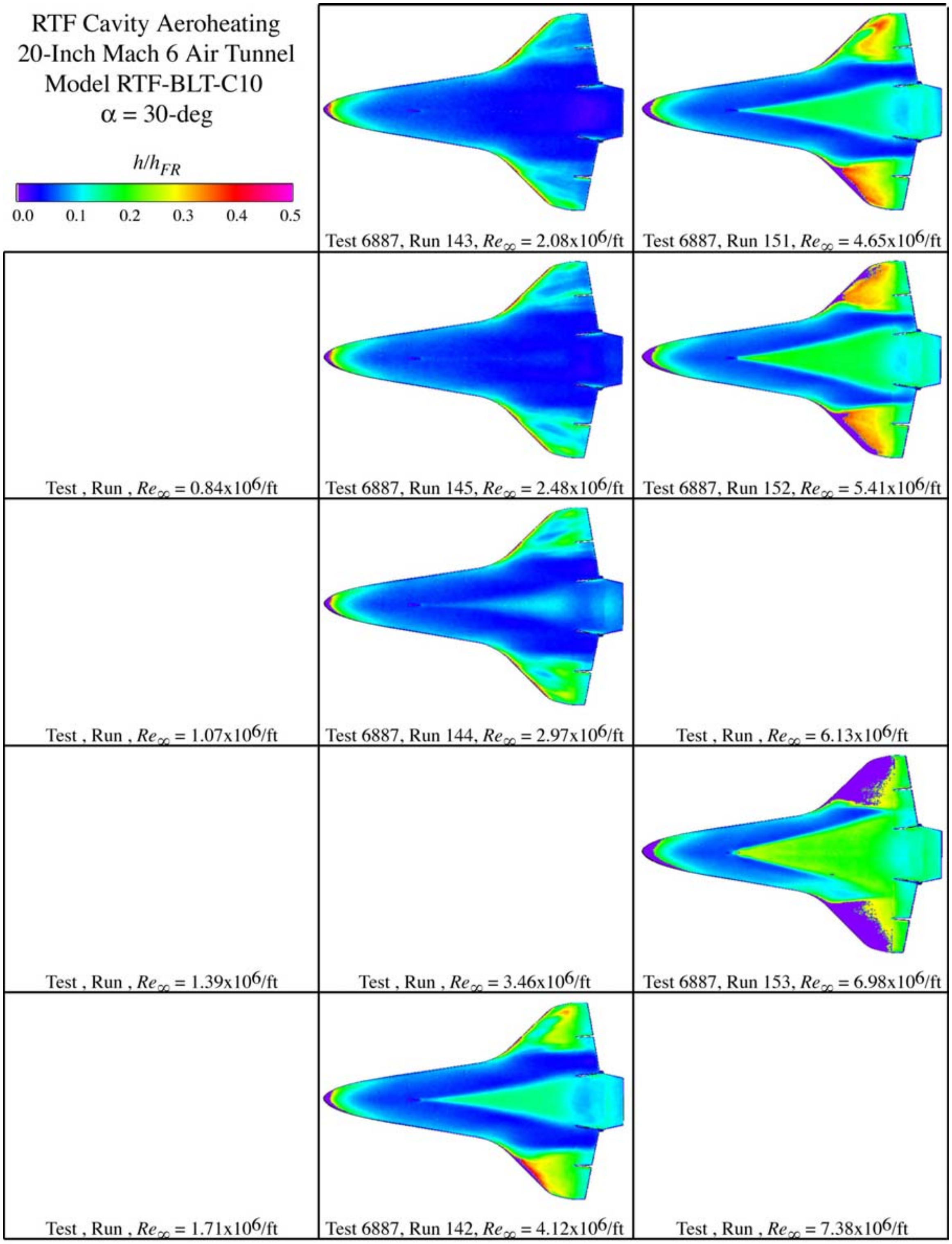

Figure A.55: RTF-BLT-C10 global aeroheating in the 20-Inch Mach 6 Air Tunnel at α = 30-deg.

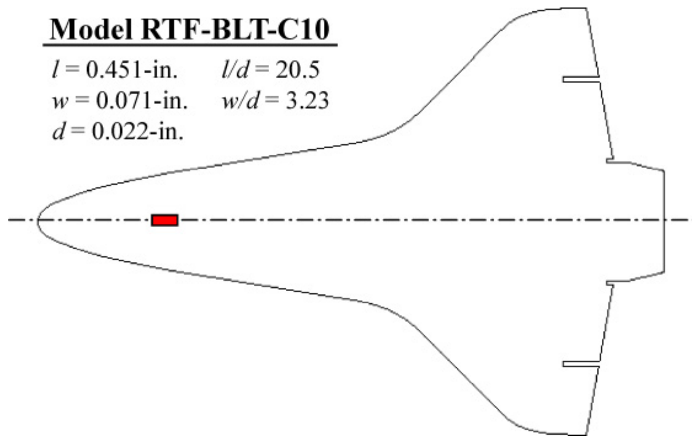

Figure A.56: RTF-BLT-C10 cavity information.

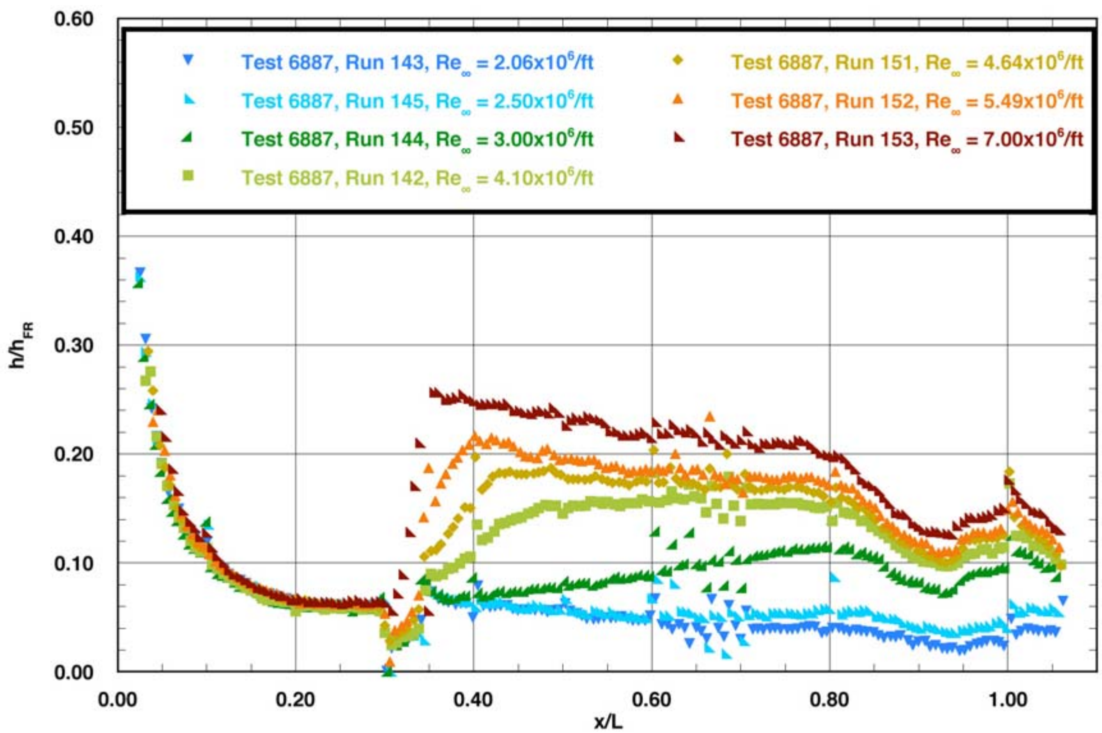

Figure A.57: RTF-BLT-C10 global aeroheating in the 20-Inch Mach 6 Air Tunnel at α = 30-deg.

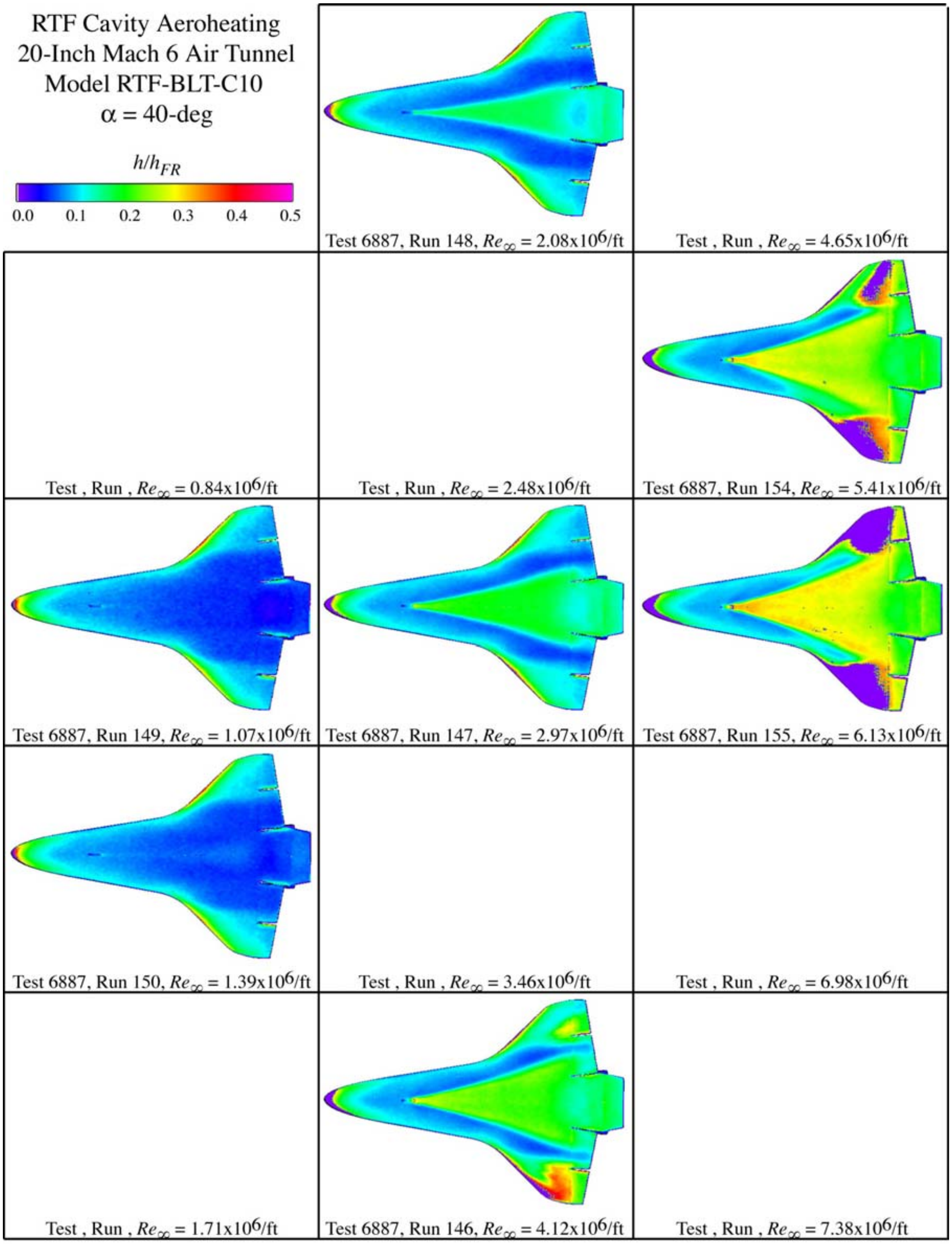

Figure A.58: RTF-BLT-C10 global aeroheating in the 20-Inch Mach 6 Air Tunnel at α = 40-deg.

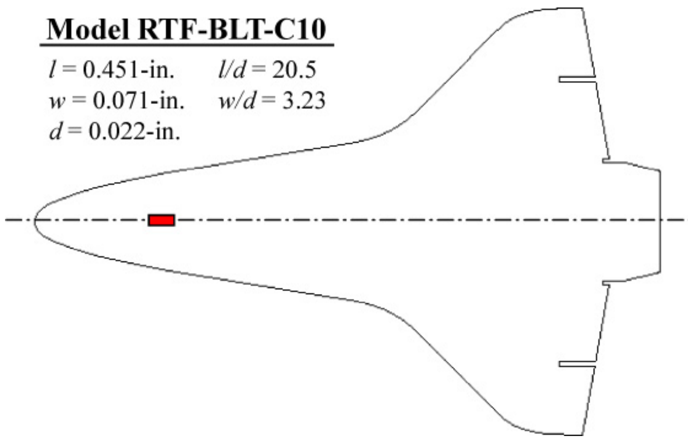

Figure A.59: RTF-BLT-C10 cavity information.

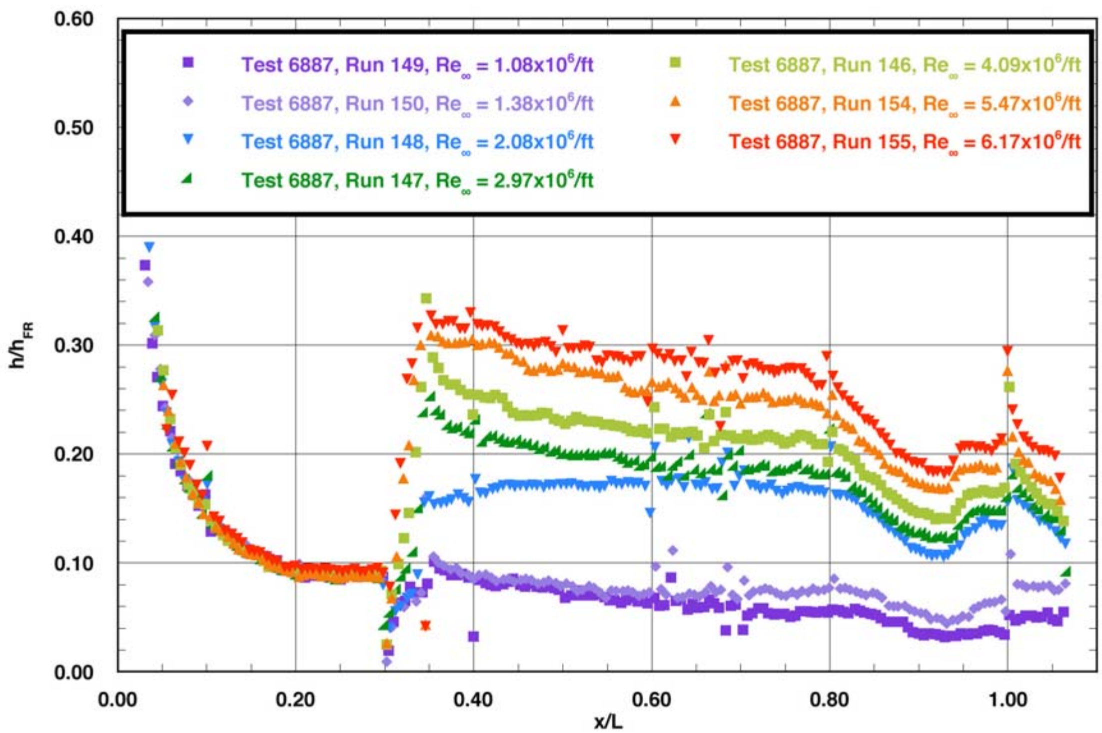

Figure A.60: RTF-BLT-C10 centerline data in the 20-Inch Mach 6 Air Tunnel at α = 40-deg.

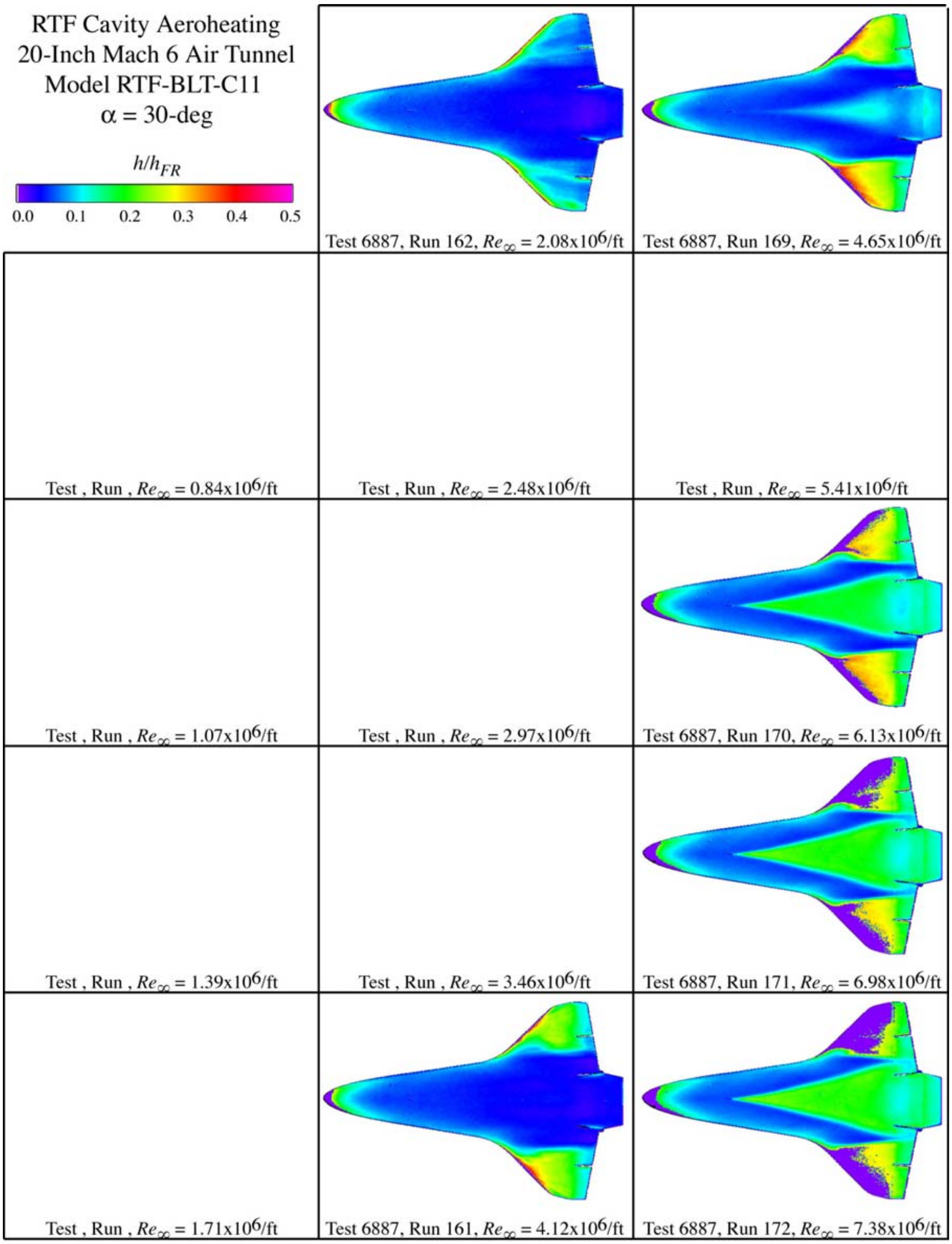

Figure A.61: RTF-BLT-C11 global aeroheating in the 20-Inch Mach 6 Air Tunnel at α = 30-deg.

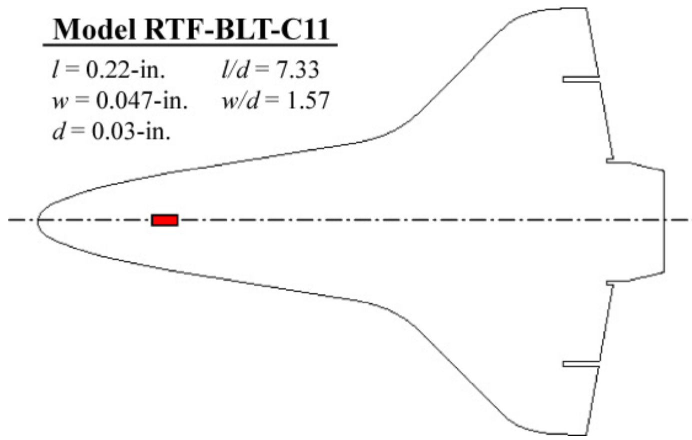

Figure A.62: RTF-BLT-C11 cavity information.

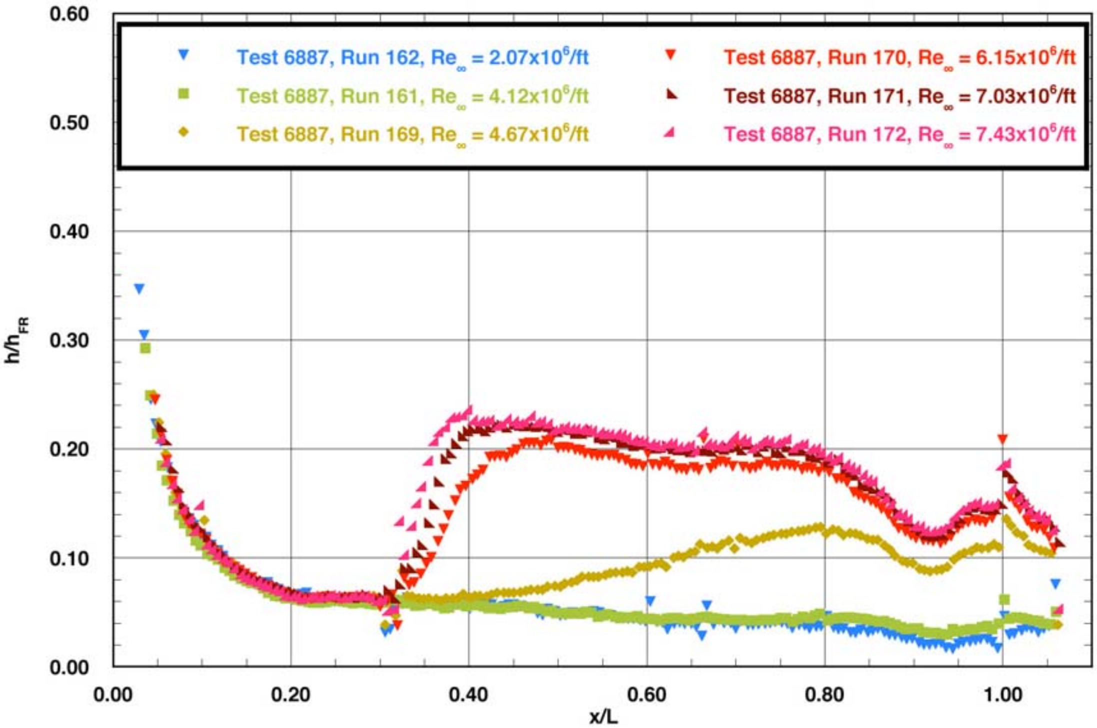

Figure A.63: RTF-BLT-C11 centerline data in the 20-Inch Mach 6 Air Tunnel at α = 30-deg.

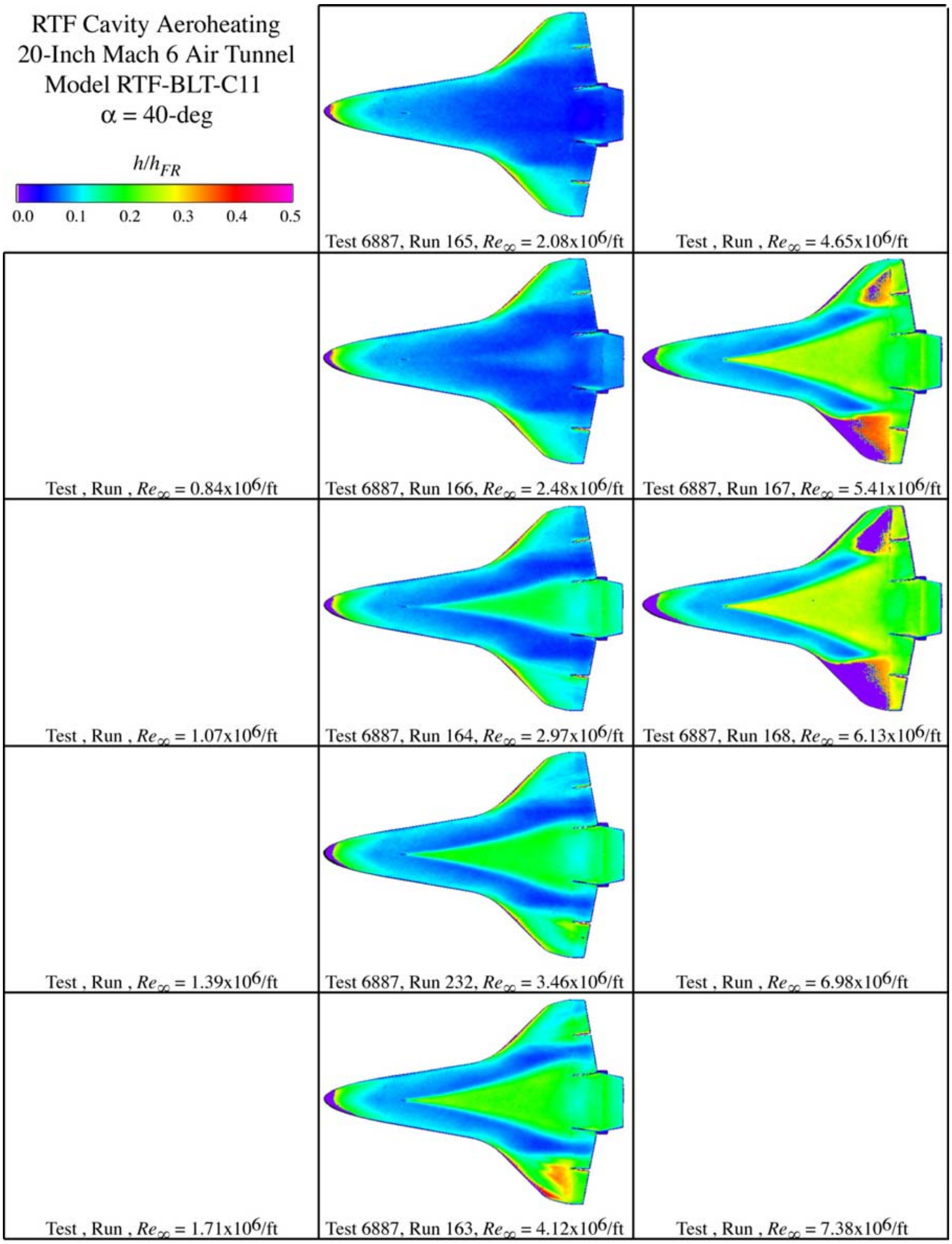

Figure A.64: RTF-BLT-C11 global aeroheating in the 20-Inch Mach 6 Air Tunnel at α = 40-deg.

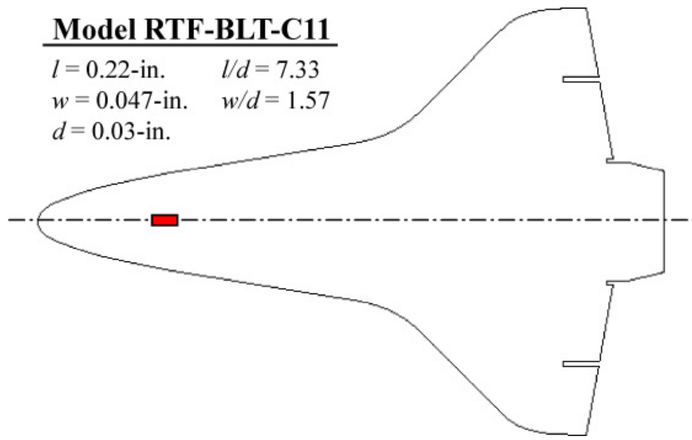

Figure A.65: RTF-BLT-C11 cavity information.

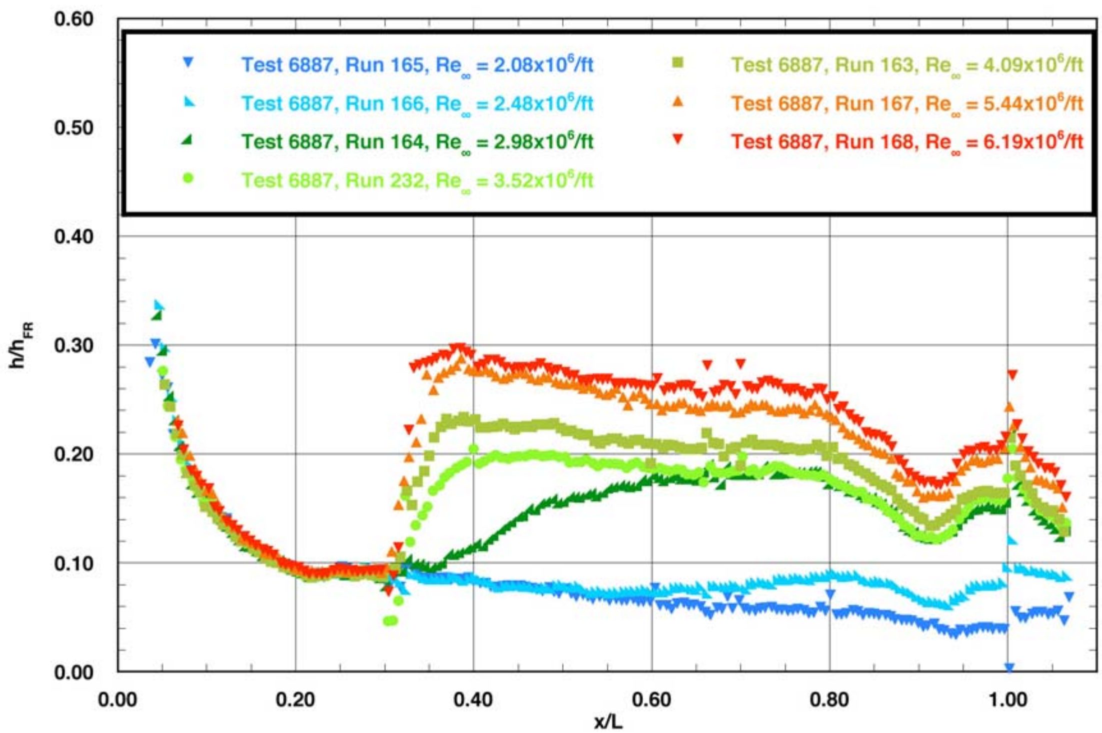

Figure A.66: RTF-BLT-C11 centerline data in the 20-Inch Mach 6 Air Tunnel at α = 40-deg.

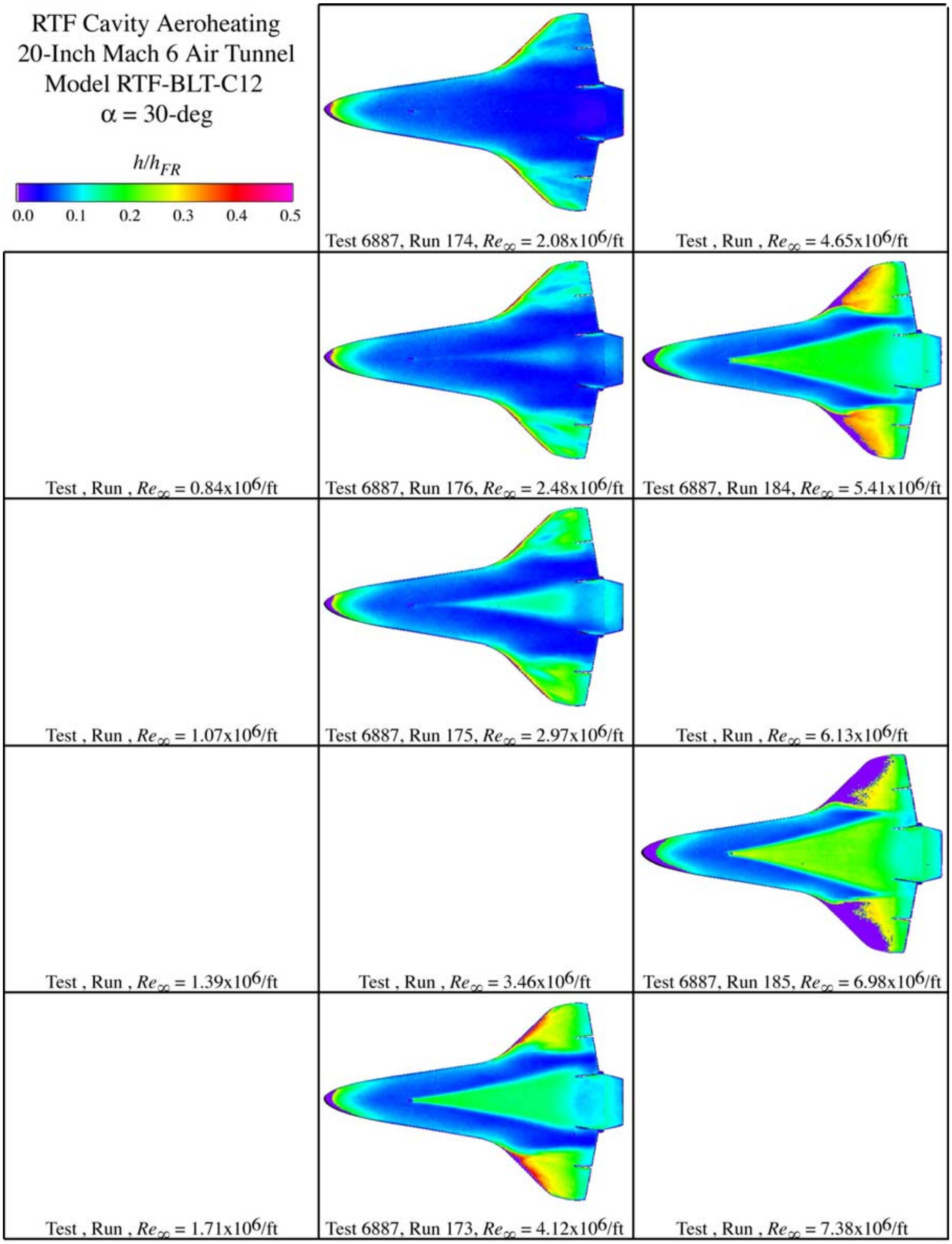

Figure A.67: RTF-BLT-C12 global aeroheating in the 20-Inch Mach 6 Air Tunnel at α = 30-deg.

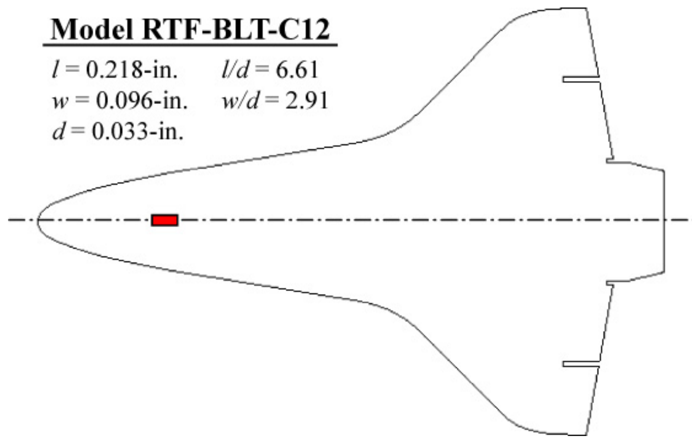

Figure A.68: RTF-BLT-C12 cavity information.

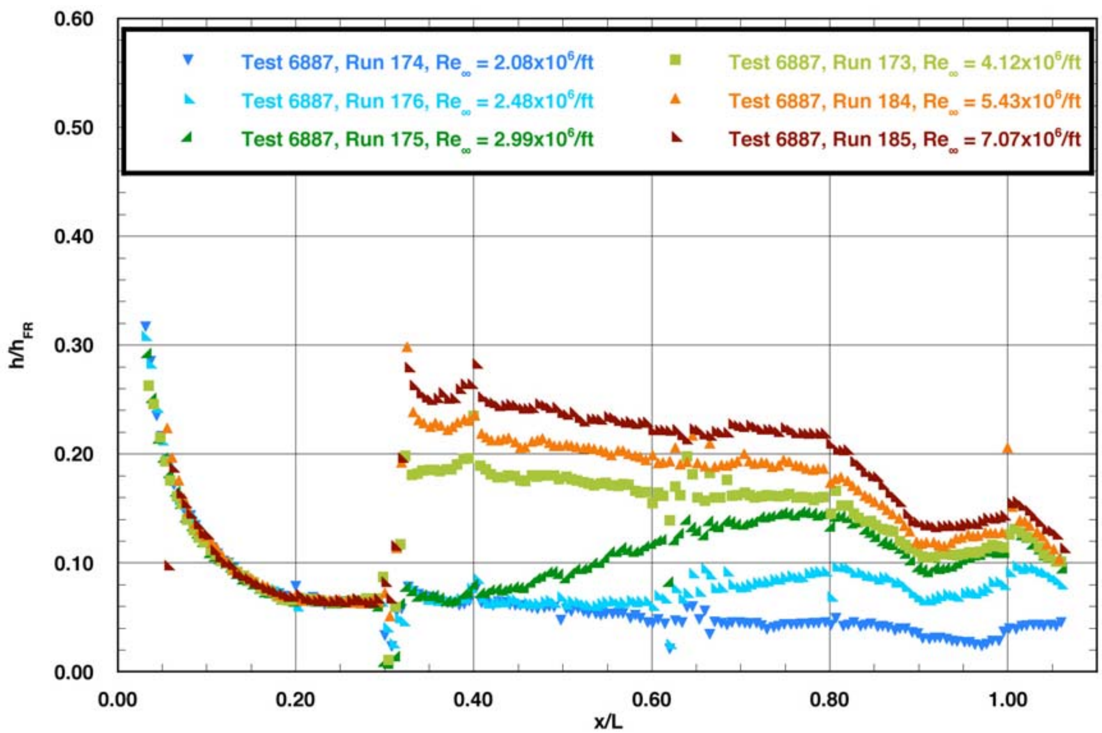

Figure A.69: RTF-BLT-C12 centerline data in the 20-Inch Mach 6 Air Tunnel at α = 30-deg.

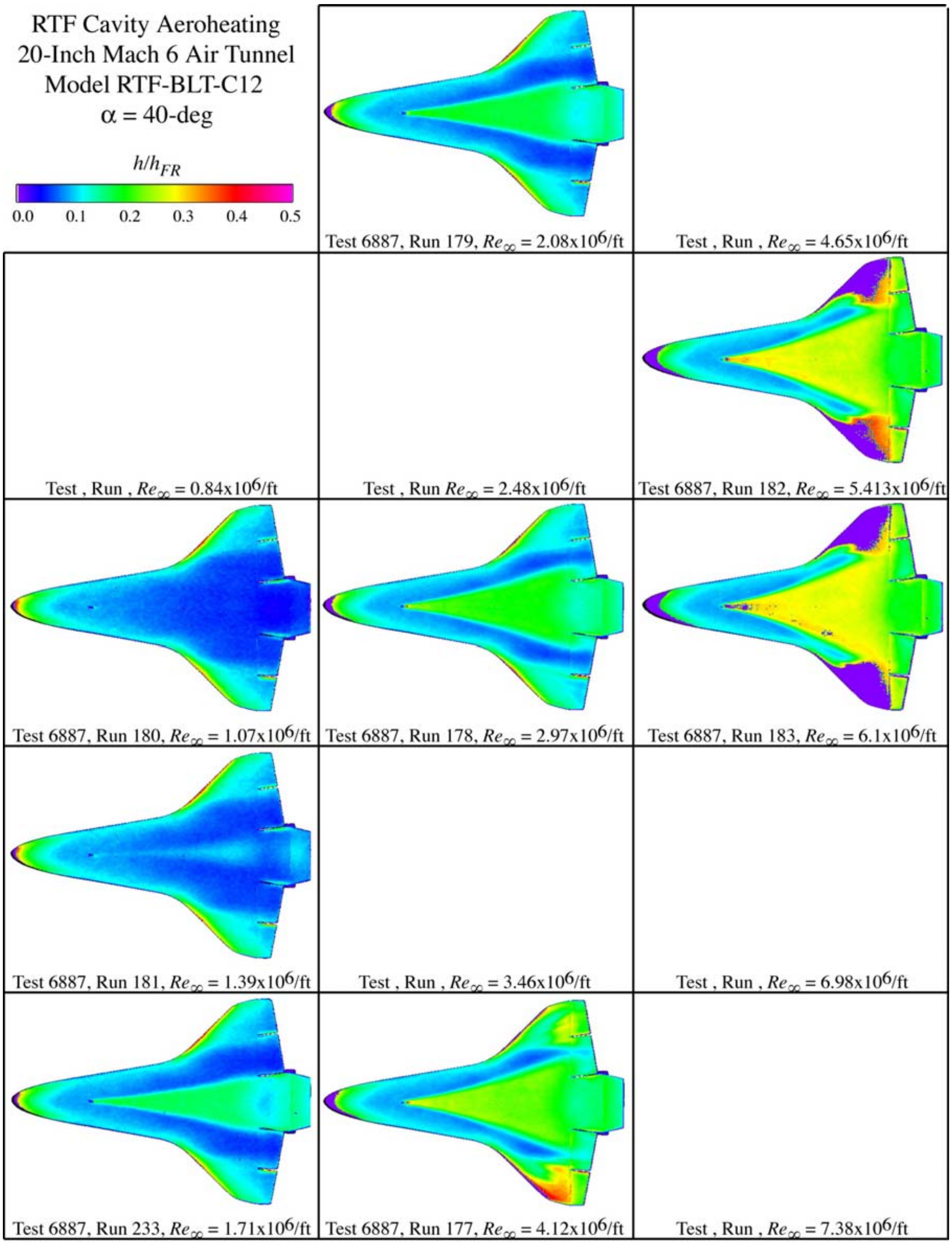

Figure A.70: RTF-BLT-C12 global aeroheating in the 20-Inch Mach 6 Air Tunnel at α = 40-deg.

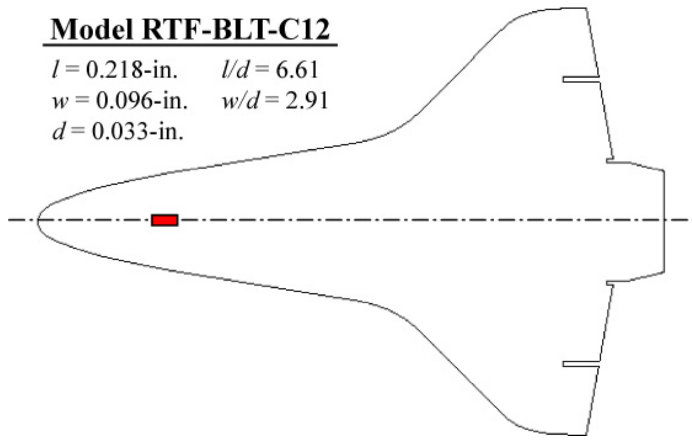

Figure A.71: RTF-BLT-C12 cavity information.

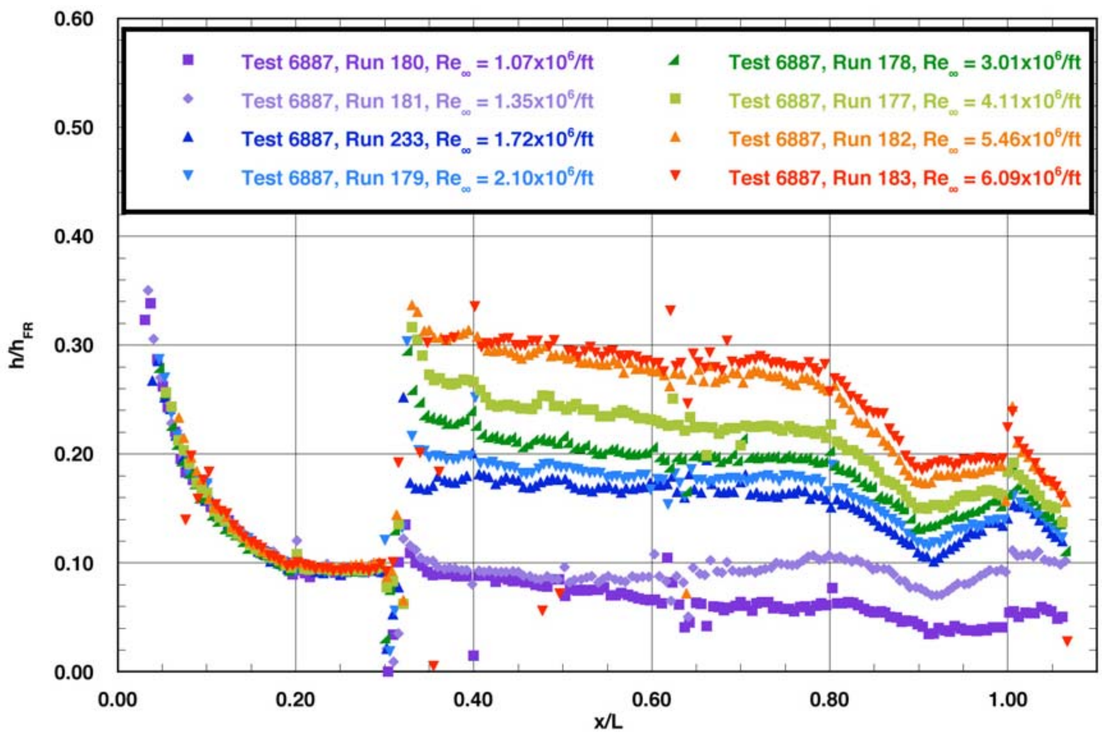

Figure A.72: RTF-BLT-C12 centerline data in the 20-Inch Mach 6 Air Tunnel at α = 40-deg.

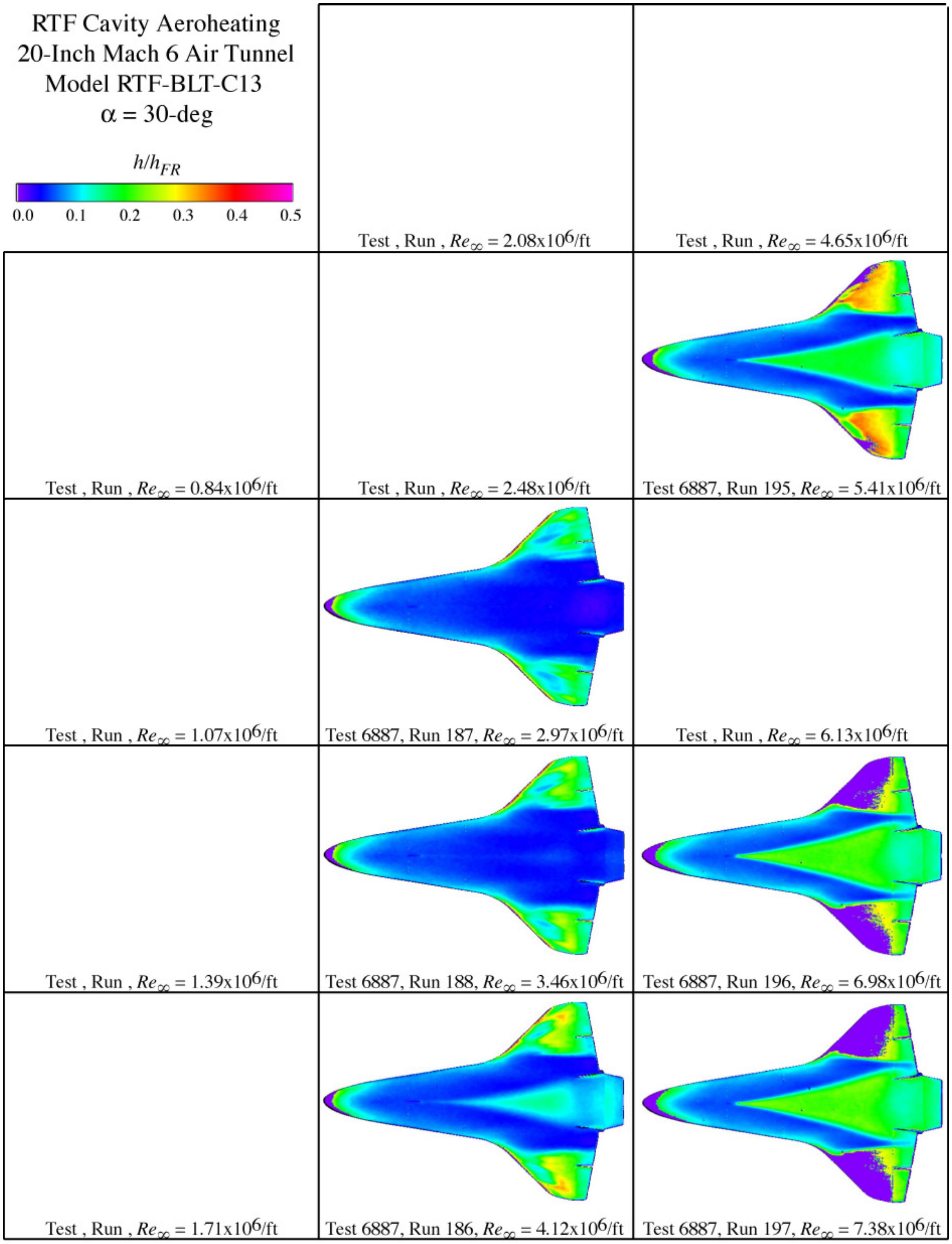

Figure A.73: RTF-BLT-C13 global aeroheating in the 20-Inch Mach 6 Air Tunnel at α = 30-deg.

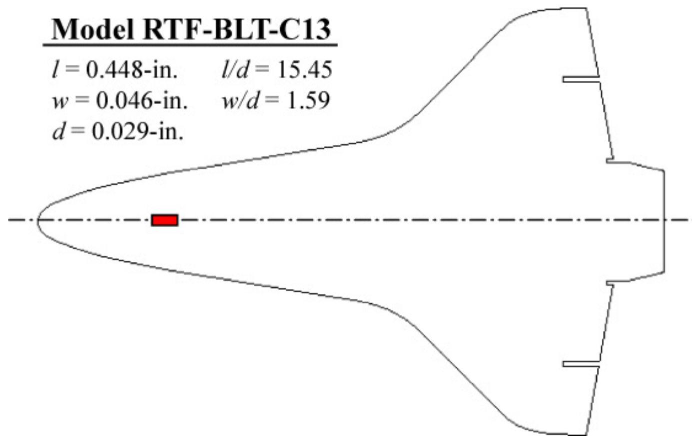

Figure A.74: RTF-BLT-C13 cavity information.

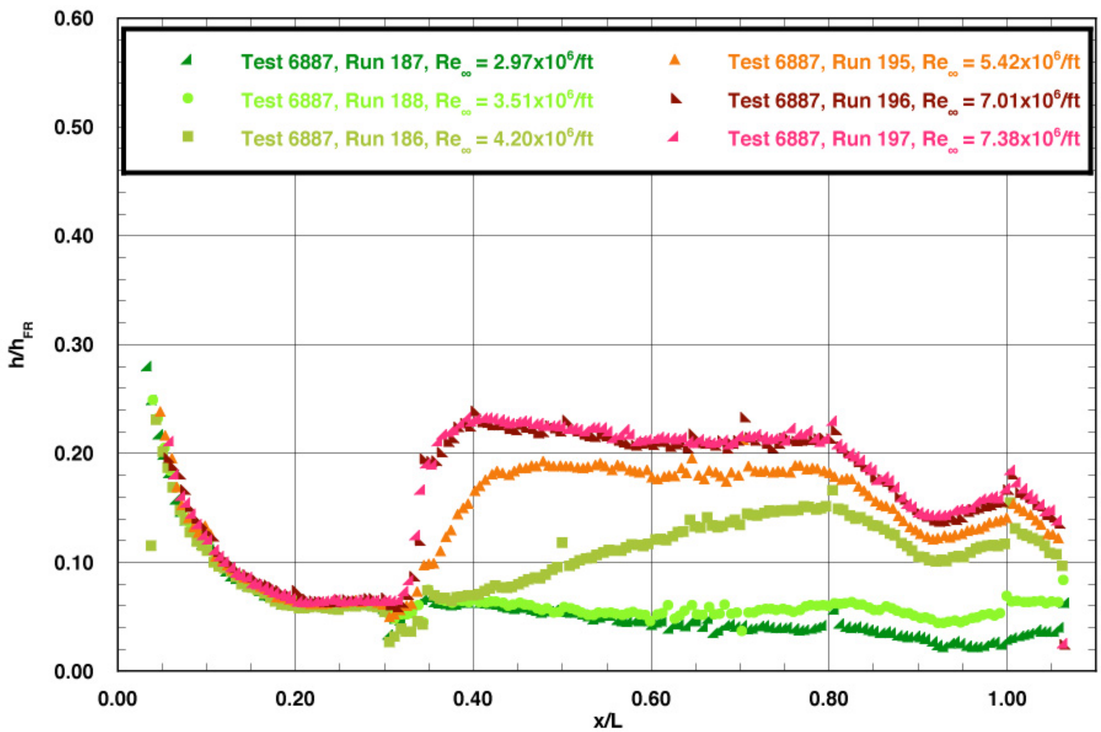

Figure A.75: RTF-BLT-C13 centerline data in the 20-Inch Mach 6 Air Tunnel at α = 30-deg.

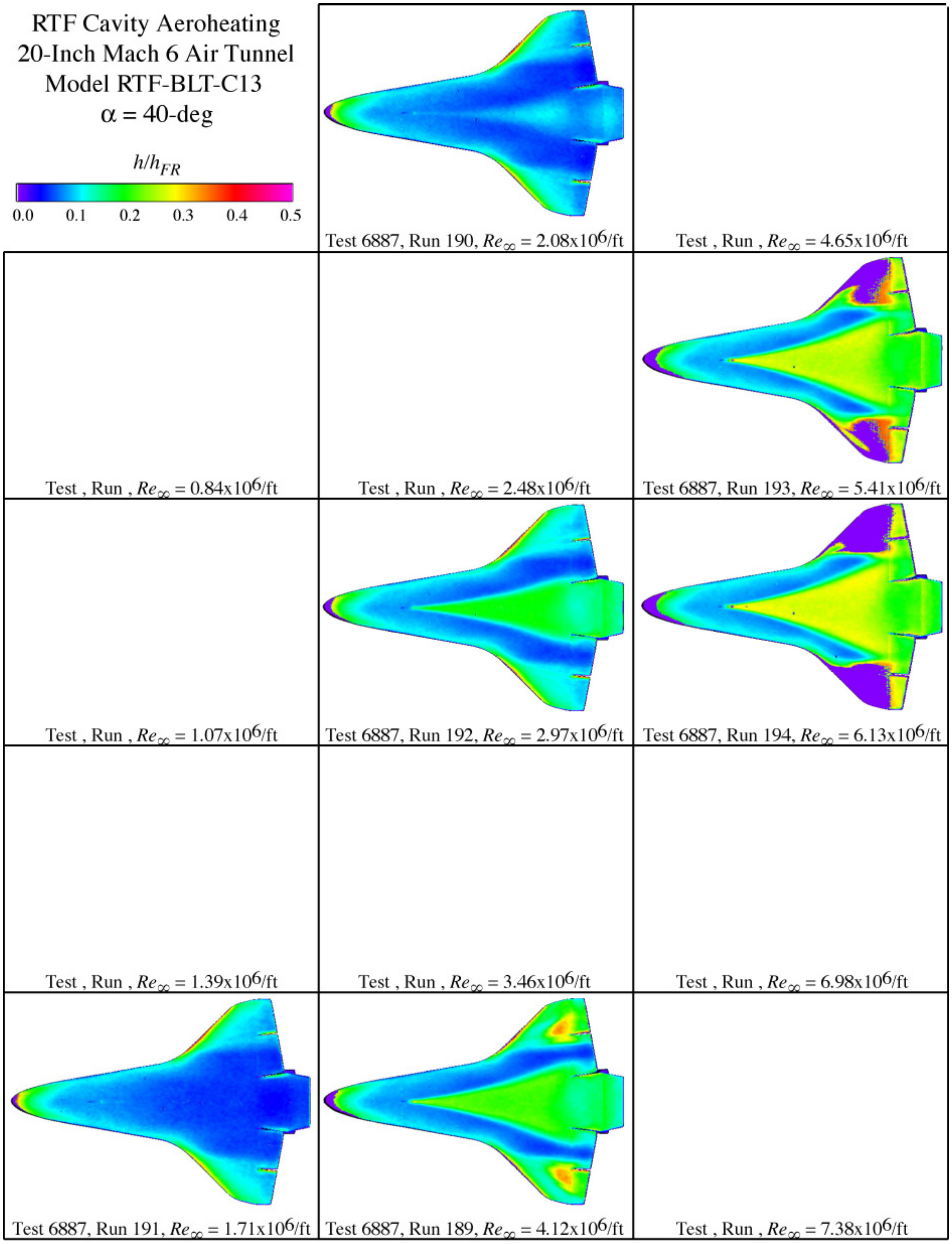

Figure A.76: RTF-BLT-C13 global aeroheating in the 20-Inch Mach 6 Air Tunnel at α = 40-deg.

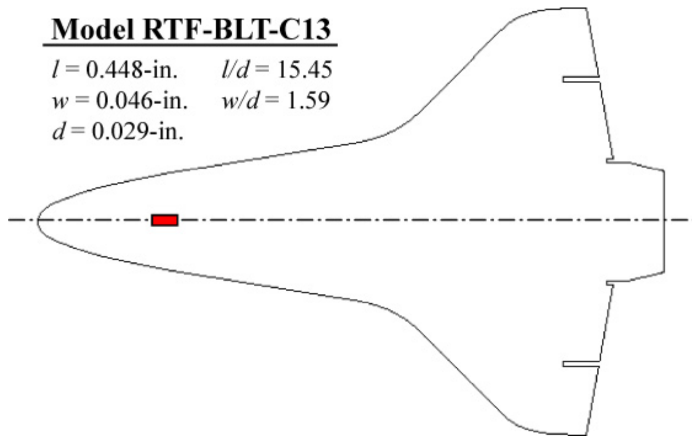

Figure A.77: RTF-BLT-C13 cavity information.

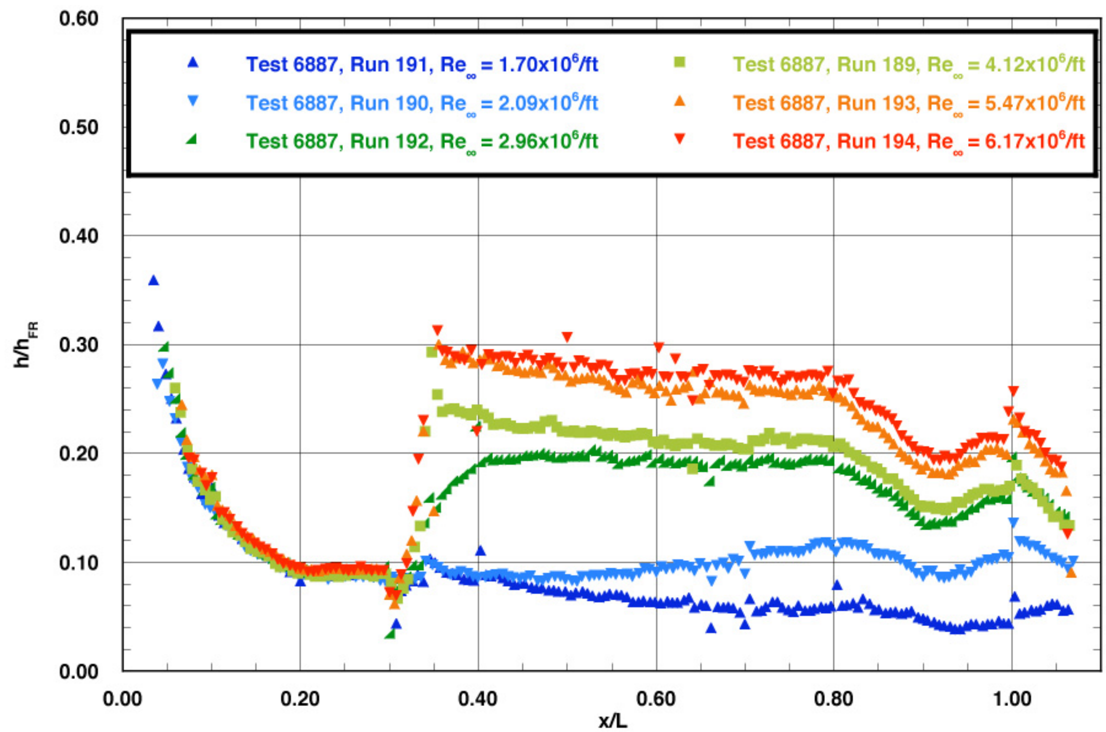

Figure A.78: RTF-BLT-C13 centerline data in the 20-Inch Mach 6 Air Tunnel at α = 40-deg.

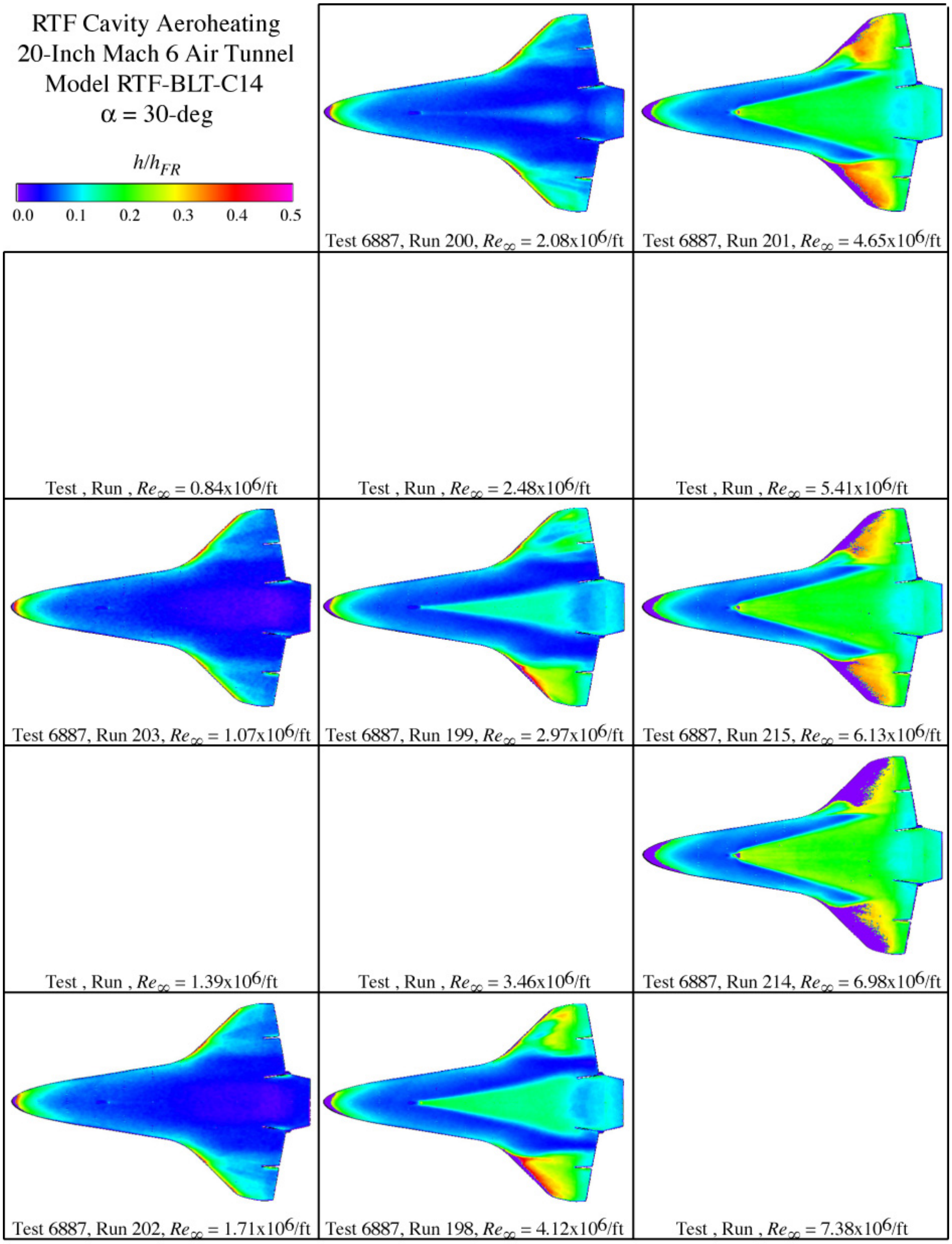

Figure A.79: RTF-BLT-C14 global aeroheating in the 20-Inch Mach 6 Air Tunnel at α = 30-deg.

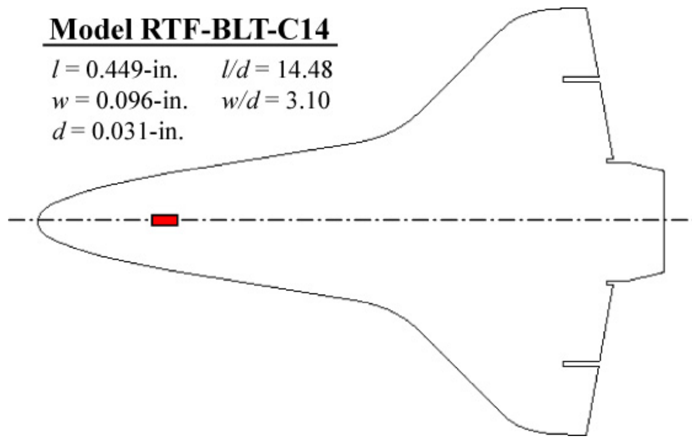

Figure A.80: RTF-BLT-C14 cavity information.

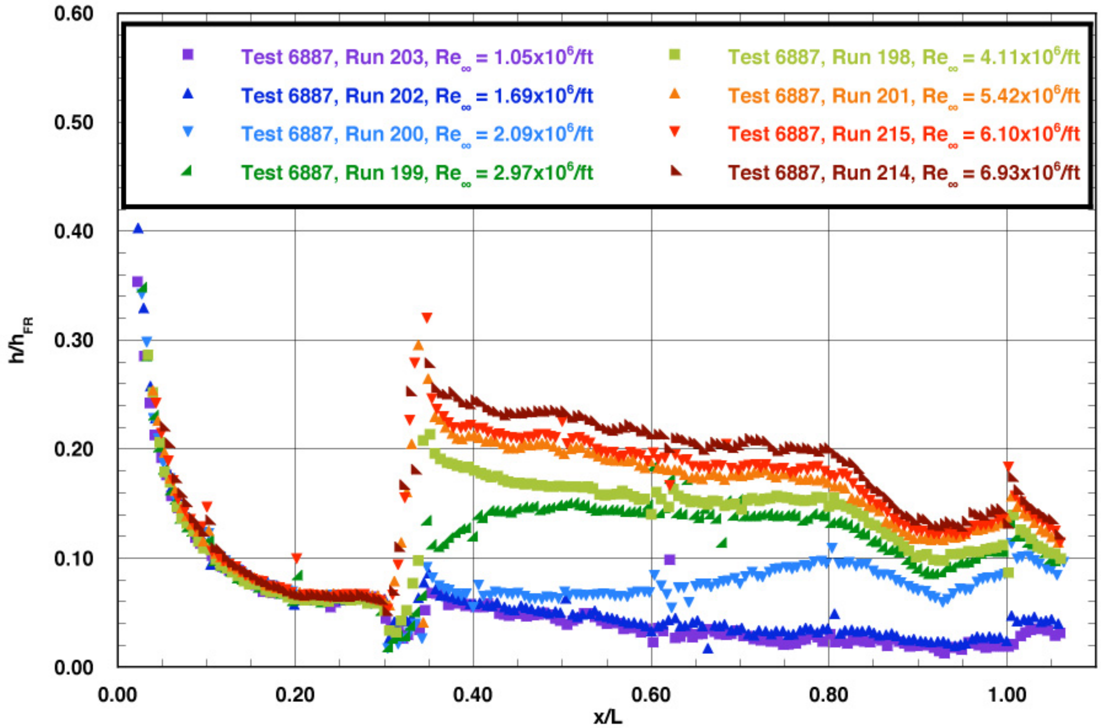

Figure A.81: RTF-BLT-C14 centerline data in the 20-Inch Mach 6 Air Tunnel at α = 30-deg.

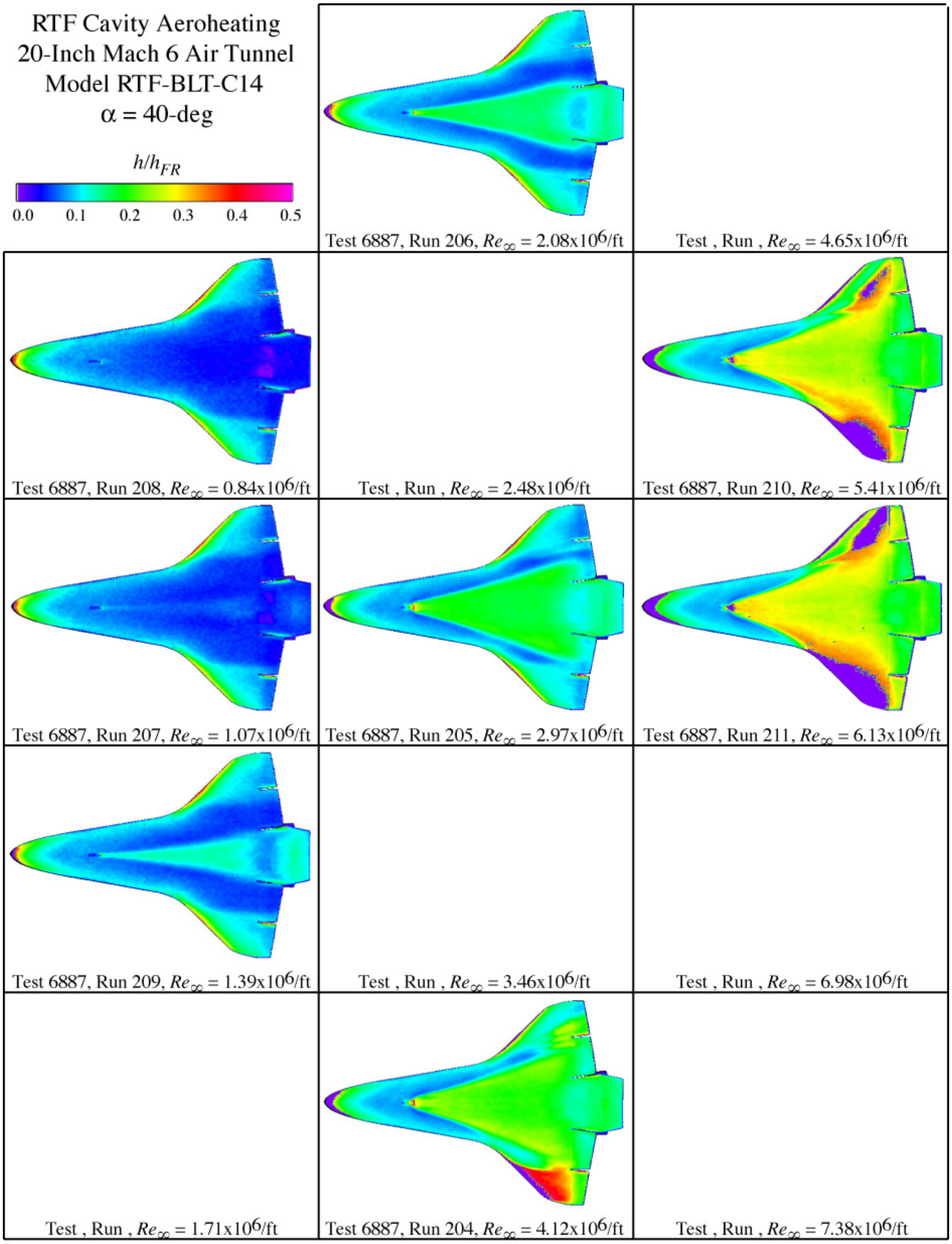

Figure A.82: RTF-BLT-C14 global aeroheating in the 20-Inch Mach 6 Air Tunnel at α = 40-deg.

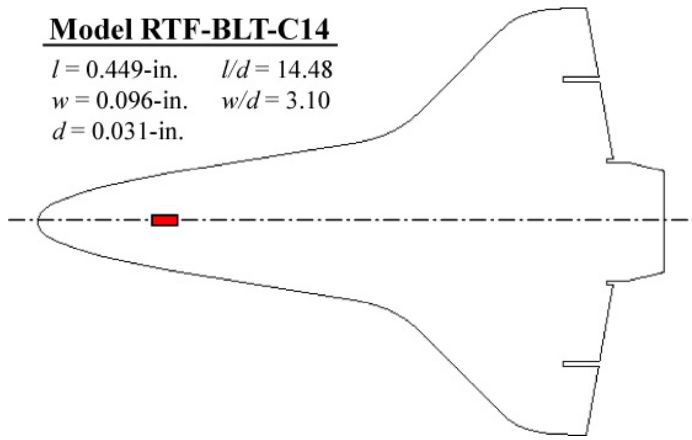

Figure A.83: RTF-BLT-C14 cavity information.

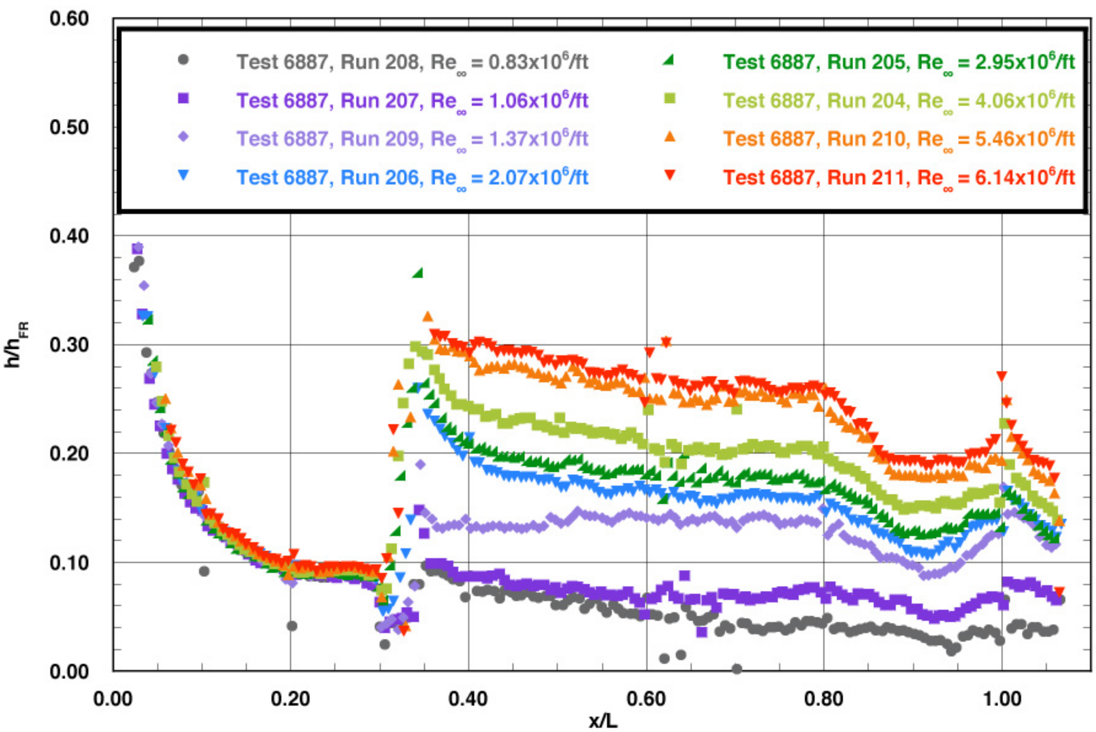

Figure A.84: RTF-BLT-C14 centerline data in the 20-Inch Mach 6 Air Tunnel at α = 40-deg.

Appendix B: 31-Inch Mach 10 Air Tunnel Aeroheating

Table B.1: Cross Reference of Figure Numbers Versus Parametrics for Phosphor Images from the 31-Inch Mach 10 Air Tunnel.

α (deg.)	Model	$(x/L)_{CL}$ (in.)	k_{CL} (in.)	Figure
40	RTF-BLT-C1	-	-	B.1
40	RTF-BLT-C2	-	-	B.4
40	RTF-BLT-C3	-	-	B.7
40	RTF-BLT-C4	-	-	B.10
40	RTF-BLT-C5	-	-	B.13
40	RTF-BLT-C6	-	-	B.16
40	RTF-BLT-C9	-	-	B.19
40	RTF-BLT-C10	-	-	B.22
40	RTF-BLT-C13	-	-	B.25
40	RTF-BLT-C14	-	-	B.28

Note: Corresponding data cuts are located immediately after figures.

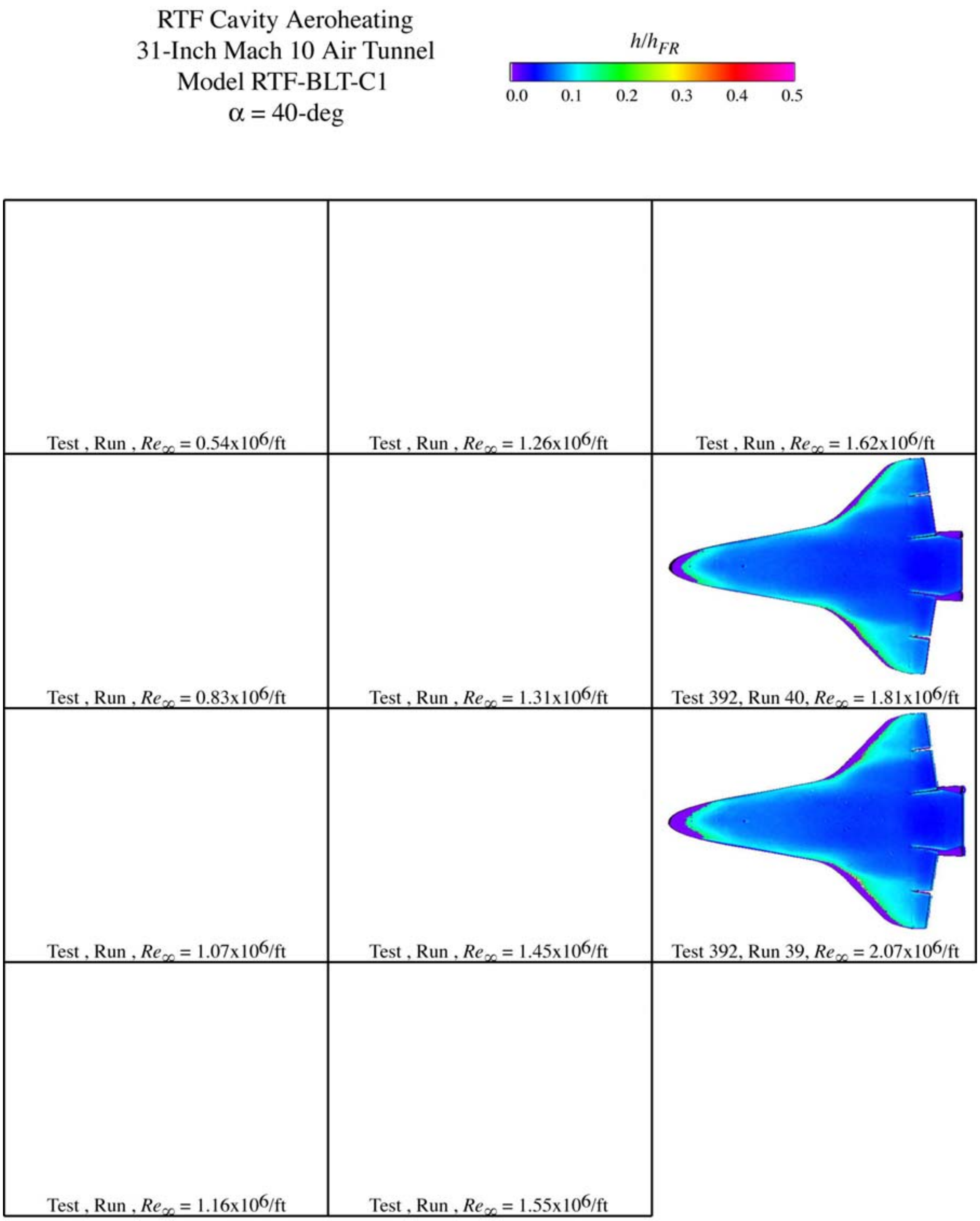

Figure B.1: RTF-BLT-C1 global aeroheating in the 31-Inch Mach 10 Air Tunnel at α = 40-deg.

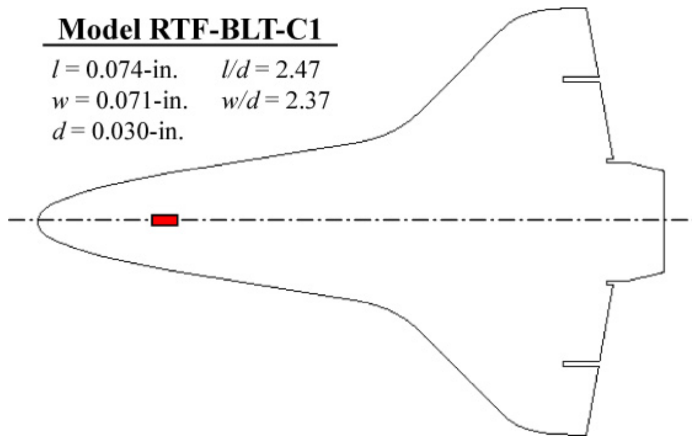

Figure B.2: RTF-BLT-C1 model information.

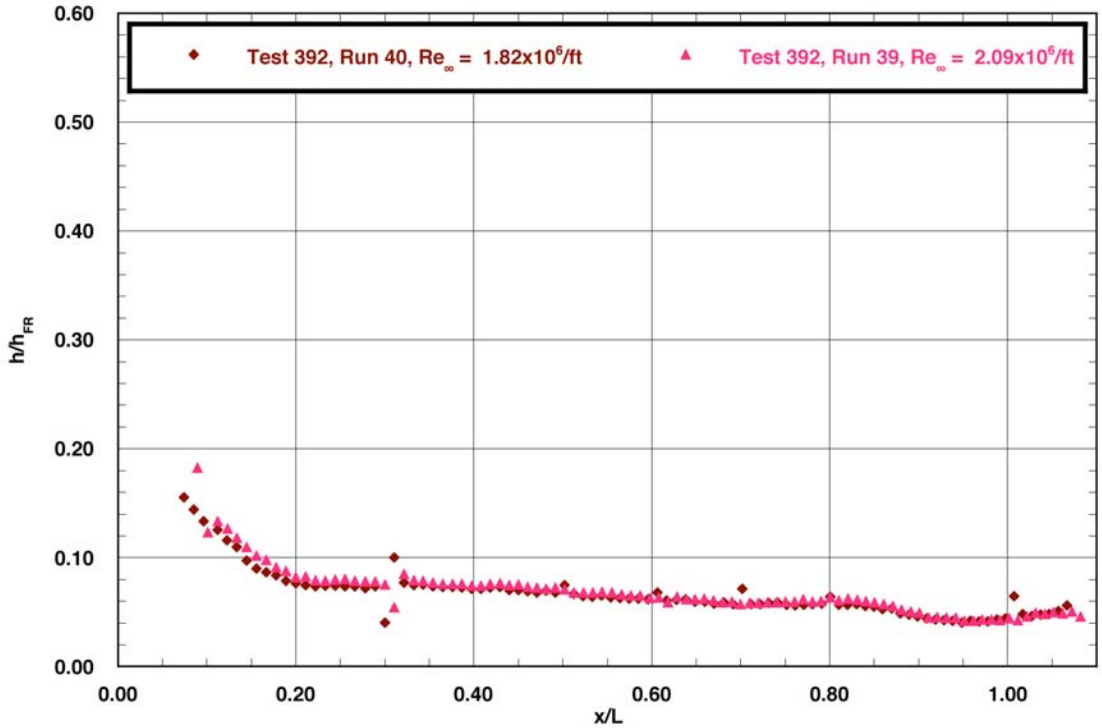

Figure B.3: RTF-BLT-C1 centerline data in the 31-Inch Mach 10 Air Tunnel at α = 40-deg.

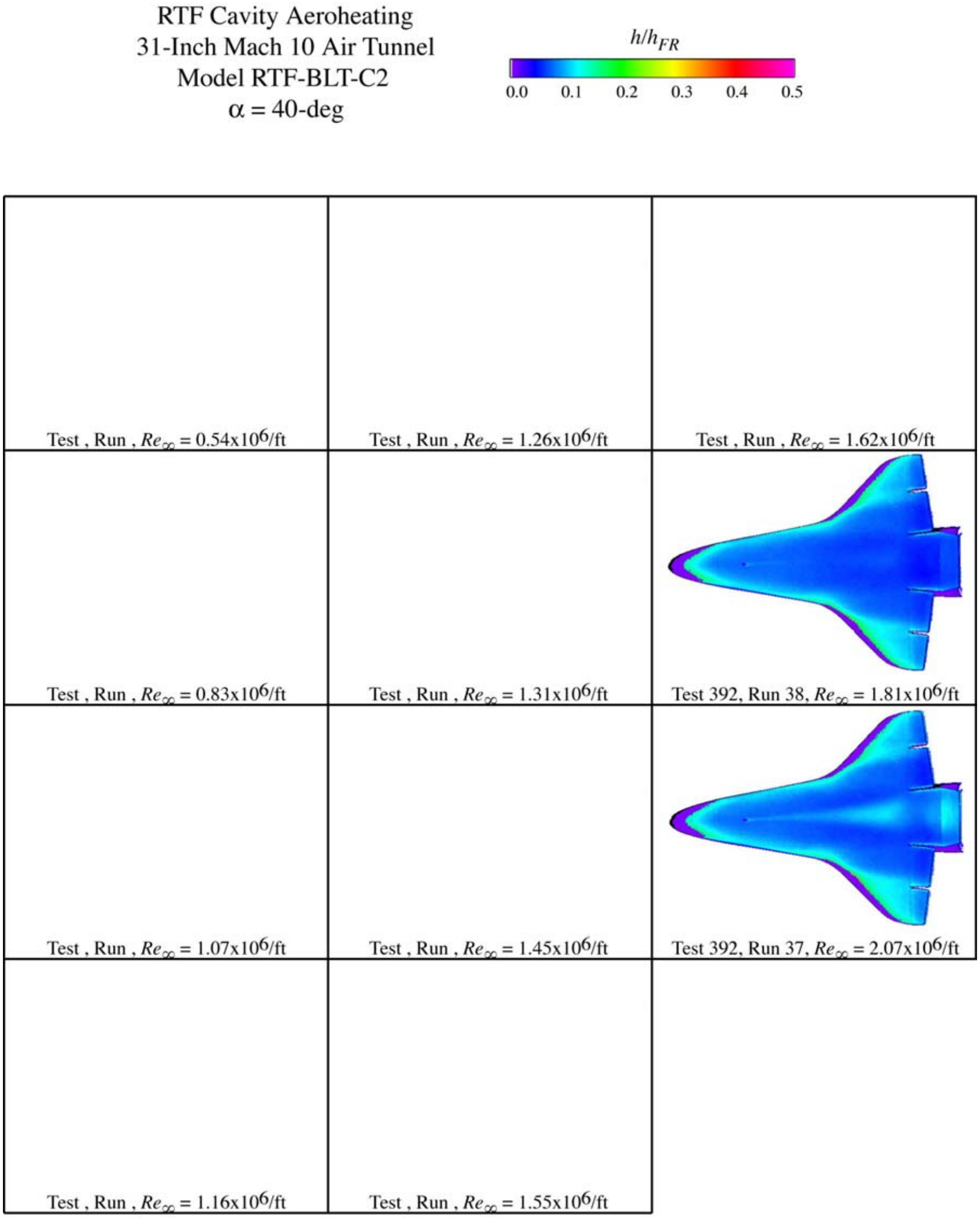

Figure B.4: RTF-BLT-C2 global aeroheating in the 31-Inch Mach 10 Air Tunnel at α = 40-deg.

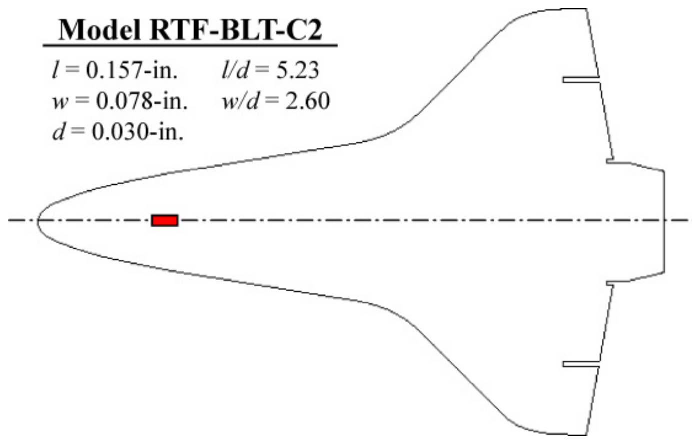

Figure B.5: RTF-BLT-C2 model information.

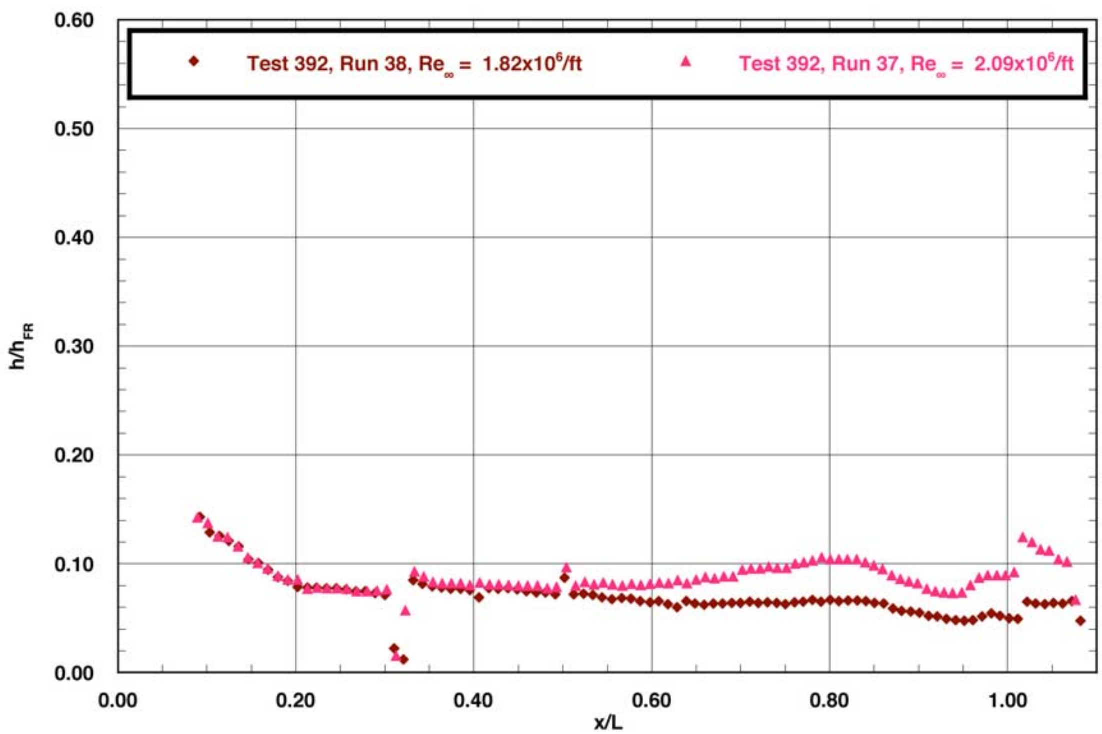

Figure B.6: RTF-BLT-C2 centerline data in the 31-Inch Mach 10 Air Tunnel at α = 40-deg.

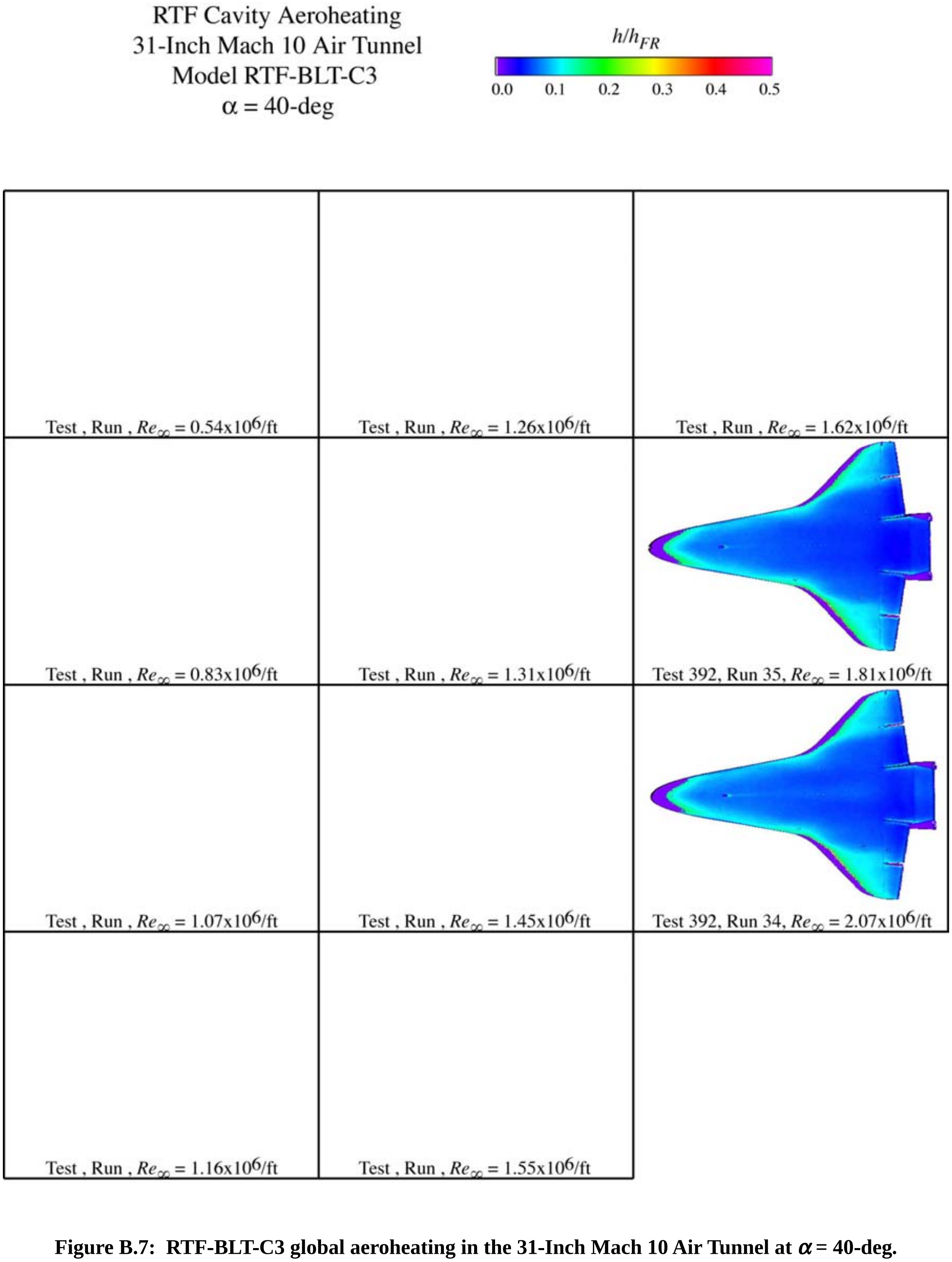

Figure B.7: RTF-BLT-C3 global aeroheating in the 31-Inch Mach 10 Air Tunnel at α = 40-deg.

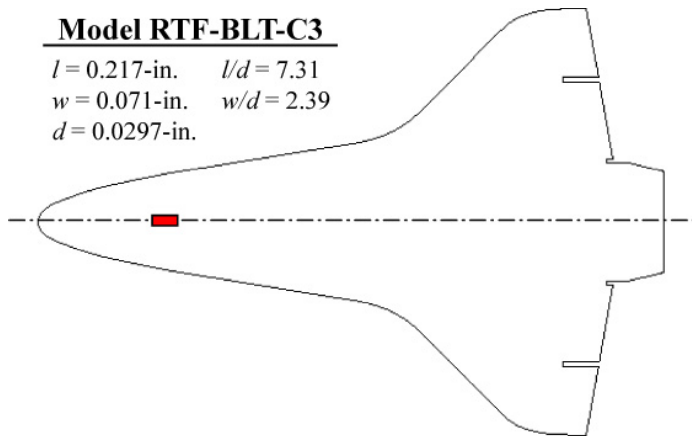

Figure B.8: RTF-BLT-C3 model information.

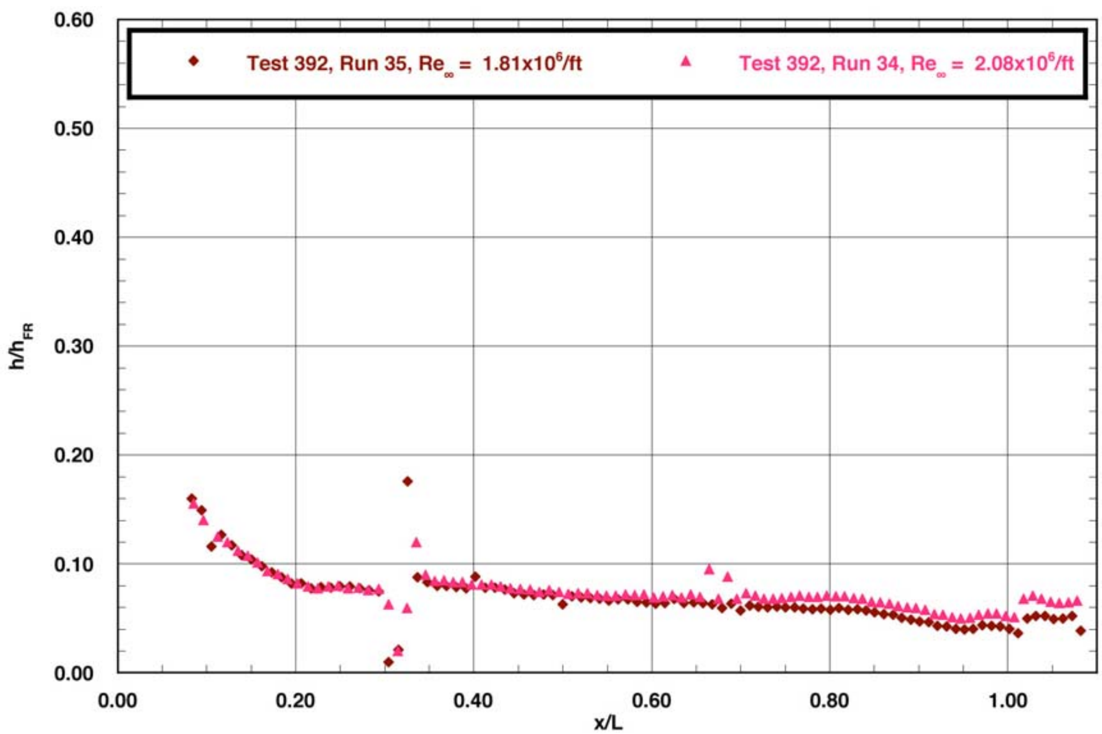

Figure B.9: RTF-BLT-C3 centerline data in the 31-Inch Mach 10 Air Tunnel at α = 40-deg.

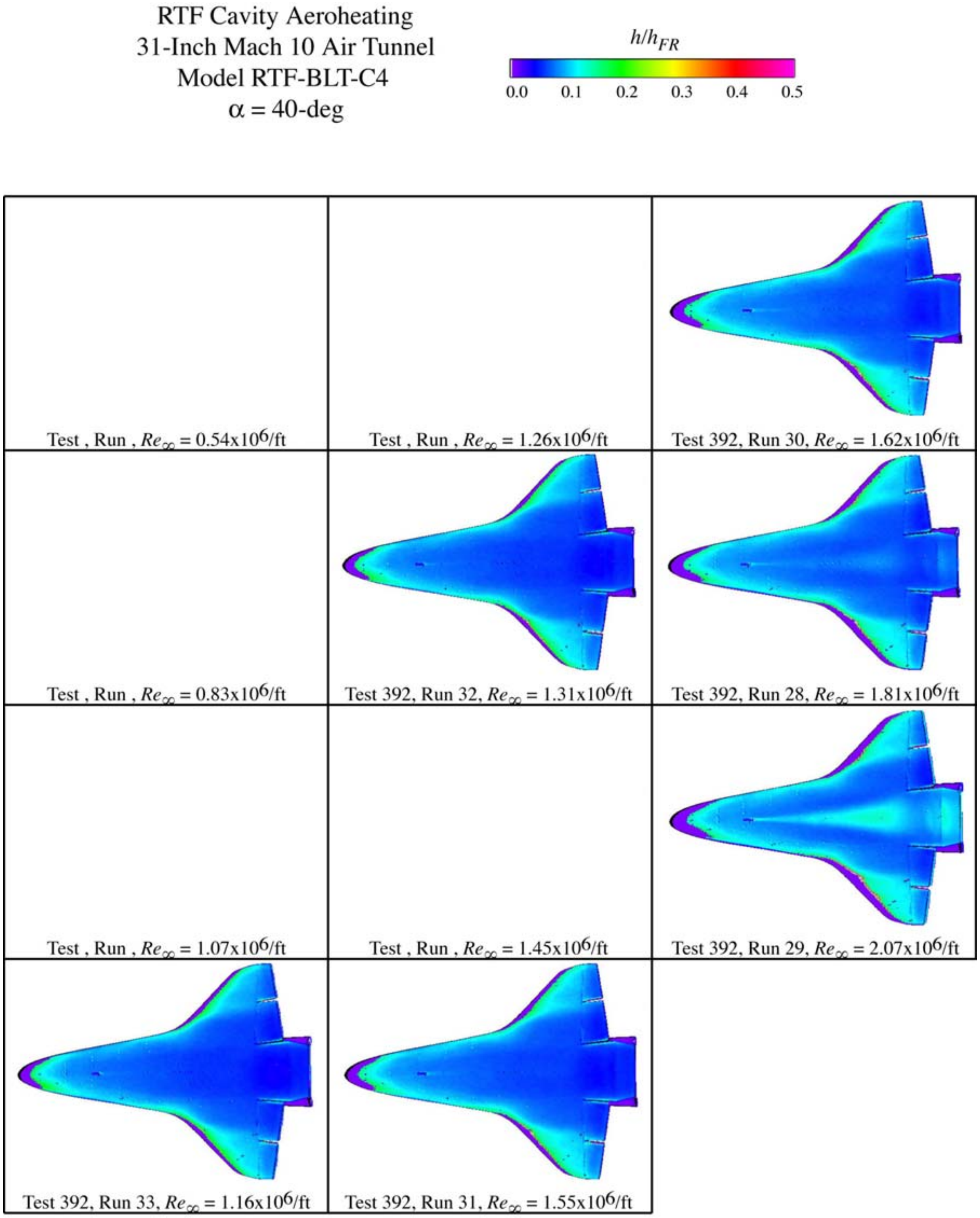

Figure B.10: RTF-BLT-C4 global aeroheating in the 31-Inch Mach 10 Air Tunnel at α = 40-deg.

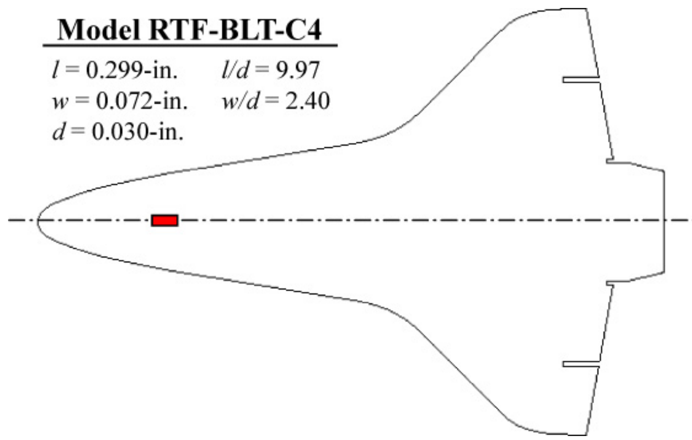

Figure B.11: RTF-BLT-C4 model information.

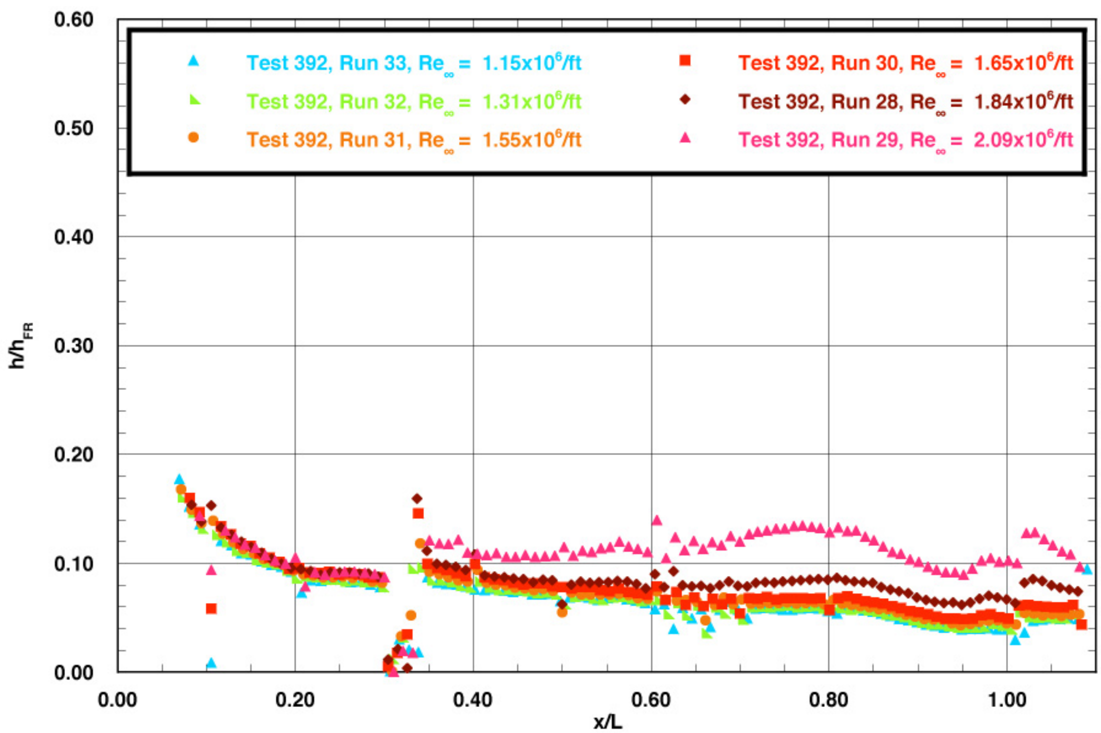

Figure B.12: RTF-BLT-C4 centerline data in the 31-Inch Mach 10 Air Tunnel at α = 40-deg.

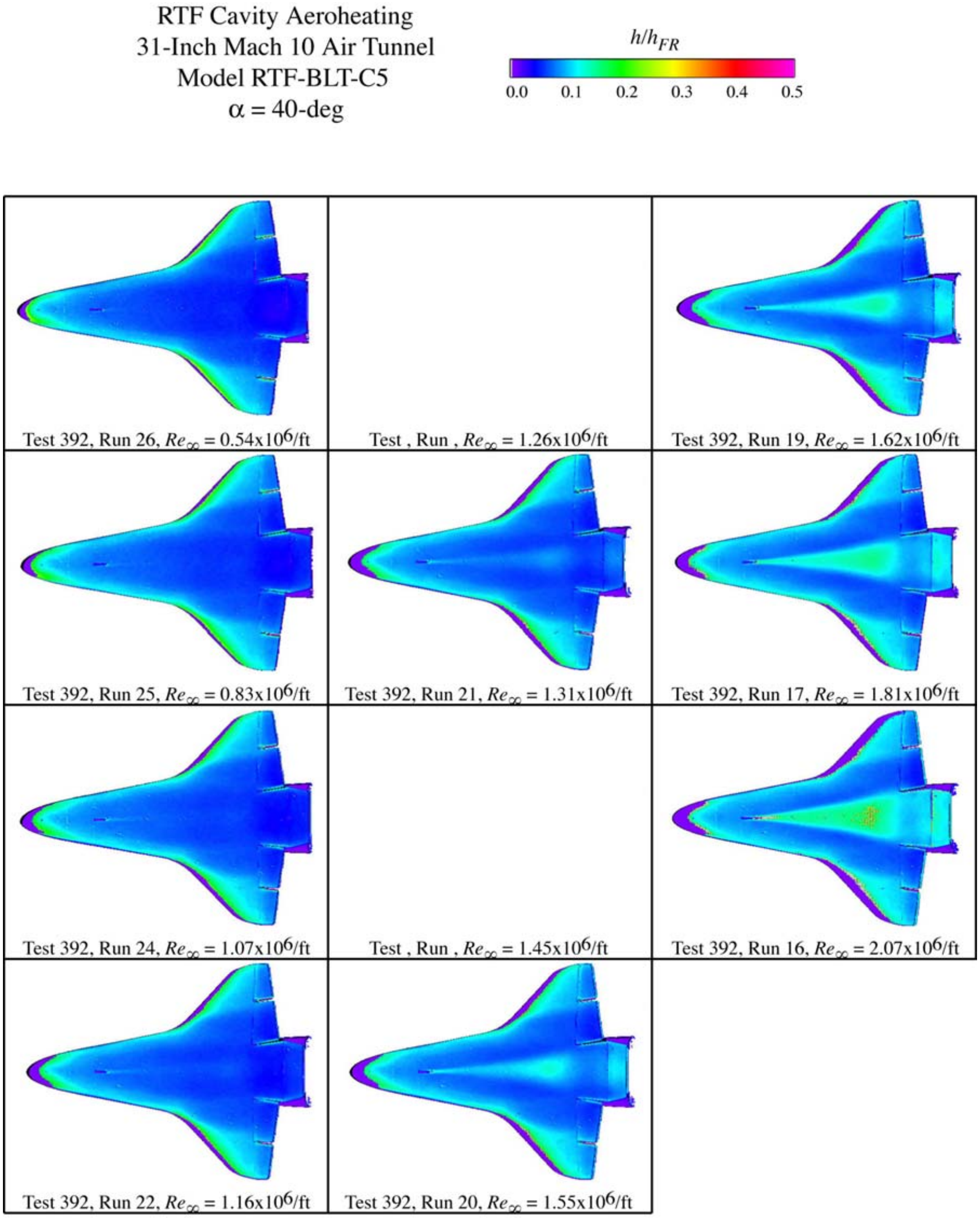

Figure B.13: RTF-BLT-C5 global aeroheating in the 31-Inch Mach 10 Air Tunnel at α = 40-deg.

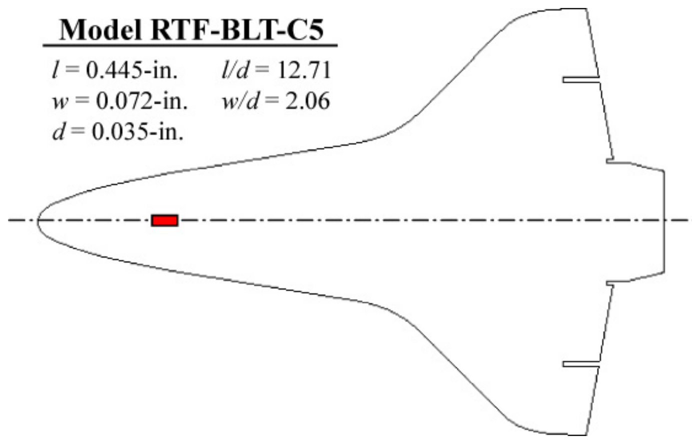

Figure B.14: RTF-BLT-C5 model information.

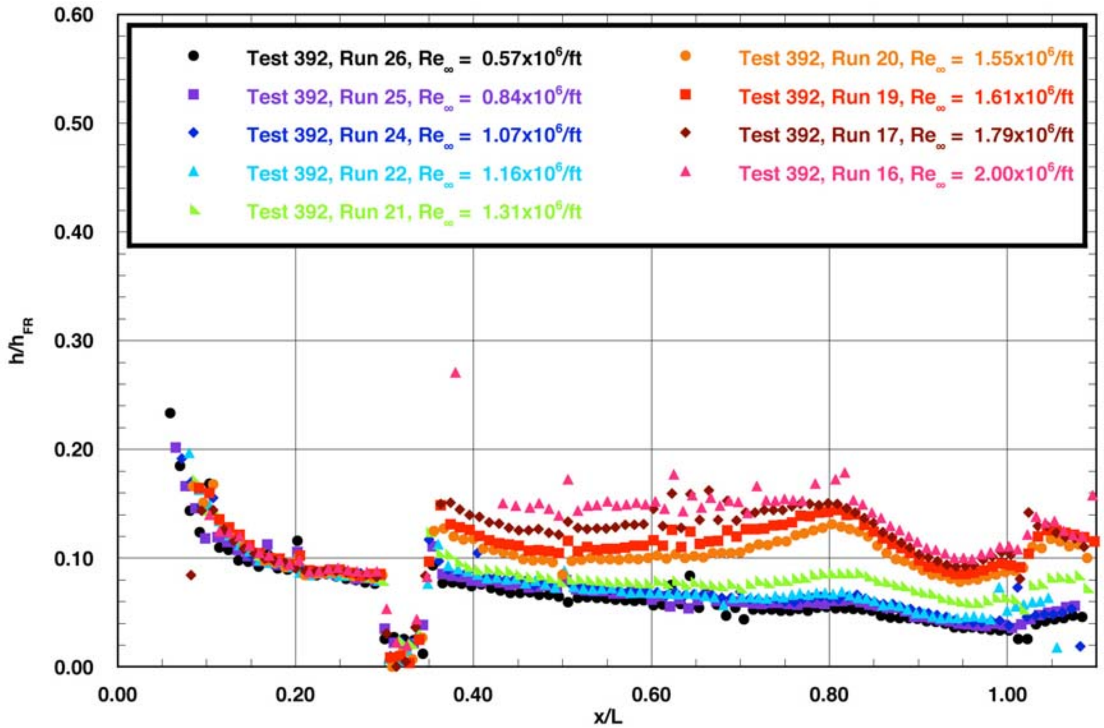

Figure B.15: RTF-BLT-C5 centerline data in the 31-Inch Mach 10 Air Tunnel at α = 40-deg.

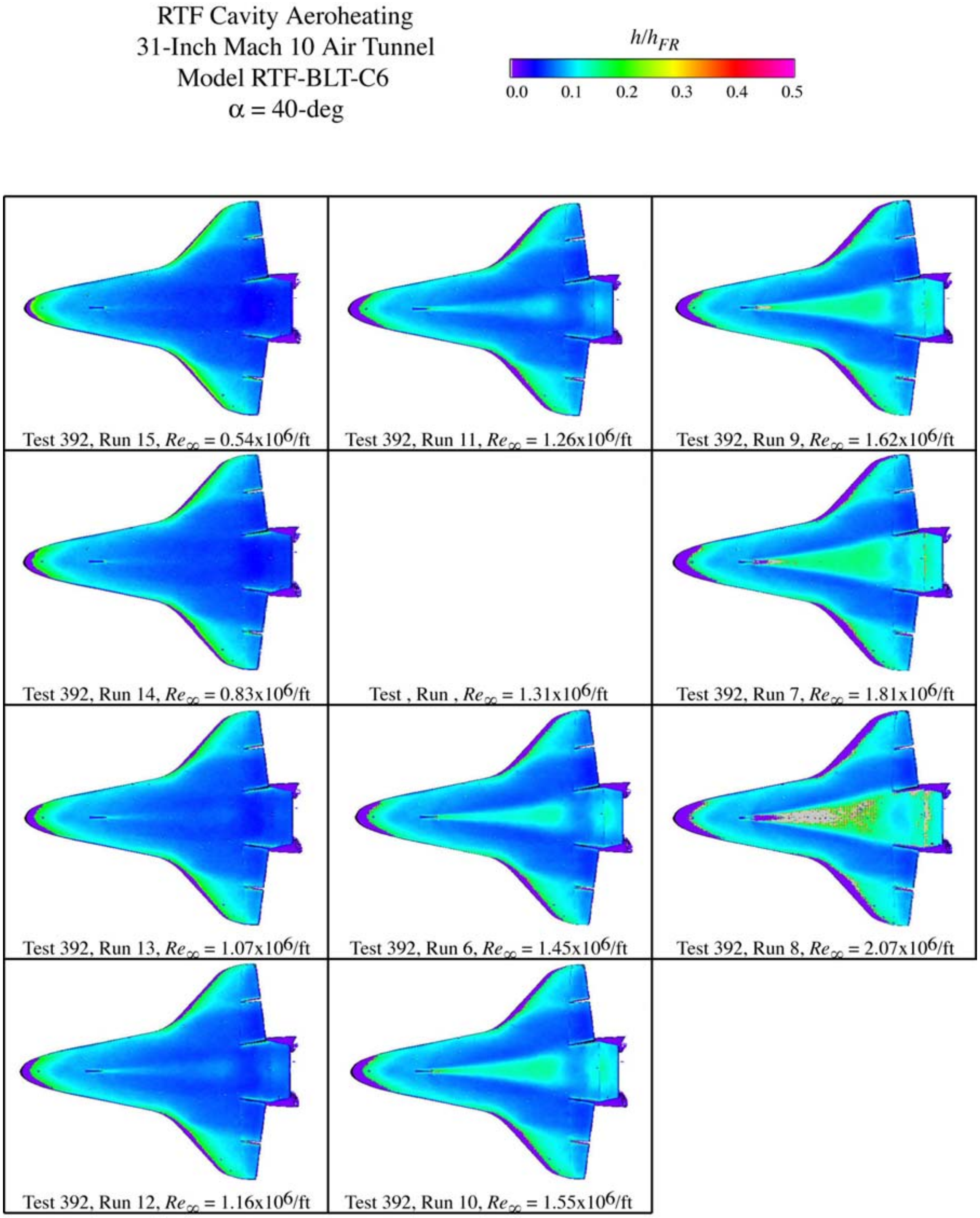

Figure B.16: RTF-BLT-C6 global aeroheating in the 31-Inch Mach 10 Air Tunnel at α = 40-deg.

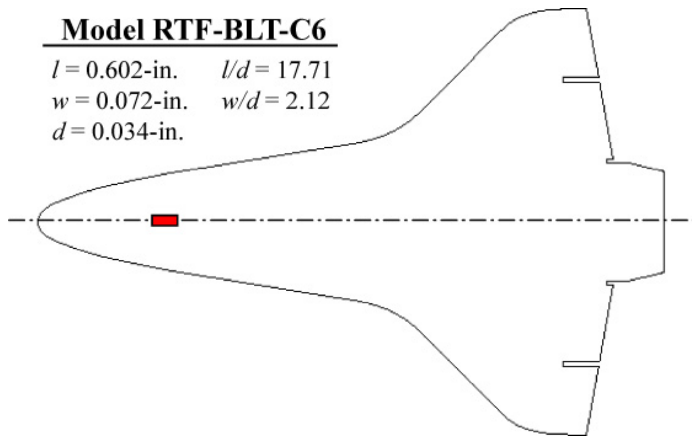

Figure B.17: RTF-BLT-C6 model information.

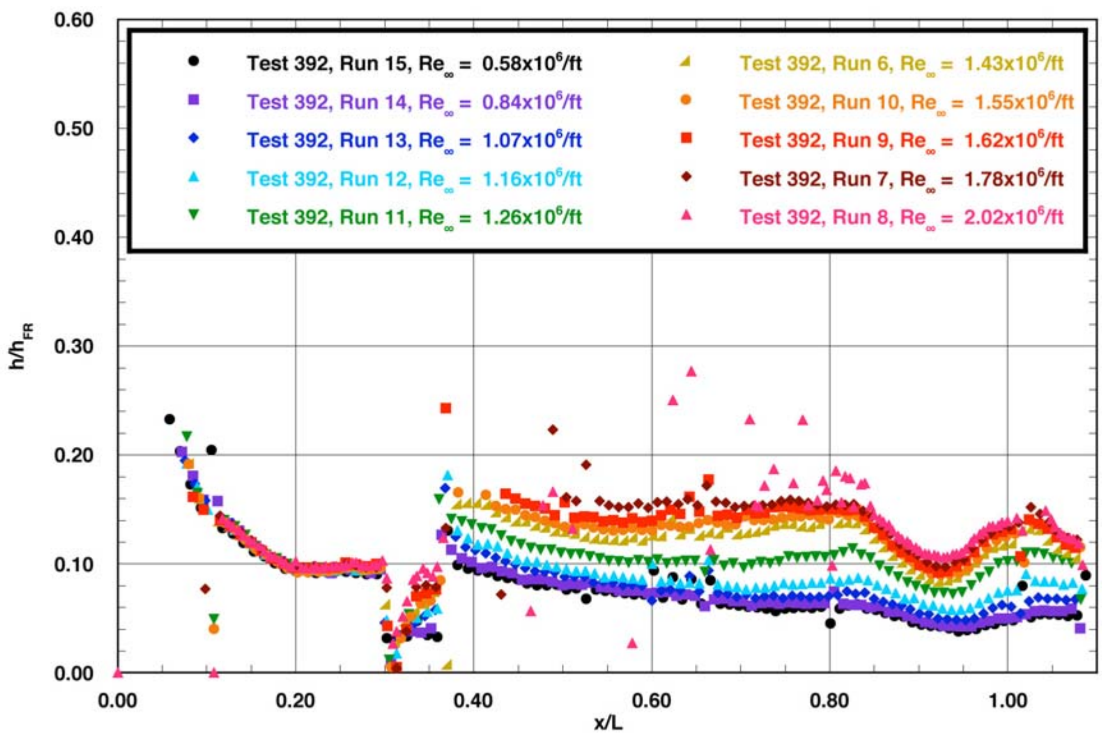

Figure B.18: RTF-BLT-C6 centerline data in the 31-Inch Mach 10 Air Tunnel at α = 40-deg.

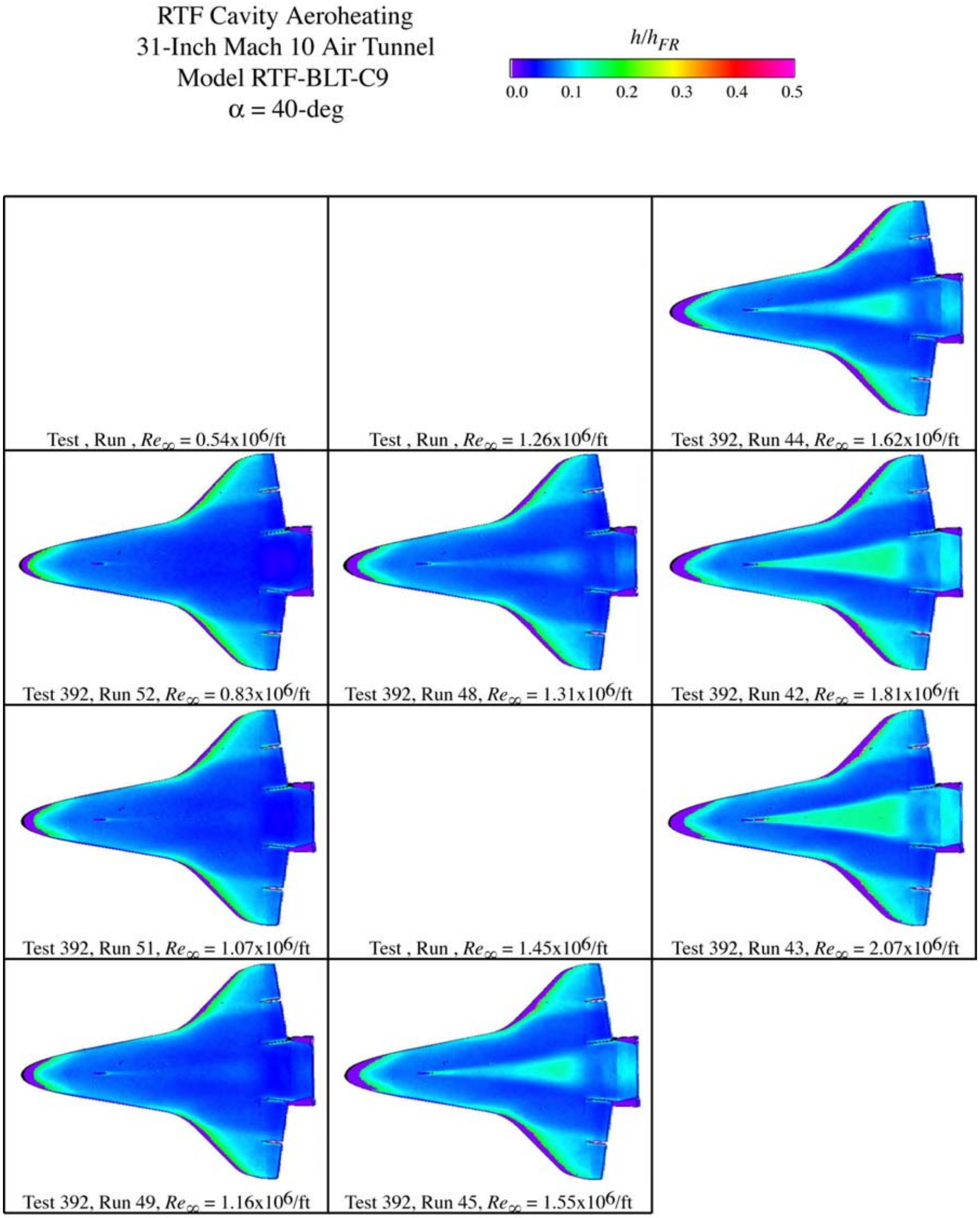

Figure B.19: RTF-BLT-C9 global aeroheating in the 31-Inch Mach 10 Air Tunnel at α = 40-deg.

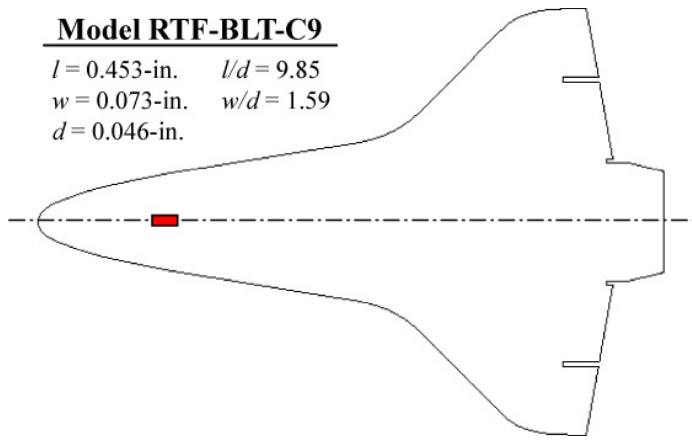

Figure B.20: RTF-BLT-C9 model information.

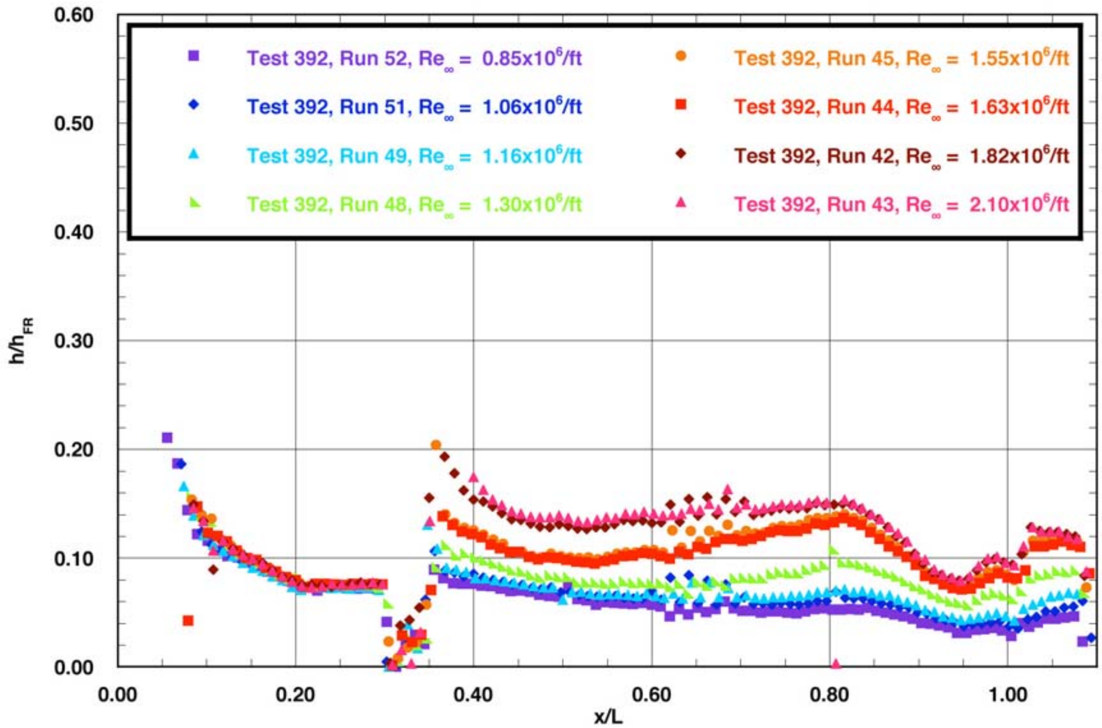

Figure B.21: RTF-BLT-C9 centerline data in the 31-Inch Mach 10 Air Tunnel at α = 40-deg.

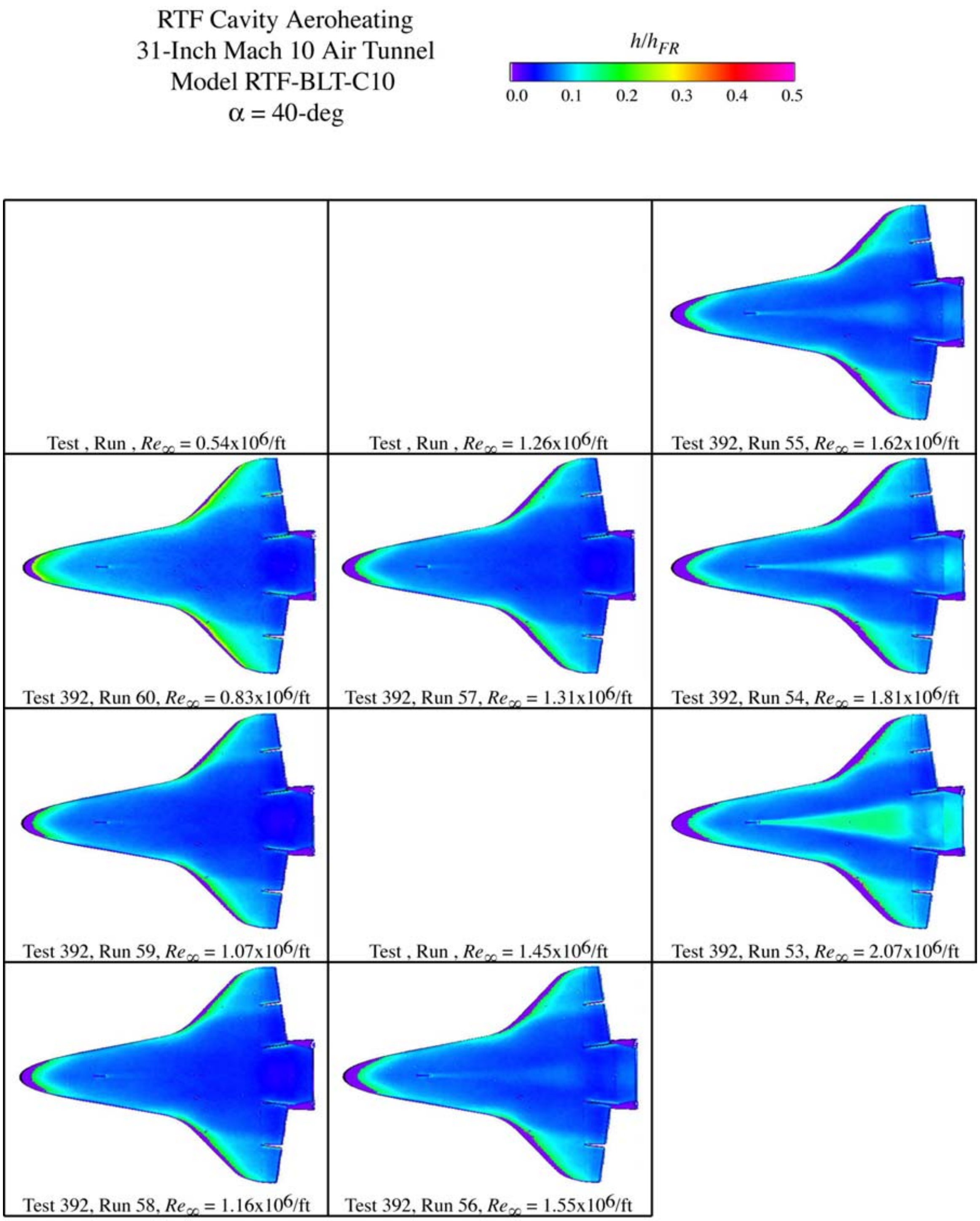

Figure B.22: RTF-BLT-C10 global aeroheating in the 31-Inch Mach 10 Air Tunnel at α = 40-deg.

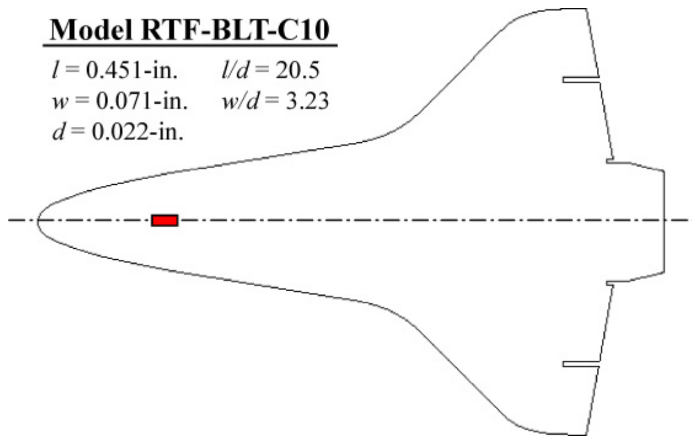

Figure B.23: RTF-BLT-C10 model information.

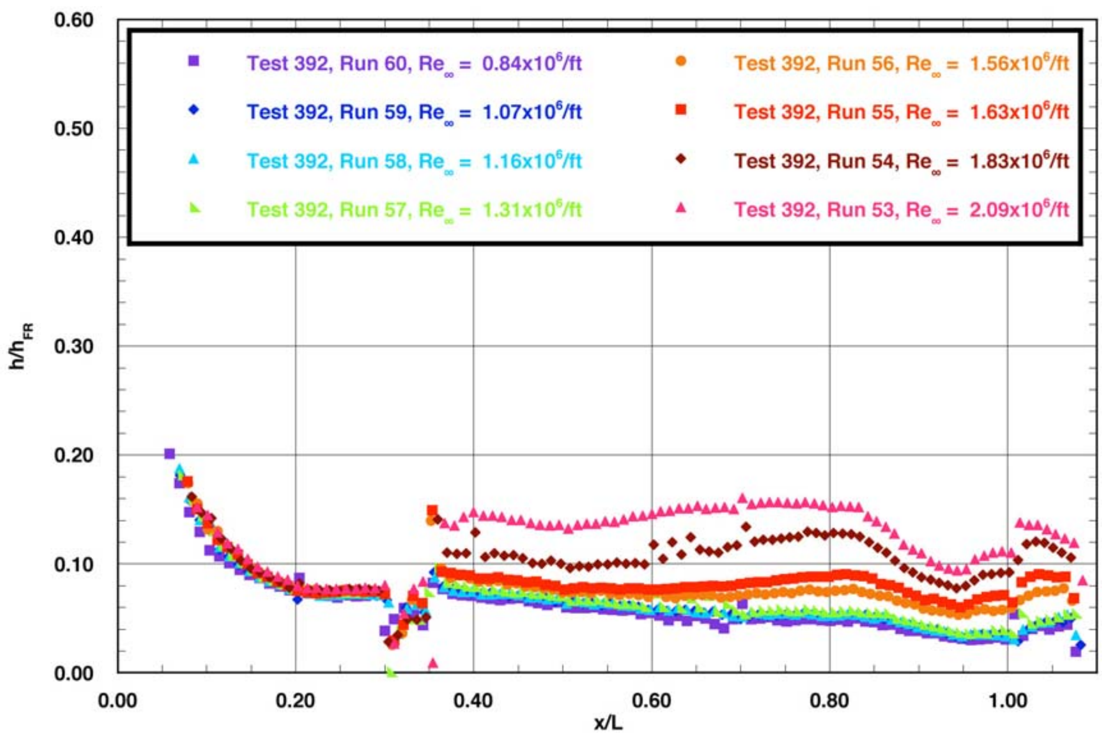

Figure B.24: RTF-BLT-C10 centerline data in the 31-Inch Mach 10 Air Tunnel at α = 40-deg.

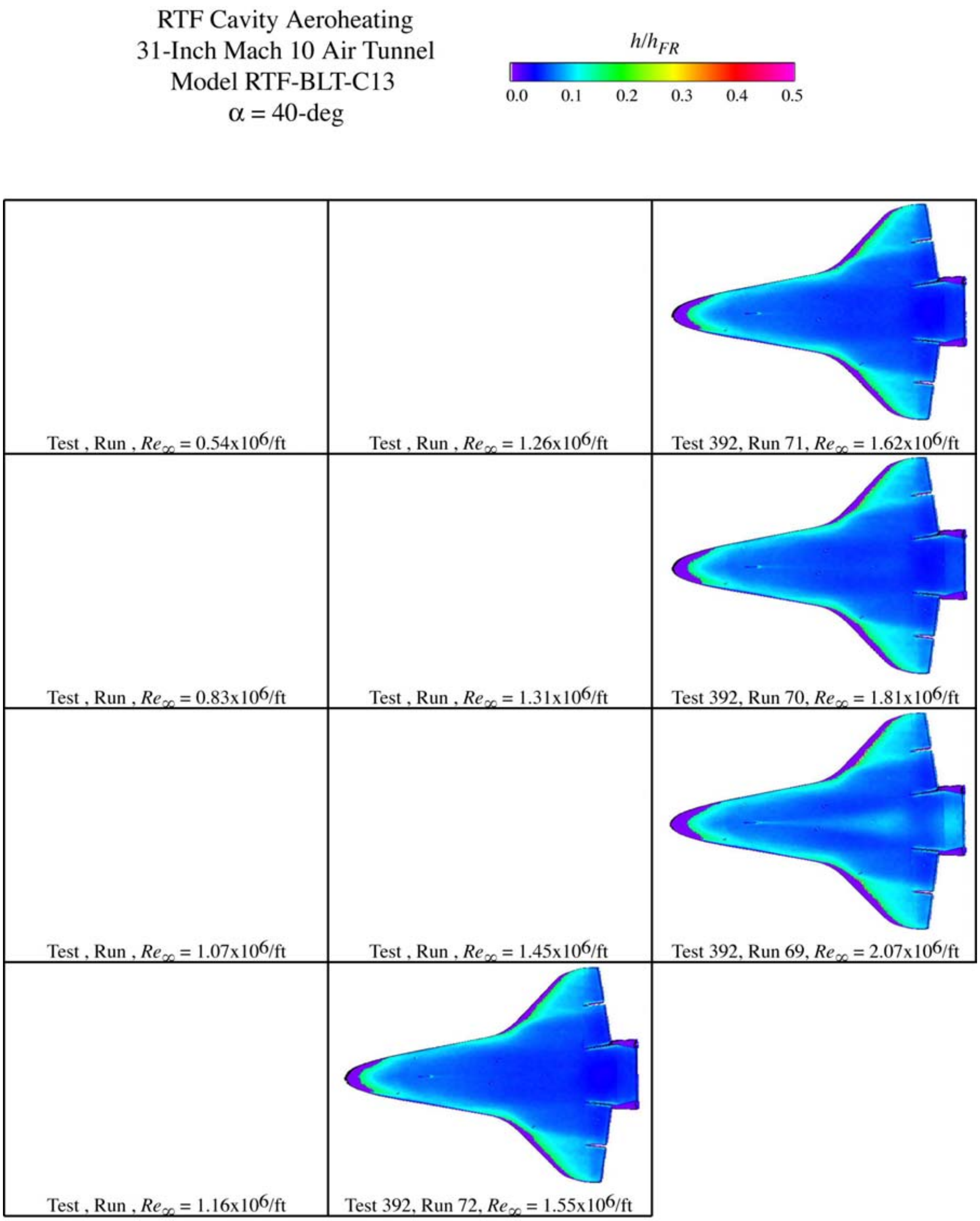

Figure B.25: RTF-BLT-C13 global aeroheating in the 31-Inch Mach 10 Air Tunnel at α = 40-deg.

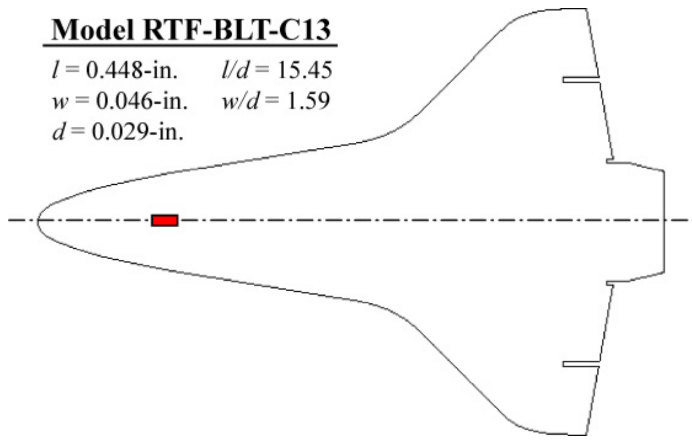

Figure B.26: RTF-BLT-C13 model information.

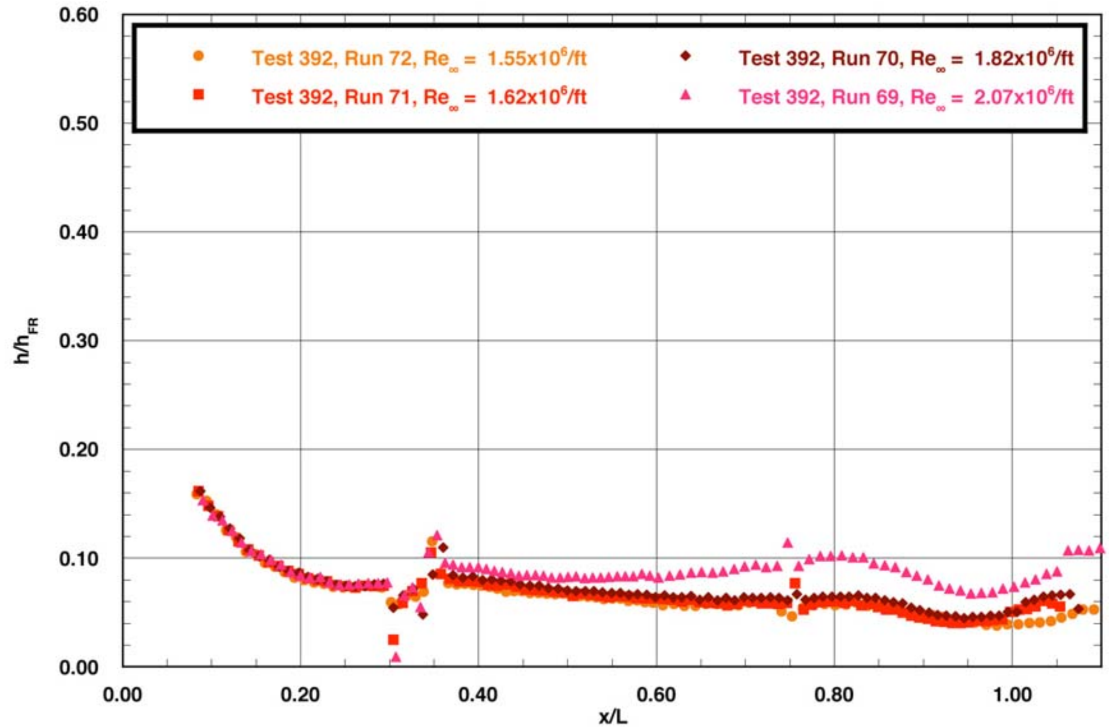

Figure B.27: RTF-BLT-C13 centerline data in the 31-Inch Mach 10 Air Tunnel at α = 40-deg.

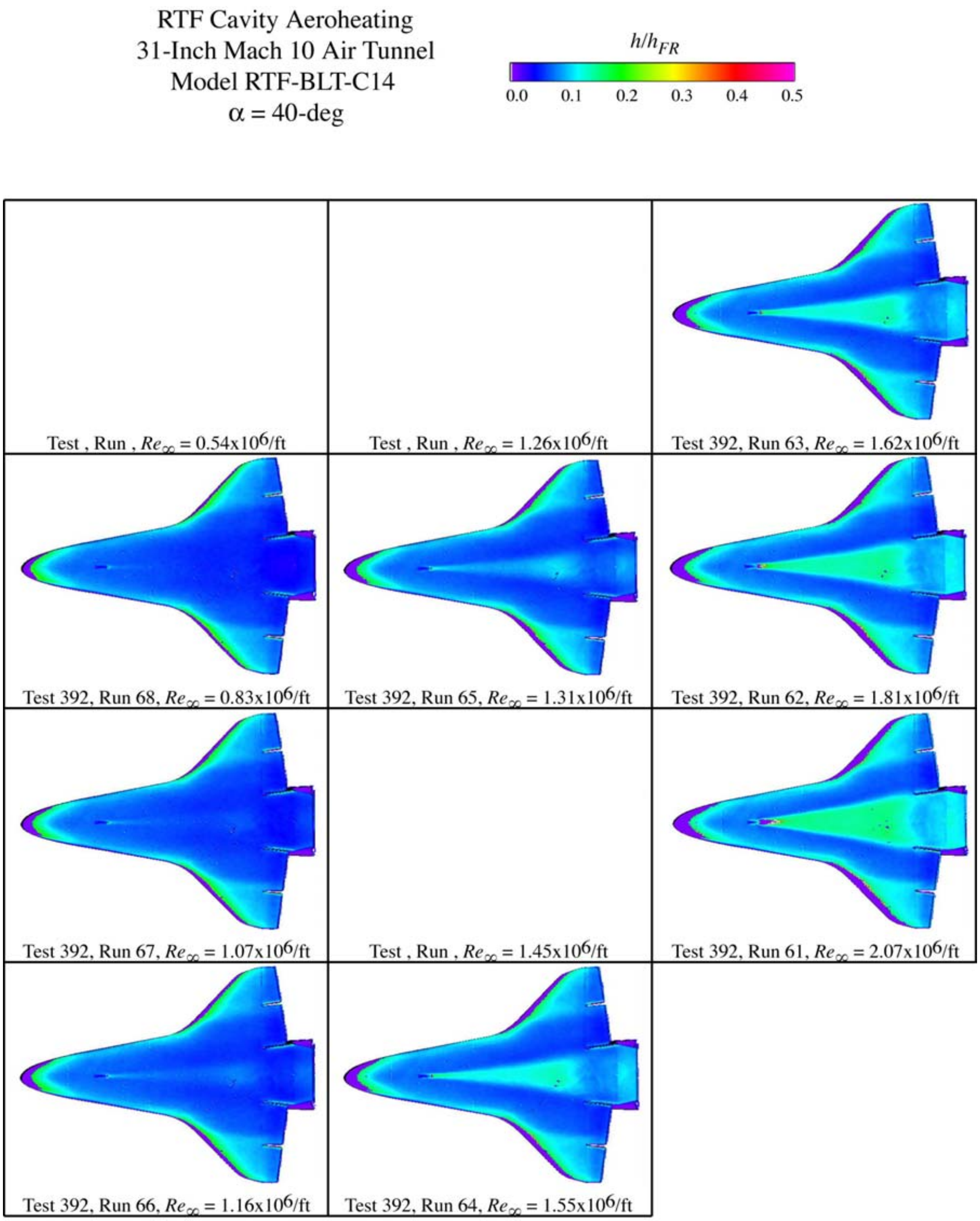

Figure B.28: RTF-BLT-C14 global aeroheating in the 31-Inch Mach 10 Air Tunnel at α = 40-deg.

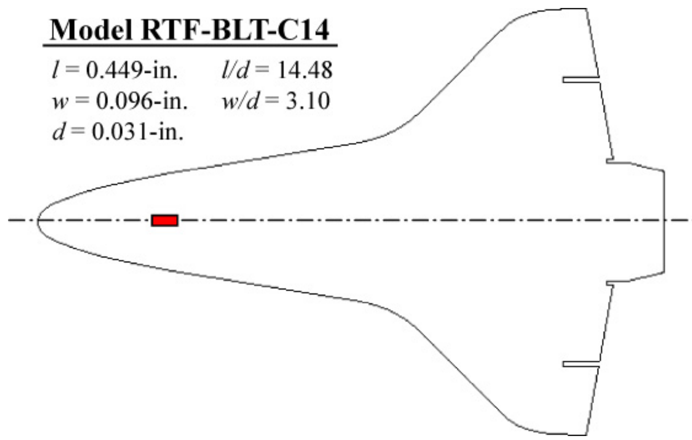

Figure B.29: RTF-BLT-C14 model information.

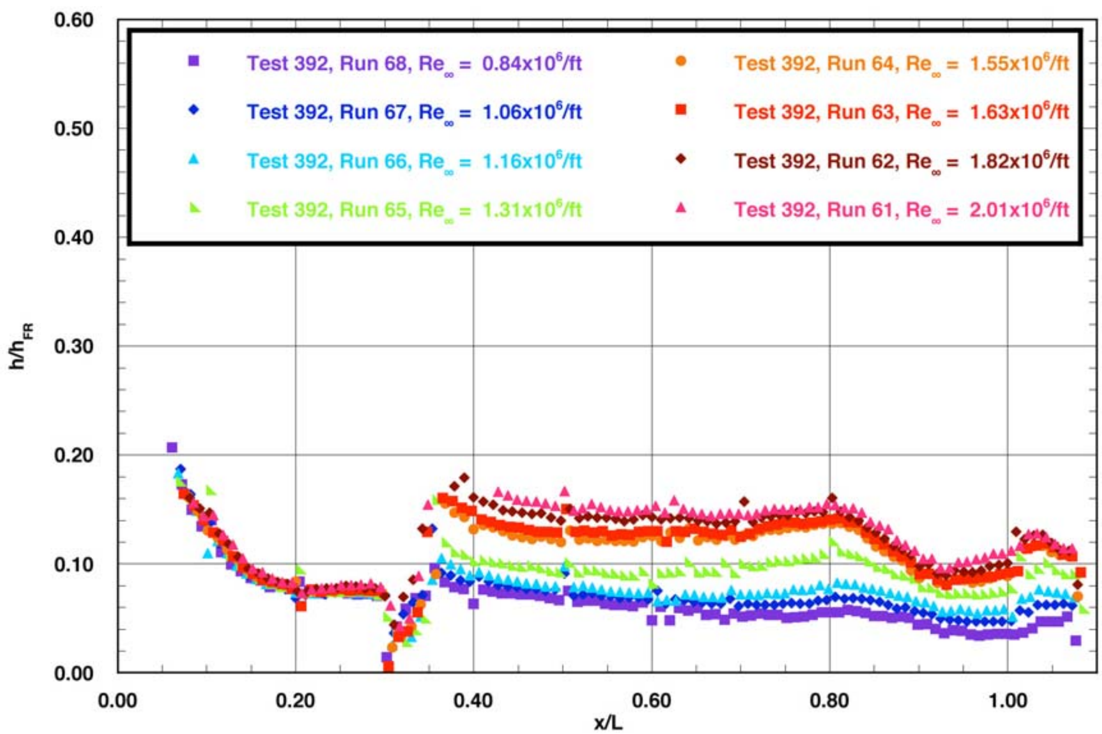

Figure B.30: RTF-BLT-C14 centerline data in the 31-Inch Mach 10 Air Tunnel at α = 40-deg.

Appendix C: 20-Inch CF_4 Tunnel Aeroheating

Table C.1: Cross Reference of Figure Numbers Versus Parametrics for Phosphor Images from the 20-Inch CF_4 Tunnel.

α (deg.)	Model	$(x/L)_{CL}$ (in.)	k_{CL} (in.)	Figure
30	RTF-BLT-P9	-	-	C.1
40	RTF-BLT-P9	-	-	C.3
40	RTF-BLT-C1	-	-	C.5
40	RTF-BLT-C2	-	-	C.8
40	RTF-BLT-C3	-	-	C.11
40	RTF-BLT-C4	-	-	C.14
40	RTF-BLT-C5	-	-	C.17
40	RTF-BLT-C6	-	-	C.20
40	RTF-BLT-C6	0.10	0.0115	C.23
40	RTF-BLT-C9	-	-	C.26
40	RTF-BLT-C10	-	-	C.29
40	RTF-BLT-C13	-	-	C.32
40	RTF-BLT-C14	-	-	C.35

Note: Corresponding data cuts are located immediately after figures.

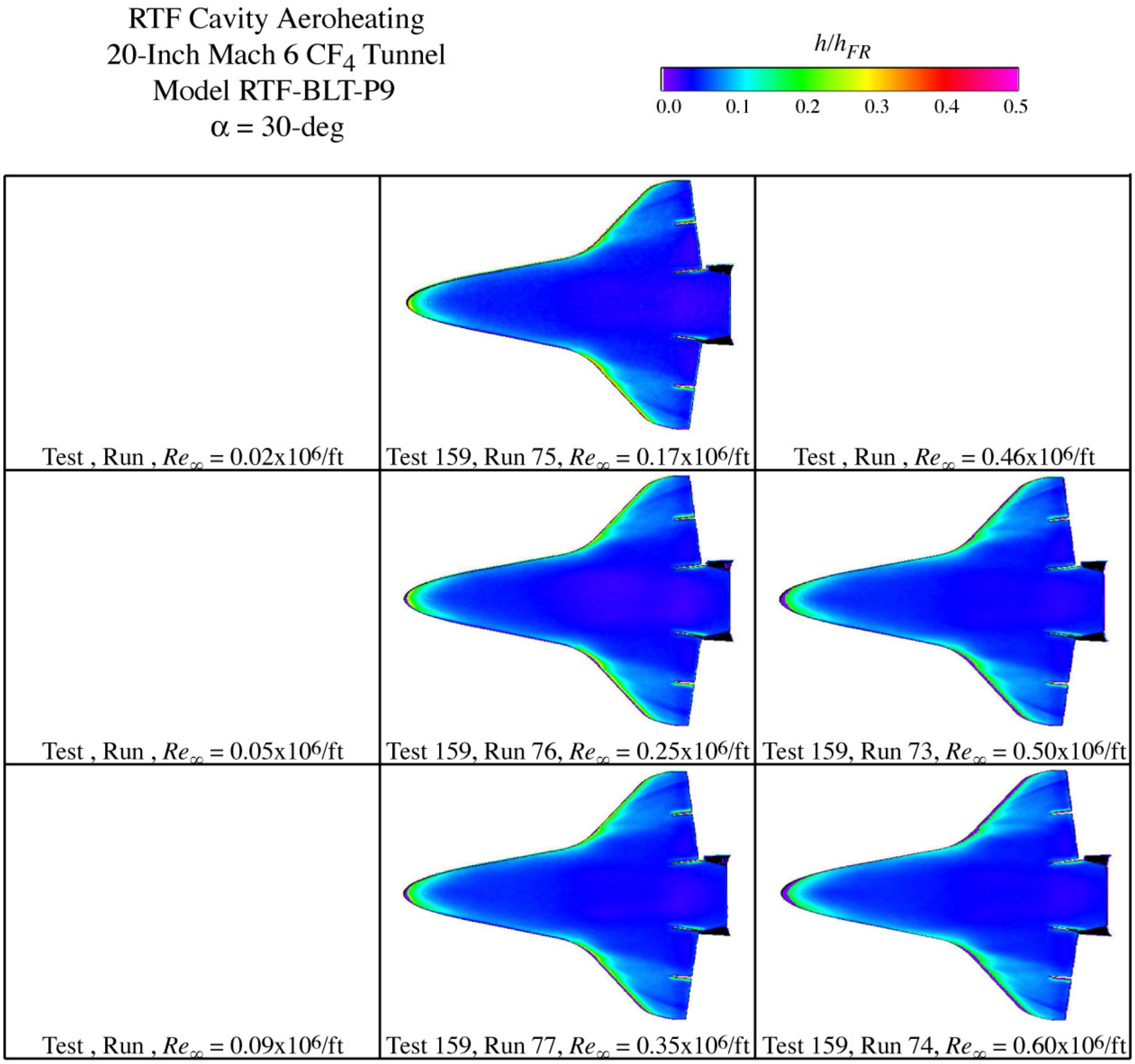

Figure C.1: RTF-BLT-P9 global aeroheating in the 20-Inch CF_4 Tunnel at α = 30-deg.

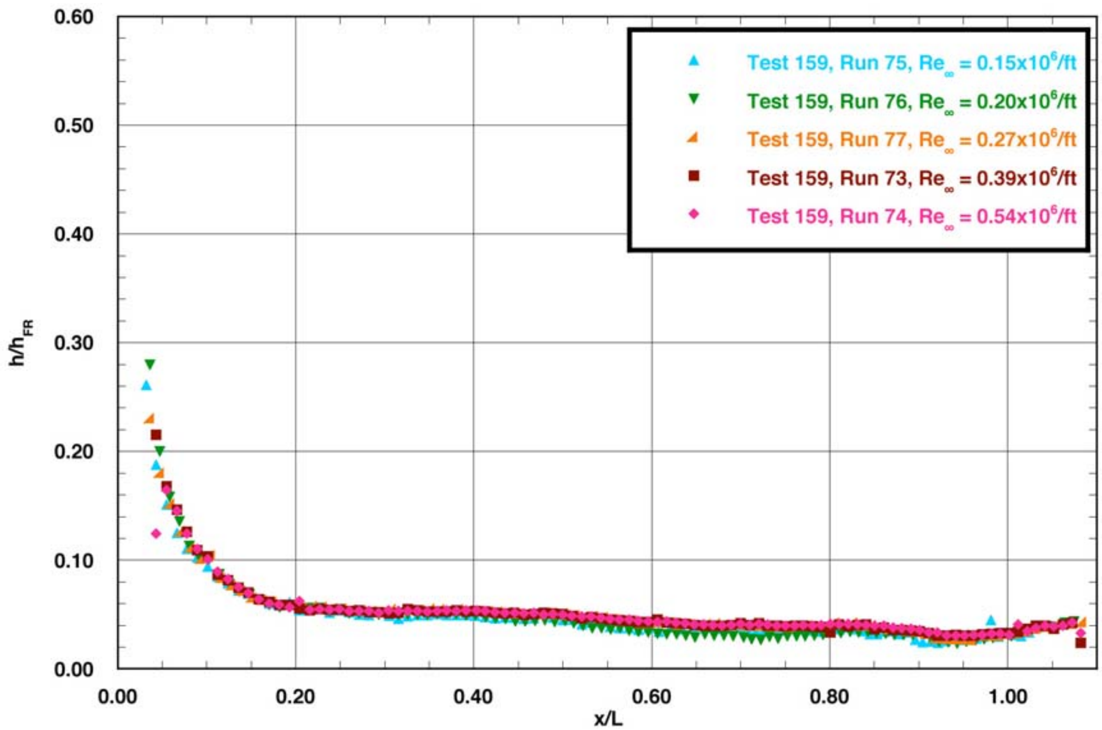

Figure C.2: RTF-BLT-P9 centerline data in the 20-Inch CF_4 Tunnel at α = 30-deg.

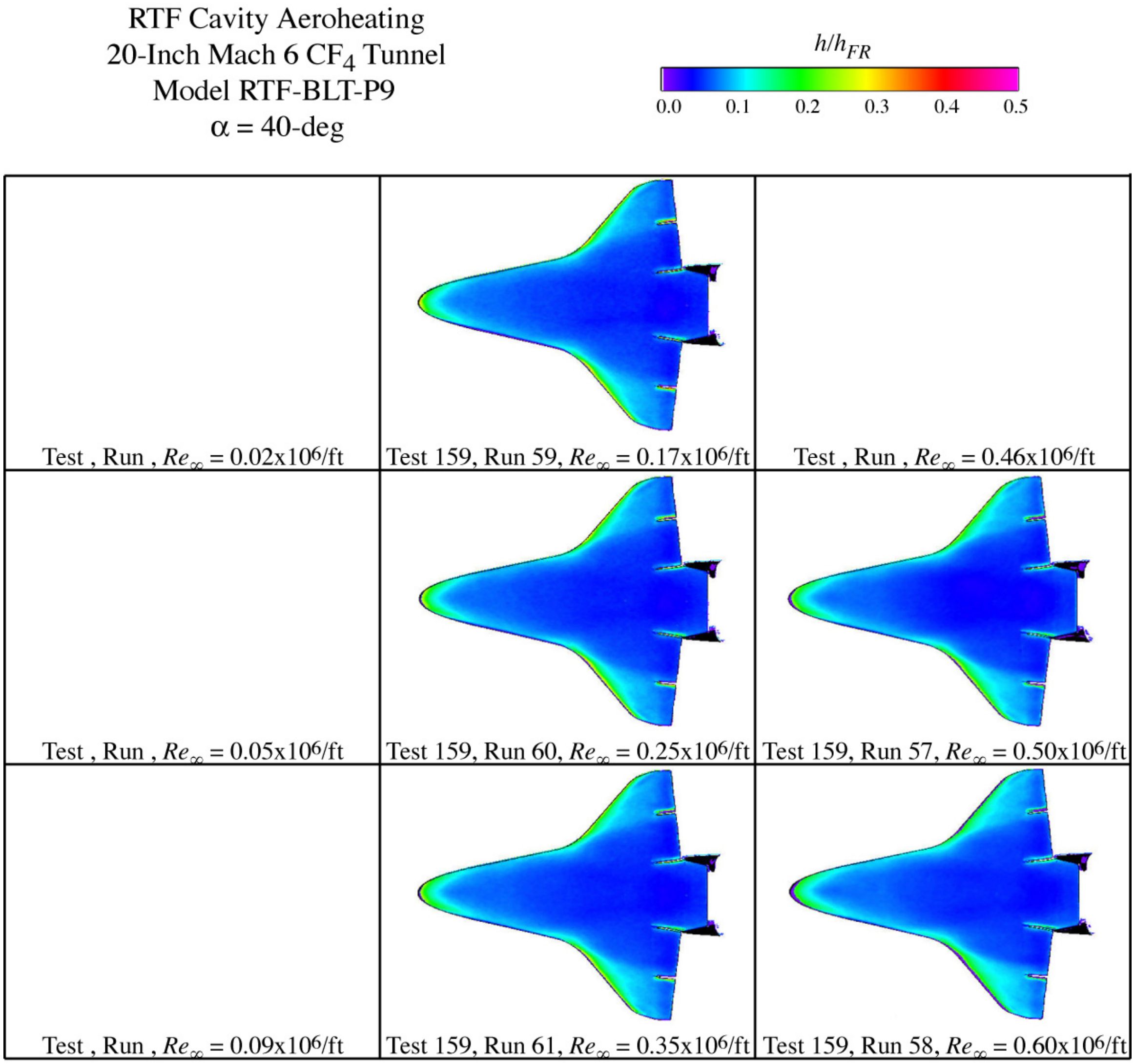

Figure C.3: RTF-BLT-P9 global aeroheating in the 20-Inch CF_4 Tunnel at α = 40-deg.

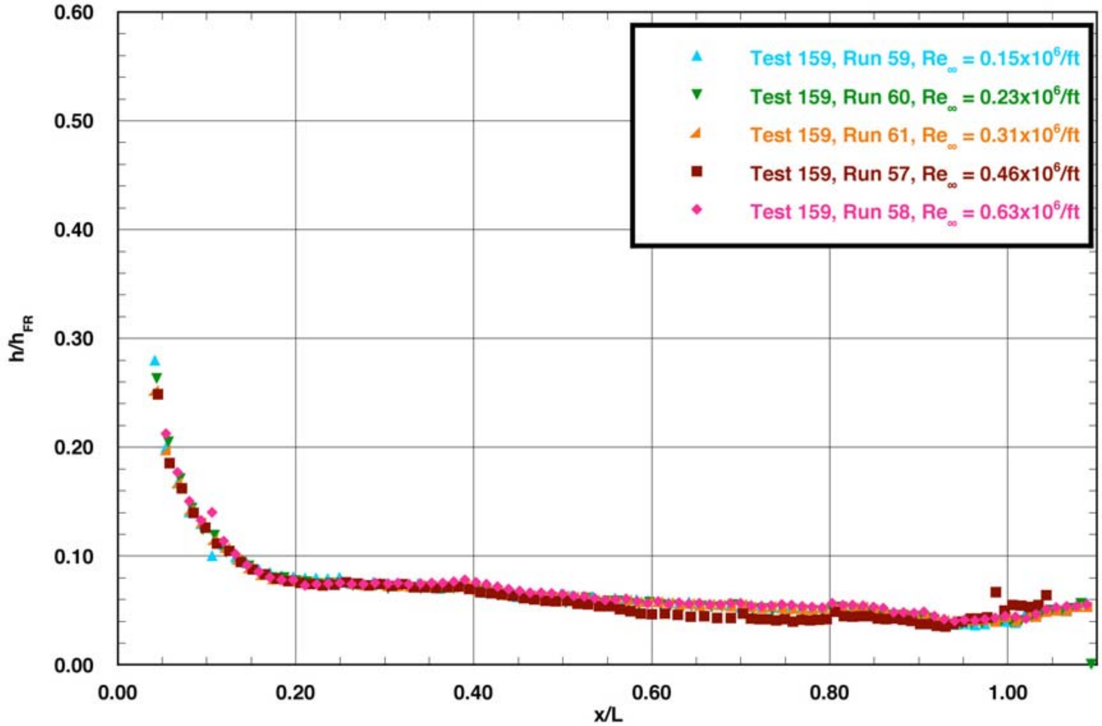

Figure C.4: RTF-BLT-P9 centerline data in the 20-Inch CF_4 Tunnel at α = 40-deg.

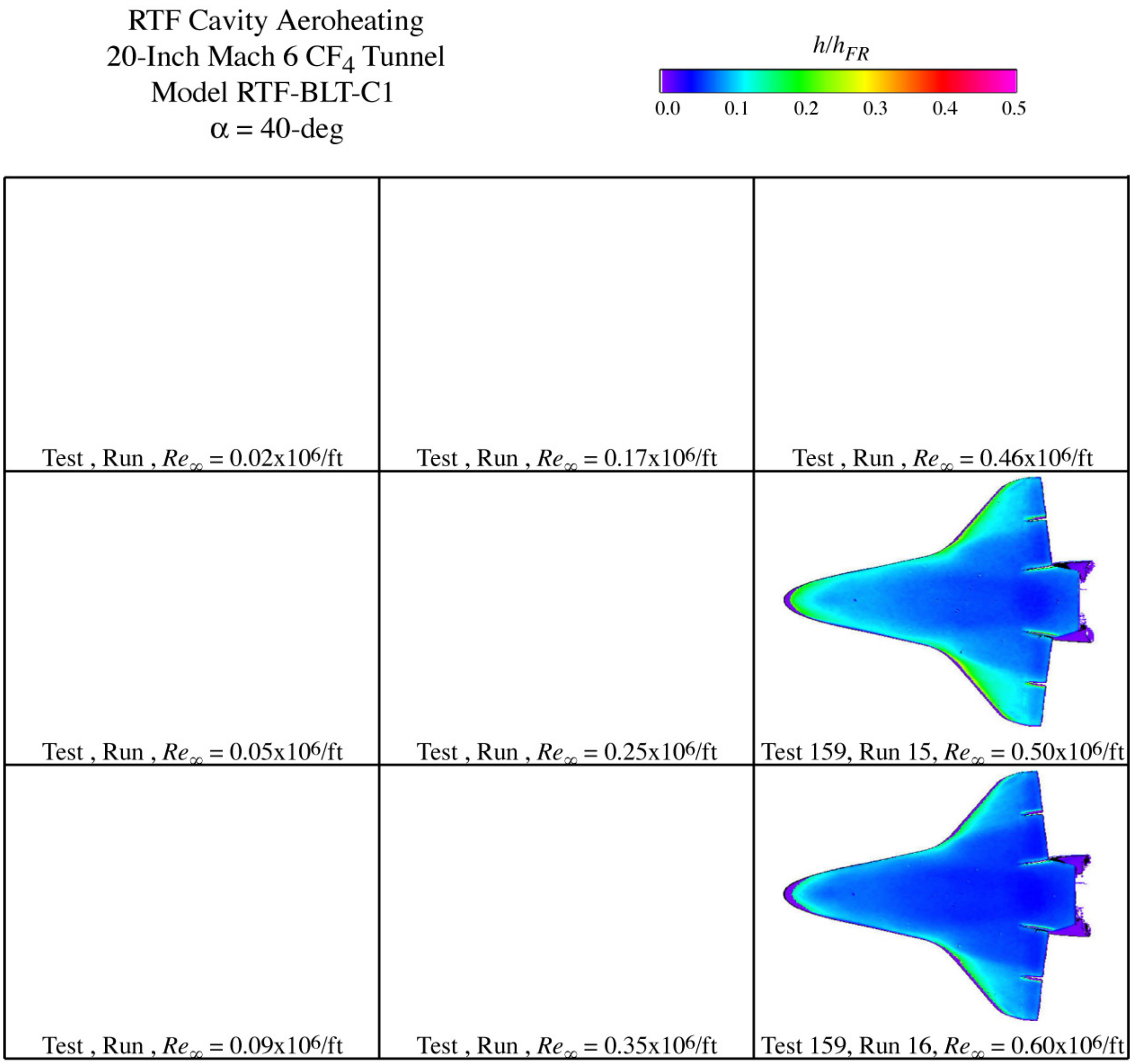

Figure C.5: RTF-BLT-C1 global aeroheating in the 20-Inch CF_4 Tunnel at α = 40-deg.

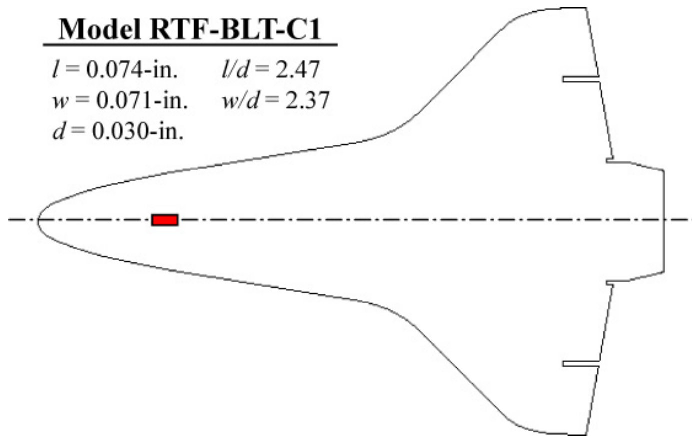

Figure C.6: RTF-BLT-C1 cavity information.

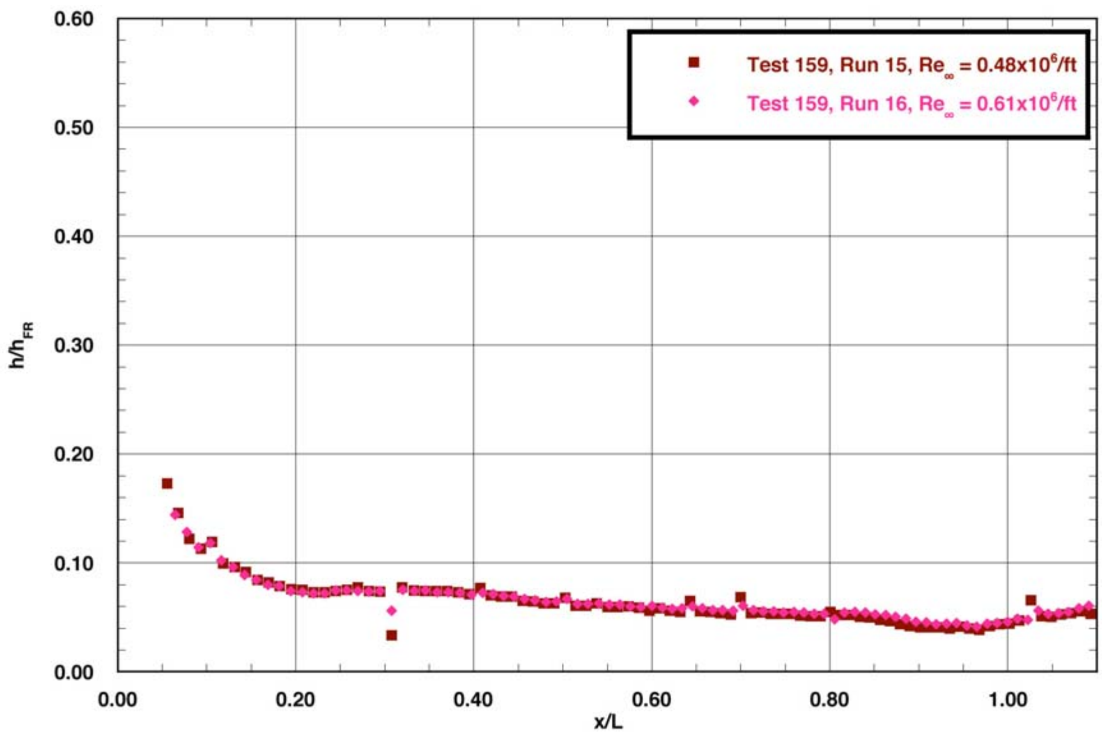

Figure C.7: RTF-BLT-C1 centerline data in the 20-Inch CF_4 Tunnel at $\alpha = 40$-deg.

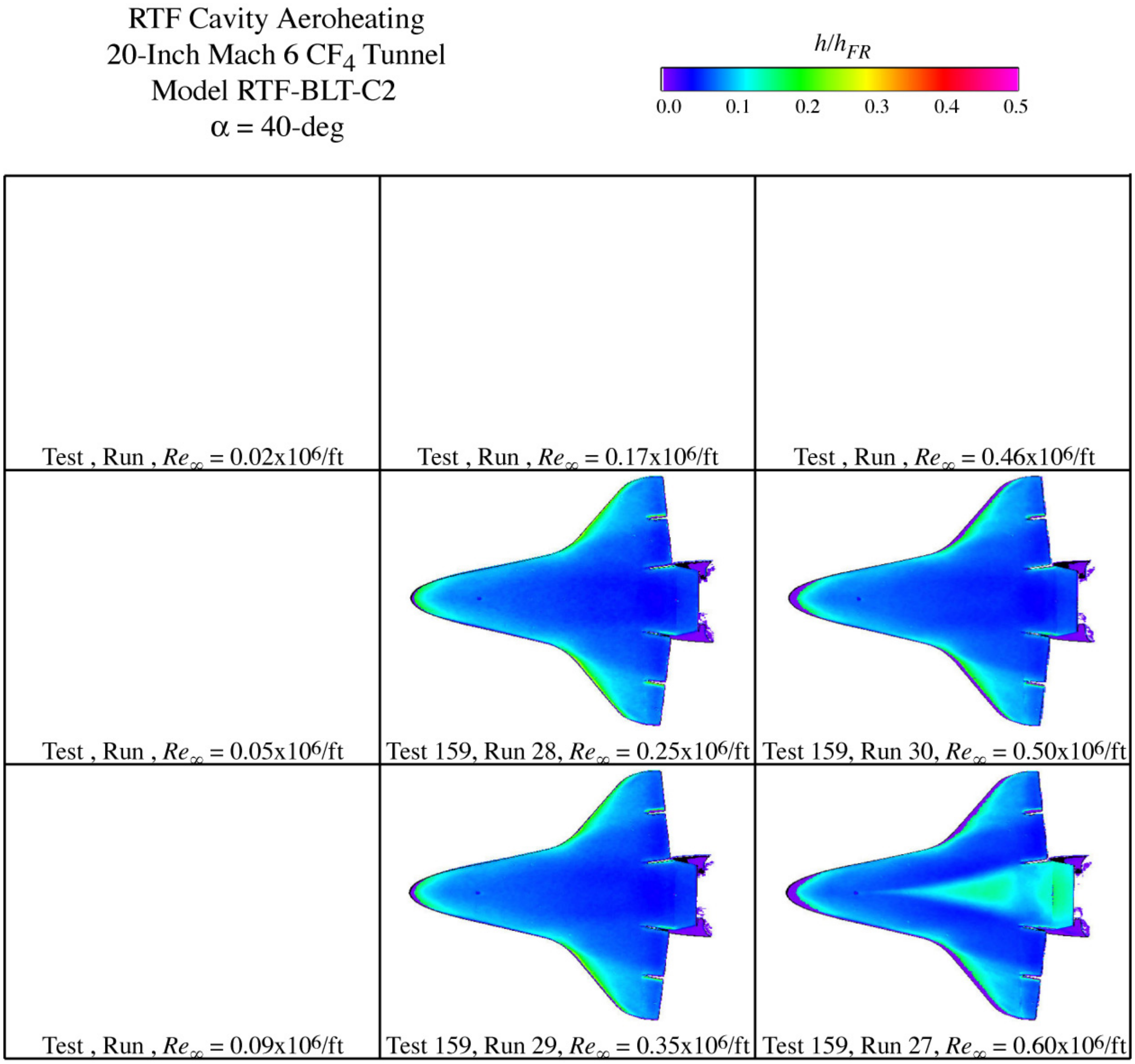

Figure C.8: RTF-BLT-C2 global aeroheating in the 20-Inch CF_4 Tunnel at α = 40-deg.

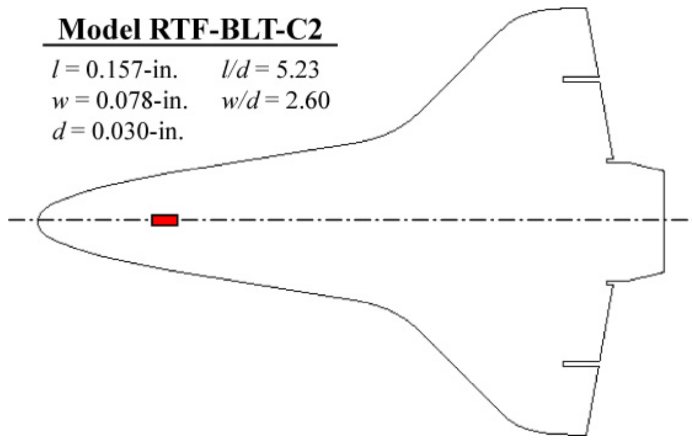

Figure C.9: RTF-BLT-C2 cavity information.

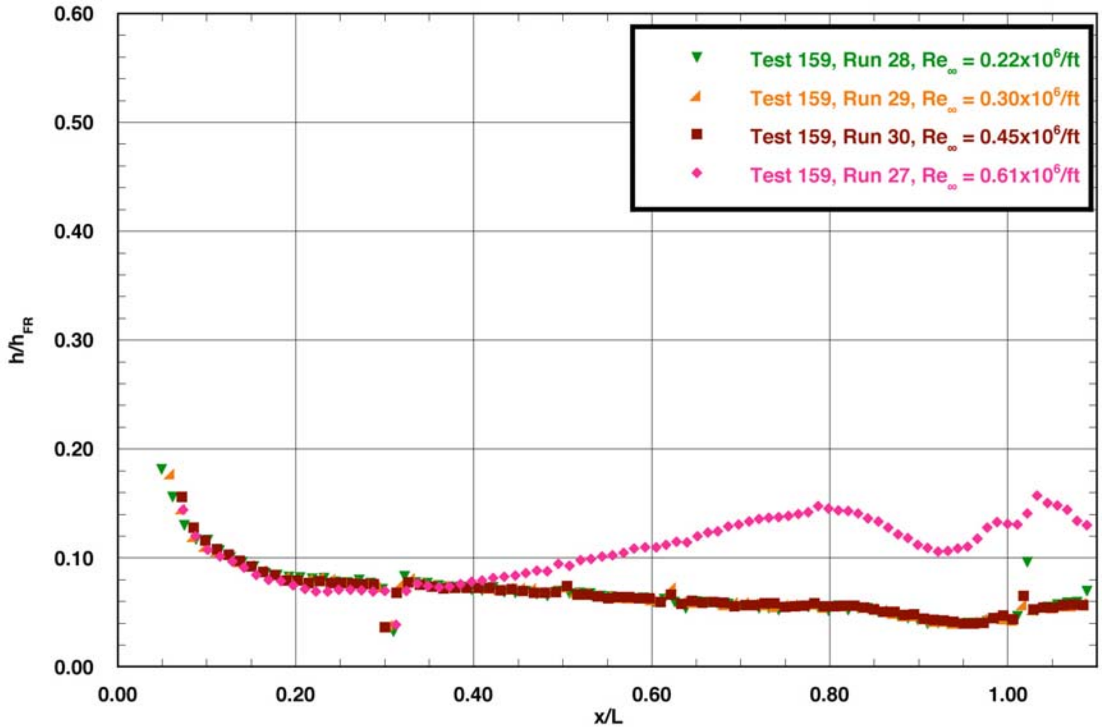

Figure C.10: RTF-BLT-C2 centerline data in the 20-Inch CF_4 Tunnel at α = 40-deg.

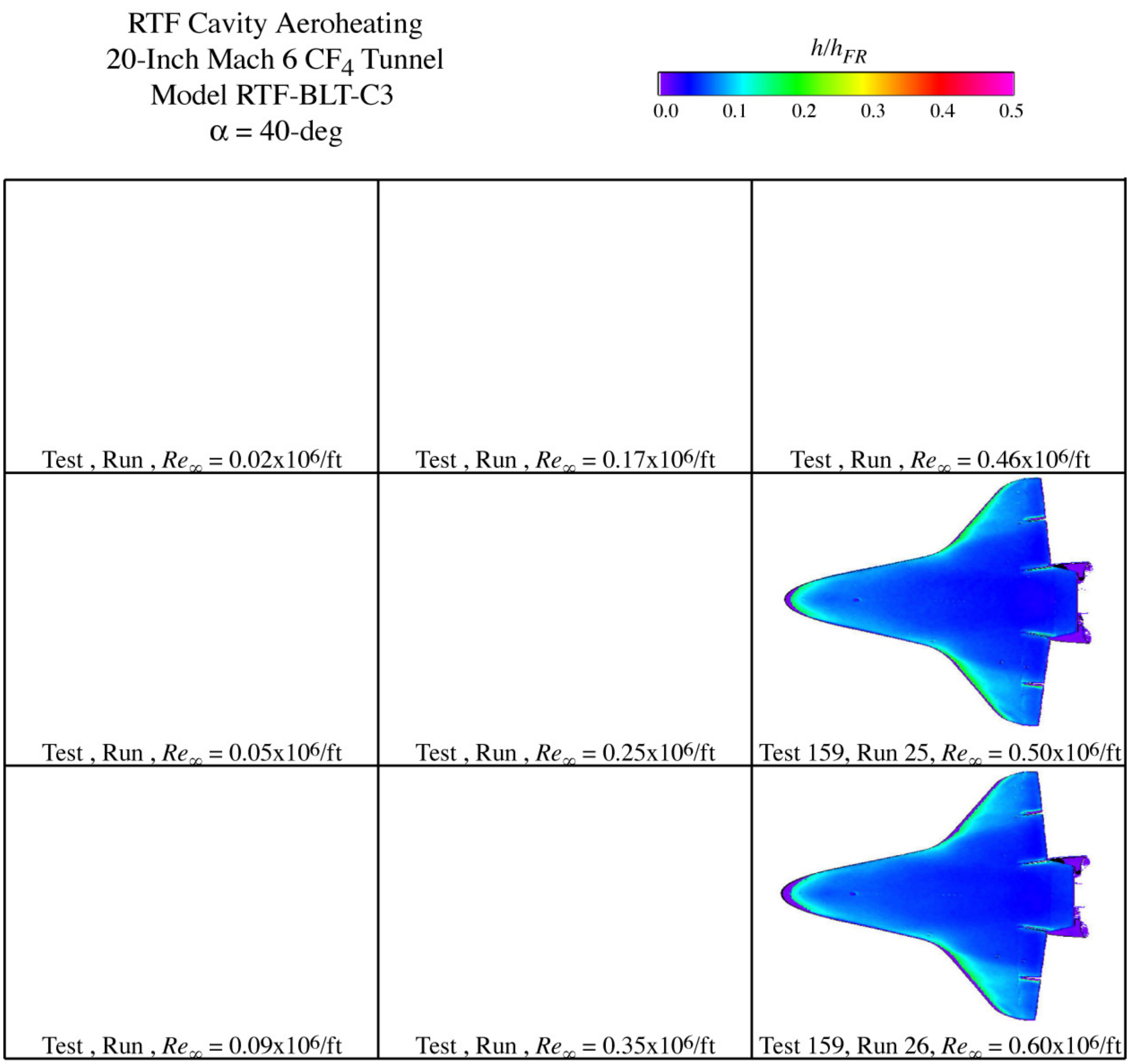

Figure C.11: RTF-BLT-C3 global aeroheating in the 20-Inch CF_4 Tunnel at α = 40-deg.

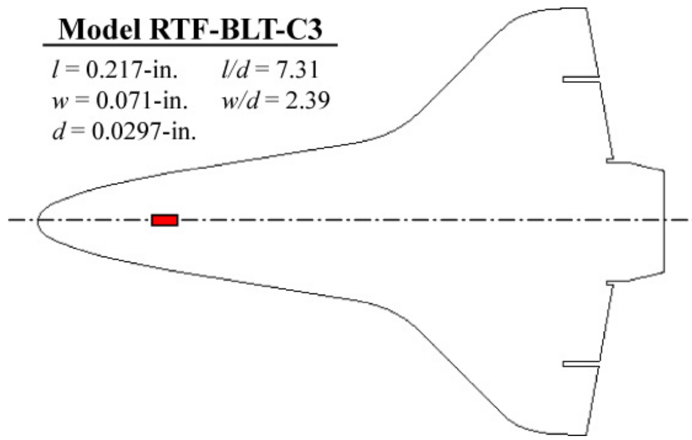

Figure C.12: RTF-BLT-C3 cavity information.

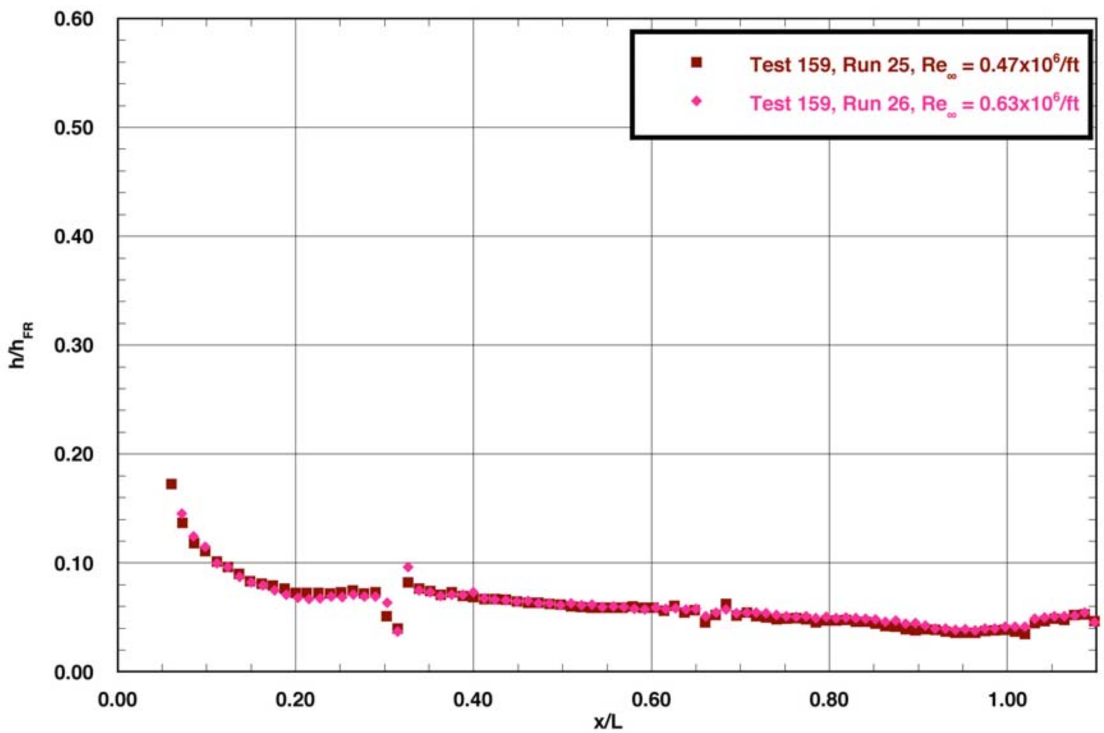

Figure C.13: RTF-BLT-C3 centerline data in the 20-Inch CF_4 Tunnel at α = 40-deg.

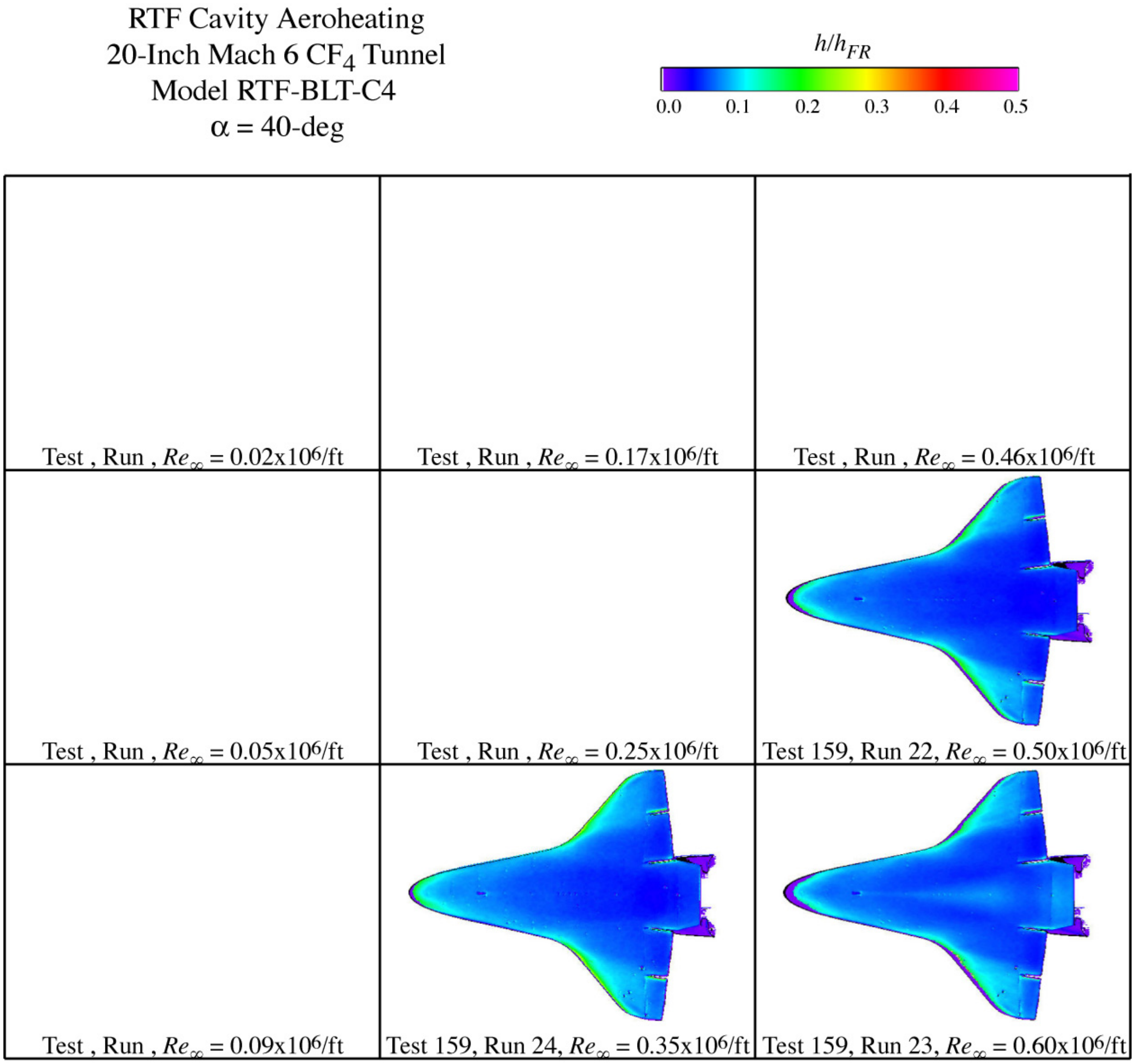

Figure C.14: RTF-BLT-C4 global aeroheating in the 20-Inch CF_4 Tunnel at α = 40-deg.

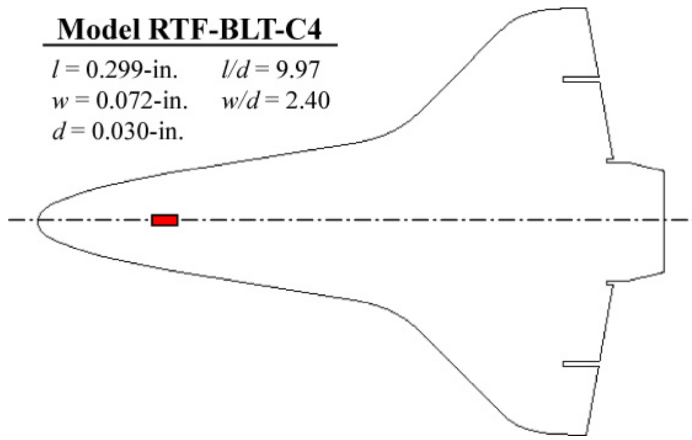

Figure C.15: RTF-BLT-C4 cavity information.

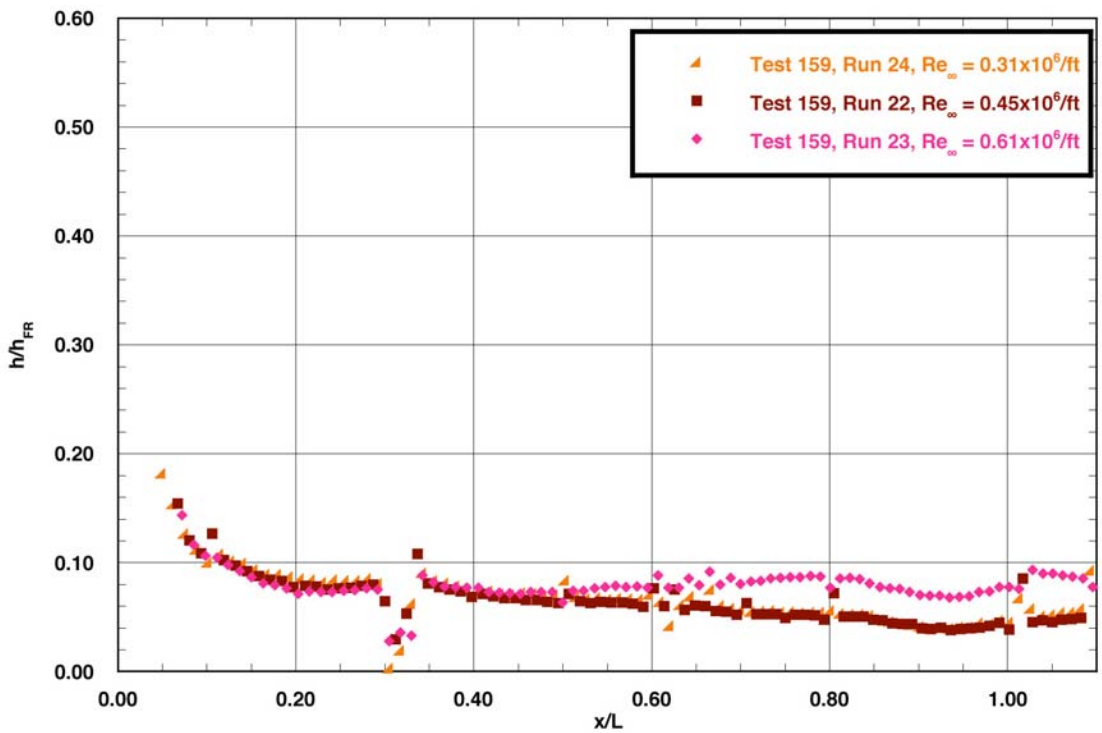

Figure C.16: RTF-BLT-C4 centerline data in the 20-Inch CF_4 Tunnel at α = 40-deg.

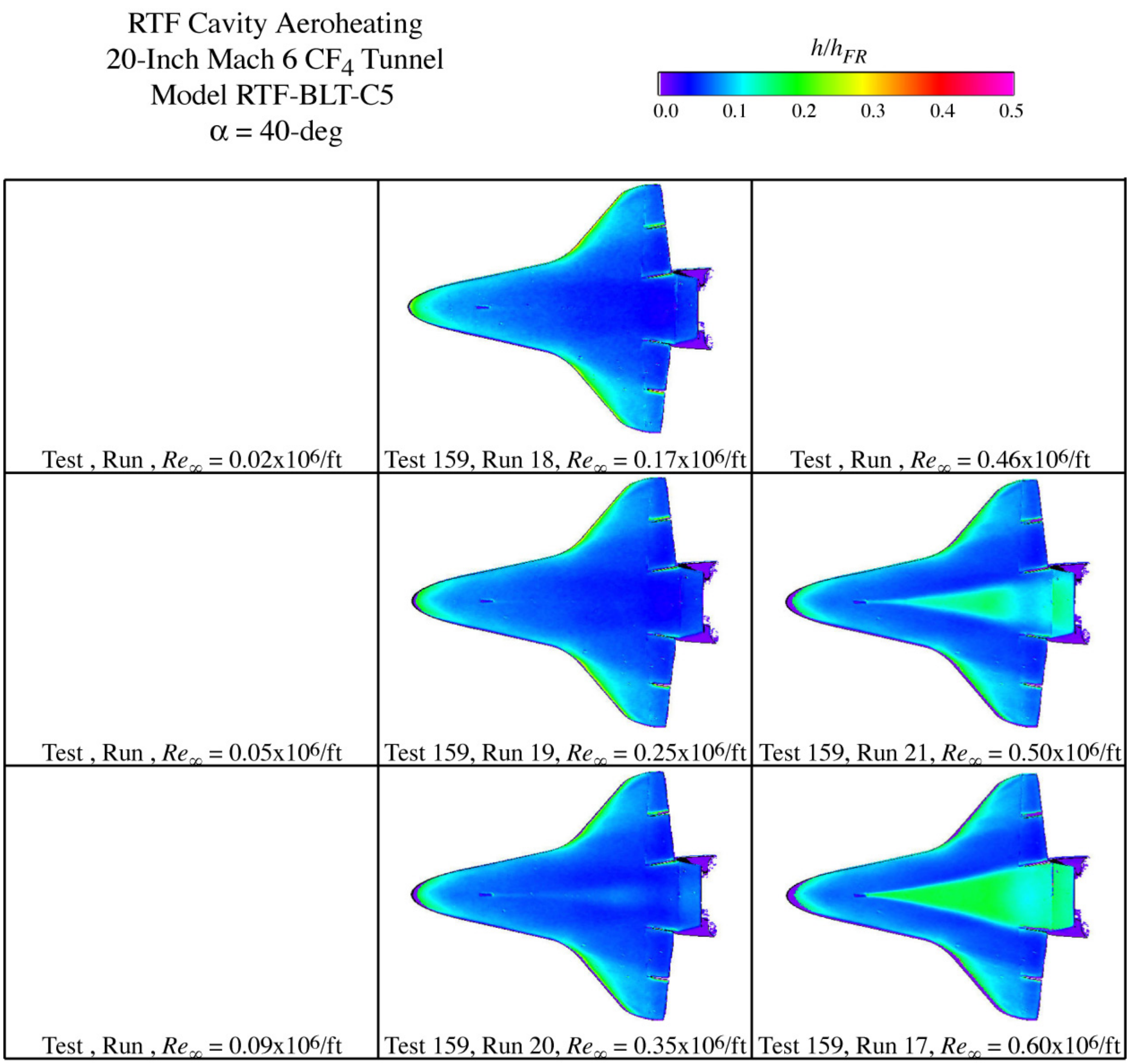

Figure C.17: RTF-BLT-C5 global aeroheating in the 20-Inch CF_4 Tunnel at α = 40-deg.

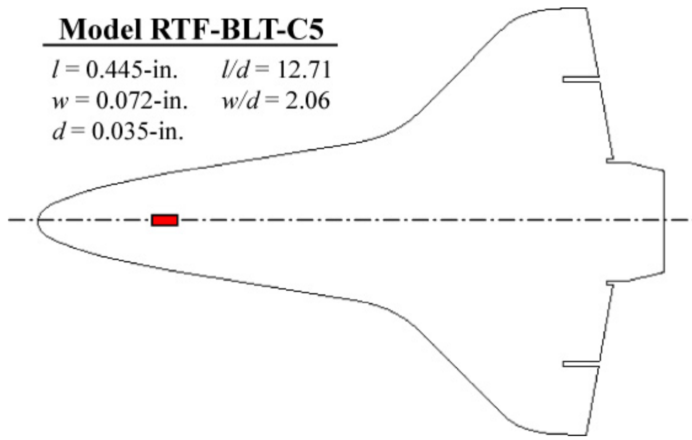

Figure C.18: RTF-BLT-C5 cavity information.

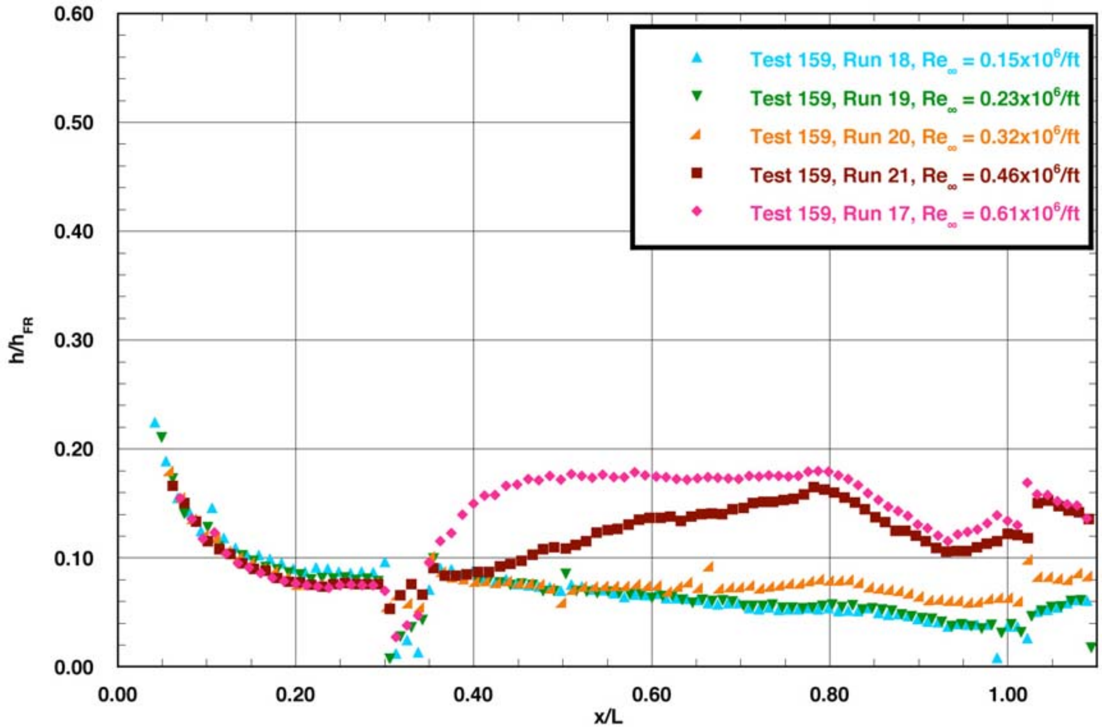

Figure C.19: RTF-BLT-C5 centerline data in the 20-Inch CF_4 Tunnel at α = 40-deg.

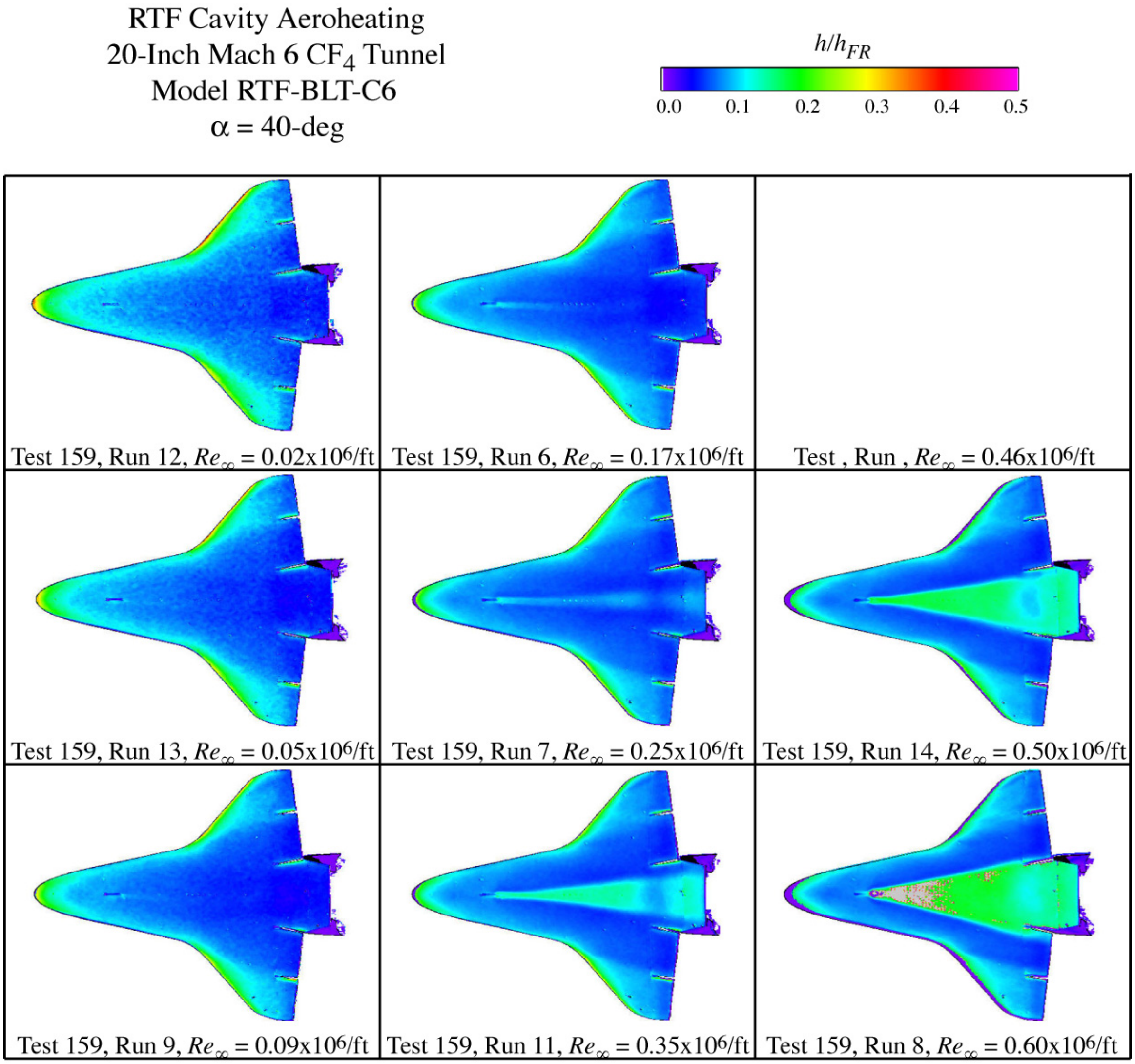

Figure C.20: RTF-BLT-C6 global aeroheating in the 20-Inch CF_4 Tunnel at α = 40-deg.

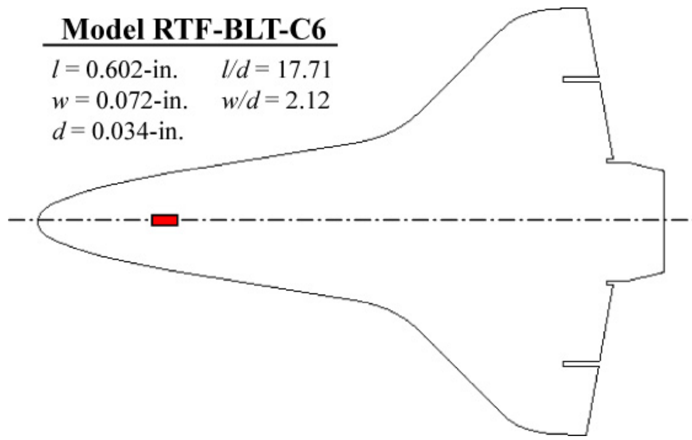

Figure C.21: RTF-BLT-C6 cavity information.

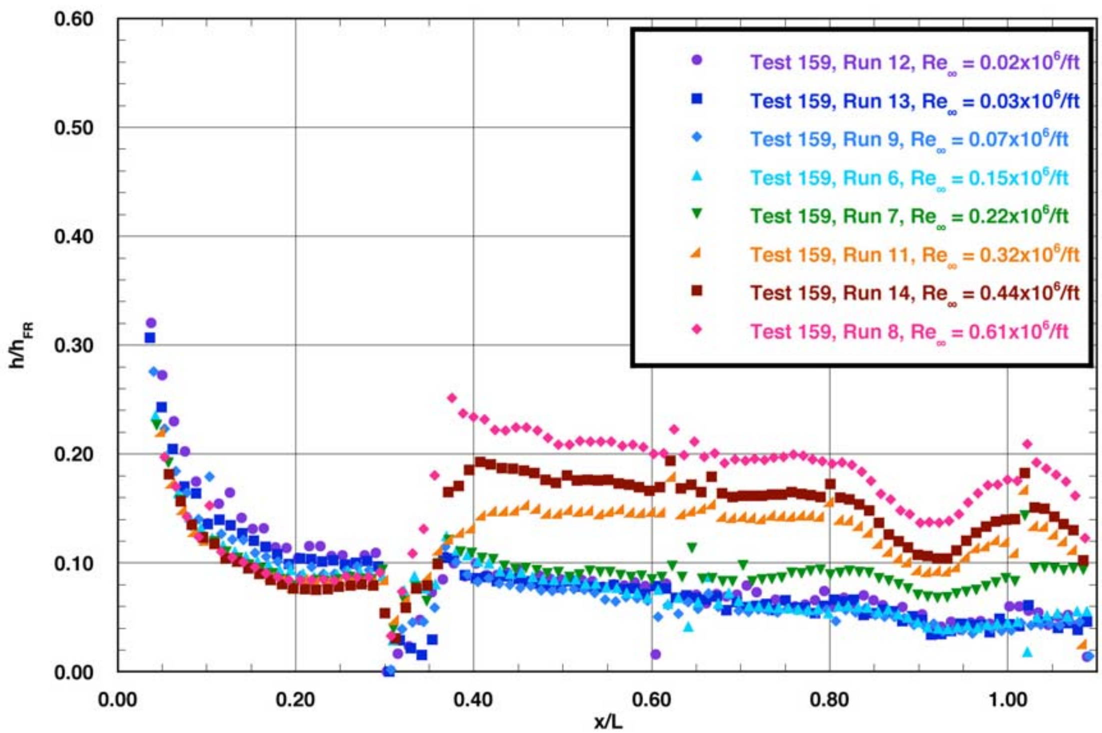

Figure C.22: RTF-BLT-C6 centerline data in the 20-Inch CF_4 Tunnel at α = 40-deg.

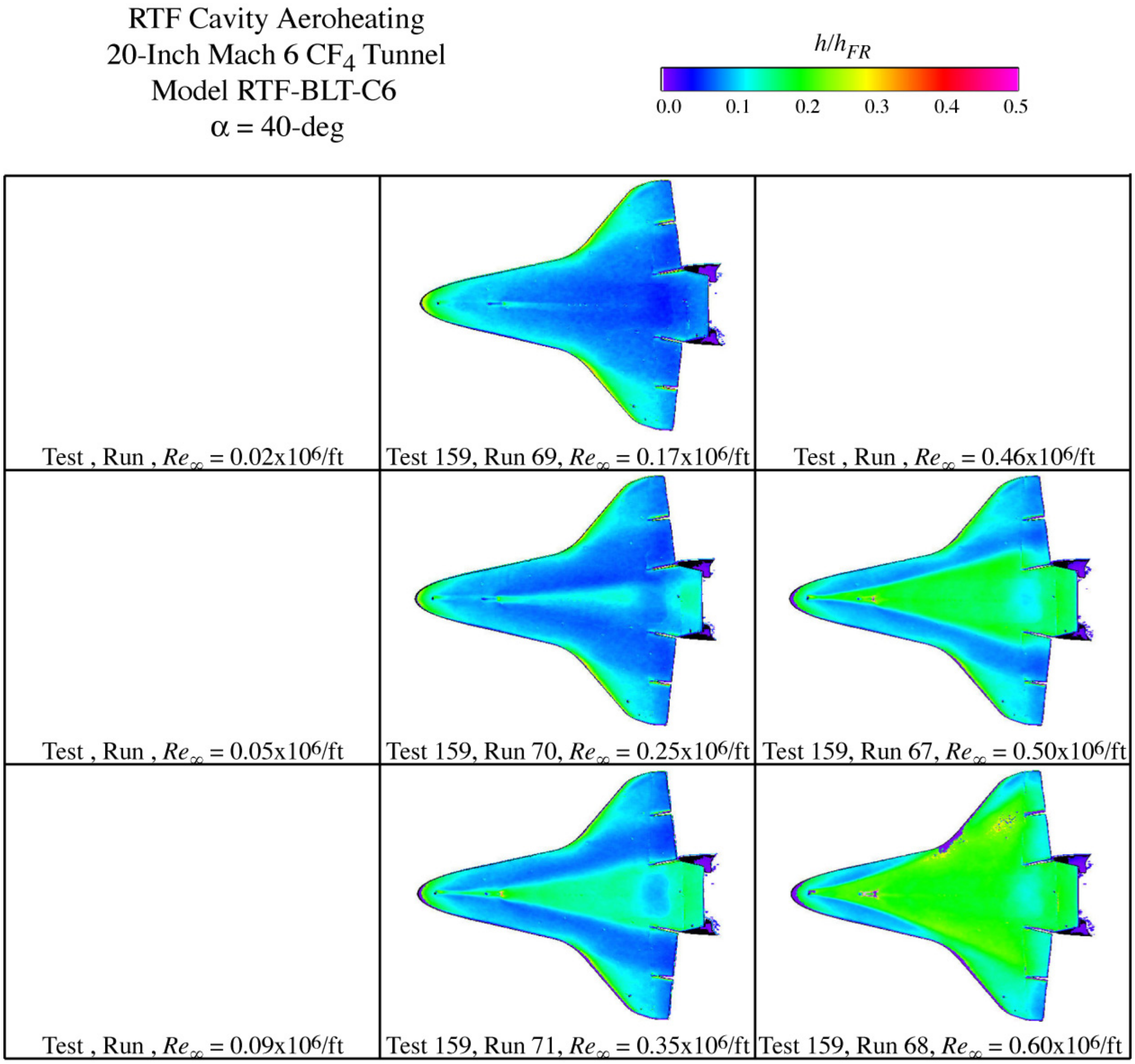

Figure C.23: RTF-BLT-C6 global aeroheating in the 20-Inch CF_4 Tunnel at α = 40-deg, *x/L* = 0.10, k_{CL} = 0.0115 in.

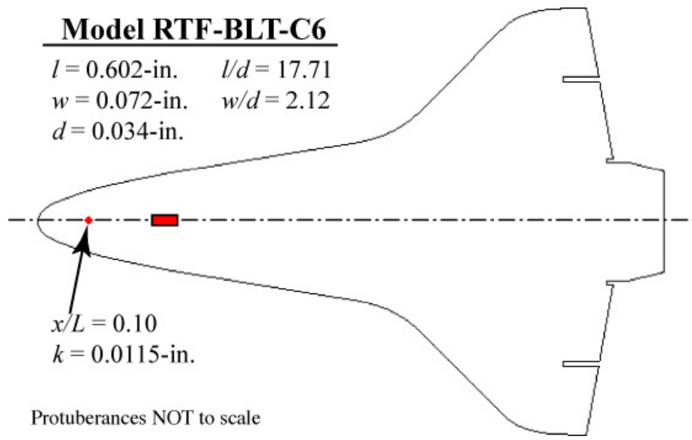

Figure C.24: RTF-BLT-C6 cavity information.

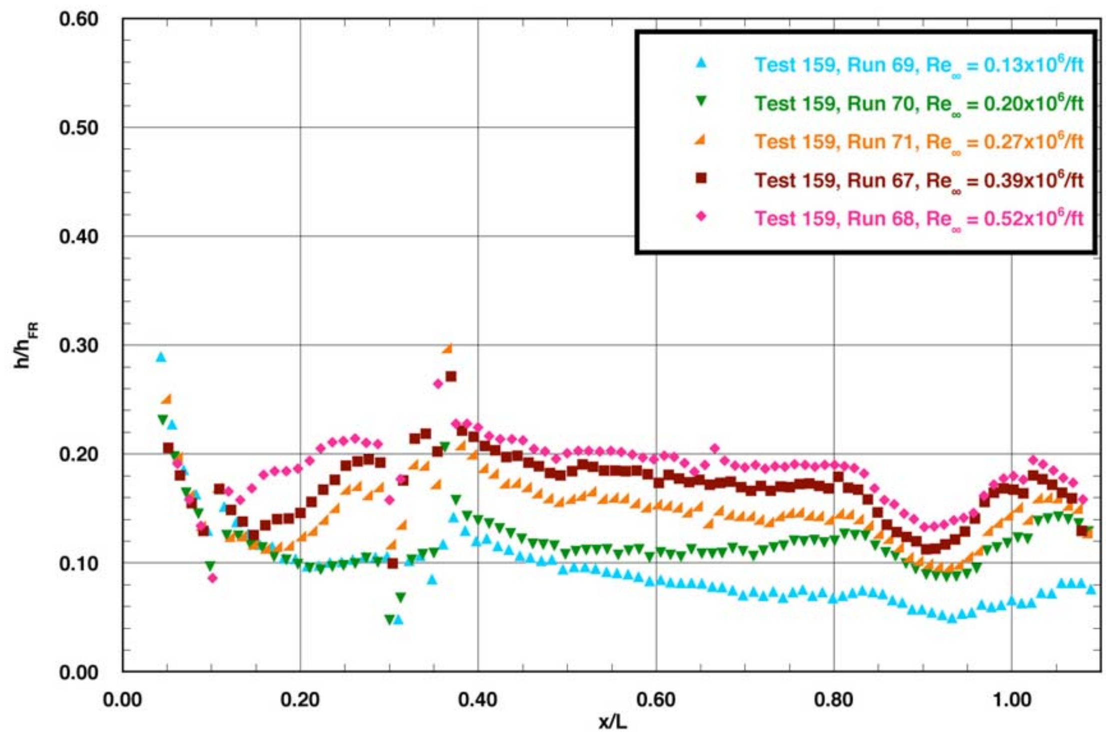

Figure C.25: RTF-BLT-C6 centerline data in the 20-Inch CF_4 Tunnel at α = 40-deg, *x/L* = 0.10, k_{CL} = 0.0115 in.

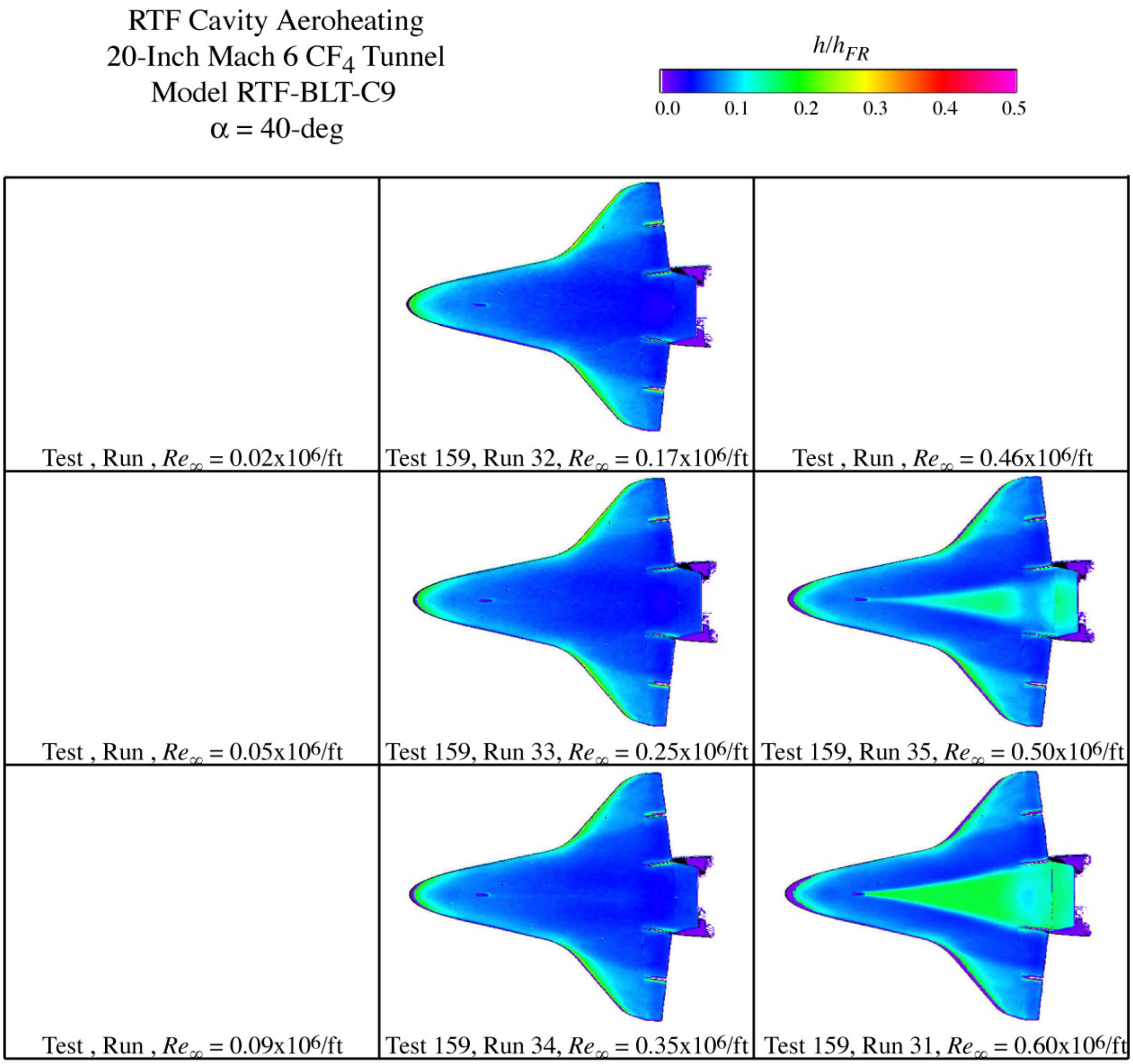

Figure C.26: RTF-BLT-C9 global aeroheating in the 20-Inch CF_4 Tunnel at α = 40-deg.

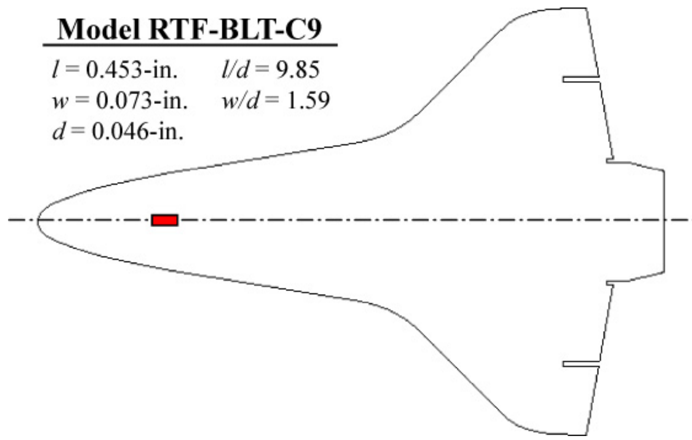

Figure C.27: RTF-BLT-C9 cavity information.

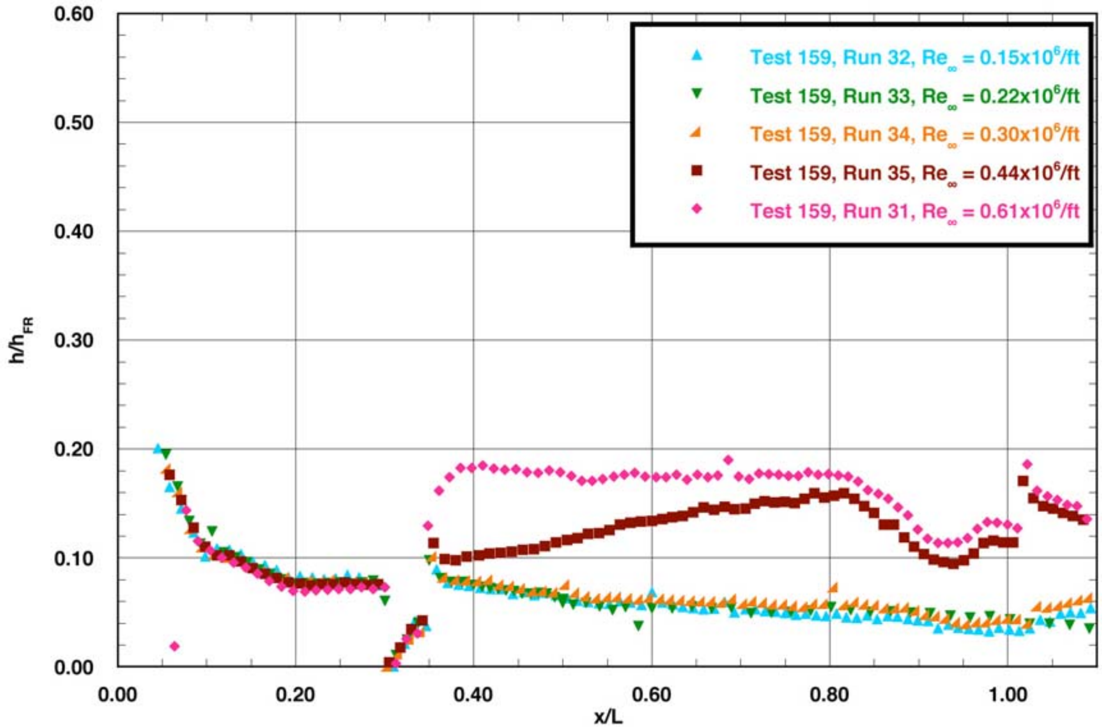

Figure C.28: RTF-BLT-C9 centerline data in the 20-Inch CF_4 Tunnel at α = 40-deg.

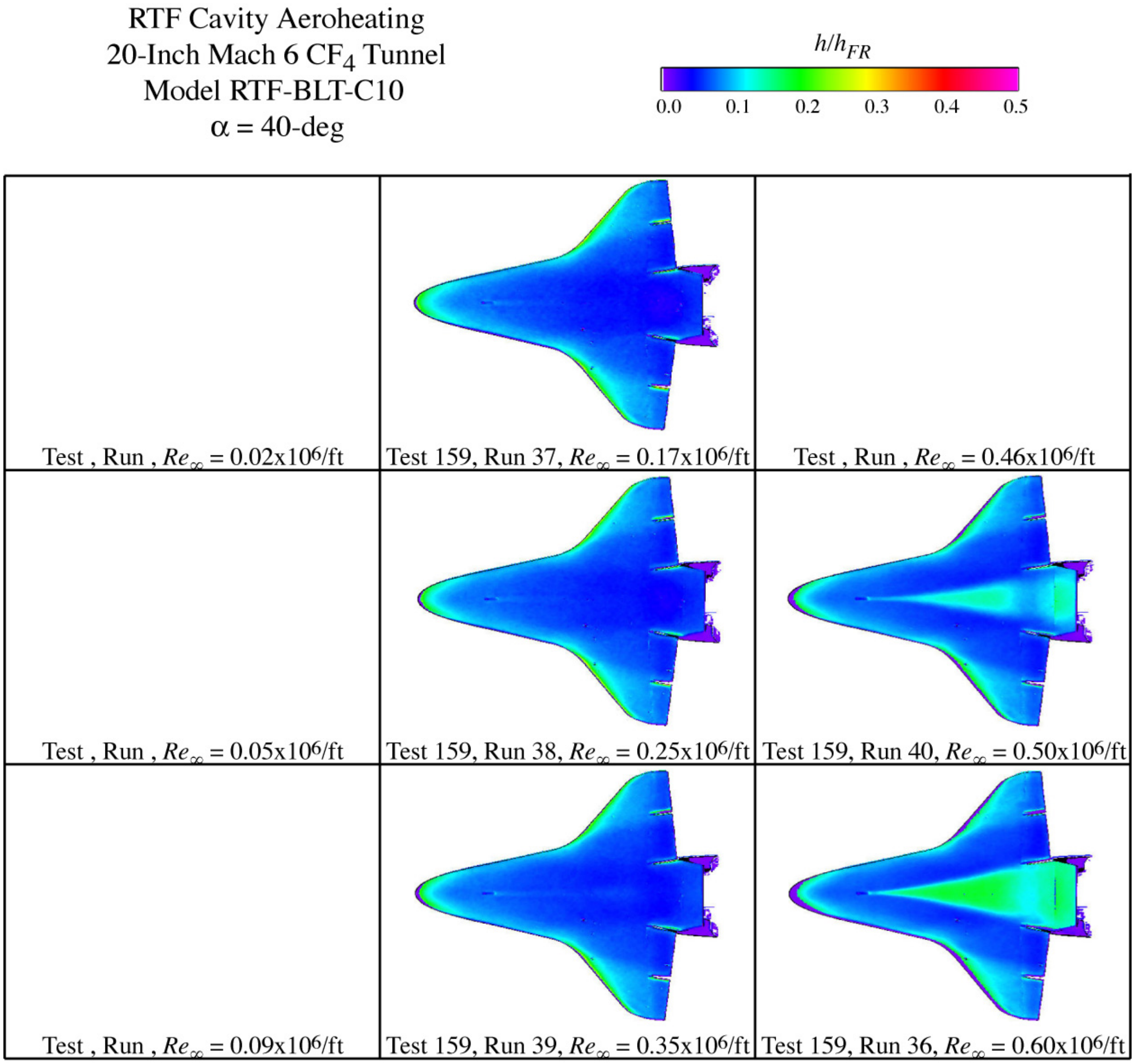

Figure C.29: RTF-BLT-C10 global aeroheating in the 20-Inch CF_4 Tunnel at α = 40-deg.

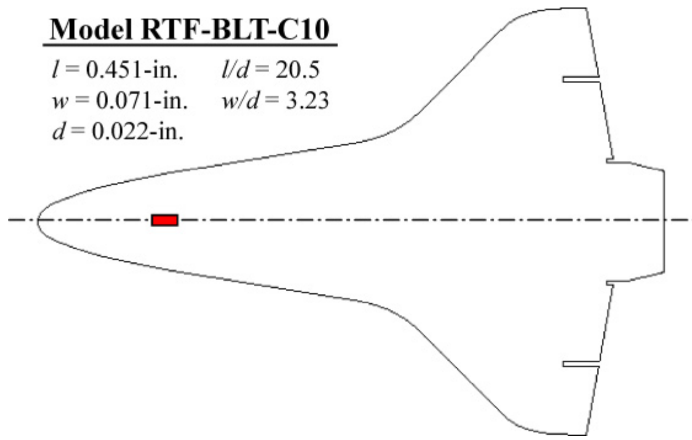

Figure C.30: RTF-BLT-C10 cavity information.

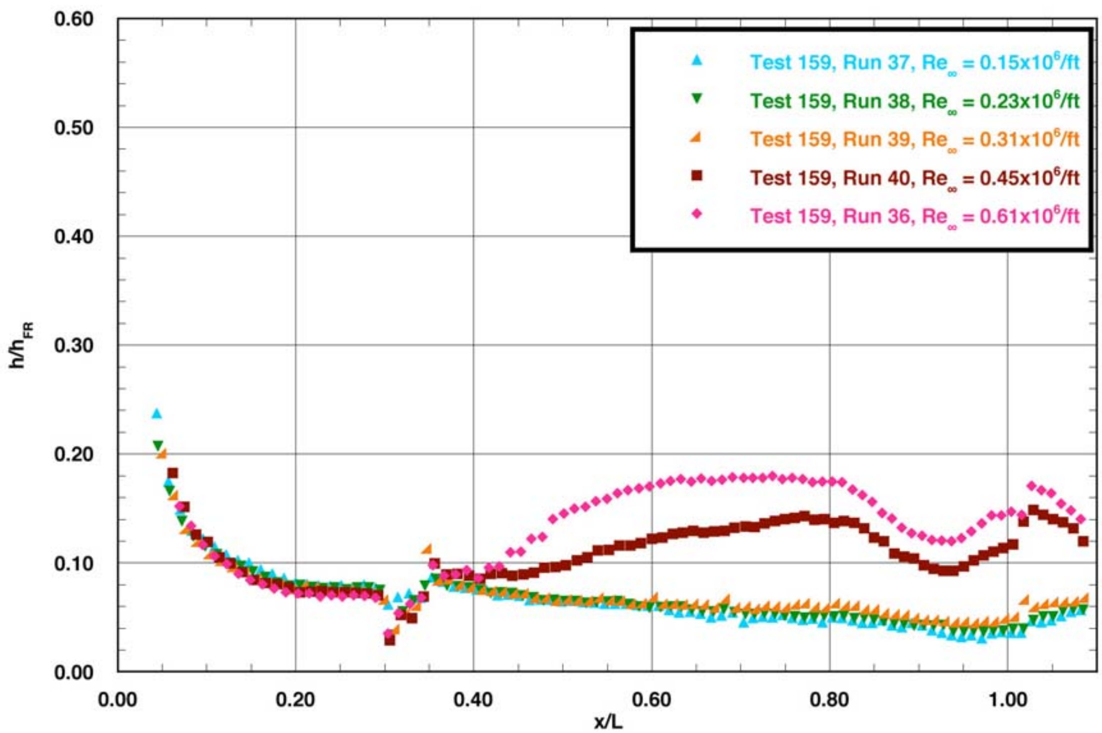

Figure C.31: RTF-BLT-C10 centerline data in the 20-Inch CF_4 Tunnel at α = 40-deg.

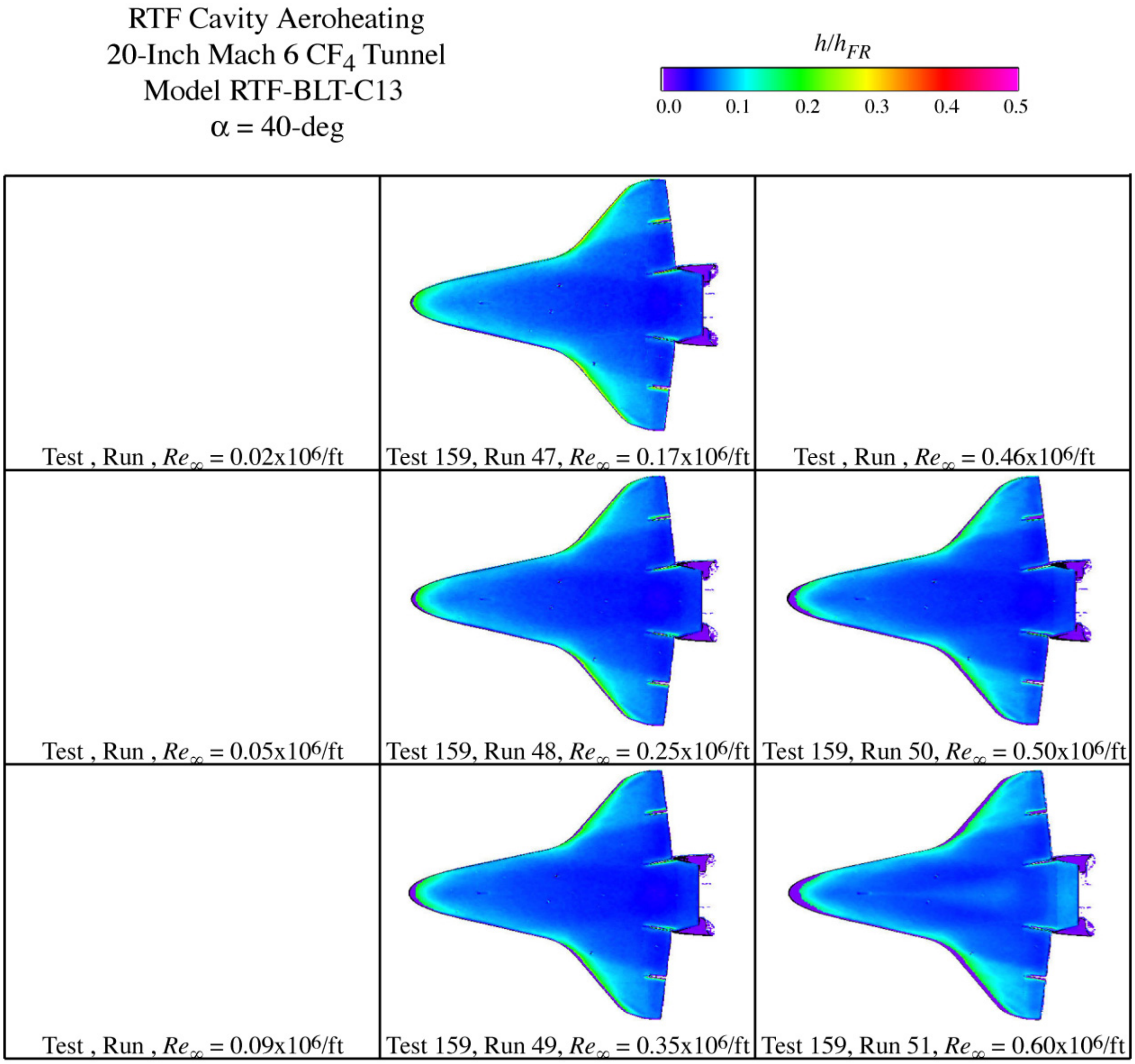

Figure C.32: RTF-BLT-C13 global aeroheating in the 20-Inch CF_4 Tunnel at α = 40-deg.

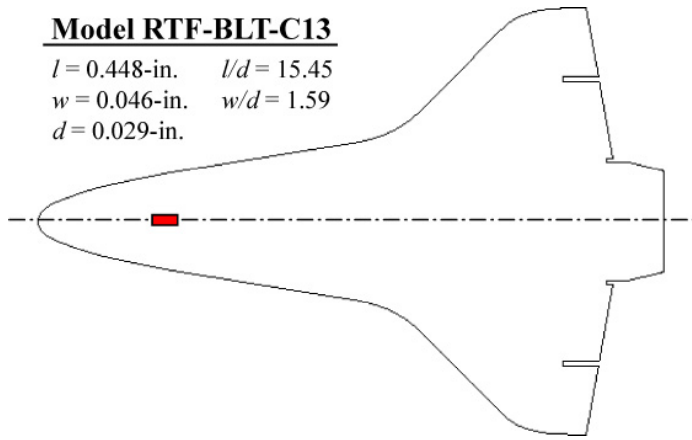

Figure C.33: RTF-BLT-C13 cavity information.

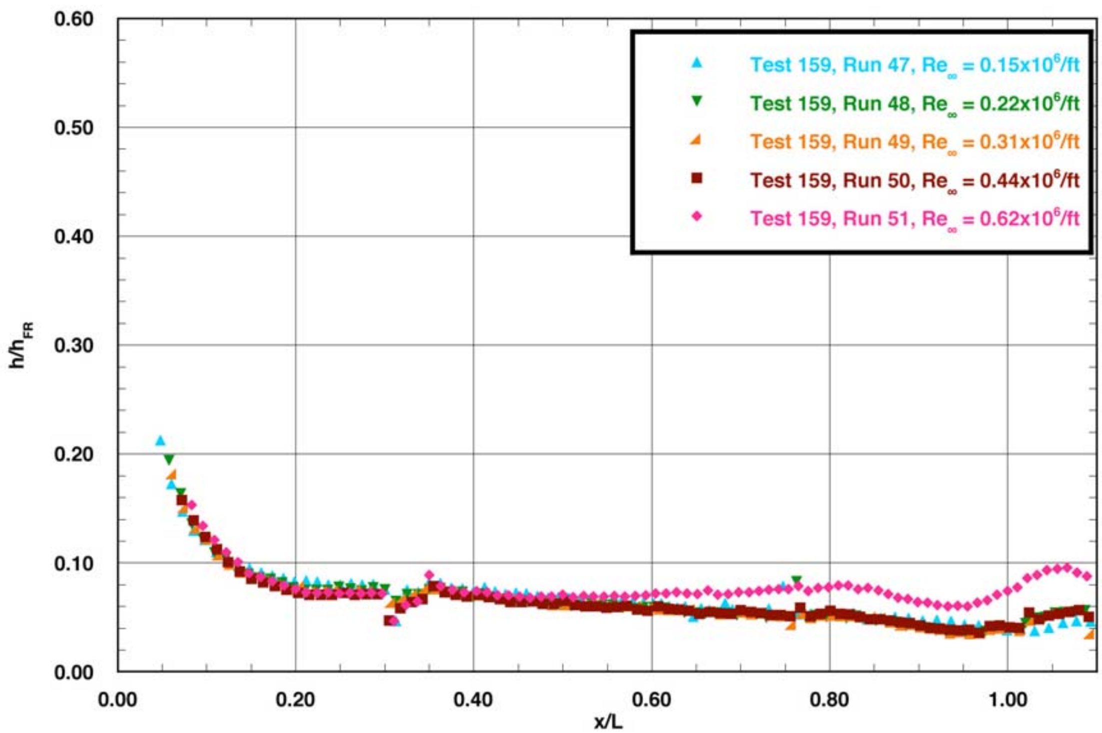

Figure C.34: RTF-BLT-C13 centerline data in the 20-Inch CF_4 Tunnel at α = 40-deg.

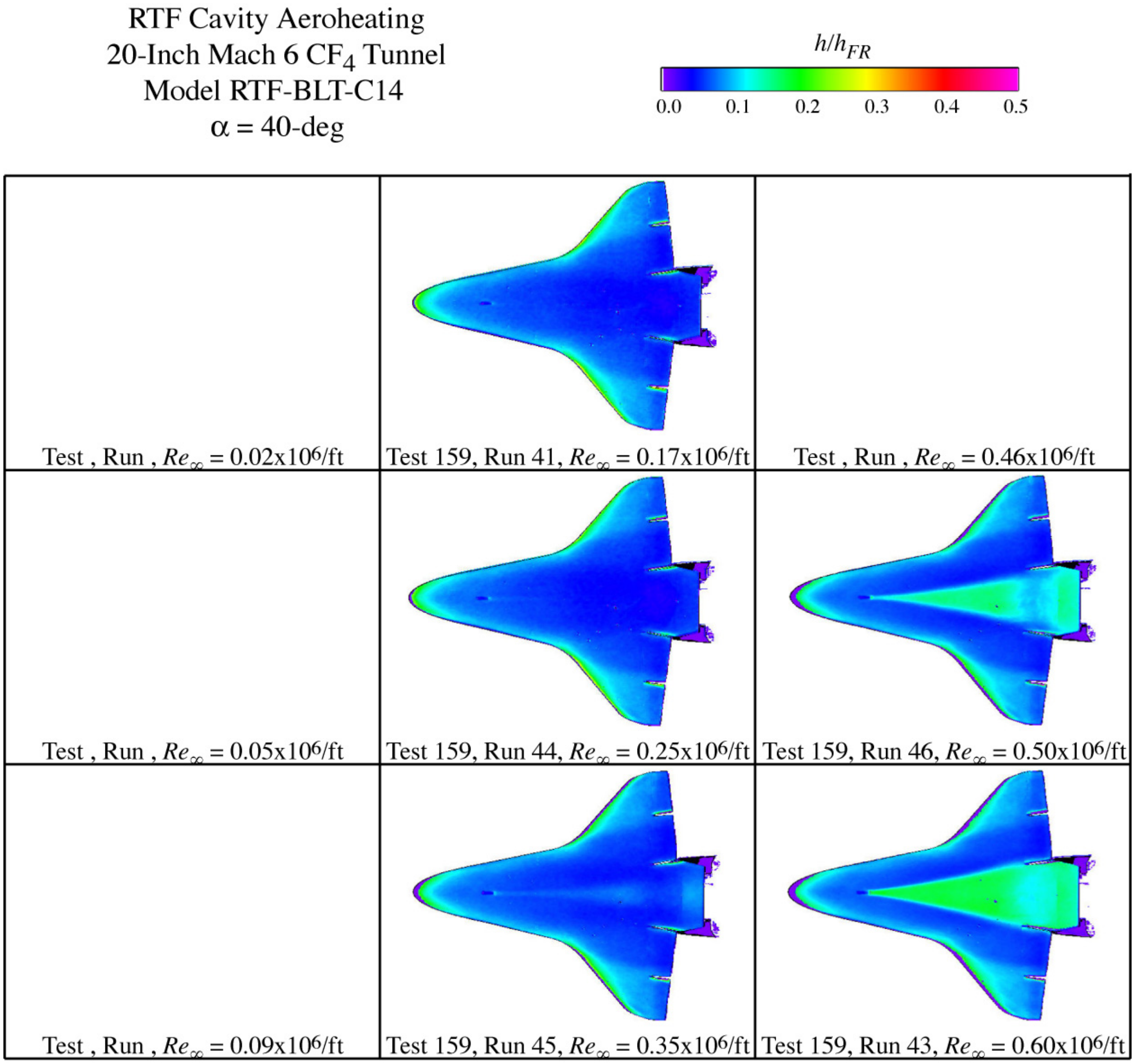

Figure C.35: RTF-BLT-C14 global aeroheating in the 20-Inch CF_4 Tunnel at α = 40-deg.

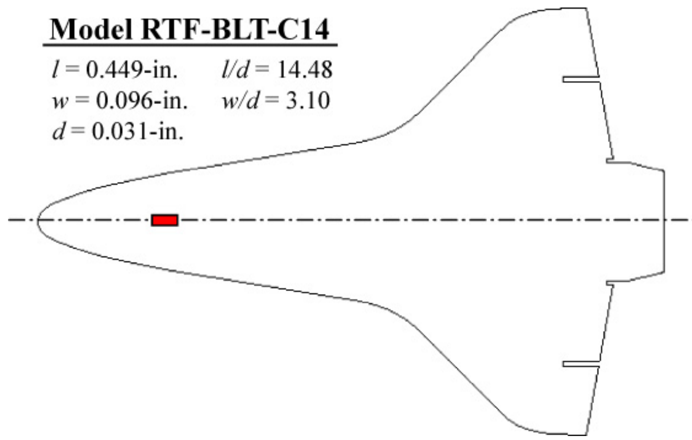

Figure C.36: RTF-BLT-C14 cavity information.

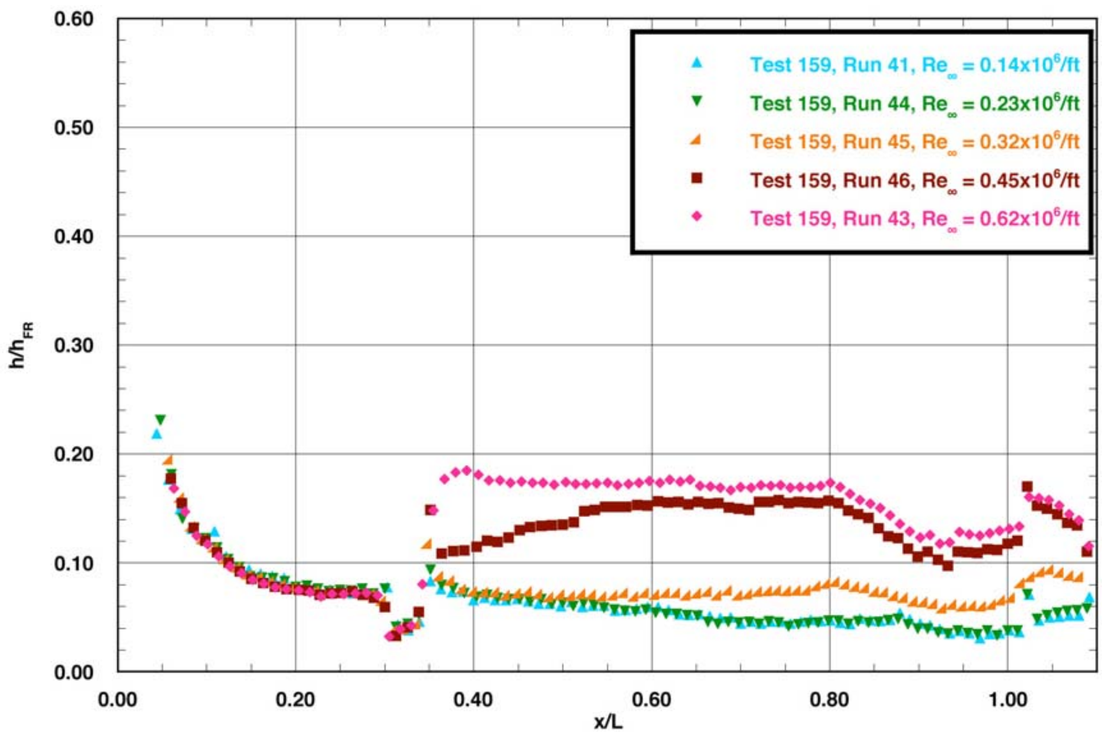

Figure C.37: RTF-BLT-C14 centerline data in the 20-Inch CF_4 Tunnel at α = 40-deg.

REPORT DOCUMENTATION PAGE	*Form Approved* *OMB No. 0704-0188*

1. REPORT DATE *(DD-MM-YYYY)*	**2. REPORT TYPE**	**3. DATES COVERED** *(From - To)*
01- 06 - 2006	Technical Memorandum	

4. TITLE AND SUBTITLE Shuttle Return To Flight Experimental Results: Cavity Effects on Boundary Layer Transition	**5a. CONTRACT NUMBER**
	5b. GRANT NUMBER
	5c. PROGRAM ELEMENT NUMBER
6. AUTHOR(S) Liechty, Derek S.; Horvath, Thomas J.; and Berry, Scott A.	**5d. PROJECT NUMBER**
	5e. TASK NUMBER
	5f. WORK UNIT NUMBER 732759.07.05
7. PERFORMING ORGANIZATION NAME(S) AND ADDRESS(ES) NASA Langley Research Center Hampton, VA 23681-2199	**8. PERFORMING ORGANIZATION REPORT NUMBER** L-19256
9. SPONSORING/MONITORING AGENCY NAME(S) AND ADDRESS(ES) National Aeronautics and Space Administration Washington, DC 20546-0001	**10. SPONSOR/MONITOR'S ACRONYM(S)** NASA
	11. SPONSOR/MONITOR'S REPORT NUMBER(S) NASA/TM-2006-214305

12. DISTRIBUTION/AVAILABILITY STATEMENT
Unclassified - Unlimited
Subject Category 34
Availability: NASA CASI (301) 621-0390

13. SUPPLEMENTARY NOTES
An electronic version can be found at http://ntrs.nasa.gov

14. ABSTRACT
The effect of an isolated rectangular cavity on hypersonic boundary layer transition of the windward surface of the Shuttle Orbiter has been experimentally examined in the Langley Aerothermodynamics Laboratory in support of an agency-wide effort to prepare the Shuttle Orbiter for return to flight. This experimental study was initiated to provide a cavity effects database for developing hypersonic transition criteria to support on-orbit decisions to repair a damaged thermal protection system. Boundary layer transition results were obtained using 0.0075-scale Orbiter models with simulated tile damage (rectangular cavities) of varying length, width, and depth. The database contained within this report will be used to formulate cavity-induced transition correlations using predicted boundary layer edge parameters.

15. SUBJECT TERMS
Space Shuttle Orbiter; Thermal protection system; Boundary layer transition; Cavity effects

16. SECURITY CLASSIFICATION OF:			**17. LIMITATION OF ABSTRACT**	**18. NUMBER OF PAGES**	**19a. NAME OF RESPONSIBLE PERSON**
a. REPORT	**b. ABSTRACT**	**c. THIS PAGE**			STI Help Desk (email: help@sti.nasa.gov)
					19b. TELEPHONE NUMBER ***(Include area code)***
U	U	U	UU	146	(301) 621-0390